Rate-induced Critical Transitions

Chun Xie
M.Sc.
116220522

NATIONAL UNIVERSITY OF IRELAND, CORK

School of Mathematical Sciences

Department of Applied Mathematics

Thesis submitted for the degree of Doctor of Philosophy

April 2020

Head of Department: Prof Sebastian Wieczorek

Supervisor: Prof Sebastian Wieczorek

April 2020

Research supported by the Innovation Training Network (ITN)-CRITICS under EU Horizon 2020 Marie Skłodowska-Curie Grant Agreement No.643073

Contents

I, Chun Xie, certify that the work I am submitting is my own and has not been submitted for another degree, either at University College Cork or elsewhere. All external references and sources are clearly acknowledged and identified within the contents. I have read and understood the regulations of University College Cork concerning plagiarism.

Chun Xie

Abstract

This thesis focuses on rate-induced critical transitions or tipping points (R-tipping points), where the system undergoes a critical transition if the time-varying external conditions vary faster than some critical rate. Such a critical transition is usually a sudden and unexpected change of the system state. The change can be either irreversible: a permanent tipping point with no return to the original state, or reversible: a temporary tipping point with self-recovery back to the original state, both of which may cause significant consequences in applications. Indeed, R-tipping is an ubiquitous nonlinear phenomenon in nature that remains largely unexplored by the scientists. From a mathematical viewpoint, it is a genuine nonautonomous instability that cannot be explained by the classical (autonomous) bifurcation theory and requires an alternative approach.

The first part of the thesis focuses on a mathematical framework for R-tipping in systems of nonautonomous differential equations, where the nonautonomous terms representing time-varying external conditions decay asymptotically. In particular, special compactification techniques for asymptotically autonomous systems are developed to simplify analysis of R-tipping.

In the second part of the thesis, the main concepts of edge states and thresholds are introduced to define the R-tipping phenomenon. Then, simple testable criteria for the occurrence of reversible and irreversible R-tipping in arbitrary dimension are given. This part extends the previous results on irreversible R-tipping in one dimension.

The third part of the thesis identifies canonical examples of R-tipping based on the system dimension, timescales and the threshold type. These examples are relatively simple low-dimensional nonlinear systems that capture different R-tipping mechanisms. R-tipping analysis of canonical examples, which is underpinned by the compactification framework developed in the second part, reveals intricate R-tipping diagrams with multiple critical rates and transitions between different types of R-tipping.

Acknowledgements

Firstly, I would like to give my highest respect and thanks to my supervisor Prof. Sebastian Wieczorek, and it is a great experience to follow Prof. Wieczorek that I could have learned so much besides the knowledge. I appreciate the help from Prof. Wieczorek during the whole project, especially during the last year when I had some health problems. I would like to thank Peter Ashwin and Chris K.R.T. Jones for the contribution to the project and useful discussions. I am also grateful for the supervision of Jan Sieber on the project of agent-based models during the secondment at University of Exeter.

This project is funded by the CRITICS Innovative Training Network via the European Union's Horizon 2020 research and innovation programme under Grant Agreement No. 643073. Thanks for the support from CRITICS, I could also have participated in those interesting and constructive scientific trainings and activities within the network, which gives me the opportunity to meet many excellent experts and researchers with different mathematical background, and provides me with a lot more insights of mathematical methodologies, e.g. the lectures of random dynamics given by Jeroen Lamb, the trainings of nonautonomous dynamical systems and the notes of measure theory given by Martin Rasmussen, the short course of the numerical methods for stochastic processes given by Kathrin Padberg-Gehle, the mini-project of single cell data analysis given by Alexander Skupin, the short course of the equation-free approaches given by Jens Starke, and etc. In addition, I got the chances to communicate and work with other early-stage researchers within the network to get through their research projects and other interesting topics.

I would also like to thank the host of University College Cork and University of Exeter, and the staffs in the mathematical school or department who gave the help and suggestion on the administration affairs. It is a good memory to be with Paul, Anthony, Christopher, Andrew, Adrian, Eduardo and all the other members in the research lab of mathematics, and thanks for their help during the three years.

Finally, I would like to thank my family members, who give me the support by all means no matter when and where what happens.

Chapter 1

Introduction

In layman's terms, "critical transitions" or "tipping points" are *large, sudden* and *unexpected* changes in the state of a complex system that are triggered by *small* or *slow* changes in the time-varying external conditions or inputs. Tipping points occur in different areas of science, including climate science [1, 2, 3, 4], biology [5, 6, 7, 8, 9] and ecology [10, 11, 12, 13], and in engineering [14, 15, 16, 17]. The main challenge is to understand mathematical mechanisms of tipping and the ensuing critical factors. This is important for the identification of the early warning signals, mitigation strategies and system control.

1.1 Tipping points

To present the scenarios of tipping points, we assume a system has one stable state and the system is initialized nearby the stable state. If there is no external disturbance, the system will settle down at the stable state over time. However, the system is subject to some time-varying external inputs, which we assume the stable state depends on. That is to say, as the external inputs change with time, the position of the stable state will also change, which we describe as a *moving stable state*; see Definition 3.2.2. In some cases, the system can *adapt* to the time-varying external inputs and *track* the moving stable state with time. However, under some other circumstances, the system cannot track the moving stable state any more but *tips* to a different state. This tracking-tipping transition might be due to different tipping mechanisms such as the loss of the stable state itself, the change in the stability of the stable state, or the system leaving the stability domain of the stable state. In fact, these tipping mechanisms can be interpreted mathematically in the context of dynamical systems.

1.1.1 Categories of tipping points

According to different tipping mechanisms, tipping points are generally classified into three categories: *bifurcation-induced tipping (B-tipping)* [18, 19, 20] also known as *dynamical bifurcation* [21] or *adiabatic bifurcation* [22], *noise-induced tipping (N-tipping)* [18], and *rate-induced tipping (R-tipping)* [23, 12, 24, 18, 25, 26, 13].

B-tipping is defined in terms of a *critical level* of the external inputs. That is to say, as the external input varies and approaches the critical level, the system undergoes a classical bifurcation, where the moving stable state of the system disappears or destabilises [19, 20, 27]. After that, the system cannot track the moving stable state any more but tips to a different state. There is a wide range of research studying critical levels. In climate science, the thermohaline circulation possibly collapses as the freshwater influx into the North Atlantic exceeds a critical level [2, Ch.16], and the reports of the *Intergovernmental Panel for Climate Change* specify the critical levels of atmospheric temperature and CO2 concentration [3]. In biology, the biological switching occurs at critical levels, e.g. the cell phase transition occurs past the critical level of concentration of cyclin-dependent kinase during the cell cycle [7, 8]. What is more, the onset of periodic oscillations at a "threshold" level in many biological processes such as neuronal oscillations and cardiac rhythms [28, 9, 29]. In ecology, the loss of submerged vegetation in shallow turbid lakes possibly happens because of the critical nutrient concentration level and the forest-to-desert transitions can take place due to a critical precipitation level [10, Ch.7, Ch.11]. In engineering, the power grid system blackouts when the power consumption exceeds a critical level [14, 15].

N-tipping is solely due to the noisy fluctuations driving the system away from the moving stable state and past its domain of stability. Such noisy fluctuations are more studied in climate science to understand the driving factors of climate variations and transitions [30, 20, 18], and the stochastic dynamics in economics, finance and other social sciences [31, 32, 33]. There are also some studies on the exploration of B-tipping in the presence of noise [19, 34].

In the absence of any critical level or noisy fluctuation, there can still be R-tipping, which cannot be explained by the mechanisms of B-tipping (i.e. classical bifurcations) or N-tipping (noise). To be more precise, R-tipping happens only when the external inputs vary fast enough. While the the moving stable state persists continuously, the system has not enough time to adapt to and track the moving stable state and, as a result, transitions to some other state. That is to say, the critical factor for R-tipping is a *critical rate of change* of the external

input. This tipping mechanism has been identified and discussed most recently. The typical examples include the sudden release of soil carbon from peatlands into the atmosphere above some critical rate of atmospheric warming [35, 24], and the collapse of herbivore-plant ecosystems above some critical plant growth rate [12]. Indeed, it is necessary to distinguish and understand those different tipping mechanisms separately so that we can explore the systems in practice, which can encompass various tipping mechanisms.

1.1.2 Motivation of R-tipping

This project is focused on R-tipping, which is least understood by the scientists but ubiquitous in nature. Systems that exhibit R-tipping may be insensitive to the level of the external inputs, but are very sensitive to the rate of change of the external inputs. That is to say, as the external inputs change faster than some critical rate, the systems can suddenly and unexpectedly tip to a different state [23, 12, 24, 18, 25, 26, 13].

Such critical rates of change are of special interest in climate science and ecology e.g. Atlantic Meridional Overturning Circulation possibly collapses as the fresh-water forcing rate varies [4], salt marsh ecosystems can be destabilized by an increasing rate of relative sea-level rise [23], climate varies too fast for animals and plants to adapt to [36, 37] and significant changes of more general ecosystems take place due to the fast environmental variability [12, 13].

Besides, there are many other areas of science and industry in which critical rates are important e.g. the critical rate of temperature rise for thermal explosion in chemical processes [38, 16], the critical oil rate for bottom water coning in anisotropic and homogeneous formations during oil production [39], the critical forcing frequency of resonance in vibration analysis [17], and the “chasing problem” in the context of supply, demand and prices trying to adapt to a changing equilibrium in competitive economy [40]. Particularly in neuroscience, the “fire” condition of type-III nerves is a fast enough increase in the applied voltage as type-III nerves are able to accommodate slow changes in the applied voltage up to very high voltage levels [5, 6, 41, 9]. This is in contrast to type-I or II nerves that require sufficient levels of the external voltage to “fire”. No matter whether the critical rate-dependence is needed to trigger some specific processes or needs to be avoided for unexpected consequences, it is crucial to study those R-tipping mechanisms. There are several challenges and difficulties for scientists to analyze and understand R-tipping.

Firstly, R-tipping is a genuine nonautonomous instability which, in general,

cannot be simply explained by a classical bifurcation of a slowly varying autonomous system [13]. Secondly, R-tipping can occur even if the varying rates of external inputs are much slower than the system convergence rate towards the stable state in the corresponding autonomous system. This is because tracking requires the convergence rate towards the moving stable state to be faster than the speed of the moving stable state. Thus, if the position of the stable state is sufficiently sensitive to the changes in the external input parameters, then tipping may occur for inputs varying much more slowly than the convergence rate towards the stable state [18, 42, 26]. Thirdly, there might be R-tipping mechanisms that have not been identified and studied to date. Without a systematic classification of R-tipping, it may be difficult to identify R-tipping given a random system at hand. Fourthly, there can be non-obvious tipping thresholds separating initial conditions that track the moving stable state from those that R-tip. Tipping thresholds in nonautonomous system may be intricate and non-obvious in the sense that they cannot always be related to a threshold in the corresponding autonomous system [24, 9, 43]. Lastly, R-tipping can be *irreversible* or *reversible*: the system fails to track the moving stable state, either moves to a different state and never returns to the original stable state, for example [12, 13]; or makes a large excursion, but returns to the original stable state (this may happen repeatedly), for example [24, 9]. Reversible R-tipping poses an additional mathematical challenge. The phenomenon is quantitative rather than qualitative in the sense that the long-term behavior below and above a critical rate is the same. This property is what makes reversible R-tipping difficult to define rigorously, even using modern concepts from the theory of nonautonomous dynamical systems [44]. The objective of this project is to develop an accessible mathematical framework for scientists to better understand and analyse R-tipping.

1.2 Prior research on R-tipping

In recent years, various notions have been proposed to study attractors and stability in nonautonomous dynamical systems with time-varying external inputs. One approach, which is favored by engineers, is to prescribe a "safe region" about the moving stable state and give criteria for the time-varying input to ensure that the nonautonomous system remains within the safe region [45, 17, 46, 18]. The criteria can be made rigorous, for example using the theory of normal [47] or uniform [45] hyperbolicity in terms of the persistence of hyperbolicity. Particularly, for R-tipping analysis, Ashwin et al. propose a tipping radius approach [18], which focuses on a upper bound of the drift of the system states with time, and the effective tipping radius, which is not necessarily the intrinsic tipping thresh-

old of the system, and may approximate the tipping threshold if the effective tipping radius is properly chosen. Similar ideas of "safe region" or "constraints" are widely implemented in control problems for example in robust control to handle with the system uncertainty and noise [48, 49, 50]. While the safe region approach quantifies the system behaviour relative to the moving stable state, it cannot capture R-tipping in its full extent because the approach is based on a *prescribed ad hoc tipping threshold*. R-tipping, on the other hand, often involves an intrinsic threshold that cannot, in general, be prescribed [51, 43].

Another approach defines pullback attractors or bounded complete solutions, and studies nonautonomous bifurcations where a pullback attractor undergoes a topological change [52, 22, 53] or a bounded complete solution as the possible bifurcating object that yields nonautonomous version of fold or other bifurcation patterns [54]. In particular, recent work of Ashwin et al. [44] and Alkhayuon et al. [55] use pullback attractors to study R-tipping in asymptotically autonomous systems where the external input varies from one asymptotic value to another. Moreover, testable criteria for tracking and irreversible R-tipping in one dimension based on qualitative changes of pullback attractors have been derived. However, these criteria fail to capture R-tipping in its full extent. A typical limitation is that reversible R-tipping need not involve any qualitative change (a bifurcation) of a pullback attractor. Therefore, an alternative framework is required to capture R-tipping in its full extent.

Besides, there are some studies of R-tipping in specific systems or applications. For example, Wieczorek et al. [24] and Perryman et al. [51] give R-tipping analysis in a family of slow-fast systems in terms of the folded singularities and canards based on geometric singular perturbation theory [47, 56, 57, 58]; Ritchie and Sieber explore the early-warning indicators of tipping (such as the increase of autocorrelation and variance in time series) in a system governed by a stochastic differential equation, by looking at the interaction of rate-induced tipping and noise [59, 60]; Gienapp et al. predict demographically sustainable rates of adaptation to the climate change through studying great tits optimal breeding time under different climate change scenarios [61].

More recently, a Steklov averages method and Q-angle method based on the theory of finite-time Lyapunov exponents and exponential dichotomy have been proposed to demonstrate that finite-time stability spectra can be used in the definition and diagnostics of R-tipping [62]. Hoyer-Leitzel et al. give another sight of defining R-tipping which leaves an open question about whether the prescribed methods can clearly and robustly yield the indicators of R-tipping in a general case according to their definition of R-tipping.

This project is based on the previous work of Wieczorek, Ashwin, Perryman et al. [24, 18, 44, 51] on R-tipping. The aim is to overcome the past challenges and develop a theory that addresses the lack of accessible mathematical framework, explores interesting mathematical questions, and is relevant for a wide range of applications. The theory is underpinned by the compactification techniques developed in Chapter 2, by the concepts of desingularisation and canards from the geometric singular perturbation theory, and is guided by the analysis of canonical examples of R-tipping in Chapter 4.

1.3 R-tipping in a nonautonomous toy model

In this section, we discuss a toy model to present a simple case of R-tipping phenomenon, which shows how R-tipping happens in a nonautonomous system and how R-tipping can be analyzed in such a simple case. The toy model inspired us to consider R-tipping analysis in a more general context, and prescribe more rigorous mathematical description of R-tipping.

As R-tipping is an instability of a *nonautonomous system*, we study R-tipping in the following system [18]:

$$\dot{x} = f(x, \Lambda(t)), \tag{1.1}$$

with the state variable $x \in \mathbb{R}^n$, time $t \in \mathbb{R}$, C^1-smooth vector field $f : \mathbb{R}^n \times \mathbb{R}^d \to \mathbb{R}^n$, and C^1-smooth time-varying external input $\Lambda : \mathbb{R} \to \mathbb{R}^d$.

Note that if $\Lambda(t) = \lambda$ at time t, we can get the corresponding autonomous system of system (1.1) at time t, which we call the *frozen system*

$$\dot{x} = f(x, \lambda), \tag{1.2}$$

where λ is the fixed-in-time input parameter.

The time-varying external input $\Lambda(t)$ in system (1.1) can give extraordinarily complex dynamics of the system, which are usually nontrivial and challenging to analyze. As indicated previously, there are three critical aspects that can induce tipping points of the system. The critical level of $\Lambda(t)$, the critical rate of change of $\Lambda(t)$, and the noise term of $\Lambda(t)$ are respectively related to B-tipping, R-tipping, and N-tipping [18].

Here we focus on the critical rate of change of $\Lambda(t)$. In order to quantify the rate, we introduce a non-negative 'rate' parameter r, rewrite $\Lambda(t)$ as $\Lambda(rt)$, and

extend (1.1) to a family of nonlinear nonautonomous systems

$$\dot{x} = f(x, \Lambda(rt)), \tag{1.3}$$

parametrised by the rate r [24, 18, 44, 55].

Note that R-tipping happens only when the external input changes fast enough, namely the rate parameter r of $\Lambda(rt)$ is large enough. To make it more concrete, we give a simple toy model [18] of (1.3) as follows

$$\dot{x} = f(x, \Lambda(rt)) = (x + \Lambda(rt))^2 - 1, \tag{1.4}$$

to show how R-tipping can happen in a nonautonomous system and to motivate our ideas for R-tipping analysis. We consider two types of $\Lambda(rt)$: a constant drift and a nonlinear shift from one asymptotic value to another.

1.3.1 Constant drift of $\Lambda(rt)$

At first, consider a constant drift of $\Lambda(rt)$ in system (1.4) such that

$$\Lambda(rt) = rt, \tag{1.5}$$

where the external input $\Lambda(rt)$ increases linearly with time. Figure 1.1 shows the dynamics of system (1.4)–(1.5) when $\Lambda(rt)$ increases from zero to a fixed value with different 'rates' r.

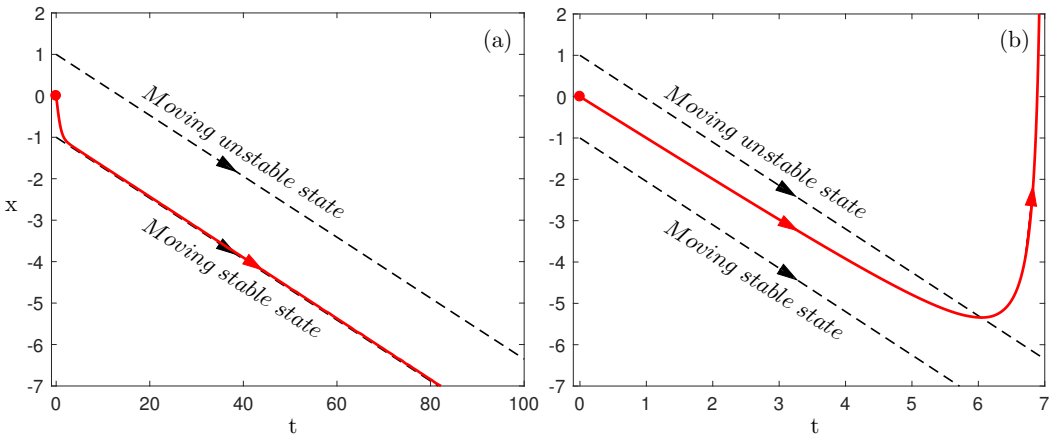

Figure 1.1: Dynamics of system (1.4)–(1.5) are indicated by the red curves when $\Lambda(rt)$ increases from 0 to 7.35 with different rates $r =$ (a) 0.0375, and (b) 1.05. The system is initialized at $(x_0, t_0) = (0, 0)$ marked as the red dots. The moving stable and unstable states are indicated by the dashed curves, which are respectively the stable and unstable equilibria of the corresponding temporal frozen system (1.2).

Shown as Fig. 1.1(a), if r is sufficiently small, the system closely tracks the

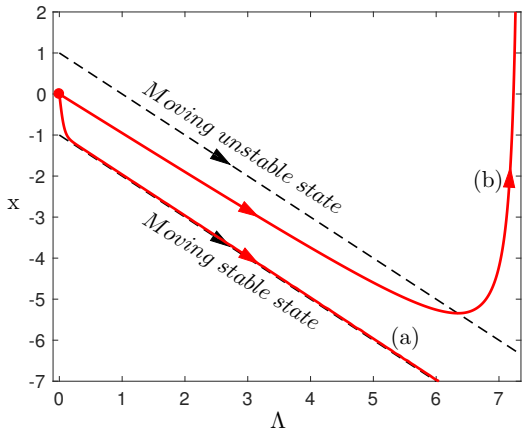

Figure 1.2: Dynamics of system (1.6) are indicated by the red curves when $\Lambda(rt)$ increases from 0 to 7.35 with different rates $r =$ (a) 0.0375, and (b) 1.05. The system is initialized at $(x_0, \Lambda_0) = (0, 0)$ marked as the red dot. The moving stable and unstable states are indicated by the dashed curves, which are respectively the stable and unstable equilibria of the corresponding temporal frozen system (1.2).

moving stable state. Note that the moving stable (unstable) state is a collection of the stable (unstable) equilibria of the corresponding frozen system (1.2) with different but fixed-in-time λ. When r reaches the critical rate, the system no longer tracks the moving stable state, but crosses over the moving unstable state and tends to infinity [Fig. 1.1(b)]. Such a significant transition of system dynamics is only due to the change of the rate r, which shows how R-tipping happens in a simple nonautonomous system. A comparison between panels (a) and (b) in Fig. 1.1 shows that:

(i) The stable equilibrium of the frozen system (the moving stable state) never bifurcates or loses stability.

(ii) The system tracks the moving stable state when r is sufficiently small, but R-tips to infinity when r increases past its critical value. Owing to the linear drift, this instability can be reduced to a classical saddle-node bifurcation of a stable state in a co-moving frame [18].

Note that system (1.4)–(1.5) can be rewritten in the (x, Λ) phase plane as

$$\begin{aligned} \dot{x} &= f(x, \Lambda(rt)) = (x + \Lambda)^2 - 1, \\ \dot{\Lambda} &= r, \end{aligned} \tag{1.6}$$

which is defined on $\mathbb{R} \times \mathbb{R}$.

Fig. 1.2 shows the dynamics of system (1.6) in the (x, Λ) phase plane with the same parameters as those shown in Fig. 1.1. We will use it for comparison with Fig. 1.4.

1.3.2 Asymptotic nonlinear shift $\Lambda(rt)$

Consider system (1.4) with a simple example of an asymptotic $\Lambda(rt)$ in the form:

$$\Lambda(rt) = \frac{\Delta}{2}\left(\tanh(rt) + 1\right), \tag{1.7}$$

where $\Delta = 4$. Figure 1.3 shows the dynamics of system (1.4) with the asymptotic shift (1.7) from zero to a fixed value at different 'rates' r.

As shown in Fig. 1.3(a), if r is sufficiently small, the system closely tracks the moving stable state. Note that the moving stable (unstable) state is a collection of the stable (unstable) equilibria of the corresponding frozen system (1.2) with different but fixed-in-time λ. When r is increased to its critical value, the system no longer tracks the moving stable state, but crosses over the moving unstable state and tends to infinity [Fig. 1.3(b)]. Such a significant transition of system dynamics is only due to the change of the rate r, which shows how R-tipping happens. A comparison between panels (a) and (b) in Fig. 1.3 shows some interesting properties of an asymptotic nonlinear shift $\Lambda(rt)$:

(i) The stable equilibrium of the frozen system (the moving stable state) never bifurcates or loses stability. In contrast to the linear shift, the moving equilibria $e(\Lambda(rt))$ tend to regular equilibria $e(\lambda^{\pm})$ as the input tends to a constant: $e(\Lambda(rt)) \to e(\lambda^{\pm})$ as $\Lambda(rt) \to \lambda^{\pm}$ as $t \to \pm\infty$.

(ii) The system tracks the moving stable state when r is sufficiently small, but R-tips to infinity when r increases past its critical value. In contrast to the linear shift, this instability cannot be reduced to a classical bifurcation of a stable state. In fact, it is not clear how to capture and analyse this genuine nonautonomous instability.

The important point is that system (1.4) with the asymptotic input (1.7) can be rewritten on the *compactified* (x, Λ) phase space as

$$\begin{aligned} \dot{x} &= f(x, \Lambda(rt)) = (x + \Lambda)^2 - 1, \\ \dot{\Lambda} &= \frac{2r}{\Delta}\Lambda(\Delta - \Lambda), \end{aligned} \tag{1.8}$$

which is defined on $\mathbb{R} \times [0, \Delta]$.

Fig. 1.4 shows the dynamics of system (1.8) in the (x, Λ) phase plane with the same parameters as those used in Fig. 1.3. The advantages of working with the compactified system (1.8) are:

(i) The compactified system contains regular equilibria, which are equilibria of

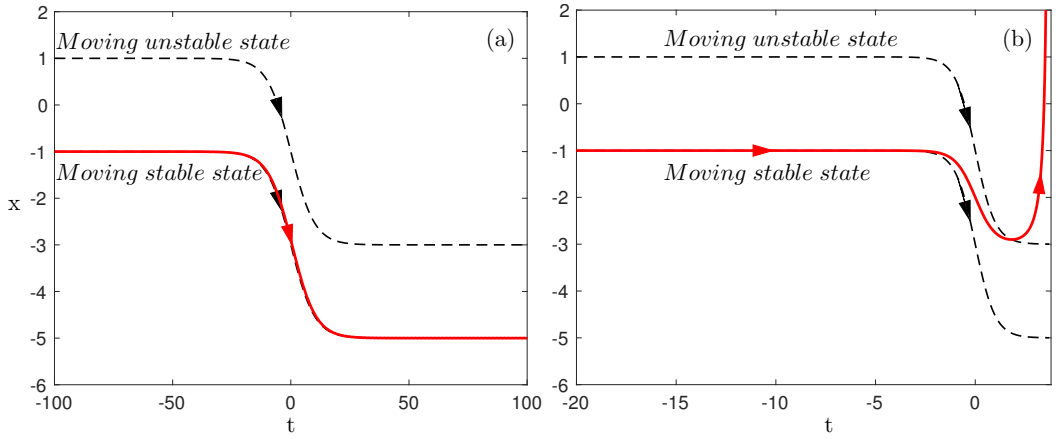

Figure 1.3: Dynamics of system (1.4)(1.7) are indicated by the red curves when $\Lambda(rt)$ increases from 0 to 4 with different rates $r =$ (a) 0.1, and (b) 1.005. The system is initialized at $(x_0, t_0) = (-1, -100)$. Note that as $t_0 = -100$, $\Lambda(rt)$ for both (a) and (b) is extremely close to zero, so in panel (b) only the important parts of system dynamics are plotted. The moving stable and unstable states are indicated by the dashed curves, which are respectively the stable and unstable equilibria of the corresponding temporal frozen system (1.2).

the frozen limit systems at positive and negative time infinity: $f(x, \Lambda(rt)) \to f(x, \lambda^{\pm})$ as $t \to \pm\infty$.

(ii) The regular equilibria of the limit systems can be used to analyse the nonautonomous R-tipping instability at finite time. Specifically, we will show that R-tipping problems in the nonautonomous system are transformed into heteroclinic orbits problems in the compactified system.

(iii) The compactified system represents a special case of a more general compactification framework discussed in Chapter 2.

1.3.3 Inspiration from the toy model

Through the analysis of the toy model (1.4) with the constant drift (1.5) and the simple asymptotic nonlinear shift (1.7), we gained insight into how R-tipping happens and the importance of the form of the external input $\Lambda(rt)$.

Generally, it is unclear whether it is feasible to work out a general theory of R-tipping for an arbitrary form of $\Lambda(rt)$, or if such theory would be accessible to scientists and engineers. Here, we focus on a case that is more specific but allows us to make further progress on the problem. We consider response of an open system to external inputs that need not be monotone but limit to a constant in the positive and (possibly) negative time infinity. Our choice is motivated and incentivised by the toy model (1.4) with the simple asymptotic nonlinear

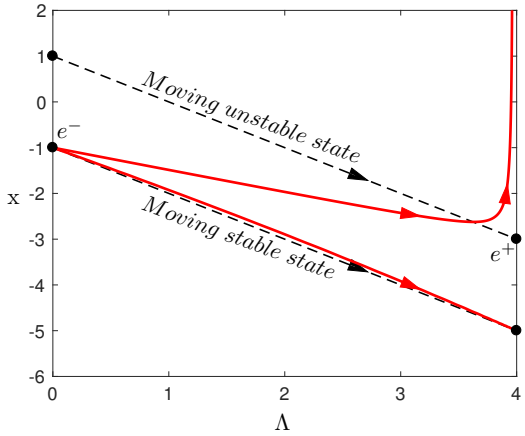

Figure 1.4: Dynamics of system (1.4)(1.7) are indicated by the red curves when $\Lambda(rt)$ increases from 0 to 4 with different rates $r =$ (a) 0.1, and (b) 1.005. The system is initialized at $(x_0, \Lambda_0) = (-1, 10^{-8})$. The moving stable and unstable states are indicated by the dashed curves, which are respectively the stable and unstable equilibria of the corresponding temporal frozen system (1.2). There are four equilibria of the system marked as the black dots, with the two saddles denoted as e^- and e^+.

shift $\Lambda(rt)$ (1.7). The key point here is that the asymptotic behavior gives us autonomous limit system from infinity that will normally contain compact invariant sets such as equilibria, limit cycles, tori and etc. Furthermore, using a suitable compactification, we can analyse R-tipping in terms of connecting heteroclinic orbits from a saddle at $-\infty$ to a saddle at $+\infty$. The main challenge is that, in general, we do not know the set of autonomous ODEs that generate the given asymptotic input $\Lambda(rt)$, meaning the nonautonomous system cannot always be reformulated as an autonomous system in the (x, Λ) phase space. Another problem is that some $\Lambda(rt)$ will be generated by a high-dimensional sets of ODEs, which would be impractical for analysis. To address these issues: we develop a general compactification method for asymptotic $\Lambda(rt)$ that uses just one additional variable, indpendently of the dimension and monotonicity of the nonautonomous input $\Lambda(rt)$.

1.4 Main results and outline

This main contributions of this thesis cover:

(i) Development of a special compactification technique for asymptotically autonomous dynamical systems.

(ii) An outline of a mathematical theory of R-tipping.

(iii) Classification and analysis of canoniocal examples of R-tipping.

The main focus on (i) and (iii).

Chapter 2: A compactification framework for asymptotically autonomous differential equations is developed, which can be applied to a range of problems such as pullback attractors, rate-induced instabilities, and nonlinear wave solutions. The compactification uses a suitable coordinate transfromation to augment the asymptotically autonomous system with an additional variable that is bounded, giving rise to an autonomous compactified system. We give the sufficient conditions for the existence of such compactification, and derive two coordinate transformation conditions to ensure that the compactified system is continuously differentiable on the extended phase space. For practical usage, we also construct the examples of parametrised compactifications. Most importantly, we show that the compactification can greatly facilitate theoretical and numerical analysis of asymptotically autonomous differential equations.

Chapter 3: An outline of mathematical theory of R-tipping analysis is introduced here. The basic idea in the theory is to relate the nonautomous system (1.3) with its corresponding autonomous frozen system (1.2) where the nonautomous term $\Lambda(rt)$ becomes an input parameter λ. Based on such a relation, we give the definitions of necessary concepts for R-tipping analysis including a parameter path, moving stable equilibrium, regular threshold and edge state, singular limit threshold and quasithreshold, moving threshold and moving edge state, and threshold instability. Note that those concepts are associated with the frozen system (1.2). Most importantly, we focus on two types of thresholds including the regular thresholds and quasithresholds in the frozen system. Then the actual R-tipping thresholds in the nonautonomous system are related to those regular thresholds or quasithresholds in the frozen system. For the types of R-tipping, we distinguish irreversible and reversible R-tipping, and furthermore give testable criteria for R-tipping to happen.

Chapter 4: Canonical examples of R-tipping are designed and analysed here, to showcase different R-tipping mechanisms. The design is guided by several properties including the system dimension and timescales, the types of thresholds (regular thresholds vs. quasithresholds), and the types of R-tipping (reversible vs. irreversible). We propose a bottom-up approach of R-tipping analysis in practice to cover theses properties and highlight different characteristics. By those canonical examples, we illustrate how to calculate the R-tipping thresholds corresponding to the prescribed concepts in Chapter 3. Specifically, R-tipping due to regular thresholds is analysed in terms of connecting orbits in the compactified system, and R-tipping thresholds are identified as the stable manifold of the R-tipping edge state. The singular R-tipping thresholds are calculated in terms of

folded singularities through desingulariation and identified as the singular canard trajectories with the relevant folded singularities as the singular R-tipping edge states. R-tipping quasithresholds are identified as nonsingular canard trajectories without any R-tipping edge state. In particular, we demonstrate numerically that, forward threshold instability is sufficient but not necessary for R-tipping to occur in two- and higher-dimensional systems. This is in contrast to one-dimensional systems, where forward threshold instability is both sufficient and necessary for R-tipping.

We finish with a summary in Chapter 5, and add the following three manuscripts that include some work of this thesis.

(i) Sebastian Wieczorek, Chun Xie, and Peter Ashwin. **Rate-Induced Tipping: Thresholds, Edge States and Testable Criteria** [63].

(ii) Sebastian Wieczorek, Chun Xie, and Chris K.R.T. Jones. **Compactification for Asymptotically Autonomous Dynamical Systems: Theory, Applications and Invariant Manifolds**, arXiv:2001.08733 [math.DS], 2020 `https://arxiv.org/abs/2001.08733` [64].

(iii) Chun Xie and Sebastian Wieczorek. **Rate-Induced Tipping: Canonical Examples, Connecting Orbits and Canards** [65].

Chapter 2

Compactification

The toy model of R-tipping from Chapter 1 shows that a suitable phase-space compactification can simplify R-tipping analysis in terms of new equilibrium points and heteroclinic connections between two saddles. In this chapter, we develop a compactification framework for asymptotically autonomous differential equations in more general and rigorous setting. We consider a nonautonomous external input $\Gamma(t)$, where the independent variable t can be time or space, and is not limited to the application in R-tipping analysis. Then, we discuss the implementation of the general compactification framework in R-tipping analysis.

2.1 Introduction

Let U and V be open subsets $U \subseteq \mathbb{R}^n$ and $V \subseteq \mathbb{R}^d$. Consider a *nonlinear nonautonomous* differential equation

$$\frac{dx}{dt} := \dot{x} = f(x, \Gamma(t)), \tag{2.1}$$

with the dependent state variable $x \in U$, independent variable $t \in \mathbb{R}$, C^1-smooth nonautonomous term $\Gamma : \mathbb{R} \to V$, and C^1-smooth vector field $f : U \times V \to U$. For an arbitrary $\Gamma(t)$, the theory of nonautonomous dynamical systems [53] summarises work on the problem, discusses useful concepts such as pullback attractors, and gives some very general results on attraction and stability. The main obstacle to the analysis of nonautonomous system (2.1) is the absence of compact invariant sets such as equilibria, limit cycles or tori. This obstacle becomes evident when the system is augmented with $\nu = t$ as an additional dependent

variable to obtain the usual *autonomous extended system*[1]

$$\begin{aligned} \dot{x} &= f(x, \Gamma(\nu)), \\ \dot{\nu} &= 1, \end{aligned} \tag{2.2}$$

that is defined on the phase space $U \times \mathbb{R}$, which is an open subset of $\mathbb{R}^{n+1}$.

2.1.1 Basic setting

The key point of this work is that one can make further progress on the problem if $\Gamma(t)$ limits to a constant as t tends to positive or negative infinity. Specifically,

Definition 2.1.1. *We say* $\Gamma(t)$ *is* bi-asymptotically constant *with future limit* Γ^+ *and past limit* Γ^- *if*

$$\lim_{t \to \pm\infty} \Gamma(t) = \Gamma^{\pm} \in \mathbb{R}^d.$$

We say $\Gamma(t)$ *is* asymptotically constant *if it has a future limit but not necessarily a past limit, or if it has a past limit but not necessarily a future limit.*

The main simplification is that nonautonomous system (2.1) becomes *asymptotically autonomous* in the terminology of [66]:

$$f(x, \Gamma(t)) \to f(x, \Gamma^+) \text{ as } t \to +\infty, \text{ or } f(x, \Gamma(t)) \to f(x, \Gamma^-) \text{ as } t \to -\infty,$$

and we can define the autonomous *future limit system*

$$\dot{x} = f(x, \Gamma^+), \tag{2.3}$$

or the autonomous *past limit system*

$$\dot{x} = f(x, \Gamma^-). \tag{2.4}$$

The autonomous dynamics of the future (2.3) or past (2.4) limit systems will typically include compact invariant sets. However, the flow of (2.1) does not contain the autonomous dynamics of (2.3) or (2.4) because it only appears as $t \to +\infty$ or $-\infty$.

We develop a framework that overcomes the main obstacle and uses the autonomous dynamics and compact invariant sets of the future limit system (2.3) or the past limit system (2.4) to analyse the nonautonomous system (2.1). Specif-

[1] We note that in the special case $\Gamma(t)$ is generated by a known set of autonomous ODEs, say $\dot{\Gamma} = g(\Gamma)$, the original system can be augmented with Γ to obtain $\dot{x} = f(x, \Gamma)$, $\dot{\Gamma} = g(\Gamma)$, that is defined on $U \times V \subseteq \mathbb{R}^{n+d}$ and increases the dimension of the vector field by d. This extended system will normally include compact invariant sets, but may be impractical for analysis if d is large and is not always possible to obtain.

ically, we bring together the nonautonomous system (2.1), the future limit system (2.3) and/or the past limit system (2.4) into one C^1-smooth and autonomous *compactified system*. The compactification approach presented in this paper is akin to the Poincaré-type phase-space compactification (of the x-dimensions) that enables analysis of dynamical behaviour at infinity [67, 68, 69, 70, 71, 72], collisions in many-body problems [73], higher-codimension bifurcations [74] and canard solutions in slow-fast systems [75, 76, 77, 78, 79] via blow up of singularities of vector fields. The main difference between our work and these studies is that we compactify the augmented ν-dimension, but not necessarily the x-dimensions. As this cannot be achieved for any asymptotically constant $\Gamma(t)$, we derive optimal conditions on $\dot{\Gamma}(t)$ that allow us to perform the compactification. In analysis of asymptotically autonomous ODEs [66], our compactification provides a new tool that complements existing approaches based on pullback attractors [80, 81] and asymptotic equivalence of the nonautonomous system and autonomous limit systems [82, 83].

2.1.2 Motivating examples

Our work is directly motivated by a range of problems from applications that can be fitted into the framework of Eq. (2.1) with asymptotically constant $\Gamma(t)$, and become simpler to analyse after compactification.

2.1.2.1 Analysis of pullback attractors

Consider a nonautonomous dynamical system (2.1) with time t and asymptotically constant $\Gamma(t)$ with a past limit

$$\Gamma(t) \to \Gamma^- \text{ as } t \to -\infty,$$

and refer to [53, Ch.3] for the notion of a local pullback attractor. Each asymptotically stable compact invariant set η^- for the past limit system (2.4) can be related to a local pullback attractor of the nonautonomous system (2.1) as shown in [44, Th.2.2] and [55, Th.II.2]. When embedded in the extended phase space of a compactified system, η^- gains one repelling direction and becomes a saddle. Thus, the pullback attractor of (2.1) associated with η^- is transformed into the unstable or centre invariant manifold of η^- in the compactified system. Relating pullback attractors to unstable invariant manifolds in the spirit of [84] gives an alternative approach to the existing nonautonomous stability theory [53], and may facilitate analysis of the nonautonomous problem.

2.1.2.2 Theory of rate-induced instabilities

A nonlinear nonautonomous dynamical system (2.1) with time t and bi-asymptotically constant

$$\Gamma(t) = \Lambda(rt) \to \lambda^{\pm} \in \mathbb{R}^d \text{ as } t \to \pm\infty,$$

is often used to describe nonlinear dynamics of open systems subject to finite-time external disturbances, growing or decaying external trends, or simply time-varying external inputs $\Lambda(rt)$. A rate-induced instability known as R-tipping occurs when the 'rate' $r > 0$ of the external input exceeds some critical value and the system transitions to a different state [24, 18, 9, 51, 59, 85, 86, 13, 63, 65]. The instability is of great interest to natural scientists but cannot, in general, be explained using the traditional (i.e. autonomous) bifurcation analysis of the frozen autonomous system

$$\dot{x} = f(x, \lambda),$$

with a fixed in time input parameter λ. In a suitable compactified system, the R-tipping problem can be transformed into a connecting heteroclinic orbit problem, which facilitates both numerical computations [65] and the derivation of rigorous criteria for R-tipping [63]. Here, the closure of an image of $\Gamma(t)$ has an important meaning: it is a parameter path in the multi-dimensional parameter space $V \subseteq \mathbb{R}^d$ of the frozen system that is traced out by the time-varying external input.

2.1.2.3 Existence of nonlinear wave solutions

For the inhomogeneous wave equation with a potential $\mathcal{V}(x)$ on $\mathbb{R}^n$:

$$\Delta_x u + f(u) + \mathcal{V}(x)u = 0,$$

spherically symmetric solutions satisfy the semilinear elliptic boundary value problems (BVPs), where $r > 0$ is the radial direction [87, 88]:

$$u_{rr} + \frac{n-1}{r}\, u_r + f(u) + \mathcal{V}(r)\, u = 0, \quad \begin{array}{l} \lim_{r\to 0} u_r(r) = 0, \\ \lim_{r\to+\infty} u(r) = 0. \end{array} \tag{2.5}$$

If the potential $\mathcal{V}(r)$ is asymptotically constant with a future limit[2], the BVP (2.5) fits naturally into the framework of (2.1). More precisely, by using r as the independent variable and introducing $v(r) = u_r(r)$ as an additional dependent variable so that

$$x(r) = \begin{pmatrix} u(r) \\ v(r) \end{pmatrix} \text{ and}$$

[2]This includes the special case $\mathcal{V}(r) = 0$.

$$\Gamma(r) = \begin{pmatrix} \Gamma_1(r) \\ \Gamma_2(r) \end{pmatrix} = \begin{pmatrix} (-n+1)/r \\ -\mathcal{V}(r) \end{pmatrix} \to \begin{pmatrix} 0 \\ -\mathcal{V}^+ \end{pmatrix} \text{ as } r \to +\infty,$$

we can rewrite (2.5) as

$$x' = f(x, \Gamma(r)) = \begin{pmatrix} v \\ \Gamma_1(r)v + \Gamma_2(r)u - f(u) \end{pmatrix}, \quad \begin{matrix} \lim_{r\to 0} v(r) = 0, \\ \lim_{r\to+\infty} u(r) = 0, \end{matrix}$$

where $' = d/dr$, and $f(0) = 0$.

The future limit system corresponds to the problem with constant potential and is easily analysed as a Hamiltonian system in the plane [87]. The analysis reveals a saddle equilibrium η^+ at the origin. The full BVP is then solved by finding appropriate trajectories on the stable or centre-stable invariant manifold of η^+ when embedded in the extended phase space of the compactified system.

There are a number of other examples of compactification used for the study of nonlinear waves, such as the lens transform [89, Ch.2], which is a special case of pseudoconformal compactification [90] for the nonlinear Schrödinger equation.

2.2 Compactification

The aim of this section is to reformulate nonautonomous system (2.1) into an autonomous system so that:

- The new system contains the flow and compact invariant sets of the future limit system (2.3) and/or the past limit system (2.4).
- The dimension of the vector field increases by one, indpendently of the dimension and monotonicity of the nonautonomous term $\Gamma(t)$.

We show that this can be achieved under quite general assumptions on $\Gamma(t)$ by augmenting system (2.1) with $s = g(t)$ depicted in Fig. 2.1 as an additional dependent variable. In other words, instead of having a problem with the additional dimension being unbounded as in the usual extended system (2.2), we augment system (2.1) so that the additional dimension becomes a compact interval. Specifically, we:

(i) Restrict to asymptotically and bi-asymptotically constant $\Gamma(t)$.

(ii) Compactify the real t-line into the compact s-interval $[-1, 1]$ if $\Gamma(t)$ is bi-asymptotically constant.

(iii) Compactify the half t-line $[t_-, +\infty)$ into the compact s-interval $[s_-, 1]$ if $\Gamma(t)$ is asymptotically constant with a future limit, or compactify the half t-line

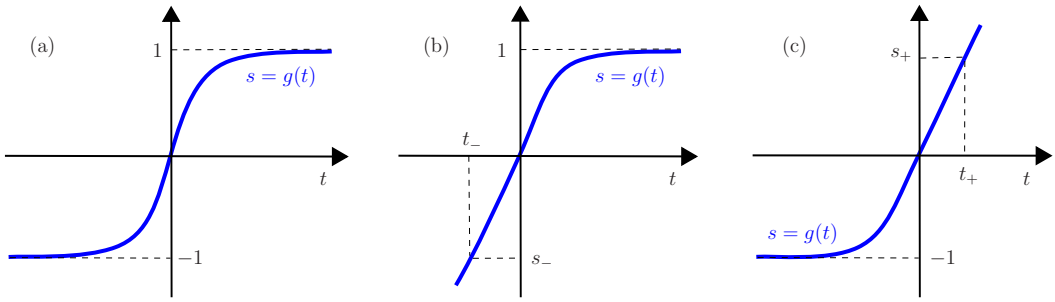

Figure 2.1: Examples of the coordinate transformation $s = g(t)$ from (a) Assumption 2.2.1, (b) Assumption 2.2.2 and (c) Assumption 2.2.3.

$(-\infty, t_+]$ into the compact s-interval $[-1, s_+]$ if $\Gamma(t)$ is asymptotically constant with a past limit.

2.2.1 Two-sided compactification for bi-asymptotically constant $\Gamma(t)$

In this section, we reformulate nonautonomous system (2.1) with a bi-asymptotically constant $\Gamma(t)$ into a compactified system that is autonomous and contains the flow and compact invariant sets of the future (2.3) and past (2.4) limit systems. This is achieved via two-sided compactification that uses the coordinate transformation $s = g(t)$ depicted in Fig. 2.1(a). More precisely, we assume

Assumption 2.2.1. *A coordinate transformation $s = g(t)$ maps the real t-line onto the finite s-interval $(-1, 1)$, is at least C^2-smooth, bi-asymptotically constant with future limit 1 and past limit -1, and strictly increasing with vanishing first derivative as $t \to \pm\infty$:*

$$\begin{aligned} &g : \mathbb{R} \to (-1, 1), \quad g \in C^{k\geq 2}, \quad \lim_{t\to\pm\infty} g(t) = \pm 1, \\ &\dot{g}(t) > 0 \text{ for } t \in \mathbb{R} \text{ and } \lim_{t\to\pm\infty} \dot{g}(t) = 0. \end{aligned} \tag{2.6}$$

Note 2.2.1. *In practice, we introduce* compactification parameter(s) *that control the rate/order of asymptotic decay of $g(t)$, and work with* parametrised coordinate transformations *in Sec. 2.4. The dependence on the compactification parameter(s) does not affect and is thus left out of general statements of this section.*

2.2.1.1 Compactified system: transformation conditions

Compactification is a three-step process. The first step is to make the additional dimension bounded by augmenting the asymptotically autonomous system (2.1)

with $s = g(t)$ as an additional dependent variable

$$\dot{x} = f(x, \Gamma(g^{-1}(s))), \tag{2.7}$$

$$\dot{s} = \dot{g}\left(g^{-1}(s)\right), \quad s(t_0) = g(t_0) \tag{2.8}$$

where $t = h(s) \coloneqq g^{-1}(s)$ is the inverse coordinate transformation. Since the practical implementation of the compactification requires the inverse coordinate transformation, we reformulate (2.7)–(2.8) in terms of $h(s)$ alone:

$$\dot{x} = f(x, \Gamma(h(s))), \tag{2.9}$$

$$\dot{s} = \gamma(s), \tag{2.10}$$

where $\gamma(s) = \dot{g}(h(s)) = 1/h'(s)$ is the augmented component of the vector field, $\dot{} = d/dt$, and $' = d/ds$. System (2.9)–(2.10) is defined on $U \times (-1, 1)$, which is an open subset of $\mathbb{R}^{n+1}$. The second step is to make the s-interval closed by including $s = \pm 1$ ($t = \pm\infty$) and extending the augmented by (2.10) vector field to $\{s = \pm 1\}$:

$$f(x, \Gamma(h(s))) = \begin{cases} f(x, \Gamma(h(s))) & \text{for} \quad s \in (-1, 1), \\ f(x, \Gamma^-) & \text{for} \quad s = -1, \\ f(x, \Gamma^+) & \text{for} \quad s = 1, \end{cases} \tag{2.11}$$

$$\gamma(s) = \begin{cases} 1/h'(s) & \text{for} \quad s \in (-1, 1), \\ 0 & \text{for} \quad s = \pm 1. \end{cases} \tag{2.12}$$

This gives an autonomous *compactified system* (2.9)–(2.12) that is defined on the extended phase space $U \times [-1, 1]$. Most importantly, subspaces $\{s = 1\}$ and $\{s = -1\}$ are flow-invariant and carry the autonomous dynamics and compact invariant sets of the future (2.3) and past (2.4) limit systems, respectively. However, it is not generally guaranteed that the extended vector field is differentiable at the added invariant subspaces $\{s = 1\}$ and $\{s = -1\}$. The third step is to give testable criteria for the extended vector field to be continuously differentiable:

Lemma 2.1. (Transformation Conditions.) *Consider a nonautonomous system (2.1) with C^1-smooth f and Γ, and bi-asymptotically constant $\Gamma(t)$. For a chosen coordinate transformation $g(t)$ from Assumption 2.2.1, the ensuing compactified system* (2.7)–(2.12) *is C^1-smooth on $U \times [-1, 1]$ if and only if*

$$\lim_{t \to \pm\infty} \frac{\dot{\Gamma}(t)}{\dot{g}(t)} \ \textit{exist}, \tag{2.13}$$

$$\lim_{t \to \pm\infty} \frac{\ddot{g}(t)}{\dot{g}(t)} \ \textit{exist}. \tag{2.14}$$

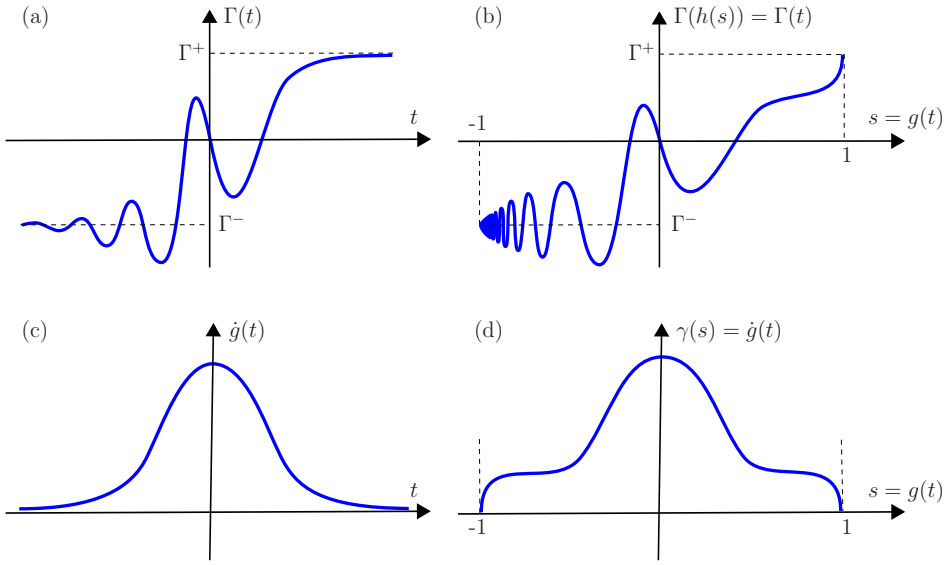

Figure 2.2: (a)–(b) Example of transformation-induced loss of differentiability of $\Gamma(h(s))$ at $s = \pm 1$ when condition (2.13) is violated. (c)–(d) Example of $\gamma(s)$ that is non-differentiable at $s = \pm 1$ when condition (2.14) is violated.

The proof of Lemma 2.1 is given in Sec. 2.2.1.3. The one-dimensional example from Fig. 2.2 gives insight into transformation conditions (2.13) and (2.14), which ensure differentiability of $\Gamma(h(s))$ and $\gamma(s)$, respectively, at $s = \pm 1$. The slope of $\Gamma(h(s))$ in Fig. 2.2(b) is given by $d\Gamma/ds = d\Gamma/dg = \dot{\Gamma}/\dot{g}$. Thus, the derivative of $\Gamma(h(s))$ becomes undefined at $s = \pm 1$ if $\dot{\Gamma}(t)$ does not limit to zero or if $\dot{\Gamma}(t)$ limits to zero slower than $\dot{g}(t)$ as $t \to \pm\infty$. (We give optimal conditions on the asymptotic decay of $\dot{\Gamma}(t)$ in Sec. 2.2.1.2.) In other words, violating condition (2.13) causes transformation-induced loss of differentiability of $\Gamma(h(s))$ at $s = \pm 1$. Similarly, the slope of $\gamma(s)$ in Fig. 2.2(d) is given by $d\gamma/ds = d\dot{s}/ds = d\dot{g}/dg = \ddot{g}/\dot{g}$. Thus, the derivative of $\gamma(s)$ becomes undefined at $s = \pm 1$ if $\ddot{g}(t)$ does not limit to zero or if $\ddot{g}(t)$ limits zero slower than $\dot{g}(t)$ as $t \to \pm\infty$. In other words, violating condition (2.14) gives $\gamma(s)$ that is non-differentiable at $s = \pm 1$. To gain insight into what types of coordinate transformation from Assumption 2.2.1 are excluded by transformation condition (2.14), consider

$$g(t) \sim \begin{cases} 1 - \exp\left(-t^n\right) & \text{as} \quad t \to +\infty, \\ -1 + \exp\left(-(-t)^n\right) & \text{as} \quad t \to -\infty, \end{cases}$$

for $n > 0$, with

$$\lim_{t\to\pm\infty} \frac{\ddot{g}(t)}{\dot{g}(t)} = \mp n \lim_{t\to\pm\infty} (\pm t)^{n-1} = \begin{cases} \mp\infty & \text{if} \quad n > 1, \\ \mp 1 & \text{if} \quad n = 1, \\ 0 & \text{if} \quad 0 < n < 1. \end{cases}$$

Thus, transformation condition (2.14) excludes transformations $g(t)$ with super-

exponential asymptotic decay[3]. This can be understood intuitively via behaviour near invariant subspaces: solutions of ODEs cannot approach invariant subspaces faster than exponentially unless they blow up and cease to exist.

The extended vector field (2.11)–(2.12) shows that the practical implementation of the compactification requires the inverse coordinate transformation $t = h(s)$ rather than $s = g(t)$. Therefore, we express the two transformation conditions from Lemma 2.1 in terms of $h(s)$.

Lemma 2.2. *Consider a coordinate transformation $s = g(t)$ from Assumption 2.2.1. Then, the limits in transformation conditions* (2.13) *and* (2.14) *from Lemma 2.1 can be given in terms of s and the inverse $h(s) \coloneqq g^{-1}(s)$:*

$$\lim_{t\to\pm\infty} \frac{\dot{\Gamma}(t)}{\dot{g}(t)} = \lim_{s\to\pm 1^{\mp}} \frac{d}{ds}\Gamma(h(s)), \tag{2.15}$$

$$\lim_{t\to\pm\infty} \frac{\ddot{g}(t)}{\dot{g}(t)} = -\lim_{s\to\pm 1^{\mp}} \frac{h''(s)}{(h'(s))^2}. \tag{2.16}$$

The proof of Lemma 2.2 is given in Sec. 2.2.1.3. We discuss further consequences of the two-sided compactification in Sec. 2.3.

2.2.1.2 Compactified system: reference envelopes and existence criteria

Here we derive optimal criteria on $\dot{\Gamma}(t)$ that guarantee a suitable coordinate transformation $g(t)$ can be found to perform the compactification. The derivation of the existence criteria is guided by the observation that typical examples of bi-asymptotically constant $\Gamma(t)$ have two additional and desirable properties. Firstly, $\dot{\Gamma}(t)$ limits to zero as t tends to positive and negative infinity. Secondly, the asymptotic approach of $\dot{\Gamma}(t)$ towards zero is not slower than the asymptotic approach of $\Gamma(t)$ towards $\Gamma^{\pm}$.

However, $\Gamma(t) \to \Gamma^{\pm} \in \mathbb{R}^d$ does not imply $\dot{\Gamma}(t) \to 0$ in general, meaning that there exist 'pathological' examples of $\Gamma(t) \to \Gamma^{\pm}$ whose derivatives do not have a future or past limit, or tend to zero arbitrarily slowly as t tends to positive or negative infinity. One example are damped oscillations with increasing frequency, where the frequency increase 'beats' the amplitude decay. For example, $\Gamma(t) \sim \sin(t^2)/t$ as $t \to +\infty$ has a future limit but its first derivative $\dot{\Gamma}(t) \sim 2\cos(t^2) - \sin(t^2)/t^2$ does not. Another example is depicted in Fig. 2.3 where $\Gamma(t) \to \Gamma^{+}$ but $\dot{\Gamma}(t)$ may not have a future limit or may approach zero arbitrarily slowly. Conversely, $\dot{\Gamma}(t) \to 0$ as $t \to \pm\infty$ does not imply $\Gamma(t) \to \Gamma^{\pm} \in \mathbb{R}^d$ either. For example, $\Gamma(t) \sim \ln(t)$ as $t \to +\infty$ does not have a future limit even though its

[3] Transformations $g(t)$ that decay faster than any exponential function.

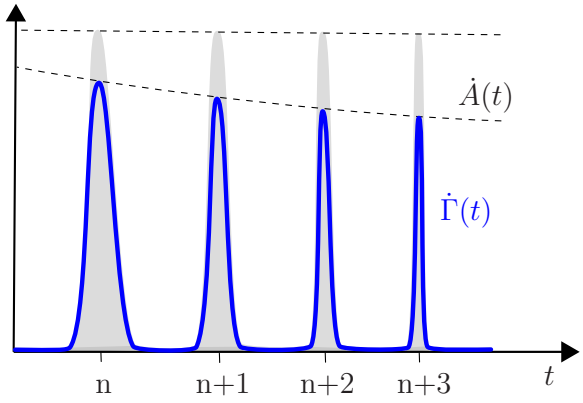

Figure 2.3: Consider C^1 bumps of equal amplitudes whose (shaded) areas form a convergent series as $t \to +\infty$. Then, $\dot{\Gamma}(t)$ is set to consist of such bumps with bump amplitudes remaining constant or decaying arbitrarily slowly to zero as $t \to +\infty$. Since the total area below $\dot{\Gamma}(t)$ is finite by construction, we have $\Gamma(t) \to \Gamma^+ \in \mathbb{R}$ as $t \to +\infty$ in spite of the envelope $\dot{A}(t)$ remaining constant or decaying arbitrarily slowly to zero.

first derivative $\dot{\Gamma}(t) \sim 1/t$ limits to zero.

To discuss 'normal' examples of bi-asymptotically constant $\Gamma(t)$ it is convenient to work with a monotone envelope of $\dot{\Gamma}(t)$, denoted by $\dot{A}(t)$ as depicted in Fig. 2.3, and ask about the slowest-decaying $\dot{A}(t) \to 0$ so that $A(t)$ has a future and past limits. Formulating this question in terms of the integral

$$\lim_{t\to+\infty} A(t) = \int_{t_0}^{\infty} \dot{A}(\mu)\, d\mu = A^+ \in \mathbb{R}, \tag{2.17}$$

shows that such slowest-decaying envelope does not exist: given any $\dot{A}(t) \to 0$ that satisfies (2.17) for some $t_0 \in \mathbb{R}$, one can construct a slower-decaying one that also satisfies (2.17). Nonetheless, it is possible to work with a parametrised family of envelopes that satisfy (2.17) and can be chosen to decay sufficiently slowly for the problem at hand. Specifically, we consider

$$A(t, m) = -\frac{1}{\ln^m(|t|)},$$

together with its derivative

$$\dot{A}(t, m) = \left(t\, \ln^m(|t|) \prod_{k=1}^{m} \ln^k(|t|) \right)^{-1}, \tag{2.18}$$

where $|t| > \exp^{m-2}(e)$, $m \in \mathbb{N}$ is any non-negative integer, $\ln^m$ denotes a composition on m logarithmic functions, and $\mathrm{sgn}(t)$ is the sign function.

Definition 2.2.1. *We call $\dot{A}(t, m)$ the* parametrised reference envelope.

The reference envelope formula (2.18) looks rather technical but one can gain

further insight by writing out examples of A and $\dot{A}$ with $m = 2$ that are defined for $|t| > e$:

$$A(t,2) = -\frac{1}{\ln(\ln(|t|)} \quad \text{and} \quad \dot{A}(t,2) = \frac{1}{t\,\ln(|t|)\,(\ln(\ln(|t|)))^2}.$$

More generally, one can verify the following properties

$$\dot{A}(t,m) \begin{cases} > 0 & \text{for} \quad t > \exp^{m-2}(e) \\ < 0 & \text{for} \quad t < \exp^{m-2}(e) \end{cases}, \quad \lim_{t\to\pm\infty} \dot{A}(t,m) = 0 \text{ and } \lim_{t\to\pm\infty} A(t,m) = 0. \tag{2.19}$$

We now use the reference envelope concept and restrict to 'normal' examples of asymptotically constant $\Gamma(t)$ to ensure the existence of a continuously differentiable compactified system.

Definition 2.2.2. *We call a bi-asymptotically constant* $\Gamma(t)$ normal *if there is an* m *such that*

$$\lim_{t\to\pm\infty} \frac{\dot{\Gamma}(t)}{\dot{A}(t,m)} \text{ exist.} \tag{2.20}$$

We call an asymptotically constant $\Gamma(t)$ normal *if one of the limits in* (2.20) *exists.*

Theorem 2.3. (Existence of a C^1-smooth Compactified System.) *Consider a nonautonomous system (2.1) with* C^1*-smooth* f *and* Γ*. If* $\Gamma(t)$ *is normal bi-asymptotically constant then there exists a coordinate transformation* $s = g(t)$ *from Assumption 2.2.1 such that the compactified system* (2.7)–(2.12) *is* C^1*-smooth on* $U \times [-1, 1]$.

In other words, the normal bi-asymptotic constant $\Gamma(t)$ condition (2.20) gives sufficient existence criteria that are both *optimal* and *easily testable*. To be more precise, the criteria are optimal in the sense that they eliminate 'pathological' bi-asymptotically constant $\Gamma(t)$, but still allow super-exponential, exponential, algebraic, logarithmic or even sub-logarithmic decay of $\Gamma(t)$. The proof of Theorem 2.3 is given in Sec. 2.2.1.3.

2.2.1.3 Proofs of Lemma 2.1, Lemma 2.2 and Theorem 2.3

Proof of Lemma 2.1

Starting with Eqs. (2.7)–(2.8), rewrite the extended vector field (2.11)–(2.12) in

terms of $g^{-1}(s)$:

$$f(x,\Gamma(g^{-1}(s))) = \begin{cases} f(x,\Gamma(g^{-1}(s))) & \text{for} \quad s \in (-1,1), \\ f(x,\Gamma^-) & \text{for} \quad s = -1, \\ f(x,\Gamma^+) & \text{for} \quad s = 1, \end{cases} \tag{2.21}$$

$$\gamma(s) = \begin{cases} \dot{g}\,(g^{-1}(s)) & \text{for} \quad s \in (-1,1), \\ 0 & \text{for} \quad s = \pm 1. \end{cases} \tag{2.22}$$

C^1-smoothness of the extended vector field (2.21)–(2.22) on $U \times (-1,1)$ follows from C^1-smoothness of f on U, C^1-smoothness of Γ on $\mathbb{R}$, and C^2-smoothness of g on $\mathbb{R}$, and C^2-smoothness of g^{-1} on $(-1,1)$ which follows from the generalised inverse function theorem [91, 92, 93]. What needs to be examined is C^1-smoothness of the extended vector field at the added right and left invariant subspaces $\{s = \pm 1\}$.

It follows from Definition 2.1.1, from Assumption 2.2.1 that $\Gamma(g^{-1}(s))$ and $\dot{g}\,(g^{-1}(s))$ are continuous at $s = \pm 1$:

$$\begin{aligned} &\lim_{s\to\pm 1^{\mp}} g^{-1}(s) = \lim_{s\to\pm\infty} t, \\ &\lim_{s\to\pm 1^{\mp}} \Gamma(g^{-1}(s)) = \lim_{t\to\pm\infty} \Gamma(t) = \Gamma^{\pm} = \Gamma(g^{-1}(\pm 1)), \\ &\lim_{s\to\pm 1^{\mp}} \gamma(s) = \lim_{s\to\pm 1^{\mp}} \dot{g}(g^{-1}(s)) = \lim_{t\to\pm\infty} \dot{g}(t) = 0 = \gamma(\pm 1). \end{aligned} \tag{2.23}$$

Thus, the extended vector field is continuous on $U \times [-1,1]$. The first derivative of the extended vector field is continuous at $\{s = \pm 1\}$ if the left- and right-sided limits $s \to \pm 1^{\mp}$ exist for all first-order partial derivatives. To check this, consider the Jacobian of the extended vector field

$$J(x,s) = \begin{pmatrix} \left(\frac{\partial f}{\partial x}\right)_{n\times n} & \left(\frac{\partial f}{\partial s}\right)_{n\times 1} \\ (0)_{1\times n} & \left(\frac{d\gamma}{ds}\right)_{1\times 1} \end{pmatrix}, \tag{2.24}$$

where the subscripts indicate the size of the matrix components of $J(x,s)$, use the chain rule and $(g^{-1}(s))' = 1/\dot{g}(g^{-1}(s))$, which follows from the inverse function theorem, to obtain

$$\begin{aligned} \left(\frac{\partial f}{\partial s}\right)_{n\times 1} &= \left(\frac{\partial f}{\partial \Gamma}\right)_{n\times d} \left(\frac{d}{ds}\Gamma(g^{-1}(s))\right)_{d\times 1} \\ &= \left(\frac{\partial f}{\partial \Gamma}\right)_{n\times d} \left(\dot{\Gamma}(g^{-1}(s))(g^{-1}(s))'\right)_{d\times 1} \\ &= \left(\frac{\partial f}{\partial \Gamma}\right)_{n\times d} \left(\frac{\dot{\Gamma}(g^{-1}(s))}{\dot{g}(g^{-1}(s))}\right)_{d\times 1}. \end{aligned} \tag{2.25}$$

$$\frac{d}{ds}\gamma(s) = \ddot{g}(g^{-1}(s))(g^{-1}(s))' = \frac{\ddot{g}(g^{-1}(s))}{\dot{g}(g^{-1}(s))}. \tag{2.26}$$

It follows from the continuity of $\Gamma(g^{-1}(s))$ at $s = \pm 1$ that both $(\partial f/\partial x)_{n\times n}$ and $(\partial f/\partial \Gamma)_{n\times d}$ are continuous at $s = \pm 1$. It follows from Eqs. (2.23) and (2.25) that $(\partial f/\partial s)_{n\times 1}$ is continuous at $s = \pm 1$ if and only if the first transformation condition (2.13) is satisfied. It follows from Eqs. (2.23) and (2.26) that the $J_{n+1,n+1}$ component of the Jacobian is continuous at $s = \pm 1$ if and only if the second transformation condition (2.14) is satisfied. Thus, the first derivative of the extended vector field is continuous on $U \times [-1, 1]$ if and only if transformation conditions (2.13) and (2.14) are satisfied. □

Proof of Lemma 2.2
It follows from Assumption 2.2.1 and from a generalised inverse function theorem [91, 92, 93] that $h(s)$ exists and is at least C^2-smooth for $s \in (-1, 1)$, and $h'(s) = 1/\dot{g}(h(s))$. Then, we can use the chain rule and Eq. (2.23) *to give the limits in condition (2.13) in terms of $h(s)$:*

$$\lim_{t\to\pm\infty} \frac{\dot{\Gamma}(t)}{\dot{g}(t)} = \lim_{s\to\pm\ 1^{\mp}} \frac{\dot{\Gamma}(h(s))}{\dot{g}(h(s))} = \lim_{s\to\pm\ 1^{\mp}} \dot{\Gamma}(h(s))h'(s) = \lim_{s\to\pm\ 1^{\mp}} \frac{d}{ds}\Gamma\left(h(s)\right).$$

Differentiating $g\left(h(s)\right) = s$ twice with respect to s shows that

$$\begin{aligned} &\dot{g}(h(s))h'(s) = 1, \\ &\ddot{g}(h(s))\ \left(h'(s)\right)^2 + \dot{g}(h(s))\, h''(s) = 0, \end{aligned}$$

which gives

$$\frac{\ddot{g}(h(s))}{\dot{g}(h(s))} = -\frac{h''(s)}{\left(h'(s)\right)^2}.$$

Thus, we can use Eq. (2.23) *to give the limits in condition (2.14) in terms of $h(s)$:*

$$\lim_{t\to\pm\infty} \frac{\ddot{g}(t)}{\dot{g}(t)} = \lim_{s\to\pm 1^{\mp}} \frac{\ddot{g}(h(s))}{\dot{g}(h(s))} = -\lim_{s\to\pm 1^{\mp}} \frac{h''(s)}{\left(h'(s)\right)^2}.$$

□

Proof of Theorem 2.3
Use the parametrised reference envelope from Definition 2.2.1 to construct a parametrised coordinate transformation $g_{(m)} : \mathbb{R} \to (-1, 1)$ that is at least C^2-smooth, strictly increasing and

$$g_{(m)}(t) \sim \begin{cases} 1 + A(t, m) & \text{as} \quad t \to +\infty, \\ -1 - A(t, m) & \text{as} \quad t \to -\infty. \end{cases}$$

It follows from the asymptotic properties of $A(t,m)$ *that*

$$\lim_{t\to\pm\infty} g_{(m)}(t) = \pm 1 \text{ and } \lim_{t\to\pm\infty} \dot{g}_{(m)}(t) = 0.$$

Thus, $g_{(m)}(t)$ *satisfies Assumption 2.2.1 by construction. By Definition 2.2.2, for any normal bi-asymptotically constant* $\Gamma(t)$ *there is an* m *such that*

$$\lim_{t\to\pm\infty} \frac{\dot{\Gamma}(t)}{\dot{g}_{(m)}(t)} = \pm \lim_{t\to\pm\infty} \frac{\dot{\Gamma}(t)}{\dot{A}(t,m)},$$

exist, meaning that $g_{(m)}(t)$ *satisfies the first transformation condition* (2.13) *by construction. Finally, one can verify by induction that*

$$\lim_{t\to\pm\infty} \frac{\ddot{g}_{(m)}(t)}{\dot{g}_{(m)}(t)} = \lim_{t\to\pm\infty} \frac{\ddot{A}(t,m)}{\dot{A}(t,m)} = 0,$$

for any non-negative $m \in \mathbb{N}$*, meaning that* $g_{(m)}(t)$ *satisfies the second transformation condition* (2.14) *by construction. It then follows from Lemma 2.1 that the extended vector field (2.11)–(2.12) is* C^1*-smooth on* $U \times [-1,1]$*.* □

2.2.2 One-sided compactification for asymptotically constant $\Gamma(t)$

Here we discuss briefly two one-sided subcases of the two-sided compactification from Sec 2.2.1. The discussion does not require new analysis, but might be helpful to readers interested in problems with asymptotically constant $\Gamma(t)$*. For asymptotically constant* $\Gamma(t)$ *with a future limit, we reformulate the nonautonomous system* (2.1) *into a compactified system that is autonomous and contains the flow and compact invariant sets of the future limit system* (2.3)*. This is achieved via one-sided compactification that uses the coordinate transformation* $s = g(t)$ *depicted in Fig. 2.1(b). For asymptotically constant* $\Gamma(t)$ *with a past limit, we reformulate the nonautonomous system* (2.1) *into a compactified system that is autonomous and contains the flow and compact invariant sets of the past limit system* (2.4)*. This is achieved via one-sided compactification that uses the coordinate transformation* $s = g(t)$ *depicted in Fig. 2.1(c).*

2.2.2.1 Right-sided compactification

Consider nonautonomous system (2.1) *with asymptotically constant* $\Gamma(t)$ *with future limit* Γ^+*, and assume that*

Assumption 2.2.2. *A coordinate transformation* $s = g(t)$ *maps the half* t*-line*

$[t_-, +\infty)$ onto the finite s-interval $[s_-, 1)$, is at least C^2-smooth, asymptotically constant with future limit 1, and strictly increasing with vanishing first derivative as $t \to +\infty$:

$$g : [t_-, +\infty) \to [s_-, 1), \quad g \in C^{k\geq 2}, \quad \lim_{t\to+\infty} g(t) = 1,$$
$$\dot{g}(t) > 0 \text{ for } t \geq t_- \text{ and } \lim_{t\to+\infty} \dot{g}(t) = 0. \tag{2.27}$$

Then consider the following autonomous compactified system

$$\dot{x} = f(x, \Gamma(h(s))), \tag{2.28}$$
$$\dot{s} = \gamma(s), \tag{2.29}$$
$$f(x, \Gamma(h(s))) = \begin{cases} f(x, \Gamma(h(s))) & \text{for} \quad s \in [s_-, 1), \\ f(x, \Gamma^+) & \text{for} \quad s = 1, \end{cases} \tag{2.30}$$
$$\gamma(s) = \begin{cases} 1/h'(s) & \text{for} \quad s \in [s_-, 1), \\ 0 & \text{for} \quad s = 1, \end{cases} \tag{2.31}$$

that is defined on the extended phase space $U \times [s_-, 1]$ with flow-invariant subspace $\{s = 1\}$ that carries the autonomous dynamics and compact invariant sets of the future limit system (2.3).

Lemma 2.1, Lemma 2.2 and Theorem 2.3 apply to compactified system (2.28)–(2.31) *after we leave out the limits $t \to -\infty$ ($s \to -1$) and replace: "bi-asymptotically constant" with "asymptotically constant with a future limit", "compactified system* (2.7)–(2.12)*" with "compactified system* (2.28)–(2.31)*", "phase space $U \times [-1, 1]$" with "phase space $U \times [s_-, 1]$" and "Assumption 2.2.1" with "Assumption 2.2.2".*

2.2.2.2 Left-sided compactification

Similarly, consider nonautonomous system (2.1) *with asymptotically constant $\Gamma(t)$ with past limit Γ^-, and assume that*

Assumption 2.2.3. *A coordinate transformation $s = g(t)$ maps the half t-line $(-\infty, t_+]$ onto the finite s-interval $(-1, s_+]$, is at least C^2-smooth, asymptotically constant with past limit -1, and strictly increasing with vanishing first derivative as $t \to -\infty$:*

$$g : (-\infty, t_+] \to (-1, s_+], \quad g \in C^{k\geq 2}, \quad \lim_{t\to-\infty} g(t) = -1,$$
$$\dot{g}(t) > 0 \text{ for } t \leq t_+ \text{ and } \lim_{t\to-\infty} \dot{g}(t) = 0. \tag{2.32}$$

Then consider the following autonomous compactified system

$$\dot{x} = f(x, \Gamma(h(s))), \tag{2.33}$$

$$\dot{s} = \gamma(s), \tag{2.34}$$

$$f(x, \Gamma(h(s))) = \begin{cases} f(x, \Gamma(h(s))) & \textit{for} \quad s \in (-1, s_+], \\ f(x, \Gamma^-) & \textit{for} \quad s = -1, \end{cases} \tag{2.35}$$

$$\gamma(s) = \begin{cases} 1/h'(s) & \textit{for} \quad s \in (-1, s_+], \\ 0 & \textit{for} \quad s = -1, \end{cases} \tag{2.36}$$

that is defined on the extended phase space $U \times [-1, s_+]$ *with flow-invariant subspace* $\{s = -1\}$ *that carries the autonomous dynamics and compact invariant sets of the past limit system* (2.4).

Lemma 2.1, Lemma 2.2 and Theorem 2.3 apply to compactified system (2.33)–(2.36) *after we leave out the limits* $t \to +\infty$ *(*$s \to 1$*) and replace: "bi-asymptotically constan" with "asymptotically constant with a past limit", "compactified system* (2.7)–(2.12)*" with "compactified system* (2.33)–(2.36)*", "phase space* $U \times [-1, 1]$*" with "phase space* $U \times [-1, s_+]$*" and "Assumption 2.2.1" with "Assumption 2.2.3".*

2.3 Compactified system dynamics

Given a nonautonomous system (2.1) *with a bi-asymptotically constant* $\Gamma(t)$*, we can relate the dynamics of the future limit system* (2.3) *and the past limit system* (2.4) *on the one hand, and the* C^1*-smooth compactified system* (2.7)–(2.12) *on the other. Specifically, we focus on the extrapolation of dynamical structure from (one of) the limit systems* (2.3) *or* (2.4).

Remark 2.3.1. *In the compactified system* (2.7)–(2.12)*, the time evolution of* $s(t)$ *is not influenced by the time evolution of* $x(t)$*. Owing to this skew-product structure:*

(i) Any compact invariant set for the future limit system (2.3) *gains one attracting direction, and any compact invariant set for the past limit system* (2.4) *gains one repelling direction in the extended phase space of* (2.7)–(2.12)*, in the sense of monotone increasing* $s(t)$*:*

$$\dot{s}(t) = \dot{g}(t) > 0,$$

which follows Eq. (2.8).

(ii) A regular compact invariant set [4] *of one of the limit systems can be viewed as*

[4] A compact invariant set is *regular* if the full Lyapunov spectrum exists.

gaining an additional Lyapunov exponent [5] *when emebedded in the extended phase space. The additional Lyapunov exponent quantifies linear stability in the s-direction, is independent of x, and is given by the $(n+1, n+1)$-th element of the Jacobian* (2.24) *or by the limit in the second transformation condition* (2.14)*:*

$$l_s^{\pm} = \frac{d}{ds}\gamma(s)\bigg|_{s=\pm 1} = -\frac{h''(s)}{(h'(s))^2}\bigg|_{s=\pm 1} = \lim_{t\to\pm\infty}\frac{\ddot{g}(t)}{\dot{g}(t)}, \tag{2.37}$$

where the second equality follows from Lemma 2.2. We note that $l_s^{\pm}$ is zero when $g(t)$ decays slower than exponentially; see Corollaries 2.4 and 2.5 ahead.

(iii) The Lyapunov vector corresponding to $l_s^{\pm}$ is independent of x. The vector is normal to $\{s = \pm 1\}$ if the top n elements in last column of the Jacobian (2.24) *are zero or if the first transformation condition* (2.13) *is zero*

$$\frac{\partial f}{\partial s}\bigg|_{s=\pm 1} = \frac{\partial f}{\partial \Gamma}\bigg|_{s=\pm 1}\frac{d}{ds}\Gamma(h(s))\bigg|_{s=\pm 1} = \frac{\partial f}{\partial \Gamma}\bigg|_{s=\pm 1}\lim_{t\to\pm\infty}\frac{\dot{\Gamma}(t)}{\dot{g}(t)} = 0,$$

where the second equality follows from Lemma 2.2.

2.3.1 Attractors, repellers, and invariant manifolds

In the particular case of an attractor in the future limit system (and a repeller in the past limit system), this can be stated more topologically. We say that a compact invariant set A is an attractor if it is the ω-limit set of a neighborhood of itself, i.e., there is an open set D with $A \subset D$, so that $\omega(D) = A$. With the notation that $\psi(t, y_0)$ is the flow evolution for time t of the initial condition y_0, which also applies to a set of initial conditions $\psi(t, D) = \{\psi(t, y) : y \in D\}$, the $\omega-$limit set is given by:

$$\omega(D) = \bigcap_{T>0}\overline{\{\psi(t, D) : t > T\}},$$

where $\overline{S}$ denotes the closure of S. Similarly, the α-limit set is given by

$$\alpha(D) = \bigcap_{T<0}\overline{\{\psi(t, D) : t < T\}},$$

and a set A is a repeller if it is the α-limit set of a neighborhood of itself. If $A \subset \{s = 1\}$ is an attractor for the future limit system (2.3)*, then it is also an attractor for the compactified system* (2.7)–(2.12) *when considered in the extended phase space. Similarly, if $A \subset \{s = -1\}$ is a repeller for the past limit system* (2.4)*, then it is a*

[5] Referred to as the *normal Lyapunov exponent* in the terminology of [94].

repeller for (2.7)–(2.12) *when considered in the extended phase space.*

In the following, it will be important to distinguish between the stable set and stable manifold of a compact invariant set (similarly unstable set and manifold). Let $\psi(t, y_0)$ *be the flow evolution for time* t *of the initial condition* y_0*. For any compact invariant set* A*, we define its stable set* $w^s(A)$ *and unstable set* $w^u(A)$*:*

$$w^s(A) = \{y : \omega(y) \subseteq A\}, \quad w^u(A) = \{y : \alpha(y) \subseteq A\}.$$

The extra condition for the stable manifold is that the decay is exponential, i.e., the stable manifold $W^s(A)$ *and unstable manifold* $W^u(A)$ *are given by*

$$W^s(A) = \{y \in w^s(A) : d(\psi(y,t), A) \leq Ke^{\beta t}, \text{ for some } K > 0, \beta < 0 \text{ and all } t > 0\},$$
$$W^u(A) = \{y \in w^u(A) : d(\psi(y,t), A) \leq Ke^{\beta t}, \text{ for some } K > 0, \beta > 0 \text{ and all } t < 0\}.$$

The distance function d *is between a point and a set, and is the greatest lower bound in the Euclidean distance between the point on the trajectory and any point in the set* A*:*

$$d(\psi(y,t), A) = \inf_{x \in A} \|\psi(y,t) - x\|.$$

We will also need local versions of the above sets/manifolds. Based on an open superset N *of a compact invariant set* A*, we define the local stable set of* A*:*

$$w^s_{\text{loc}}(A) = \{y : y \in w^s(A) \text{ and } \psi(y,t) \in N \text{ for all } t > 0\},$$

and a local stable manifold of A*:*

$$W^s_{\text{loc}}(A) = \{y : y \in W^s(A) \text{ and } \psi(y,t) \in N \text{ for all } t > 0\}.$$

The local unstable set of A*, denoted* $w^u_{\text{loc}}(A)$*, and the local unstable manifold of* A*, denoted* $W^u_{\text{loc}}(A)$*, are defined similarly for* $t < 0$*.*

Due to the possibility that $l^{\pm}_s = 0$*, we need to consider compact invariant sets with centre directions, and from now we focus on equilibria, denoted as* η*. The corresponding invariant manifolds cannot be described in terms of decay rates so straightforwardly. They are characterised as the graphs of functions over the relevant subspaces from the linearised system. Specifically, let* E^c, E^s *and* E^u *be the subspaces based at* η *and spanned by the sets of eigenvectors corresponding to centre (zero real-part) eigenvalues, stable (negative real-part) eigenvalues and unstable (positive real-part) eigenvalues, respectively. They are referred to as the centre (*E^c*), stable (*E^s*) and unstable (*E^u*) eigenspaces, and are invariant under the linearised system at* η*.*

A (local) centre manifold is given as the graph of a Lipschitz function h^c that is tangential to E^c at η and flow-invariant relative to some chosen neighborhood N of the equilibrium η. More precisely,

$$W^c_{loc}(\eta) = \{\mathrm{gr}(h^c) \text{ where } h^c : E^c \cap N \to E^s \oplus E^u\}.$$

The (local) centre-stable manifold is defined similarly, as the graph of a Lipschitz function h^{cs} that is tangential to $E^c \oplus E^s$ at η and flow-invariant relative to some chosen neighborhood N of the equilibrium η:

$$W^{cs}_{loc}(\eta) = \{\mathrm{gr}(h^{cs}) \text{ where } h^{cs} : E^c \oplus E^s \cap N \to E^u\}.$$

and $W^{cs}_{loc}(\eta)$ is tangential to $E^c \oplus E^s$ at η and invariant relative to N.

In general, neither the centre nor centre-stable manifold are unique in that there may well be other functions whose graphs satisfy the tangency conditions and are invariant relative to N with the corresponding domains and ranges.

2.3.2 Dynamics from the future limit system

Of particular interest in both the R-tipping and nonlinear wave problems mentioned in Sec.2.1.2 is the situation where a hyperbolic saddle equilibrium, denoted η^+, is present for the future limit system. In the extended phase space of the compactified system, this saddle becomes

$$\tilde{\eta}^+ = (\eta^+, 1).$$

If the decay of $\dot{\Gamma}(t)$ to zero as $t \to +\infty$ is exponential or faster, then it is possible to construct a transformation $s = g(t)$ [e.g. (2.41)*] so the saddle gains an exponentially stable direction and remains hyperbolic with a higher-dimensional stable manifold when embedded in the extended phase space of* (2.7)–(2.12)*; see Corollary 2.4. In this case, it follows from the stable manifold theorem that*

$$W^s(\tilde{\eta}^+) = w^s(\tilde{\eta}^+).$$

However, this may not be true in general.

An interesting situation occurs when the decay of $\dot{\Gamma}(t)$ is slower than exponential. In this case, the saddle gains a neutrally stable center direction when embedded in the extended phase space of (2.7)–(2.12)*, meaning that $W^s(\tilde{\eta}^+) \neq w^s(\tilde{\eta}^+)$ because $W^s(\tilde{\eta}^+) \subset \{s = 1\}$; see Corollary 2.5 and Fig. 2.4(a)–(b). Nonetheless, we can form a local center-stable manifold W^{cs}_{loc} based on some neighborhood N of $\tilde{\eta}^+$. Because of*

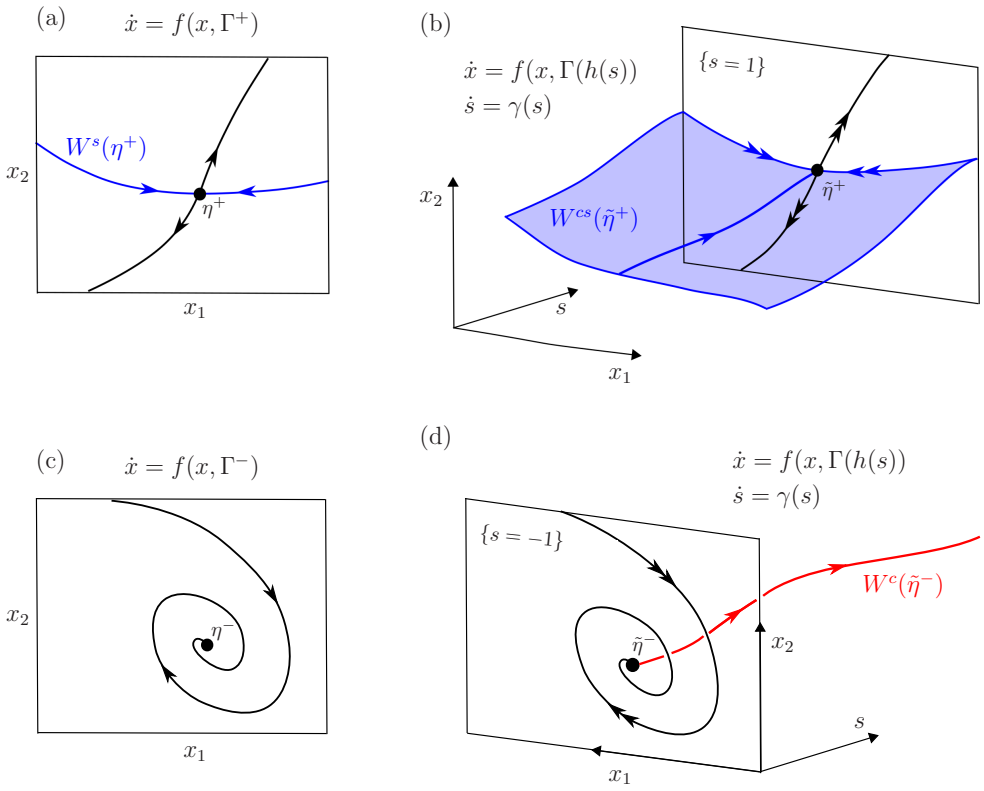

Figure 2.4: (a) A hyperbolic saddle η^+ for the future limit system (2.3) gains a neutrally stable center direction and becomes (b) a non-hyperbolic saddle $\tilde{\eta}^+ = (\eta^+, 1)$ in the extended phase space of the compactified system (2.7)–(2.12). (c) A hyperbolic stable focus η^- for the past limit system (2.4) gains a neutrally unstable center direction and becomes (d) a non-hyperbolic saddle-focus $\tilde{\eta}^- = (\eta^-, -1)$ with one-dimensional center manifold in the extended phase space of (2.7)–(2.12).

the special structure inherent in the compactified system, $s(t)$ tends monotonically to 1, $W^{cs}_{\text{loc}}(\tilde{\eta}^+)$ is forward invariant by construction, and one can show that [64]:

$$W^{cs}_{\text{loc}}(\tilde{\eta}^+) = w^s_{\text{loc}}(\tilde{\eta}^+).$$

2.3.3 Dynamics from the past limit system

Analogues discussion can be given for the past limit. Of particular interest in the pullback attractor and R-tipping problems mentioned above is the situation where a hyperbolic sink is present for the past limit system. In the extended phase space of the compactified system, this sink becomes

$$\tilde{\eta}^- = (\eta^-, -1).$$

If the decay of $\dot{\Gamma}(t)$ to zero as $t \to -\infty$ is exponential or faster, then it is possible to construct a transformation $s = g(t)$ [e.g. (2.41)*] so the sink gains an exponentially unstable direction and becomes a hyperbolic saddle with a one-dimensional unstable manifold in the extended phase space of* (2.7)–(2.12)*; see Corollary 2.4. In this case, it follows from the stable manifold theorem that*

$$W^u(\tilde{\eta}^-) = w^u(\tilde{\eta}^-).$$

However, this may not be true in general.

An interesting situation occurs when the decay of $\dot{\Gamma}(t)$ is slower than exponential. In this case the sink gains a neutrally unstable center direction when embedded in the extended phase space of (2.61)–(2.12)*, meaning that $W^u(\tilde{\eta}^-) \neq w^u(\tilde{\eta}^-)$ because $W^u(\tilde{\eta}^-) = \emptyset$; see Corollary 2.5 and Fig. 2.4(c)–(d). Nonetheless, we can work with a local center manifold W^c_{loc} based on some neighborhood N of $\tilde{\eta}^-$. Because of the special structure inherent in the compactified system, $s(t)$ tends monotonically to -1 as $t \to -\infty$, $W^c_{\text{loc}}(\tilde{\eta}^-)$ is backward invariant, and one can show that [64]:*

$$W^c_{\text{loc}}(\tilde{\eta}^-) = w^u_{\text{loc}}(\tilde{\eta}^-).$$

2.3.4 Applications

The key point of this section is that relations between nonautonomous and compactified system dynamics can be used to simplify analysis of the nonautonomous system (2.1) *as follows:*

(i) Unlike the original system (2.1)*, the compactified system* (2.7)–(2.12) *is autonomous and may contain compact invariant sets $\tilde{\eta}^+ \subset \{s = 1\}$ or $\tilde{\eta}^- \subset \{s = -1\}$.*

(ii) The spatial or temporal variation of the nonautonomous term $\Gamma(t)$ becomes in a certain sense 'encoded' in the geometric shape of the stable (or centre-stable) invariant manifold $W^s(\tilde{\eta}^+)$ or the unstable (or center) invariant manifold $W^u(\tilde{\eta}^-)$ in the extended phase space of (2.7)–(2.12)*.*

(iii) Solutions to nonautonomous system (2.1) *that remain bounded as t tends to positive infinity are contained in the stable (or center-stable) invariant manifold $W^s(\tilde{\eta}^+)$ in the extended phase space of* (2.7)–(2.12)*. For example, if $\tilde{\eta}^+$ is a saddle, then $W^s(\tilde{\eta}^+)$ may form the R-tipping threshold in the R-tipping problem, or contain the family of wave solutions in the nonlinear wave problem.*

Solutions to nonautonomous system (2.1) *that remain bounded as t tends to*

negative infinity are contained in the unstable (or center) invariant manifold $W^u(\tilde{\eta}^-)$ in the extended phase space of (2.7)–(2.12). *For example, if η^- is asymptotically stable, then $W^u(\tilde{\eta}^-)$ contains local pullback attractors of* (2.1).

Solutions to (2.1) *that remain bounded as t tends to positive and negative infinity are transformed into connecting heteroclinic orbits from $\tilde{\eta}^-$ to $\tilde{\eta}^+$ in the extended phase space of* (2.7)–(2.12). *For example, difficult to pin down nonautonomous instabilities in* (2.1)*, such as R-tipping, become codimension-one heteroclinic connections in the extended phase space.*

We believe the results above for equilibria also hold for more complicated compact invariant sets $\eta^\pm$ of the limit systems such as periodic orbits or tori.

2.4 Examples of parametrised compactification

In this section we construct actual examples of coordinate transformations $g(t)$ that are useful in practice. This raises the problem of the 'rate' of compactification relative to the rate of asymptotic decay of $\Gamma(t)$. To address this issue, we introduce compactification parameters and work with parametrised compactifications. *The additional freedom acquired in parametrisation of $g(t)$ allows us to:*

(i) Fulfill the compactification conditions (2.13)–(2.14) *by a suitable choice of the compactification parameter(s).*

(ii) Control the direction of the additional Lyapunov vector transverse to invariant subspaces $\{s = \pm 1\}$ to facilitate analysis.

What is more, we consider different types of asymptotic decay of $g(t)$ giving rise to different behaviour of $s(t)$ near $\{s = \pm 1\}$.

2.4.1 Γ-compactification

In some cases, the compactification transformation can be constructed in terms of (one component of) the nonautonomous term $\Gamma(t) \in \mathbb{R}^d$ itself; see [18, 43] for examples. Let $\dot{\Gamma}(t) = (\dot{\Gamma}_1(t), \ldots, \dot{\Gamma}_d(t))$ be ordered such that $\dot{\Gamma}_1(t)$ does not decay faster than the other components

$$\lim_{t\to\pm\infty} \frac{\dot{\Gamma}_i(t)}{\dot{\Gamma}_1(t)} = L^\pm \in \mathbb{R} \text{ for } i = 2, \ldots, d.$$

We can construct a coordinate transformation (2.6) *in terms of* $\Gamma_1(t)$*:*

$$g(t) = \frac{2\Gamma_1(t) - \Gamma_1^+ - \Gamma_1^-}{\Gamma_1^+ - \Gamma_1^-}, \tag{2.38}$$

if $\Gamma_1(t)$ *satisfies Assumption 2.2.1 with future limit* Γ_1^+ *and past limit* Γ_1^-*. One can verify that such* $g(t)$ *satisfies the first transformation condition (2.13):*

$$\lim_{t\to\pm\infty} \frac{\dot{\Gamma}_i(t)}{\dot{g}(t)} = \begin{cases} (\Gamma_1^+ - \Gamma_1^-)/2 \neq 0 & \text{for} \quad i = 1, \\ (\Gamma_1^+ - \Gamma_1^-)/2 \neq 0 \text{ or } 0 & \text{for} \quad i = 2, \dots, d, \end{cases}$$

and satisfies the second transformation condition (2.14):

$$\lim_{t\to\pm\infty} \frac{\ddot{g}(t)}{\dot{g}(t)} = \lim_{t\to\pm\infty} \frac{\ddot{\Gamma}_1(t)}{\dot{\Gamma}_1(t)},$$

if $\Gamma_1(t)$ *satisfies (2.14). Similarly, one can construct a coordinate transformation* (2.27)*:*

$$g(t) = \frac{\Gamma_1(t) - \Gamma_1(0)}{\Gamma_1^+ - \Gamma_1(0)}, \tag{2.39}$$

if $\Gamma_1(t)$ *satisfies Assumption 2.2.2 with future limit* Γ_1^+*, or a coordinate transformation* (2.32)*:*

$$g(t) = -\frac{\Gamma_1(t) - \Gamma_1(0)}{\Gamma_1^- - \Gamma_1(0)}, \tag{2.40}$$

if $\Gamma_1(t)$ *satisfies Assumption 2.2.3 with past limit* Γ_1^-*.*

For example, one can use $g(t) = \tanh(t)$ *if* $\Gamma_1(t) = \tanh(t)$*. This approach can be extended to certain non-monotone* $\Gamma(t)$ *if they can be expressed in terms of monotone functions. For example, one can also use* $g(t) = \tanh(t)$ *if* $\Gamma_1(t) = \mathit{sech}(t) = \sqrt{1 - \tanh^2(t)}$*.*

Constructing $g(t)$ *in terms of* $\Gamma_1(t)$ *is not always possible, for example it does not work for non-monotone* $\Gamma_1(t)$*. When it is possible, it has certain limitations. For example, there may be no algebraic formula for the inverse* $h(s)$ *required for the augmented component* (2.8) *of the vector field. To facilitate numerical analysis, one may wish to work with transverse eigenvectors that are normal to invariant subspaces* $\{s = \pm 1\}$*, which does not occur typically for a* Γ*-compactification because the Jacobian* (2.24) *is not block-diagonal. Therefore, more universal compactification transformations will be required in general.*

2.4.2 Exponential compactification

Guided by Assumption 2.2.1 and Lemma 2.1, we construct an example of a parametrised coordinate transformation *(2.6) with exponential asymptotic decay in the form*

$$s = g_{(\alpha)}(t) = \tanh\left(\frac{\alpha t}{2}\right), \quad t = h_{(\alpha)}(s) = \frac{1}{\alpha}\ln\frac{1+s}{1-s}, \tag{2.41}$$

where the compactification parameter $\alpha > 0$ *parametrises the* rate *of exponential decay of* $\dot{g}_{(\alpha)}(t)$.

One can verify that this transformation satisfies Assumption 2.2.1 and the second transformation condition (2.14)*:*

$$\lim_{t\to\pm\infty}\frac{\ddot{g}_{(\alpha)}(t)}{\dot{g}_{(\alpha)}(t)} = -\alpha\lim_{t\to\pm\infty}\tanh\left(\frac{\alpha t}{2}\right) = \mp\alpha. \tag{2.42}$$

The augmented component $\gamma_{(\alpha)}(s)$ *of the vector field is obtained by computing and then inverting* $dh_{(\alpha)}/ds$*, so that the compactified system* (2.7)–(2.10) *becomes*

$$\left.\begin{aligned}\dot{x} &= f(x,\Gamma(h_{(\alpha)}(s))),\\ \dot{s} &= \frac{\alpha}{2}\left(1-s^2\right).\end{aligned}\right\} \tag{2.43}$$

We then examine properties of (2.43) *with dependence on* α *and the asymptotic decay of* $\dot{\Gamma}(t)$.

Corollary 2.4. (Compactification for $\dot{\Gamma}(t)$ with exponential or faster decay.) *Consider a nonautonomous system (2.1) with* C^1*-smooth* f *and* Γ*, and bi-asymptotically constant* $\Gamma(t)$*. Moreover, suppose there is a* $\rho > 0$ *such that*

$$\lim_{t\to\pm\infty}\frac{\dot{\Gamma}(t)}{e^{\mp\rho t}} \text{ exist}. \tag{2.44}$$

Then, given the coordinate transformation (2.41) *with any* $\alpha \in (0,\rho]$*, the ensuing autonomous compactified system* (2.43) *is* C^1*-smooth on the extended phase space* $U\times[-1,1]$*. The distance between any trajectory of* (2.43) *and* $\{s=\pm1\}$ *decays exponentially as* $t\to\pm\infty$.

In other words, regular compact invariant sets for the limit systems gain one non-zero Lyapunov exponent (2.42) *when embedded in the extended phase space of* (2.43)*, but* (2.43) *requires exponentially or faster decaying* $\dot{\Gamma}(t)$ *to be* C^1*-smooth.*

Proof. Given (2.44), it follows from the asymptotic properties of $\dot{g}_{(\alpha)}(t)$:

$$\dot{g}_{(\alpha)}(t) \sim 2\alpha\, e^{\mp\alpha t} \text{ as } t\to\pm\infty, \tag{2.45}$$

and from the algebraic limit theorem

$$\begin{aligned}\lim_{t\to\pm\infty}\frac{\dot{\Gamma}(t)}{\dot{g}_{(\alpha)}(t)} &= \lim_{t\to\pm\infty}\frac{\dot{\Gamma}(t)}{e^{\mp\rho t}}\frac{e^{\mp\rho t}}{\dot{g}_{(\alpha)}(t)}\\ &= \lim_{t\to\pm\infty}\frac{\dot{\Gamma}(t)}{e^{\mp\rho t}}\lim_{t\to\pm\infty}\frac{e^{\mp\rho t}}{\dot{g}_{(\alpha)}(t)}\\ &= \frac{1}{2\alpha}\lim_{t\to\pm\infty}\frac{\dot{\Gamma}(t)}{e^{\mp\rho t}}\lim_{t\to\pm\infty}e^{\mp(\rho-\alpha)t},\end{aligned} \tag{2.46}$$

that the first transformation condition (2.13) is satisfied if $0<\alpha\leq\rho$. It follows from (2.42) that the second transformation condition (2.14) is satisfied if $\alpha>0$. It then follows from Lemma 2.1 that the compactified system (2.43) is C^1-smooth on the extended phase space $U\times[-1,1]$ for any $0<\alpha\leq\rho$.

The Hausdorff semi-distance $d(p(t),S^{\pm})$ between the point $p(t)=(x(t),s(t))$ on a trajectory and invariant subspace $S^{\pm}=\{(x,s):s=\pm1\}$ in the extended phase space is the distance between $s(t)$ and ±1. Thus, exponential decay of $d(p(t),S^{\pm})$ follows from exponential approach of $s(t)$ towards ±1 as $t\to\pm\infty$:

$$d(p(t),S^{\pm})=\inf_{y\in S^{\pm}}\|p(t)-y\|=1\mp s(t)=\frac{2}{e^{\pm\alpha t}+1}.$$

□

Similarly, one can discuss one-sided subcases of the two-sided compactification above using parametrised coordinate transformation (2.27) with exponential decay in the form

$$s=g_{(\alpha)}(t)=1-e^{-\alpha t},\ \ t=h_{(\alpha)}(s)=-\frac{1}{\alpha}\ln(1-s), \tag{2.47}$$

or parametrised coordinate transformation (2.32) with exponential decay in the form

$$s=g_{(\alpha)}(t)=-1+e^{\alpha t},\ \ t=h_{(\alpha)}(s)=\frac{1}{\alpha}\ln(1+s). \tag{2.48}$$

2.4.3 Algebraic compactification

Guided by Assumption 2.2.1 and Lemma 2.2, construct an inverse of *parametrised compactification transformation* (2.6) with algebraic asymptotic decay in the form akin to stereographic projection

$$t=h_{(\alpha)}(s)=\frac{s}{(1-s^2)^{\frac{1}{\alpha}}}, \tag{2.49}$$

where the *compactification parameter* $\alpha > 0$ parametrises the *order* of algebraic decay of $\dot{g}_{(\alpha)}(t)$. There is no formula for the corresponding compactification transformation $s = g_{(\alpha)}(t)$ in the general case $\alpha > 0$. However, there is one in the special case $\alpha = 1$:

$$s = g(t) = \frac{-1 + \sqrt{1 + 4t^2}}{2t}, \quad t = h(s) = \frac{s}{1 - s^2}. \tag{2.50}$$

One can use Lemma 2.2 to verify that transformation (2.49) satisfies Assumption 2.2.1 and the second transformation condition (2.14):

$$\begin{aligned} \lim_{t\to\pm\infty} \frac{\ddot{g}_{(\alpha)}(t)}{\dot{g}_{(\alpha)}(t)} &= -\lim_{s\to\pm 1} \frac{d^2 h_{(\alpha)}/ds^2}{(dh_{(\alpha)}/ds)^2} \\ &= -\lim_{s\to\pm 1} \frac{(1-s^2)^{\frac{1}{\alpha}} \left(2(2-\alpha)s^3 + 6\alpha s\right)}{\left[\alpha(1-s^2) + 2s^2\right]^2} = 0, \end{aligned} \tag{2.51}$$

The augmented component $\gamma_{(\alpha)}(s)$ of the vector field is obtained by computing and then inverting $dh_{(\alpha)}/ds$, so that the compactified system (2.7)–(2.8) becomes

$$\left.\begin{aligned} \dot{x} &= f(x, \Gamma(h_{(\alpha)}(s))), \\ \dot{s} &= \frac{\alpha(1-s^2)^{1+\frac{1}{\alpha}}}{\alpha(1-s^2) + 2s^2}. \end{aligned}\right\} \tag{2.52}$$

We then examine properties of (2.52) with dependence on α and the asymptotic decay of $\dot{\Gamma}(t)$.

Corollary 2.5. (Compactification for $\dot{\Gamma}(t)$ with algebraic or faster decay.) *Consider a nonautonomous system (2.1) with C^1-smooth f and Γ, and bi-asymptotically constant $\Gamma(t)$. Moreover, suppose there is an $m > 1$ such that*

$$\lim_{t\to\pm\infty} \frac{\dot{\Gamma}(t)}{t^{-m}} \text{ exist}. \tag{2.53}$$

Then, given the coordinate transformation (2.49) *with any $\alpha \in (0, m-1]$, the ensuing autonomous compactified system* (2.52) *is C^1-smooth on the extended phase space $U \times [-1, 1]$. The distance between any trajectory of* (2.52) *and $\{s = \pm 1\}$ decays algebraically (i.e. slower than exponentially) as $t \to \pm\infty$.*

In other words, algebraically (or faster) decaying $\dot{\Gamma}(t)$ is sufficient for (2.52) to be C^1-smooth, but regular compact invariant sets for the limit systems gain one zero Lyapunov exponent (2.51) when embedded in the extended phase space of (2.52).

Proof. Given (2.53), it follows from the asymptotic properties of $h_{(\alpha)}(t)$ and from

the algebraic limit theorem

$$\begin{aligned}\lim_{t\to\pm\infty}\frac{\dot{\Gamma}(t)}{\dot{g}_{(\alpha)}(t)} &= \lim_{t\to\pm\infty}\frac{\dot{\Gamma}(t)}{t^{-m}}\frac{t^{-m}}{\dot{g}_{(\alpha)}(t)} = \lim_{t\to\pm\infty}\frac{\dot{\Gamma}(t)}{t^{-m}}\lim_{t\to\pm\infty}\frac{t^{-m}}{\dot{g}_{(\alpha)}(t)}\\ &= \lim_{t\to\pm\infty}\frac{\dot{\Gamma}(t)}{t^{-m}}\lim_{s\to\pm1}\frac{(h_{(\alpha)}(s))^{-m}}{\gamma_{(\alpha)}(s)}\\ &= \lim_{t\to\pm\infty}\frac{\dot{\Gamma}(t)}{t^{-m}}\lim_{s\to\pm1}\frac{1}{\alpha s^m}\left(\alpha(1-s^2)^{\frac{m-1}{\alpha}}+2s^2(1-s^2)^{\frac{m-1-\alpha}{\alpha}}\right), \quad (2.54)\end{aligned}$$

that the first transformation condition (2.13) is satisfied if both $(1-s^2)$ terms above have non-negative powers, or if $0<\alpha\leq m-1$. It follows from (2.51) that the second transformation condition (2.14) is satisfied if $\alpha>0$. It then follows from Lemma 2.1 that the compactified system (2.52) is C^1-smooth on the extended phase space $U\times[-1,1]$ for any $0<\alpha\leq m-1$.

The Hausdorff semi-distance $d(p(t),S^{\pm})$ between a point $p(t)=(x(t),s(t))$ on a trajectory and invariant subspace $S^{\pm}=\{(x,s):s=\pm1\}$ in the extended phase space is the distance between $s(t)$ and ±1. Thus, algebraic decay of $d(p(t),S^{\pm})$ follows from algebraic approach of $s(t)$ towards ±1 as $t\to\pm\infty$:

$$d(p(t),S^{\pm})=\inf_{y\in S^{\pm}}\|p(t)-y\|=1\mp s(t).$$

□

Similarly, one can discuss one-sided subcases of the two-sided compactification above using parametrised inverse coordinate transformation (2.27) with algebraic decay in the form

$$t=h_{(\alpha)}(s)=\frac{s}{(1-s)^{\frac{1}{\alpha}}}, \quad (2.55)$$

with the special case $\alpha=1$:

$$s=g(t)=\frac{t}{1+t},\ \ t=h(s)=\frac{s}{1-s}, \quad (2.56)$$

or parametrised inverse coordinate transformation (2.32) with algebraic decay in the form

$$t=h_{(\alpha)}(s)=\frac{s}{(1+s)^{\frac{1}{\alpha}}}, \quad (2.57)$$

with the special case $\alpha=1$:

$$s=g(t)=\frac{t}{1-t},\ \ t=h(s)=\frac{s}{1+s}. \quad (2.58)$$

2.4.4 Other compactification types and asymptotic decay limitations

The previous sections discuss suitable candidates for parametrised coordinate transformations $g_{(\alpha)}(t)$ whose derivatives $\dot{g}_{(\alpha)}(t)$ have the same rates of exponential (2.41) or algebraic (2.49) decay as $t \to +\infty$ and $t \to -\infty$. Transformations with other types of asymptotic decay, or with different types or rates of asymptotic decays as $t \to +\infty$ and $t \to -\infty$ are also possible, although there are limitations imposed by the second compactification condition (2.14). While coordinate transformations with super-exponential decay are excluded by condition (2.14) as explained below Lemma 2.1, transformations with slower than algebraic decay are allowed by condition (2.14); see for example the (sub)logarithmic transformation $g_{(m)}(t)$ in the proof of Theorem 2.3 in Sec. 2.2.1.3,

In case of bi-asymptotically constant $\Gamma(t)$ whose derivative $\dot{\Gamma}(t)$ has the same type and rate of asymptotic decay as $t \to +\infty$ and $t \to -\infty$, the natural choice is transformation (2.6) whose derivative $\dot{g}_{(\alpha)}(t)$ also has one type and rate of asymptotic decay and satisfies the second compactification condition (2.14). The first transformation condition (2.13) is then satisfied if α can be chosen so that the asymptotic decay of $\dot{g}_{(\alpha)}(t)$ is not faster than the asymptotic decay of $\dot{\Gamma}(t)$.

In case of bi-asymptotically constant $\Gamma(t)$ whose derivative $\dot{\Gamma}(t)$ has different types or rates of asymptotic decay as $t \to +\infty$ and $t \to -\infty$, there are different options. The simplest option is transformation (2.6) whose derivative $\dot{g}_{(\alpha)}(t)$ has one type and rate of asymptotic decay and satisfies the second compactification condition (2.14). Another option is transformation (2.6) that, unlike examples (2.41) and (2.49), has the same type but different rates of asymptotic decays as $t \to +\infty$ and $t \to -\infty$. For example, transformation (2.41) can be generalised to

$$t = h_{(\alpha_-,\alpha_+)}(s) = \frac{1}{\alpha_-}\ln(1+s) - \frac{1}{\alpha_+}\ln(1-s), \tag{2.59}$$

where the *compactification parameters* α_- and $\alpha_+ > 0$ parametrise the *rates* of exponential decay of $\dot{g}_{(\alpha_-,\alpha_+)}(t)$ as $t \to -\infty$ and $t \to +\infty$, respectively. Similarly, transformation (2.49) can be generalised to

$$t = h_{(\alpha_-,\alpha_+)}(s) = \frac{s}{(1+s)^{\frac{1}{\alpha_-}}\,(1-s)^{\frac{1}{\alpha_+}}}, \tag{2.60}$$

where α_- and $\alpha_+ > 0$ parametrise the *orders* of algebraic decay of $\dot{g}_{(\alpha_-,\alpha_+)}(t)$ as $t \to -\infty$ and $t \to +\infty$, respectively. Yet another option is a 'hybrid' transformation (2.6) that, unlike examples (2.59) and (2.60), has different types of

asymptotic decays as $t \to +\infty$ and $t \to -\infty$. For each option, the first transformation condition (2.13) is satisfied if the compactification parameter(s) can be chosen so that the asymptotic decays of $\dot{g}_{(\alpha)}(t)$ are not faster than the corresponding asymptotic decays of $\dot{\Gamma}(t)$.

2.5 Compactification in R-tipping analysis

In the previous sections of this chapter we described the general compactification formalism. Here, we want to adapt the general formalism to the R-tipping problem:

$$\dot{x} = f(x, \Lambda(rt)),$$

which corresponds to system (2.1) with

$$\Gamma(t) = \Lambda(rt),$$

where we introduced the 'rate' parameter $r > 0$. In other words, we reformulate some of the statements to account for the explicit dependence on r. To be more precise, for the general setting, we have the nonautonomous term $\Gamma(t)$, coordinate transformation $s = g_{(\alpha)}(t)$, inverse transformation $t = h_{(\alpha)}(s) := g^{-1}_{(\alpha)}(s)$, and the augmented component $\gamma_{(\alpha)}(s)$ of the vector field as follows:

$$\begin{aligned}
&\Gamma(t) \to \Gamma^{\pm} \in \mathbb{R}^d \ \text{ as } \ t \to \pm\infty,\\
&s = g_{(\alpha)}(t),\\
&t = h_{(\alpha)}(s) := g^{-1}_{(\alpha)}(s),\\
&\gamma_{\alpha}(s) = 1/h'_{(\alpha)}(s).
\end{aligned}$$

For the setting in R-tipping analysis, we introduce slightly modified versions of the above:

$$\begin{aligned}
&\Gamma(t) = \Lambda(rt) \to \lambda^{\pm} \in \mathbb{R}^d \ \text{ as } \ t \to \pm\infty,\\
&s = g_{(\alpha)}(t) = \tilde{g}_{(\alpha)}(rt),\\
&rt = \tilde{h}_{(\alpha)}(s) := \tilde{g}^{-1}_{(\alpha)}(s) \ \Rightarrow \ t = \frac{\tilde{h}_{(\alpha)}(s)}{r},\\
&\tilde{\gamma}_{(\alpha)} = 1/\tilde{h}'_{(\alpha)}(s).
\end{aligned}$$

The main difference is that now, in addition to the compactification parameter α, the compactification transformation depends on the 'rate' r. In line with the previous sections, we leave out the dependence on the compactification parameter α in general statements, but include it for the actual examples of compactification.

Moreover, to avoid repetitions, we focus on two-sided compactification only.

Then, $g_{(\alpha)}(t)$ in Assumption 2.2.1 is replaced with $\tilde{g}_{(\alpha)}(rt)$, and the autonomous compactified system (2.7)-(2.12) becomes

$$\dot{x} = f(x, \Lambda(\tilde{h}(s))), \tag{2.61}$$
$$\dot{s} = r\tilde{\gamma}(s), \tag{2.62}$$

$$f(x, \Lambda(\tilde{h}(s))) = \begin{cases} f(x, \Lambda(\tilde{h}(s))) & \text{for} \quad s \in (-1, 1), \\ f(x, \lambda^-) & \text{for} \quad s = -1, \\ f(x, \lambda^+) & \text{for} \quad s = 1, \end{cases} \tag{2.63}$$

$$\tilde{\gamma}(s) = \begin{cases} 1/\tilde{h}'(s) & \text{for} \quad s \in (-1, 1), \\ 0 & \text{for} \quad s = \pm 1. \end{cases} \tag{2.64}$$

The main point is that the compactified system (2.61)-(2.64) is in the form of a singularly perturbed slow-fast system [95] with a slow variable s, small parameter r, and a natural singular limit $\dot{s} \to 0$ as $r \to 0$. This means that $\Lambda(\tilde{h}(s))$ becomes an additional parameter when $r = 0$, and the problem reduces to the *frozen system*

$$\dot{x} = f(x, \lambda).$$

The first (2.13) and second (2.14) transformation conditions from Lemma 2.1 hold for $\Lambda(rt)$ and $\tilde{g}(rt)$. The first condition (2.15) from Lemma 2.2 holds for $\tilde{h}(s)$, but an extra r factor appears in the second condition (2.16) from Lemma 2.2:

$$\lim_{t \to \pm\infty} \frac{\dddot{\tilde{g}}(rt)}{\dot{\tilde{g}}(rt)} = -r \lim_{s \to \pm 1^{\mp}} \frac{\tilde{h}''(s)}{\left(\tilde{h}'(s)\right)^2}. \tag{2.65}$$

The 'normal' bi-asymptotically constant condition from Definition 2.2.2 applies to $\Lambda(rt)$ and Theorem 2.3 holds without any modification. Most importantly, the proofs of Lemma 2.1, Lemma 2.2, and Theorem 2.3 remain valid for $r > 0$. Again, to avoid repetitions, we leave out the details of the proofs in terms of the modified quantities, and highlight the examples of compactification in R-tipping analysis in the following sections.

2.5.1 Λ-compactification

Corresponding to Γ-compactification in Sec. 2.4.1, by substitution of $\Gamma(t) = \Lambda(rt)$, under the similar setting, we have Λ-compactification in R-tipping analysis.

2.5.2 Exponential compactification

In R-tipping analysis, we construct a parametrised coordinate transformation $\tilde{g}_{(\alpha)}(rt)$ with exponential decay in the form

$$s = \tilde{g}_{(\alpha)}(rt) = \tanh\left(\frac{\alpha r t}{2}\right), \quad rt = \tilde{h}_{(\alpha)}(s) = \frac{1}{\alpha}\ln\frac{1+s}{1-s}. \tag{2.66}$$

One can verify that this transformation satisfies Assumption 2.2.1 and the second transformation condition (2.14):

$$\lim_{t\to\pm\infty}\frac{\ddot{\tilde{g}}_{(\alpha)}(rt)}{\dot{\tilde{g}}_{(\alpha)}(rt)} = -\alpha r \lim_{t\to\pm\infty}\tanh\left(\frac{\alpha r t}{2}\right) = \mp\alpha r. \tag{2.67}$$

The augmented component $\tilde{\gamma}_{(\alpha)}(s)$ of the vector field is obtained by computing $1/\tilde{h}'(s)$, so that the compactified system (2.61)–(2.62) becomes

$$\left.\begin{aligned} \dot{x} &= f(x, \Lambda(\tilde{h}_{(\alpha)}(s))), \\ \dot{s} &= r\,\frac{\alpha}{2}\left(1-s^2\right). \end{aligned}\right\} \tag{2.68}$$

Since r affects the rate of exponential decay, we need to reformulate Corollary 2.4:

Corollary 2.6. *Consider a nonautonomous system (1.3) with C^1-smooth f and Λ, $r > 0$, and bi-asymptotically constant $\Lambda(rt)$. Moreover, suppose there is a $\tilde{\rho} > 0$ such that*

$$\lim_{t\to\pm\infty}\frac{\dot{\Lambda}(rt)}{e^{\mp\tilde{\rho}rt}} \ \textit{exist}. \tag{2.69}$$

Then, given the coordinate transformation (2.66) *with any $\alpha \in (0, \tilde{\rho}]$, the ensuing autonomous compactified system* (2.68) *is C^1-smooth on the extended phase space $U \times [-1, 1]$. The distance between any trajectory of* (2.68) *and $\{s = \pm 1\}$ decays exponentially as $t \to \pm\infty$.*

In other words, compact invariant sets for the limit systems gain one nonzero and r-dependent Lyapunov exponent (2.67) in the extended phase space of (2.68), but (2.68) requires exponentially or faster decaying $\dot{\Lambda}(rt)$ to be C^1-smooth. We leave out the proof here as it is similar to the proof of Corollary 2.4.

2.5.2.1 Exponential decay with oscillation

Given an asymptotically constant $\Lambda(rt)$ with exponential decay, the exponential coordinate transformation (2.66) for compactification is a natural choice,

although a slower-decaying coordinate transformation (e.g. algebraic, logarithmic or sub-logarithmic) would also be suitable.

Let's consider a class of asymptotically constant $\Lambda(rt)$ with monotone exponential decay

$$\Lambda(rt) \sim e^{-brt}, \text{ as } t \to +\infty, \tag{2.70}$$

where b is a positive constant, and choose the exponential coordinate transformation. According to Corollary 2.6, the corresponding compactified system is continuously differentiable on the extended phase space if

$$0 < \alpha \leq b.$$

Now consider a class of asymptotically constant $\Lambda(rt)$ with oscillations and exponentially decaying amplitude

$$\Lambda(rt) \sim e^{-brt} \cos \omega t, \text{ as } t \to +\infty, \tag{2.71}$$

where ω is *the angular oscillation frequency*. To check condition (2.69) from Corollary 2.6 we obtain

$$\lim_{t\to+\infty} \frac{\dot{\Lambda}(rt)}{e^{-\tilde{\rho}rt}} = -\lim_{t\to+\infty} e^{-(b-\tilde{\rho})rt} \left(br \cos \omega t + \omega \sin \omega t\right), \tag{2.72}$$

which exists if $0 < \tilde{\rho} < b$. It then follows from Corollary 2.6 that the corresponding compactified system is continuously differentiable on the extended phase space if

$$0 < \alpha < b.$$

A comparison between the allowed range of α for (2.70) and (2.71) reveals that an asymptotically constant $\Lambda(rt)$ with a monotone exponential decay at the rate br admits a marginally faster-decaying exponential transformation $\tilde{g}(rt)$ than a $\Lambda(rt)$ with an oscillatory exponential decay at the same rate br.

2.5.3 Algebraic compactification

In R-tipping analysis, we construct a parametrised inverse transformation $\tilde{h}_{(\alpha)}(rt)$ with algebraic asymptotic decay in the form

$$rt = \tilde{h}_{(\alpha)}(s) = \frac{s}{(1-s^2)^{\frac{1}{\alpha}}}. \tag{2.73}$$

One can verify that transformation (2.73) satisfies Assumption 2.2.1 and the second transformation condition (2.65):

$$\begin{aligned}\lim_{t\to\pm\infty}\frac{\ddot{\tilde{g}}_{(\alpha)}(rt)}{\dot{\tilde{g}}_{(\alpha)}(rt)} &= -r\lim_{s\to\pm1}\frac{d^2\tilde{h}_{(\alpha)}/ds^2}{(d\tilde{h}_{(\alpha)}/ds)^2}\\ &= -r\lim_{s\to\pm1}\frac{(1-s^2)^{\frac{1}{\alpha}}\left(2(2-\alpha)s^3+6\alpha s\right)}{\left[\alpha(1-s^2)+2s^2\right]^2}=0.\end{aligned} \tag{2.74}$$

The augmented component $\tilde{\gamma}_{(\alpha)}(s)$ of the vector field is obtained by computing $1/\tilde{h}'(s)$, so that the compactified system (2.61)–(2.62) becomes

$$\left.\begin{aligned}\dot{x} &= f(x,\Lambda(\tilde{h}_{(\alpha)}(s))),\\ \dot{s} &= r\,\frac{\alpha(1-s^2)^{1+\frac{1}{\alpha}}}{\alpha(1-s^2)+2s^2}.\end{aligned}\right\} \tag{2.75}$$

Since r does not affect the order of algebraic decay, there is no need to reformulate Corollary 2.5. We simply replace $\Gamma(t)$ with $\Lambda(rt)$ and restate the result

Corollary 2.7. *Consider a nonautonomous system (1.3) with C^1-smooth f and Λ, $r>0$, and bi-asymptotically constant $\Lambda(rt)$. Moreover, suppose there is an $m>1$ such that*

$$\lim_{t\to\pm\infty}\frac{\dot{\Lambda}(rt)}{t^{-m}}\ \textit{exist}. \tag{2.76}$$

Then, given the coordinate transformation (2.73) *with any $\alpha\in(0,m-1]$, the ensuing autonomous compactified system* (2.75) *is C^1-smooth on the extended phase space $U\times[-1,1]$. The distance between any trajectory of* (2.75) *and $\{s=\pm1\}$ decays algebraically (i.e. slower than exponentially) as $t\to\pm\infty$.*

In other words, algebraically (or faster) decaying $\dot{\Lambda}(rt)$ is sufficient for (2.75) to be C^1-smooth, but compact invariant sets for the limit systems gain one zero Lyapunov exponent (2.74) in the extended phase space of (2.75). We leave out the proof here as it is similar to the proof of Corollary 2.5.

2.5.3.1 Algebraic decay with oscillation

Given an asymptotically constant $\Lambda(rt)$ with algebraic decay, the algebraic coordinate transformation (2.73) for compactification is a natural choice, although a slower-decaying coordinate tranformation (e.g. logarithmic or sub-logarithmic) would also be suitable.

Let's consider a class of asymptotically constant $\Lambda(rt)$ with monotone algebraic

decay

$$\Lambda(rt) \sim \frac{1}{(rt)^{b-1}}, \text{ as } t \to +\infty, \tag{2.77}$$

where $b > 2$, and choose the algebraic coordinate transformation. According to Corollary 2.7, the corresponding compactified system is continuously differentiable on the extended phase space if

$$0 < \alpha \leq b - 1.$$

Now consider a class of asymptotically constant $\Lambda(rt)$ with oscillations and algebraically decaying amplitude

$$\Lambda(rt) \sim \frac{1}{(rt)^{b-1}} \cos \omega t, \text{ as } t \to +\infty, \tag{2.78}$$

where ω is *the angular oscillation frequency*. To check condition (2.76) from Corollary 2.7 we obtain

$$\lim_{t\to+\infty} \frac{\dot{\Lambda}(rt)}{t^{-m}} = -\lim_{t\to+\infty} r^{1-b} \left(t^{m-b}(-1+b)\cos\omega t + t^{m-b+1}\omega \sin \omega t \right), \tag{2.79}$$

which exists if $0 < m < b - 1$. It then follows from Corollary 2.7 that the corresponding compactified system is continuously differentiable on the extended phase space if

$$0 < \alpha \leq m - 1 < (b-1) - 1,$$

or if

$$0 < \alpha < b - 2.$$

A comparison between the allowed range of α for (2.77) and (2.78) reveals that an asymptotically constant $\Lambda(rt)$ with a monotone algebraic decay of the order $(b-1)$ admits a noticeably faster-decaying (with one-order difference) algebraic transformation $\tilde{g}(rt)$ than a $\Lambda(rt)$ with an oscillatory algebraic decay of the same order $(b-1)$.

2.5.4 Other compactification types

In R-tipping analysis, the other types of compactification, and the choices of coordinate transformations in practice are in line with those of the general form of compactitifcation, which we discussed in Sec. 2.4.4.

Chapter 3

Basic Concepts and Simple R-tipping Criteria

The goal of this chapter is to use certain properties of the frozen system (1.2) to give simple and testable criteria for R-tipping in the original nonautonomous system (1.3). Specifically, we introduce the main concepts of thresholds and edge states and define the key property of threshold instability in the frozen system (1.2). Then, we define the phenomenon of R-tipping and give testable criteria for R-tipping to occur in the nonautonomous system (1.3). This chapter builds on and extends the previous work of Wieczorek, Ashwin, Perryman et al. [24, 18, 51, 44], and forms the basis for our R-tipping analysis.

3.1 Setting

In Chapter 2, we introduce compactification techniques, which are designed for systems (1.3) with “normal" (bi-)asymptotically constant external input $\Lambda(rt)$ defined in Definition 2.2.2. As a result, we always consider such external inputs[1] in our R-tipping analysis, even though such external inputs are not required under certain circumstances; see Section 4.6.

Assuming that $\Lambda(rt)$ is asymptotically constant, we can define the autonomous *future limit system*

$$\dot{x} = f(x, \lambda^+), \tag{3.1}$$

and (if the past limt exists) the autonomous *past limit system*

$$\dot{x} = f(x, \lambda^-), \tag{3.2}$$

[1]The setting of a“normal” (bi-)asymptotically constant external input $\Lambda(rt)$ is required when a compactification is needed in the process of R-tipping analysis.

which are special examples of the frozen system (1.2). The aim is to use the autonomous dynamics and equilibria of the future limit system (3.1) and (if it exists) the past limit system (3.2) to analyse R-tipping instabilities in the nonautonomous system (1.3). By doing so we can give easily-testable criteria for R-tipping in arbitrary dimension.

3.2 Concepts and basic ideas

3.2.1 Parameter path and moving equilibrium

A parameter path P_λ in the parameter space $\mathbb{R}^d$ is traced out by the external input $\Lambda(rt)$. We write $\overline{S}$ to denote the closure[2] of S, and define:

Definition 3.2.1. *A* parameter path $P_\lambda \subset \mathbb{R}^d$ *is a compact set that is the closure of an image of a continuous function from* $\mathbb{R}$ *to* $\mathbb{R}^d$.

Remark 3.2.1. *We say an external input* $\Lambda(rt)$ traces out P_λ *if*

$$P_\lambda = \overline{\{\Lambda(rt) : t \in \mathbb{R}\}} \subset \mathbb{R}^d. \tag{3.3}$$

Note that P_λ is independent of the *rate* r. Moreover, the future limit λ^+ and (if it exists) the past limit λ^- of $\Lambda(rt)$ may correspond to any element of the path P_λ. In other words, the limits λ^+ and λ^-, need not correspond to the boundaries of P_λ.

Moreover, we focus on stable equilibria of the frozen system (1.2) that vary smoothly with λ and do not bifurcate along the chosen parameter path P_λ. More precisely,

Definition 3.2.2. *Consider nonautonomous system (1.3) with some* $\Lambda(rt)$ *that traces out a path* P_λ*. Suppose the corresponding frozen system (1.2) has an equilibrium* $e(\lambda)$ *that exists continuously for all* $\lambda \in P_\lambda$*. Then we say* $e\left(\Lambda(rt)\right)$ *is a* moving equilibrium*. If in addition* $e(\lambda)$ *is a hyperbolic sink for all* $\lambda \in P_\lambda$*, we say* $e\left(\Lambda(rt)\right)$ *is a* moving stable equilibrium*.*

A moving equilibrium is sometimes called a *quasistatic equilibrium* or an *equilibrium for the frozen system*. It depends on f and on the external input $\Lambda(rt)$. If $\Lambda(rt)$ is bi-asymptotically constant, we define the future and past limits of the moving equilibrium

$$e^\pm := \lim_{t\to\pm\infty} e(\Lambda(rt)) = e(\lambda^\pm),$$

[2]The smallest closed subset of $\mathbb{R}^d$ containing S.

which are equilibria of the autonomous future (3.1) and past (3.2) limit systems, respectively.

3.2.2 Thresholds and edge states for frozen systems

R-tipping instabilities in the nonautonomous system can be understood in terms of certain "thresholds" in the frozen system [18, 44]. Generally, thresholds are codimension-one orientable invariant manifolds in phase space that are normally repelling. There are two desired properties of a threshold: their dimension and orientability allow us to define *two sides* of a threshold, while the normal repulsion gives qualitatively different behaviour of trajectories started on different sides of a threshold. Our notion of a regular threshold generalises and unifies the concepts of "excitability thresholds" for excitable systems [96, 97], and "multi-basin boundaries" and "edge states" [98, 99, 100] for multistable systems.

As we introduce two types of thresholds, in order to guide readers, we give a short summary below:

(i) For the frozen system (1.2) with a fixed in time external input $\Lambda(rt) = \lambda$, we distinguish between *regular thresholds* and *quasithresholds*, both of which are denoted as $\theta(\lambda)$. The regular threshold has an edge state, defined in Definition 3.2.4, while the quasithreshold may not have any edge state, which we need to review in Section 4.6.

(ii) Given thresholds in the frozen system (1.2), and a certain time-dependent external input $\Lambda(rt)$ tracing out the parameter path P_λ, we define *moving thresholds*; see Definition 3.2.12. Furthermore, we give the definitions of threshold instability and forward threshold instability; see Definition 3.3.1 and Definition 3.3.2.

(iii) The main challenge is to pin down the *R-tipping thresholds* in the nonautonomous system (1.3) as they separate the solutions that R-tip from those that do not. In Chapter 4, we use the compactification to study R-tipping thresholds as n-dimensional stable manifolds of a saddle edge state in the compactified system.

3.2.2.1 Regular thresholds and edge states

In order to define regular thresholds, we recall some properties of invariant manifolds (for a more general discussion, see [101]). A set $S \in \mathbb{R}^n$ is an *immersed codimension-one manifold* if there is an $(n-1)$-dimensional manifold V and a

smooth map

$$F : V \to \mathbb{R}^n,$$

such that $F(V) = S$ and $DF(v)$ has maximal rank at all $v \in V$. The immersed manifold S is *embedded* if F can be chosen such that F is a homeomorphism onto its image. For the particular case of an embedded codimension-one manifold, $F(V) = S \subset \mathbb{R}^n$ is *orientable* if there is a smoothly varying unit vector $\nu(x)$ defined on $x \in S$ that is everywhere normal to the tangent space T_xS. Note that $\mu \in T_xS$ if and only if $\nu(x) \cdot \mu = 0$. We say an embedded manifold S *varies continuously (or smoothly) with* λ if the embedding map F can be chosen to be continuous (or smooth) in λ.

If S is a codimension-one invariant stable manifold of a hyperbolic invariant set then it is an injectively immersed repelling manifold (e.g. [101]). However, it may be neither orientable nor embedded. For example, if S is the stable manifold of a saddle periodic orbit with a real negative Floquet multiplier then it is non-orientable. If S is contained in a basin boundary then it does form a threshold, but such a threshold need not be embedded: it may be remarkably complex, locally disconnected and even fractal in structure; see [102] for a review. In case S is not embedded, one may be able to restrict to an embedded submanifold of S, though this is not possible in general.

In this thesis we restrict to regular thresholds in the following sense and leave all others. More precisely:

Definition 3.2.3. *For the n-dimensional frozen system* (1.2)*, a* regular threshold *is an orientable codimension-one forward-invariant embedded manifold $\theta \subset \mathbb{R}^n$ that is normally hyperbolic and repelling.*

A regular threshold θ will typically be contained in the basin boundary of one or more attractors. However, the two sides of the threshold may lie in the basin of the same attractor as depicted in Fig. 3.1(a). Moreover, not all points on the basin boundary need to be in regular thresholds. For example, the regular threshold in Fig. 3.1(a) is a manifold with boundary that is a source: this is part of the basin boundary but not the threshold.[3]

The assumption of forward invariance means that a threshold will contain one or more invariant sets that are attractors for the flow restricted to the threshold; see Section 2.3.1 to refer the notion of attractors. If there is more than one such attractor we can restrict to a smaller threshold that contains just one, and we

[3]The basin of attraction of the equilibrium e is $B(e) = \{x : \omega(x) \subset e\}$ and its boundary is $\overline{B(e)} \setminus B(e)$, where the basin closure is $\overline{B(e)}$. In general, a codimension-one basin boundary need not divide the phase space into different basins of attraction. What is more, a basin boundary need not be connected or even locally connected.

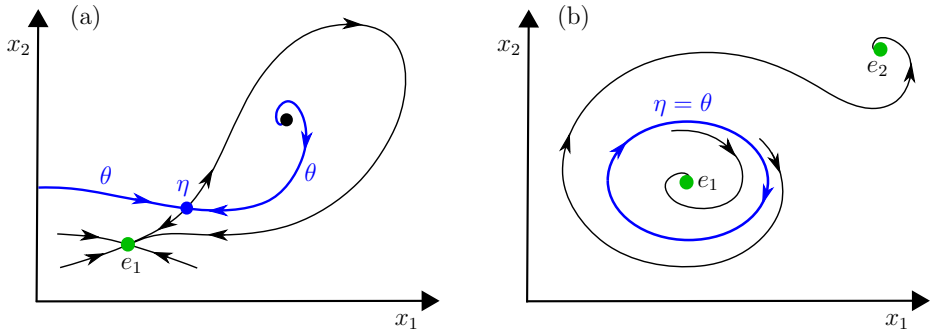

Figure 3.1: Two examples of an edge state η and (blue) the associated regular threshold θ in a two-dimensional frozen system (1.2). (a) A regular threshold θ within the stable manifold of the saddle equilibrium η. In this case θ lies in the basin boundary of one attractor and the two sides of θ are in the basin of the same attractor e_1. Moreover, θ is any forward-invariant subset of the stable manifold of η. (b) This regular threshold θ is a repelling limit cycle η where θ lies on the basin boundary of two attractors and the two sides of θ lie in the basins of different attractors e_1 and e_2.

assume this is a hyperbolic invariant set η that is stable within θ: the assumption of normal repulsion means there will be a transversely unstable direction. Using notation inspired by work on fluid instabilities [98, 99, 100], we define a regular edge state as follows:

Definition 3.2.4. *For the n-dimensional frozen system* (1.2) *we say η is a* regular edge state *if it is a compact normally hyperbolic invariant set whose stable manifold is a regular threshold.*

A regular edge state $\eta(\lambda)$ may have dimension $(n-1)$, in which case $\eta(\lambda) = \theta(\lambda)$, but more generally a regular edge state $\eta(\lambda)$ will be of lower dimension than the threshold $\theta(\lambda)$. Typical examples of a regular edge state in two dimensions are a hyperbolic repelling limit cycle as depicted in Fig. 3.1(b), and a hyperbolic saddle equilibrium with a one-dimensional embedded stable manifold as depicted in Fig. 3.1(a), respectively.

We now relate existing notions of "excitability threshold" for excitable systems and "multi-basin boundary" for multistable systems as being different kinds of regular thresholds for regular edge states.

Definition 3.2.5. *Suppose that $\theta(\lambda)$ is a regular threshold for the frozen system (1.2) with fixed λ.*

(i) If $\theta(\lambda)$ is contained in the basin boundary of a single attractor, we say that the frozen system (1.2) *is* excitable *with* excitability threshold $\theta(\lambda)$.

(ii) If $\theta(\lambda)$ is contained in the basin boundary of two or more attractors, we say that the frozen system (1.2) *is* multistable *with* multi-basin boundary $\theta(\lambda)$.

3.2.2.2 Quasithresholds in slow-fast systems

While regular thresholds are typical in the frozen system (1.2), "quasithresholds" [96] require that the frozen system (1.2) is slow-fast in the sense that its time-scale separation can be quantified by a small parameter $0 < \varepsilon \ll 1$; see [95] for a recent monograph on such systems. To reveal quasithresholds, the frozen system (1.2) is reformulated in terms of its fast $Y \in \mathbb{R}^m$ and slow $Z \in \mathbb{R}^{n-m}$ components of $x = (Y, Z) \in \mathbb{R}^n$, as a *(singularly perturbed) slow-fast system*, on two different timescales. For the slow timescale t, we have

$$\varepsilon \frac{dY}{dt} = f_1(Y, Z, \lambda, \varepsilon), \tag{3.4}$$

$$\frac{dZ}{dt} = f_2(Y, Z, \lambda, \varepsilon), \tag{3.5}$$

with 'slow' solutions sought in the form of asymptotic expansion in ε:

$$Y(t, \varepsilon) = y(t) + \varepsilon y_1(t) + \mathcal{O}(\varepsilon^2), \quad Z(t, \varepsilon) = z(t) + \varepsilon z_1(t) + \mathcal{O}(\varepsilon^2). \tag{3.6}$$

For the fast timescale $\tau = t/\varepsilon$, we have

$$\frac{dY}{d\tau} = f_1(Y, Z, \lambda, \varepsilon), \tag{3.7}$$

$$\frac{dZ}{d\tau} = \varepsilon f_2(Y, Z, \lambda, \varepsilon), \tag{3.8}$$

with 'fast' solutions also sought in the form of asymptotic expansion in ε:

$$Y(\tau, \varepsilon) = y(\tau) + \varepsilon y_1(\tau) + \mathcal{O}(\varepsilon^2), \quad Z(\tau, \varepsilon) = z(\tau) + \varepsilon z_1(\tau) + \mathcal{O}(\varepsilon^2). \tag{3.9}$$

The idea is to examine the slow and fast solutions independently in the *singular limit* $\varepsilon = 0$, and use asymptotic matching along with desingularisation and blow-up [77] to obtain slow-fast composite solutions for ε small but non-zero. Taking the limit $\varepsilon \to 0$ for the slow time t, which is equivalent to substituting (3.6) into (3.4)–(3.5) and equating terms $\mathcal{O}(1)$ on both sides, gives the *frozen slow subsystem* often referred to as the reduced system

$$\frac{dz}{dt} = f_2(y, z, \lambda, 0), \tag{3.10}$$

that evolves on the $(n-m)$-dimensional *critical manifold*

$$S_0(\lambda) = \{(y, z) : 0 = f_1(y, z, \lambda, 0)\}. \tag{3.11}$$

Similarly, taking the limit $\varepsilon \to 0$ for the fast time τ, which is equivalent to substituting (3.9) into (3.7)–(3.8) and equating terms $\mathcal{O}(1)$ on both sides, gives the *frozen fast subsystem* often referred to as the layer system

$$\frac{dy}{d\tau} = f_1(y, z, \lambda, 0), \tag{3.12}$$

where the slow z-component becomes an additional parameter. Stable parts of $S_0(\lambda)$ contain the slow dynamics and stable equilibria $e(\lambda)$ of the system. For the purpose of R-tipping, we are interested in stable parts of $S_0(\lambda)$ that terminate in a quadratic (nondegenerate) fold $F(\lambda)$ tangent to the fast y-component, where transitions between the slow and fast dynamics may occur.

A comparison between (3.11) and (3.12) shows that the critical manifold $S_0(\lambda)$ consists of all equilibrium points for the frozen fast subsystem (3.12) parametrised by z. Thus, stable parts of S_0 are identified as stable equilibria of the frozen fast subsystem. What is more, a quadratic fold $F(\lambda)$ of $S_0(\lambda)$ is the union of generic saddle-node bifurcation points of equilibria $(y^*(\lambda), z^*(\lambda))$ in the n-dimensional (y, z)-bifurcation diagram for the frozen fast subsystem (3.12). This means that we can construct a stable set of $F(\lambda)$, denoted $w^s(F(\lambda))$, as a subset of $\mathbb{R}^n$ that consists of the union of trajectories of the frozen fast subsystem (3.12):

Definition 3.2.6. *Consider a slow-fast frozen system* (3.4)–(3.5). *Suppose a stable part of a critical manifold $S_0(\lambda)$ contains a stable equilibrium $e(\lambda)$ for the frozen slow subsystem (3.10), and terminates in a quadratic fold $F(\lambda)$ that is tangent to the fast y-component. We define a* singular-limit threshold $\theta_0(\lambda)$ *as a $(n-1)$-dimensional stable set of such $F(\lambda)$ in the frozen fast subsystem (3.12):*

$$\theta_0(\lambda) = w^s(F(\lambda)) = \left\{(y_0, z^*(\lambda)) \in \mathbb{R}^{n-1} : y(\tau, y_0) \to F(\lambda) \ \text{ as } \ \tau \to +\infty\right\}. \tag{3.13}$$

The key result of the geometric singular perturbation theory is that a singular-limit threshold $\theta_0(\lambda)$ persists for $0 < \varepsilon \ll 1$ as a nearby $\theta_\varepsilon(\lambda)$ of the same dimension in the slow-fast frozen system (3.4)–(3.5) [47, 74, 56]. However, for a single $\theta_0(\lambda)$ there can be a continuum of $\theta_\varepsilon(\lambda)$ candidates, and hence the name *quasithreshold*.

Definition 3.2.7. *Suppose the fast frozen subsystem (3.12) has a singular limit threshold θ_0. We call the corresponding θ_ε in the slow-fast frozen system* (3.4)–(3.5) *a* quasithreshold *if it is not a regular threshold.*

Figure 3.2 shows an example of (a) a singular-limit threshold $\theta_0(\lambda)$ in the fast frozen subsystem (3.12) that corresponds to either (b) a regular threshold $\theta_\varepsilon(\lambda)$ or (c) a quasithreshold $\theta_\varepsilon(\lambda)$ in different slow-fast frozen systems (3.4)–(3.5)

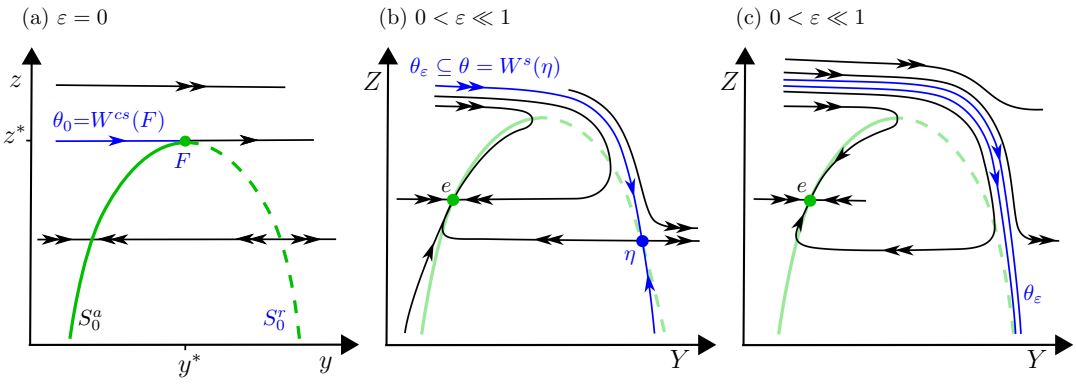

Figure 3.2: (a) Bifurcation diagram for a fast frozen subsystem (3.12) showing the fold point F and the singular limit threshold θ_0. (b) Phase portrait of a slow-fast frozen system (3.4)–(3.5) where θ_ε is (blue) a single trajectory contained within the stable manifold of saddle η. Thus, θ_ε is a regular threshold. (c) Phase portrait of a different slow-fast frozen system (3.4)–(3.5) where θ_ε is a continuum of (blue) canard trajectories. Hence the term "quasithreshold". In the diagrams, e denotes the stable equilibrium, S_0^a and S_0^r denote the normally hyperbolic attracting and repelling parts, respectively, of $S_0 = S_0^a \cup F \cup S_0^r$, double arrows indicate fast solutions and single arrows indicate slow solutions.

that limit to the same fast frozen subsystem. In the slow-fast system from figure 3.2(b), there is a continuum of canard trajectories that follow the repelling part of the slow manifold S_ε^r. However, only a single (blue) canard trajectory θ_ε is contained in the stable manifold W^s of saddle η and never leaves S_ε^r. Thus, this $\theta_\varepsilon \subseteq W^s(\eta)$ is already captured by the regular threshold definition 3.2.3. In the other slow-fast system from figure 3.2(c), there is a continuum of (blue) canard trajectories θ_ε that follow the repelling part of the slow manifold S_ε^r. Since none of these canard trajectories is contained in a repelling limit cycle or a stable manifold of a saddle equilibrium, we have a quasithreshold.

Remark 3.2.2. *In contrast to a regular threshold, a quasithreshold θ_ε need not be contained within a basin boundary and does not appear to contain any regular edge state. In other words, initial conditions on both sides of a quasithreshold will normally be within the basin of attraction of the same attractor. Therefore, quasithresholds will typically give rise to reversible R-tipping.*

3.2.3 R-tipping thresholds, R-tipping edge states, and Compactification

3.2.3.1 Regular R-tipping thresholds and R-tipping edge states

A regular threshold with an edge state $\eta(\lambda)$ in the frozen system (1.2) gives rise to a compact invariant saddle $\tilde{\eta}^+$ at $\{s = 1\}$ in the compactified system (2.61)–

(2.62). This simplifies analysis of R-tipping because $\tilde{\eta}^+$ becomes the R-tipping edge state and its stable invariant manifold in the compactified phase space becomes the R-tipping threshold for the nonautonomous system (1.3). In other words, the compactification reveals R-tipping thresholds.

The trouble with quasithresholds is that they do not appear to have any obvious edge states; e.g. compare panels (b) and (c) in Fig. 3.2. Thus, compactification does not reveal R-tipping quasithresholds in the same way as it reveals regular R-tipping thresholds. Nonetheless, it turns out that an augmented slow-fast nonautonomous system can have *singular edge states* [43]. These singular edge states, which are not present in the frozen system (1.2), give rise to *R-tipping quasithresholds*. Below we explain how the singular edge states come about.

3.2.3.2 R-tipping quasithresholds and singular R-tipping edge-states in slow-fast systems: Canards and folded singularities

Consider a slow-fast non-autonomous system (1.3), relax the asumption of asymptotically constant $\Lambda(rt)$, and suppose that the frozen slow-fast system (1.2) has a quasithreshold. To reveal singular R-tipping edge states and R-tipping quasithresholds it is sufficient to augment the slow-fast nonautonomous system with an additional dependent variable. The most straightforward approach is to consider the extended slow-fast autonomous system

$$\varepsilon \frac{dY}{dt} = f_1(Y, Z, \Lambda(u), \varepsilon), \tag{3.14}$$

$$\frac{dZ}{dt} = f_2(Y, Z, \Lambda(u), \varepsilon), \tag{3.15}$$

$$\frac{du}{dt} = r, \tag{3.16}$$

where $u = rt \in \mathbb{R}$ becomes an additional slow variable. Note that the compactification discussed in Section 2.5 is a more intricate way of augmenting the nonautonomous system. Thus, we first discuss R-tipping quasithresholds and singular R-tipping edge states for the extended slow-fast system above, and then for the compactified slow-fast system.

To reveal singular R-tipping edge states [43], we concentrate on the slow subsystem

$$\frac{dz}{dt} = f_2(y, z, \Lambda(u), 0), \tag{3.17}$$

$$\frac{du}{dt} = r, \tag{3.18}$$

that evolves on the $(n-m+1)$-dimensional critical manifold

$$S_0 = \{(y,z,u) \in \mathbb{R}^n \times \mathbb{R} : 0 = f_1(y,z,\Lambda(u),0)\}\,. \tag{3.19}$$

Alternatively, S_0 can be defined as the union of all equilibrium points for the fast subsystem

$$\frac{dy}{d\tau} = f_1(y,z,\Lambda(u),0), \tag{3.20}$$

where u and z become additional parameters. Thus, transverse stability of different parts of S_0 can be determined from the Jacobian $D_y(f_1)$ of the fast subsystem evaluated at S_0. Our focus is on trajectories within stable normally hyperbolic parts of S_0 near a quadratic (or nondegenarate) fold F tangent to the fast y-component of the flow, where the interesting dynamics such as R-tipping occur. More precisely, we define [58, 103, 95]:

Definition 3.2.8. *Let S_0 be a $(n-m+1)$-dimensional critical manifold for the extended slow-fast system* (3.14)–(3.16). *A* quadratic fold F of S_0 tangent to the fast y-component of the flow *is a $(n-m)$-dimensional submanifold of S_0 given by*

$$F = \left\{(y,z,u) \in S_0 : rk[D_y f_1] = m-1,\, l\cdot[(D^2_{yy}f_1)(r,r)] \neq 0,\, l\cdot[D_z f_1] \neq 0\right\},$$

where l is the left nullvector and r is the right nullvector of the Jacobian $D_y f_1$.

Here, the rank 1 deficiency of the Jacobian defines the fold, while the other two conditions ensure that the fold is quadratic or nondegenerate. In the simple case of a one-dimensional f_1, a quadratic fold F is a point on S_0 where $\partial f_1/\partial y = 0$ and $\partial^2 f_1/\partial y^2 \neq 0$.

The slow subsystem (3.17)–(3.18) describes the evolution of the slow z- and u-components on S_0. However, R-tipping involves a rapid change in the fast y-component. Therefore, we need to analyse the evolution of the fast y-component on S_0 in slow time t. This is obtained by differentiating the critical manifold condition (3.19) with respect to t:

$$-D_y f_1 \cdot \frac{dy}{dt} = D_z f_1 \cdot f_2\,(y,z,\Lambda(u),0) + r\cdot D_\Lambda f_1 \cdot \frac{d\Lambda}{du}, \tag{3.21}$$

where $(y,z,u) \in S_0$. The obstacle to obtaining the slow y-flow on S_0 is the singularity of the $m\times m$ Jacobian $D_y f_1$ on F, meaning that $(D_y f_1)^{-1}$ is not defined on F. To overcome this obstacle we use the definition of the *adjugate* of a square matrix

$$D_y f_1 \cdot \mathrm{adj}(D_y f_1) = \mathrm{adj}(D_y f_1)\cdot D_y f_1 = \det(D_y f_1)\cdot I,$$

where I is the identity matrix and adj$(D_y f_1)$ denotes the adjugate of $D_y f_1$, which is a $m \times m$ matrix given by the transpose of the cofactor matrix of $D_y f_1$; the (i, j) element of the cofactor matrix of $D_y f_1$ is the product of $(-1)^{i+j}$ and the (i, j) minor of $D_y f_1$. The adjugate of a square matrix is well defined even if the square matrix is singular with rank 1 deficiency. The key point is that the singularity can be moved from the matrix $D_y f_1$ to the scalar $\det(D_y f_1)$. Applying adj$(D_y f_1)$ to the left of Eq. (3.21) and adding Eqs. (3.17)–(3.18) gives the slow subsystem for all the variables:

$$-\det(D_y f_1)\frac{dy}{dt} = \text{adj}(D_y f_1) \cdot \left(D_z f_1 \cdot f_2\left(y, z, \Lambda(u), 0\right) + r \cdot D_\Lambda f_1 \cdot \frac{d\Lambda}{du} \right), \quad (3.22)$$

$$\frac{dz}{dt} = f_2(y, z, \Lambda(u), 0), \quad (3.23)$$

$$\frac{du}{dt} = r, \quad (3.24)$$

where $(y, z, u) \in S_0$. Now, we can identify the implications of the singularity on the slow y-flow within S_0 and near F:

(a) *Regular points* on F are defined where the r.h.s of Eq. (3.22) is nonzero. These points are either attracting or repelling within S_0 [see the attracting and repelling F-components in Fig. 3.3(a)]. This follows because $\det(D_y f_1)$ changes sign when moving past F while the r.h.s of Eq. (3.22) does not, resulting in a change in the sign (i.e. direction) of dy/dt.

(b) Trajectories of the slow subsystem that arrive at a regular and attracting part of F cease to exist on S_0. This is because the r.h.s of Eq. (3.22) is nonzero, $\det(D_y f_1) = 0$, and their ratio is not defined. In other words, dy/dt becomes undefined on F, and $y(t)$ tends to infinity in finite slow time t (blows up in t). This singular behaviour corresponds to a transition between the slow and fast flow in the extended autonomous system (3.14)–(3.16) with $0 < \varepsilon \ll 1$ [57]. Hence, regular fold points are also known as *jump points* [see JP in Fig. 3.3(a)].

(c) There can be special points on F, where both the r.h.s of Eq. (3.22) and $\det(D_y f_1)$ are zero. This opens up a possibility for special trajectories across F along which the r.h.s of Eq. (3.22) and $\det(D_y f_1)$ go through zero at the same 'speed', so that their ratio is finite on F, and dy/dt remains well defined. As both the r.h.s of Eq. (3.22) and $\det(D_y f_1)$ change sign at F, there is no change in the sign (i.e. direction) of dy/dt, and the flow points across F. Therefore, these special trajectories go past F and continue on the unstable part of S_0 [see the blue trajectories across FS in Fig. 3.3(a)]. More precisely, we define [76, 104, 105, 103]:

Definition 3.2.9. *Consider a slow subsystem with a folded critical manifold S_0. A* folded singularity *is a special fold point $(y, z, u) \in F \subset S_0$ where*

$$det(D_y f_1) = adj(D_y f_1) \cdot \left(D_z f_1 \cdot f_2 \left(y, z, \Lambda(u), 0\right) + r \cdot D_\Lambda f_1 \cdot \frac{d\Lambda}{du} \right) = 0. \quad (3.25)$$

Definition 3.2.10. *A* singular canard trajectory *(or* a singular canard*) is a trajectory of a slow subsystem that goes past F via a folded singularity.*

The difference between tracking and R-tipping appears to be whether a trajectory started on the stable part of S_0 is repelled from F and remains on the stable part of S_0, or the trajectory is attracted towards F away from the folded singularity and blows up. Singular canards separate these two behaviours. Thus, the problem of singular R-tipping edge states and singular R-tipping thresholds can be reduced to the analysis of folded singularities and singular canards.

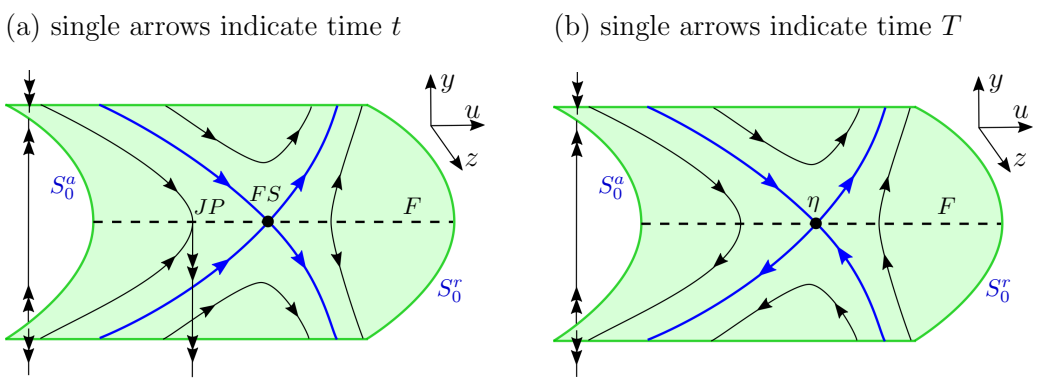

Figure 3.3: Phase portraits for (a) slow subsystem (3.17)–(3.18) and (3.22) showing an example of a jump point JP and a folded saddle singularity FS with (blue) singular canard trajectories, (b) the corresponding desingularised system (3.27)–(3.29) where FS becomes a regular saddle equilibrium η that is not present in the extended autonomous system (3.14)–(3.16); the (blue) singular canards from (a) can be computed as the stable and unstable invariant manifolds of η. Shown are attracting S_0^a and repelling S_0^r parts of the folded critical manifold $S_0 = S_0^a \cup F \cup S_0^a$, (dashed line) regular fold points F, (black dot) the special fold point, (single arrows) slow solutions in time (a) t or (b) T, and (double arrows) fast solutions in time τ.

To facilitate this analysis, the singularity in Eq. (3.22) is removed by a state-dependent rescalling of time, also know as *desingularisation* [106]. Specifically, we introduce a new slow time T:

$$dt = -\det(D_y f_1) dT, \quad (3.26)$$

that passes infinitely faster and reverses direction on F (see Figure 3.4). This

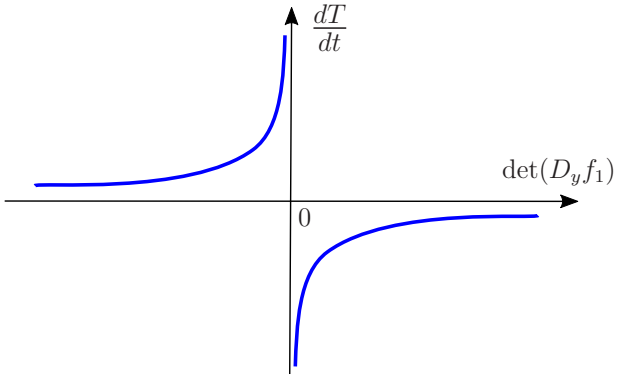

Figure 3.4: A graph of dT/dt vs. $\det(D_y f_1)$ illustrating time rescalling (3.26) used for desingularisation. Note the singularity at the fold F where $\det(D_y f_1) = 0$, and the time reversal on the parts of S_0 where $\det(D_y f_1) > 0$.

gives the desingularised slow subsystem for the slow dynamics on S_0:

$$\frac{dy}{dT} = \text{adj}(D_y f_1) \cdot \left(D_z f_1 \cdot f_2 \left(y, z, \Lambda(u), 0\right) + r \cdot D_\Lambda f_1 \cdot \frac{d\Lambda(u)}{du} \right), \tag{3.27}$$

$$\frac{dz}{dT} = -\det(D_y f_1) f_2(y, z, \Lambda(u), 0), \tag{3.28}$$

$$\frac{du}{dT} = -r \det(D_y f_1), \tag{3.29}$$

where $(y, z, u) \in S_0$. Note that a folded singularity for the slow subsystem (3.22)–(3.24) becomes a regular equilibrium in the desingularised slow subsystem (3.27)–(3.29). More precisely, we define

Definition 3.2.11. *A* folded equilibrium *is a special equilibrium in the desingularised slow subsystem* (3.27)–(3.29) *that corresponds to a folded singularity in the slow subsystem* (3.22)–(3.24).

The desingularised slow subsystem (3.27)–(3.29) has a number of advantages that facilitate analysis of trajectories near folded singularities in slow subsystem (3.22)–(3.24):

(a) The vector field becomes well-defined everywhere on F.

(b) Folded singularities become regular equilibria that are not present in the extended autonomous system (3.14)–(3.16). In particular, we speak of a "folded saddle" singularity in the slow subsystem (3.22)–(3.24) if an equilibrium of the desingularised slow subsystem (3.27)–(3.29) has real eigenvalues with different signs. Similarly, we speak of a "folded node" singularity in the slow subsystem (3.22)–(3.24) if an equilibrium of the desingularised system (3.27)–(3.29) has real eigenvalues with the same sign.

(c) Singular canards for the slow subsystem (3.22)–(3.24) become trajectories

tangent to an eigenspace of a folded equilibrium in the desingularised slow subsystem (3.27)–(3.29). In particular, a singular folded-saddle canard is the stable manifold of the folded-saddle equilibrium.

(d) The slow subsystem and desingularised slow subsystem have the same trajectories (up to the arrows indicating the direction of the flow). This means that the phase portrait for the slow subsystem can be obtained from the phase portrait of the desingularised slow subsystem by reversing the direction of the flow (i.e. the arrows) on the parts of S_0 where $\det(D_y f_1) > 0$.

Note 3.2.1. *Equations* (3.27)–(3.29) *define a* $(n+1)$*-dimensional dynamical system describing the slow dynamics on a* $(n-m+1)$*-dimensional critical manifold* S_0*. Therefore, it is convenient to eliminate the dependence on* z *in the desingularised system (3.27)–(3.29) using the critical manifold condition (3.19), and work with the projection of the slow dynamics onto the* $(n-m+1)$*-dimensional* (y,u)*-subspace.*

Folded singularities, especially *folded saddles* and *folded nodes*, are the key feature of the desingularised system because they may become *singular R-tipping edge states*. What is more, a folded-saddle singular canard and, possibly, folded-node singular canards, may become *singular R-tipping thresholds.* When $0 < \varepsilon \ll 1$, folded singularities are no longer defined. However, singular canards owing to folded saddles and folded nodes persist as regular canards in the extended slow-fast system (3.14)–(3.16) [76, 105, 107, 103, 108]. Those regular canards, together with suitably defined stable sets, may become *R-tipping quasithresholds* in the (Y,Z,u) phase space.

3.2.3.3 Compactified desingularised system

The slow subsystem (3.22)–(3.24) already captures singular R-tipping thresholds for $\varepsilon = 0$, which approximate R-tipping quasithresholds in the extended slow-fast system (3.14)–(3.16) for $0 < \varepsilon \ll 1$. Nonetheless, compactification can still be useful for (bi-)asymptotically constant $\Lambda(rt)$ because it can reveal interesting nonlinear phenomena that arise from the interaction between folded singularities for $s \in (-1,1)$ and regular equilibria $\tilde{e}^{\pm}$ at $\{s = \pm 1\}$. By utilizing the additional dependent variable $s = \tilde{g}_{(\alpha)}(rt)$ instead of $u = rt$, we obtain the *compactified*

slow-fast system:

$$\varepsilon\frac{dY}{dt} = f_1(Y, Z, \Lambda(s), \varepsilon), \tag{3.30}$$
$$\frac{dZ}{dt} = f_2(Y, Z, \Lambda(s), \varepsilon), \tag{3.31}$$
$$\frac{ds}{dt} = \frac{r}{d\tilde{h}_{(\alpha)}/ds}. \tag{3.32}$$

where $\tilde{h}_{(\alpha)}(s) = \tilde{g}^{-1}_{(\alpha)}(s)$ is the inverse of the compactification transformation $\tilde{g}_{(\alpha)}(rt)$, and $\Lambda(s)$ is defined by Eq. (2.63) in Section 2.5. Now, the compactified slow subsystem for all the variables

$$-\text{det}(D_y f_1)\frac{dy}{dt} = \text{adj}(D_y f_1)\cdot\left(D_z f_1 \cdot f_2\left(y, z, \Lambda(s), 0\right) + r\cdot D_\Lambda f_1 \cdot \frac{d\Lambda/ds}{d\tilde{h}_{(\alpha)}/ds}\right), \tag{3.33}$$
$$\frac{dz}{dt} = f_2(y, z, \Lambda(s), 0), \tag{3.34}$$
$$\frac{ds}{dt} = \frac{r}{d\tilde{h}_{(\alpha)}/ds}, \tag{3.35}$$

evolves on the $(n-m+1)$-dimensional critical manifold

$$S_0 = \{(y, z, s) \in \mathbb{R}^n \times [-1, 1] : 0 = f_1(y, z, \Lambda(s), 0)\}. \tag{3.36}$$

We then use the time rescalling (3.26) to obtain the *compactified desingularised slow subsystem*

$$\frac{dy}{dT} = \text{adj}(D_y f_1)\cdot\left(D_z f_1 \cdot f_2\left(y, z, \Lambda(s), 0\right) + r\cdot D_\Lambda f_1 \cdot \frac{d\Lambda/ds}{d\tilde{h}_{(\alpha)}/ds}\right), \tag{3.37}$$
$$\frac{dz}{dT} = -\text{det}(D_y f_1)\cdot f_2(y, z, \Lambda(s), 0), \tag{3.38}$$
$$\frac{ds}{dT} = -\text{det}(D_y f_1)\cdot\frac{r}{d\tilde{h}_{(\alpha)}/ds}. \tag{3.39}$$

In Chapter 4, we analyse system (3.37)–(3.39) to reveal singular R-tipping thresholds, and system (3.30)–(3.32) to obtain R-tipping quasithresholds. The concepts discussed in Section 3.2.2 and Section 3.2.3 are summarised in Table 3.1.

3.2.4 Moving thresholds and edge states

Similarly to the moving equilibria defined in Definition 3.2.2, we define moving thresholds and moving edge states as follows.

Definition 3.2.12. *Suppose that system (1.3) is defined for some $\Lambda(rt)$ that traces*

Table 3.1: Summary of concepts discussed in Section 3.2.2 and Section 3.2.3

Frozen system $\Lambda(rt) = \lambda = const.$		
Edge state $\eta(\lambda)$, see Definition 3.2.4, e.g. a saddle with $(n-1)$-dim stable manifold.	Regular threshold $\theta(\lambda)$, see Definition 3.2.3, e.g. $(n-1)$-dim stable manifold of a saddle.	$\epsilon = 0$ Singular limit threshold $\theta_0(\lambda)$, see Definition 3.2.6, e.g. stable set of a fold.	$0 < \epsilon \ll 1$ Quasithreshold $\theta_\epsilon(\lambda)$, see Definition 3.2.7, e.g. canard trajectories.
Compactified system $\Lambda(rt) = \Lambda(s)$			
R-tipping edge state: $\tilde{\eta}^+ = (\eta(\lambda^+), 1)$.	Regular R-tipping threshold: stable set of $\tilde{\eta}^+$, denoted as $W^s(\tilde{\eta}^+)$.	$\epsilon = 0$ Singular R-tipping threshold $\theta_0(\lambda)$: singular canard trajectory. Singular R-tipping edge state: folded singularity.	$0 < \epsilon \ll 1$ R-tipping quasithreshold: canard trajectories and their stable sets.

out a path P_λ.

(i) Suppose there is a threshold $\theta(\lambda)$ *that exists and varies continuously on a subset of the path* $Q_\lambda = \overline{\{\Lambda(rt) : t \in (t_1, t_2)\}} \subseteq P_\lambda$. *Then, we say*

$$\theta\left(\Lambda(rt)\right) \quad \textit{for} \quad t \in (t_1, t_2), \tag{3.40}$$

is a moving threshold.

(ii) Suppose there is a regular edge state $\eta(\lambda)$ *that exists and varies continuously on a subset of the path* $Q_\lambda = \overline{\{\Lambda(rt) : t \in (t_1, t_2)\}} \subseteq P_\lambda$. *Then, we say*

$$\eta\left(\Lambda(rt)\right) \quad \textit{for} \quad t \in (t_1, t_2), \tag{3.41}$$

is a moving edge state.

A moving threshold and a moving edge state are the properties of the frozen system (1.2) and the external input $\Lambda(rt)$. Unlike the stable equilibrium $e(\lambda)$, neither a threshold $\theta(\lambda)$ nor an edge state $\eta(\lambda)$ need to exist for all λ on the path P_λ. However, except the canonical example of *R-B-tipping* in Chapter 4, we restrict to R-tipping due to regular thresholds and edge states that exist and vary continuously on a subset of the path

$$Q_\lambda = \overline{\{\Lambda(rt) : t \in (t_1, +\infty)\}} \subseteq P_\lambda,$$

that contains λ^+. In other words, given $\theta(\lambda)$ and $\eta(\lambda)$, we consider external inputs $\Lambda(rt)$ that give rise to moving regular thresholds $\theta(\Lambda(rt))$ and edge states $\eta(\Lambda(rt))$ for $t \in (t_1, +\infty)$. Then we define the future limit of a moving edge state

$$\eta^+ \coloneqq \lim_{t \to +\infty} \eta(\Lambda(rt)) = \eta(\lambda^+),$$

which is the edge state of the autonomous future system (3.1).

3.2.5 Tracking moving stable equilibria and R-tipping

Note that if $\Lambda(rt)$ is (bi-)asymptotically constant then any limit ($e^\pm$ or η^+) as well as the parameter path P_λ traced out, will be independent of $r > 0$. However, as we vary $r > 0$, trajectories $x^{[r]}(t, x_0, t_0)$ started at some fixed initial state (x_0, t_0) will also vary. For a bi-asymptotically constant input, we sometimes consider a special solution $x^{[r]}(t, x_0, t_0) \to e^-$ as $t \to -\infty$ and write this as

$$x^{[r]}(t, e^-).$$

As shown in [55, 44] this is unique (if e^- is a hyperbolic attractor) and can be understood as a *local pullback attractor* of the nonautonomous system (1.3) that limits to the attractor e^- of the past limit system. We sometimes simply write $x^{[r]}(t)$ to mean either $x^{[r]}(t, x_0, t_0)$ or $x^{[r]}(t, e^-)$ depending on the context.

As noted in [55, 44] there are several ways to understand adiabatic tracking of a moving stable state (a branch of attractors), depending on whether we need closeness at all points in time, or just in the future limit. The following definition formalizes this. Recall that a moving stable equilibrium is exponentially stable by Definition 3.2.2.

Definition 3.2.13. *Consider a nonautonomous system (1.3) with an asymptotically constant input $\Lambda(rt)$ that traces out P_λ and limits to λ^+. Suppose there is a moving stable equilibrium $e(\Lambda(rt))$ on P_λ and recall that $e(\Lambda(rt)) \to e^+$ as $t \to +\infty$. For any given $\delta > 0$ and $r > 0$:*

(i) We say $x^{[r]}(t, x_0, t_0)$ δ-close tracks *$e(\Lambda(rt))$ if*

$$\left|x^{[r]}(t, x_0, t_0) - e(\Lambda(rt))\right| < \delta \ \text{ for all } \ t > t_0. \tag{3.42}$$

(ii) If in addition $\Lambda(rt)$ is bi-asymptotically constant, then $e(\Lambda(rt)) \to e^-$ as $t \to -\infty$, and we say $x^{[r]}(t, e^-)$ δ-close tracks *$e(\Lambda(rt))$ if*

$$\left|x^{[r]}(t, e^-) - e(\Lambda(rt))\right| < \delta \ \text{ for all } \ t \in \mathbb{R}. \tag{3.43}$$

(iii) We say $x^{[r]}(t)$ end-point tracks *$e(\Lambda(rt))$, if*

$$x^{[r]}(t) \to e^+ \ \text{ as } \ t \to +\infty. \tag{3.44}$$

Any value $r = r_c > 0$ where the parametrised family of solutions $x^{[r]}(t)$ fails to track that we call a critical rate for R-tipping, and say the system undergoes *R-tipping* at this r_c. More precisely,

Definition 3.2.14. *Consider a nonautonomous system (1.3) with an asymptotically constant input $\Lambda(rt)$ that traces out P_λ and limits to λ^+. Suppose there is a moving stable equilibrium $e(\Lambda(rt))$ on P_λ and a moving regular threshold $\theta(\Lambda(rt))$ with regular edge state $\eta(\Lambda(rt))$, and recall that $e(\Lambda(rt)) \to e^+$ and $\eta(\Lambda(rt)) \to \eta^+$ as $t \to +\infty$.*

(i) We say the nonautonomous system (1.3) undergoes R-tipping from *(x_0, t_0) if there are $0 < r_1 < r_2$*

$$x^{[r_1]}(t, x_0, t_0) \to e^+ \ \text{ and } \ x^{[r_2]}(t, x_0, t_0) \to \eta^+ \ \text{ as } \ t \to +\infty.$$

(ii) Suppose in addition that $\Lambda(rt)$ *is bi-asymptotically constant and* $e(\Lambda(rt)) \to e^-$ *as* $t \to -\infty$. *We say the nonautonomous system (1.3) undergoes* R-tipping from e^- *if there are* $0 < r_1 < r_2$ *such that*

$$x^{[r_1]}(t, e^-) \to e^+ \quad \textit{and} \quad x^{[r_2]}(t, e^-) \to \eta^+ \ \textit{ as } \ t \to +\infty.$$

(iii) If a rate r_2 *is isolated in the sense that there is a* $\delta > 0$ *such that*

$$x^{[r_2]}(t) \to \eta^+ \ \textit{ and } \ x^{[r]}(t) \nrightarrow \eta^+ \ \textit{ for } \ 0 < |r - r_2| < \delta \ \textit{ as } \ t \to +\infty,$$

then we call r_2 *a* critical rate *and denote it with* r_c.

Definition 3.2.15. *Suppose a nonautonomous system* (1.3) *undergoes R-tipping at the critical rate* r_c *by Definition 3.2.14,*

(i) Irreversible R-tipping *occurs at* $r = r_c$ *if there is a limit state*[4] q^+ *other than* e^+, *and a* $\delta > 0$, *so that the solution limits to a different state for* r *either side of* r_c:

$$\lim_{t\to+\infty} x^{[r]}(t) = \begin{cases} e^+ & \textit{for} \quad r \in (r_c - \delta, r_c), \\ q^+ & \textit{for} \quad r \in (r_c + \delta, r_c). \end{cases} \tag{3.45}$$

(ii) Reversible R-tipping *occurs at* $r = r_c$ *if there is a* $\delta > 0$, *so that the solution limits to* e^+ *for* r *either side of* r_c:

$$\lim_{t\to+\infty} x^{[r]}(t) = e^+ \ \textit{ for } \ 0 < |r - r_c| < \delta.$$

3.3 Testable criteria

Here, we introduce the notion of *threshold instability* which generalises the notion of "basin stability" from [44, Def.3.3] and allows us to formulate testable criteria for R-tipping due to regular thresholds and quasithresholds in arbitrary dimension.

The notion of "forward basin stability" for a moving stable equilibrium was introduced in [44, Def.3.3] for one-dimensional systems of the form (1.2), where a regular threshold necessarily separates the phase space into disconnected components, possibly basins of attraction. Specifically, a moving stable equilibrium is "forward basin stable" if, at each point in time, $e(\Lambda(rt))$ is contained in the basin of attraction of its every future position or, alternatively, if at each point in time,

[4]The limit state need not to be defined, i.e. $+\infty$.

the basin of attraction of $e(\Lambda(rt))$ contains all the previous positions of $e(\Lambda(rt))$. This notion was used in [44, Th.3.2] to give simple criteria to exclude and to guarantee irreversible R-tipping in one dimension.

However, a theory that captures both irreversible and reversible R-tipping and works in arbitrary dimension requires a different concept. In particular, the concept of "forward basin stability" [44] is no longer useful if trajectories started within the basin of attraction approach the attractor non-monotonically in time. Specifically, "forward basin stability" in system (1.2) no longer excludes R-tipping in system (1.3). Our canonical example III from Sec. 4.4 and Refs. [85, 65] demonstrate that irreversible R-tipping may occur in spite of forward basin stability in two dimensions. What is more, in two or more dimensions, reversible R-tipping can occur near a regular threshold that lies in the basin boundary of a single attractor, or near quasithresholds that do not even lie in a basin boundary.

To give testable criteria for both irreversible and reversible R-tipping to occur in arbitrary dimension, and to capture R-tipping due to quasithresholds, we introduce a notion of *(forward) threshold instability* .

Definition 3.3.1. *Let an equilibrium $e(\lambda)$ for* (1.2) *be stable on a path P_λ. We say $e(\lambda)$ is* threshold unstable on P_λ *if there exists a threshold $\theta(\lambda)$ and $\lambda_a, \lambda_b \in P_\lambda$ such that*

$$e(\lambda_a) \in \theta(\lambda_b),$$

and $e(\lambda)$ can lie on different sides of $\theta(\lambda_b)$ for λ arbitrarily close to λ_a.

If in addition $\theta(\lambda_b)$ is contained in the basin of boundary of more than one attractor, we say $e(\lambda)$ is basin unstable on P_λ.

Remark 3.3.1. *Alternatively, one can define* threshold instability *in terms of $e(\lambda_a)$ that lies on different sides of $\theta(\lambda)$ for λ arbitrarily close to λ_b. The two formulations are equivalent if $e(\lambda)$ varies with λ at λ_a and $\theta(\lambda)$ varies with λ at λ_b.*

Definition 3.3.2. *Now consider some $\Lambda(rt)$ that traces out P_λ and a moving stable equilibrium $e(\Lambda(rt))$. We say this $e(\Lambda(rt))$ is* forward threshold unstable for $\Lambda(rt)$ *if it crosses a future position of a moving threshold from one side to the other. In other words, there exist a moving threshold $\theta(\Lambda(rt))$, $t_a < t_b$ and a $\delta > 0$ such that*

$$e(\Lambda(rt_a)) \in \theta(\Lambda(rt_b)),$$

and $e(\Lambda(rt))$ lies on different sides of $\theta(\Lambda(rt_b))$ for $t \in (t_a - \delta, t_a)$ and $t \in (t_a, t_a + \delta)$. If in addition $\theta(\Lambda(rt_b))$ is contained in the basin boundary of more than one attractor, we say $e(\Lambda(rt))$ is forward basin unstable for $\Lambda(rt)$.

Note that while *forward threshold instability* is a property of the frozen system (1.2) and some external input $\Lambda(rt)$, *threshold instability* is a property of the frozen system (1.2) and the path P_λ. Threshold instability on P_λ guarantees the existence of some $\Lambda(rt)$ that traces out the P_λ and gives forward threshold instability. However, there might be other inputs $\Lambda(rt)$ that trace out the same P_λ but do not give forward threshold instability.

Following [44], we use properties of the frozen system (1.2) and the external input $\Lambda(rt)$ to give testable criteria for R-tipping in the parametrised nonautonomous system (1.3). In particular, we extend some results from [44] to arbitrary dimension, and to include the possibility of reversible R-tipping due to regular thresholds.

Recall that [44, Theorem 3.2] uses the notion of "forward basin stability" to give sufficient conditions for irreversible R-tipping to occur, and to be excluded, in one dimensional systems. Recent work [65, 85] suggests that simple testable criteria to exclude R-tipping will be much more difficult to formulate for higher dimensional systems unless there are additional constraints. The main difference between one- and higher-dimensional systems is that, in higher dimensions, forward basin stability does not exclude the possibility of R-tipping.

Below, we use the notion of "(forward) threshold instability" defined in Definition 3.3.1 and Definition 3.3.2 to generalise the testable conditions for R-tipping to occur from [44] to arbitrary dimension, and to include reversible R-tipping due to regular thresholds. In case (i) we give a simple testable criterion to identify systems that exhibit R-tipping for suitably chosen inputs $\Lambda(rt)$. In case (ii), we give a simple testable condition for R-tipping to occur given a prescribed external input $\Lambda(rt)$.

Conjecture 3.1. *Consider the frozen system (1.2) with $x \in \mathbb{R}^n$, a parameter path P_λ, an equilibrium $e(\lambda)$ that is stable on P_λ, and a regular threshold $\theta(\lambda)$ with a regular edge state $\eta(\lambda)$.*

(i) If $e(\lambda)$ is threshold unstable on the path P_λ, then there is a bi-asymptotically constant $\Lambda(rt)$ that traces out P_λ and gives R-tipping from e^- in the nonautonomous system (1.3).

(ii) Suppose the bi-asymptotically constant input $\Lambda(rt)$ tracing out P_λ is prescribed, the moving edge state $\eta(\Lambda(rt)) \to \eta^+$ as $t \to +\infty$, and the corresponding moving stable equilibrium $e(\Lambda(rt))$ is forward threshold unstable due to $\theta(\Lambda(rt))$. Then, there is a bi-asymptotically constant input $\tilde{\Lambda}(rt)$ and an $r_c > 0$ that gives R-tipping from e^- in the nonautonomous system (1.3) *at $r = r_c$.*

Remark 3.3.2. *The input $\tilde{\Lambda}(rt)$ is constructed by reparametrisation $\tilde{\Lambda}(rt) := \Lambda(\sigma(rt))$ using a smooth and monotone σ.*

Conjecture 3.1 is proved in paper [63], which is not covered in this thesis. The results can be understood intuitively referring to Fig. 4.3, which shows phase portraits of the frozen system (4.11), for different values of the input parameter $\lambda =$ (a) 0, (b) $\lambda_1 = 2\sqrt{\mu}$, and (c) $\lambda_2 > 2\sqrt{\mu}$. The frozen system has two stable equilibria $e_1(\lambda)$ and $e_2(\lambda)$, and the threshold $\theta(\lambda)$. For the corresponding nonautonomous system with $\Lambda(rt)$ instead of λ, suppose that $\Lambda(rt)$ increases smoothly from 0 to λ_2 at a 'rate' r, and the system starts near the stable equilibrium $e_1(0)$ for $\lambda = 0$. Now consider two limiting scenarios. On the one hand, when $\Lambda(rt)$ is increased arbitrarily slowly $(r \to 0)$, the nonautonomous system adiabatically follows the moving stable equilibrium $e_1(rt)$ for all time. On the other hand, when $\Lambda(rt)$ changes smoothly but abruptly from 0 to λ_2 at some point in time $(r \to \infty)$, remains almost constant otherwise, and the "abrupt" change is faster than the natural timescales of the system, the dynamics are very different. Initially, the system approaches $e_1(0)$ because $\Lambda(rt)$ is almost constant. Then comes the abrupt change, but the system is too slow to respond. Therefore, just after the abrupt change, the system is still at its earlier position near $e_1(0)$, which now lies on the other side of the threshold $\theta(\lambda_2)$ [Fig. 4.3(c)]. Since $\Lambda(rt)$ remains almost constant from then on, the system evolves away from $e_1(\lambda_2)$ and R-tips to $e_2(\lambda_2)$. These two limiting scenarios indicate that there is at least one (nonzero but finite) critical rate $r = r_c$, which defines the transition from tracking to R-tipping.

The concepts introduced above in conjunction with the compactification framework developed in the previous Chapter give us a convenient setting for R-tipping analysis.

Chapter 4

Canonical Examples of R-tipping

In this chapter, we construct canonical examples of the vector field f and the external input $\Lambda(rt)$ in (1.3) that give rise to different types of R-tipping. We numerically examine these canonical examples guided by the theory of R-tipping, in particular the concepts of moving equilibria and threshold instability, outlined in Chapter 3. To discuss the strengths and limitation of our approach, we include an example of R-tipping that is not captured by the rigorous theory from [63], but can still be analysed in terms of moving equilibria and threshold instability.

4.1 Setup for R-tipping analysis

At first, we propose canonical examples of system (1.3) that exhibit the nonlinear phenomenon of R-tipping. These examples are relatively simple low-dimensional nonlinear systems that capture different R-tipping mechanisms. Specifically, we discuss:

(i) seven different forms of the vector field $f(x, \lambda)$ to discuss irreversible and reversible R-tipping with dependence on different number of degrees of freedom (one-dimensional vs. higher-dimensional), different time scales (single timescale vs. multiple timescales), and different threshold types (regular threshold vs. quasithreshold); see Fig. 4.1.

(ii) three basic forms of external input $\Lambda(rt)$ to illustrate R-tipping effects with dependence on mononotone vs. non-monotone $\Lambda(rt)$, and asymptotically constant vs. bi-asymptotically constant $\Lambda(rt)$; see Fig. 4.2.

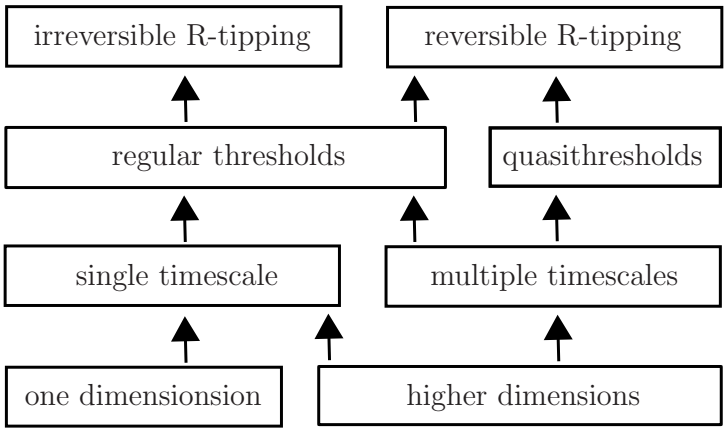

Figure 4.1: A directed graph identifying links between the nonlinear phenomenon of R-tipping, the two threshold types, multiple timescales, and phase-space dimension.

4.1.1 Canonical forms of the vector field

Selecting canonical examples of $f(x, \lambda)$ to classify different R-tipping mechanisms in system (1.3) is not a straightforward task. The reason is that R-tipping mechanisms depend on various factors including the phase-space dimension, multiple timescales, and different threshold types. What is more, these factors are not independent of each other.

In our bottom-up approach illustrated by the directed graph in Fig. 4.1, we first recognise that the system may have different phase-space dimension, and two- or higher-dimensional systems may evolve on different timescales. Then, we recognise that there are two threshold types, namely regular thresholds and quasithresholds. Regular thresholds occur in any dimension and can be found in either single- or multiple-timescale systems. Quasithresholds require at least two different timescales, and thus at least two dimensions. This brings us to two R-tipping types shown in the top row of the graph. Irreversible R-tipping can occur in any dimension, but requires regular thresholds. Reversible R-tipping can occur in any dimension for regular thresholds and quasithresholds, but is typically found in two or more dimensions. Following the arrows in the directed graph, there are seven possible pathways from the bottom row to the top row. Thus, in our classification, we identify seven canonical examples of R-tipping, one for each possible pathway in the directed graph.

4.1.2 Canonical forms of external input

We choose three basic forms of the external input $\Lambda(rt)$ to illustrate different R-tipping effects. Each $\Lambda(rt)$ is normal asymptotically constant (see Def. 2.2.2), meaning that there exists a suitable compactification (see Theorem 2.3). Furthermore, each $\Lambda(rt)$ is parameterised by the *magnitude* Δ and the *'rate'* r. This enables parametric study to identify critical rates r_c with dependence on Δ, and to produce two-dimensional *R-tipping diagrams* in the (Δ, r)-plane of the input parameters. The three chosen forms of $\Lambda(rt)$ are:

(i) Asymptotically constant approach towards $\Lambda = \Delta$:

$$\Lambda(rt) = \Delta\left(1 - e^{-rt}\right), \tag{4.1}$$

defined for $t \geq 0$ and shown in Fig. 4.2(a). This form illustrates applicability of the compactification framework to external inputs with arbitrary past behaviour.

(ii) Monotone and bi-asymptotically constant logistic growth from 0 to Δ:

$$\Lambda(rt) = \frac{1}{2}\Delta\left(\tanh\left(rt\right) + 1\right), \tag{4.2}$$

defined for $t \in \mathbb{R}$ and shown in Fig. 4.2(b). This form highlights the main advantage of working with inputs that change from one asymptotic value to another, which is that an R-tipping problem can be transformed into a connecting heteroclinic orbit problem.

(iii) Non-monotone and bi-asymptotically constant impulse

$$\Lambda(rt) = \Delta\,\mathrm{sech}(rt) = \Delta\frac{2}{e^{rt} + e^{-rt}}, \tag{4.3}$$

defined for $t \in \mathbb{R}$ and shown in Fig. 4.2(c). In addition to the main advantage of changing from one asymptotic value to another, this form is used to demonstrate existence of multiple critical rates.

4.1.3 Compactification for canonical forms of external input

To take advantage of asymptotically constant external inputs, nonautonomous system (1.3) is transformed into an autonomous compactified system (2.61)–(2.64) by a suitable compactification $s = \tilde{g}_{(\alpha)}(rt)$, where $\tilde{g}_{(\alpha)} : \mathbb{R} \to (s_-, 1)$; see Section 2.5 for details of compactification in R-tipping. The main idea of compactification is to construct an autonomous compactified system with an invari-

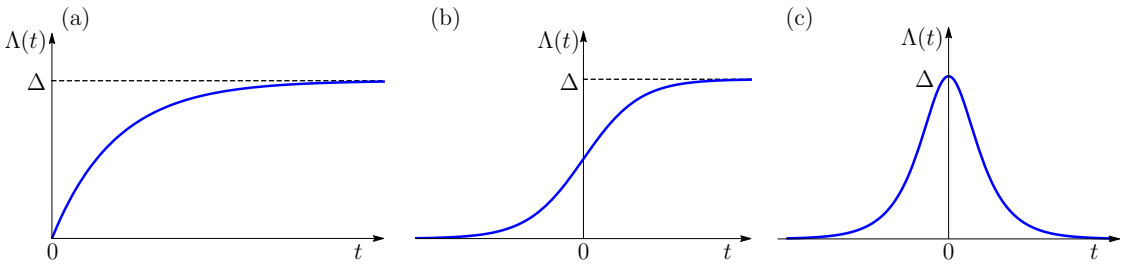

Figure 4.2: The three basic forms of external input chosen for canonical examples of R-tipping: (a) monotone asymptotically constant, (b) monotone bi-asymptotically constant, and (c) non-monotone bi-asymptotically constant.

ant subspace $\{s = 1\}$ that may contain compact invariant sets such as equilibrium points, limit cycles, tori, etc. If the external input is bi-asymptotically constant, then $\{s = -1\}$ becomes another invariant subspace.

The compactification transformation is independent of the overall temporal shape of $\Lambda(rt)$, and depends just on the form of its asymptotic decay. Since all three chosen external inputs (4.1)–(4.3) have exponential asymptotic decay, we can work with one form of compactification transformation, namely with the exponential transformation (2.66) constructed in Section 2.5.2. This transformation is parametrised by a single compactification parameter α, which needs to be chosen for each input $\Lambda(rt)$ individually as explained in the last paragraph of this section.

As shown in Section 2.5, the compactification transformation (2.66) gives a common equation for $\dot{s}$, and the compactified autonomous system (2.68):

$$\left.\begin{aligned} \dot{x} &= f(x, \Lambda(s)), \\ \dot{s} &= \frac{\alpha r}{2}\left(1 - s^2\right). \end{aligned}\right\} \tag{4.4}$$

For input (4.1), we define

$$\Lambda(s) = \begin{cases} \Lambda(\tilde{h}_{(\alpha)}(s)) & \text{for} \quad s \in [0, 1), \\ \Delta & \text{for} \quad s = 1, \end{cases} \tag{4.5}$$

where $\Lambda(\tilde{h}_{(\alpha)}(s))$ is obtained by substituting $rt = \tilde{h}_{(\alpha)}(s)$ given by (2.66) into (4.1):

$$\Lambda(\tilde{h}_{(\alpha)}(s)) = \Delta\left(1 - \left(\frac{1-s}{1+s}\right)^{1/\alpha}\right). \tag{4.6}$$

The phase space $\mathbb{R}^n \times [0, 1]$ has one invariant subspace $\{s = 1\}$. This subspace is stable, and the dynamics within the subspace are given by the future limit system $\dot{x} = f(x, \Delta)$.

For input (4.2), we define

$$\Lambda(s) = \begin{cases} \Lambda(\tilde{h}_{(\alpha)}(s)) & \text{for} \quad s \in (-1,1), \\ \Delta & \text{for} \quad s = 1, \\ 0 & \text{for} \quad s = -1, \end{cases} \tag{4.7}$$

where $\Lambda(\tilde{h}_{(\alpha)}(s))$ is obtained by substituting $rt = \tilde{h}_{(\alpha)}(s)$ given by (2.66) into (4.2):

$$\Lambda(\tilde{h}_{(\alpha)}(s)) = \Delta \frac{(1+s)^{2/\alpha}}{(1+s)^{2/\alpha} + (1-s)^{2/\alpha}}. \tag{4.8}$$

The phase space $\mathbb{R}^n \times [-1,1]$ has one stable invariant subspace $\{s = 1\}$, and one unstable invariant subspace $\{s = -1\}$. The dynamics within $\{s = -1\}$ are given by the past-limit system $\dot{x} = f(x, 0)$, while the dynamics within $\{s = 1\}$ are given by the future-limit system $\dot{x} = f(x, \Delta)$.

For input (4.3), we define

$$\Lambda(s) = \begin{cases} \Lambda(\tilde{h}_{(\alpha)}(s)) & \text{for} \quad s \in (-1,1), \\ 0 & \text{for} \quad s = \pm 1, \end{cases} \tag{4.9}$$

where $\Lambda(\tilde{h}_{(\alpha)}(s))$ is obtained by substituting $rt = \tilde{h}_{(\alpha)}(s)$ given by (2.66) into (4.3):

$$\Lambda(\tilde{h}_{(\alpha)}(s)) = 2\Delta \frac{(1-s^2)^{1/\alpha}}{(1+s)^{2/\alpha} + (1-s)^{2/\alpha}}. \tag{4.10}$$

The phase space $\mathbb{R}^n \times [-1,1]$ has one stable invariant subspace $\{s = 1\}$, and one unstable invariant subspace $\{s = -1\}$. The dynamics within each subspace are identical and given by the common limit system $\dot{x} = f(x, 0)$.

An important point of compactification is a suitable choice of the compactification parameter α. Specifically, inputs (4.1) and (4.3) have an exponential asymptotic decay at the rate r, and thus require $0 < \alpha \leq 1$ to satisfy condition (2.13) from Lemma 2.1. Input (4.2) has an exponential asymptotic decay at the rate $2r$, and thus requires $0 < \alpha \leq 2$ to satisfy condition (2.13) from Lemma 2.1; see Corollary 2.6. One can see that choosing the maximum value of α gives the simplest form of $\Lambda(\tilde{h}_{(\alpha)}(s))$ in (4.6), (4.8) and (4.10). This, however, need not be the optimal choice. For example, one may prefer to choose α such that the eigenvector owing to the additional s-direction is normal to invariant subspaces $\{s = \pm 1\}$. What is more, α gives flexibility to 'place' the interesting R-tipping dynamics within a desired range of s in the compactified system. Our choices of α are given in the discussion of individual canonical examples.

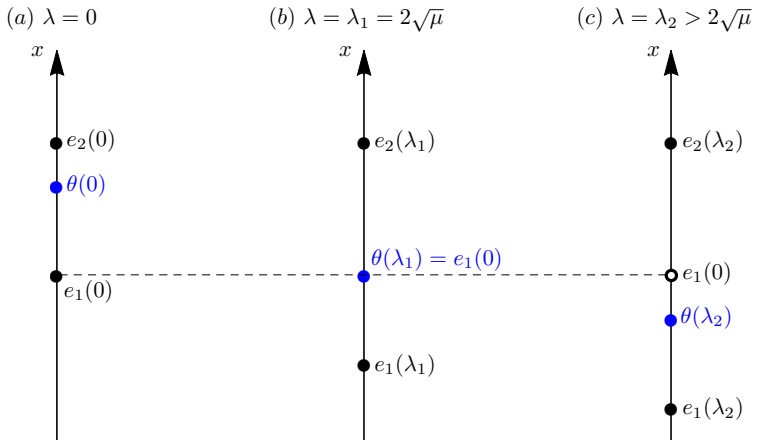

Figure 4.3: Phase portraits of autonomous canonical example I (4.11), for different values of the input parameter (a) $\lambda = 0$, (b) $\lambda = \lambda_1 = 2\sqrt{\mu}$, and (c) $\lambda = \lambda_2 > 2\sqrt{\mu}$, illustrate (forward) threshold instability of stable equilibrium e_1.

4.2 Canonical example I

This canonical example:

- Is the simplest bistable system with regular thresholds that exhibits irreversible R-tipping.

Consider the following path in the directed graph from Fig. 4.1: one dimension $\rightarrow$ single timescale $\rightarrow$ regular thresholds $\rightarrow$ irreversible R-tipping, together with a bistable frozen system:

$$\dot{x} = f(x, \lambda) = -\left((x + \lambda)^2 - \mu\right)(x - 2\sqrt{\mu}), \tag{4.11}$$

where $x \in \mathbb{R}$, $\mu > 0$, and $\lambda \geq 0$ is the fixed-in-time input parameter. The frozen system has two stable equilibria

$$e_1(\lambda) = -\sqrt{\mu} - \lambda, \quad \text{and} \quad e_2 = 2\sqrt{\mu},$$

and one unstable equilibrium which is the regular threshold and the edge state at the same time

$$\theta(\lambda) = \eta(\lambda) = \sqrt{\mu} - \lambda.$$

The threshold $\theta(\lambda)$ is a basin boundary of the two attractors.

Figure 4.3 shows three phase portraits for different values of the input parameter λ along the parameter path

$$P_\lambda = \{\lambda : 0 \leq \lambda \leq \Delta\}.$$

If $\Delta > 2\sqrt{\mu}$, then $e_1(0) = \theta(2\sqrt{\mu})$ and $e_1(0)$ lies on different sides of $\theta(\lambda)$ for λ arbitrarily close to $2\sqrt{\mu}$, meaning the stable equilibrium $e_1(\lambda)$ is *threshold unstable* (*basin unstable*) on P_λ; see Definition 3.3.2. Threshold instability on P_λ implies that there exists a time-varying external input $\Lambda(rt)$ that traces out P_λ and gives rise to R-tipping from $e_1(rt)$; see [44, Th.3.2].

We now analyse irreversible R-tipping from $e_1(rt)$ to $e_2(rt)$ in the nonautonomous **canonical example I**:

$$\dot{x} = -\left(\left(x + \Lambda(rt)\right)^2 - \mu\right)(x - 2\sqrt{\mu}), \tag{4.12}$$

parametrised by μ and the magnitude Δ and rate r of the parameter shift. For an increasing $\Lambda(rt)$, the moving stable equilibrium $e_1(rt)$ is forward threshold unstable if $\Delta > 2\sqrt{\mu}$. For a decreasing $\Lambda(rt)$, $e_1(rt)$ is forward threshold stable.

4.2.1 Monotone bi-asymptotically constant input

Combining (4.4), (4.7) with $\alpha = 1$, and (4.12) gives the compactified canonical example I with monotone external input:

$$\begin{aligned} \dot{x} &= -\left(\left(x + \frac{\Delta}{2}\frac{(1+s)^2}{1+s^2}\right)^2 - \mu\right)(x - 2\sqrt{\mu}), \\ \dot{s} &= \frac{r}{2}\left(1 - s^2\right). \end{aligned} \tag{4.13}$$

The choice of the compactification parameter α satisfies the compactification condition $0 < \alpha \leq 2$ and ensures that invariant subspaces $\{s = \pm 1\}$ have an orthogonal transverse eigenvector.

The dynamics of system (4.13) are summarised in Fig. 4.4, which shows the (Δ, r) tipping diagram together with selected (x, s) phase portraits for $\mu = 0.04$, $\Delta = 1$ and different rates r. The invariant subspace $\{s = -1\}$ contains the saddle $\tilde{e}_1^-$, which is stable within the subspace and unstable in the transverse s-direction. The invariant subspace $\{s = 1\}$ contains the stable equilibria $\tilde{e}_1^+$ and $\tilde{e}_2^+$, together with the *R-tipping edge state* $\tilde{\eta}^+$. The *R-tipping threshold* is the stable invariant manifold $W^{s,[r,\Delta]}(\tilde{\eta}^+)$ whose shape depends on r and Δ. The R-tipping threshold $W^{s,[r,\Delta]}(\tilde{\eta}^+)$ separates the phase space into two basins of attraction, with the basin of attraction of $\tilde{e}_1^+$ shaded in blue.

If r is sufficiently small, the unstable manifold $W^{u,[r,\Delta]}(\tilde{e}_1^-)$ closely approximates the moving stable equilibrium $e_1(rt)$, while the R-tipping threshold $W^{s,[r,\Delta]}(\tilde{\eta}^+)$ closely approximates the moving threshold/edge state $\eta(rt)$. $W^{u,[r,\Delta]}(\tilde{e}_1^-)$ accumulates on $\tilde{e}_1^+$, meaning that there is an open half-disk of initial states centred at

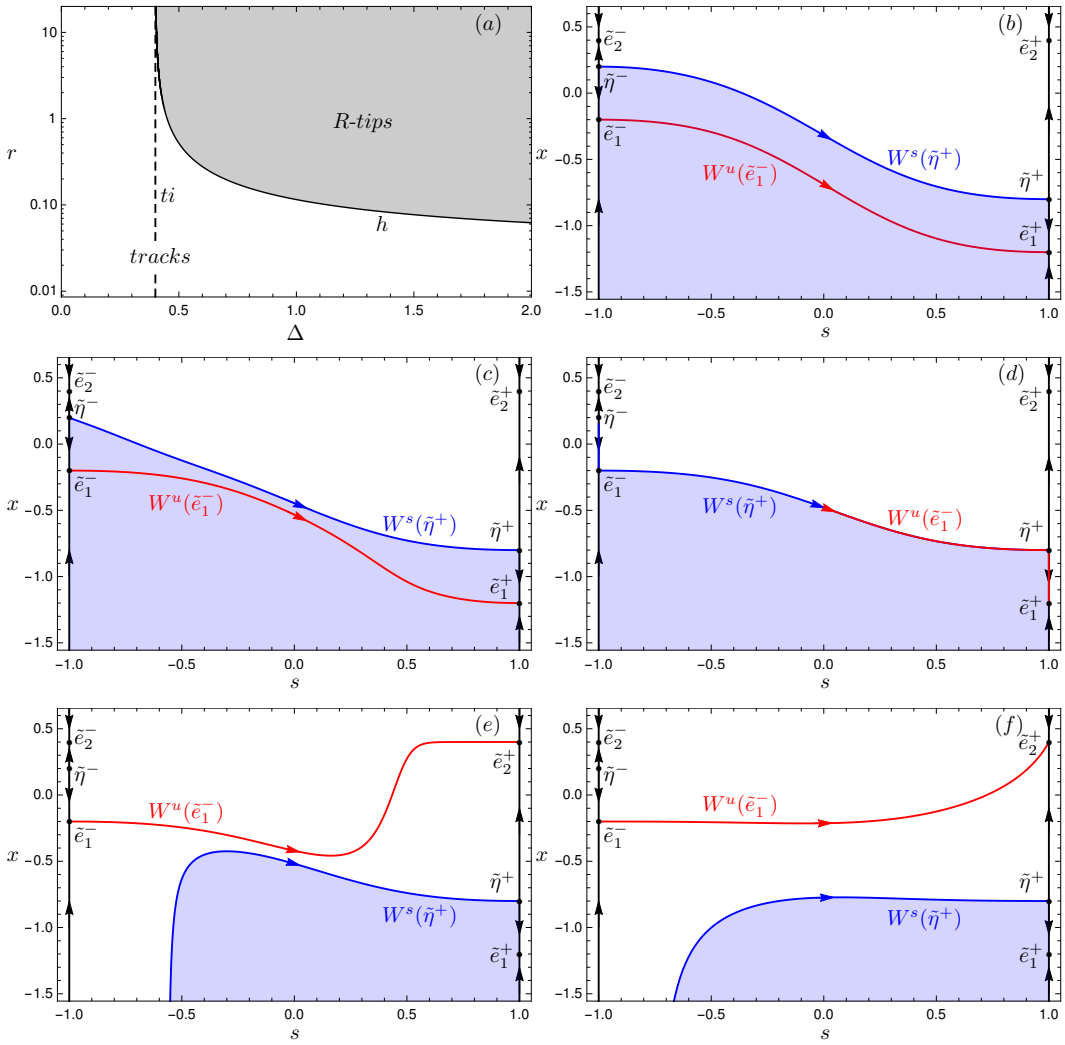

Figure 4.4: (a) The (Δ, r) tipping diagram for the canonical example (4.12) with monotone external input (4.2) contains regions of (white) tracking the moving stable equilibrium $e_1(rt)$ and (grey) irreversible R-tipping from $\tilde{e}_1^-$ to $\tilde{e}_2^+$. The (dashed) ti line denotes the forward threshold instability boundary for e_1. (b)-(f) Phase portraits of the compactified system (4.13) for $\mu = 0.04$, $\Delta = 1$ and different 'rates' $r =$ (b) 0.01, (c) 0.09, (d) 0.115294190888285, (e) 0.15, and (f) 2.00. The basin of attraction of $\tilde{e}_1^+$ is shaded in blue. (d) The heteroclinic $\tilde{e}_1^-$-to-$\tilde{\eta}^+$ connection for $r = r_c$ defines the tracking-tipping transition. For clarity, the Δ- and r-dependent invariant manifolds $W^{u,[r,\Delta]}(\tilde{e}_1^-)$ and $W^{s,[r,\Delta]}(\tilde{\eta}^+)$ are labeled as $W^u(\tilde{e}_1^-)$ and $W^s(\tilde{\eta}^+)$, and we keep this for other examples.

$\tilde{e}_1^-$, all of which evolve on one side of the threshold and track the moving stable equilibrium $e_1(rt)$ [Fig. 4.4(b)]. As r is increased, $W^{u,[r,\Delta]}(\tilde{e}_1^-)$ and $W^{s,[r,\Delta]}(\tilde{\eta}^+)$ change shape and get closer, the (blue) basin of attraction of $\tilde{e}_1^+$ shrinks, but $W^{u,[r,\Delta]}(\tilde{e}_1^-)$ still accumulates on $\tilde{e}_1^+$ [Fig. 4.4(c)]. When r reaches the critical value r_c, $W^{u,[r,\Delta]}(\tilde{e}_1^-)$ no longer accumulates on $\tilde{e}_1^+$ [Fig. 4.4(d)]. Rather, there is a heteroclinic connection from $\tilde{e}_1^-$ to $\tilde{\eta}^+$, given by the coalescing invariant mani-

folds

$$W^{u,[r_c,\Delta]}(\tilde{e}_1^-) \cap W^{s,[r_c,\Delta]}(\tilde{\eta}^+).$$

Now, any open half-disk of initial states centred at $\tilde{e}_1^-$, however small, contains initial states that converge to $\tilde{e}_1^+$ as well as initial states that converge to $\tilde{e}_2^+$. The heteroclinic connection gives a computable condition for R-tipping that is continued in the plane of the input parameters by implementing the Lin's method [109] in the continuation software AUTO [110]. The result of numerical continuation is a tracking-tipping transition curve h in the (Δ, r) tipping diagram [Fig. 4.4(a)]. The curve separates the regions of (white) tracking $e_1(rt)$ and (grey) irreversible e_1-to-e_2 R-tipping, and approaches the threshold instability boundary ti at $\Delta = 2\sqrt{\mu}$ from the right.

For $r > r_c$, $W^{u,[r,\Delta]}(\tilde{e}_1^-)$ accumulates on $\tilde{e}_2^+$, meaning that there is an open half-disk of initial states centred at $\tilde{e}_1^-$, all of which evolve on the other side of the threshold and converge to the other stable equilibrium $\tilde{e}_2^+$ [Fig. 4.4(e)-(f)].

4.2.2 Non-monotone bi-asymptotically constant input

Combining (4.4), (4.9) with $\alpha = 1$, and (4.12) gives the compactified canonical example I with non-monotone external input:

$$\begin{aligned} \dot{x} &= -\left(\left(x + \Delta\frac{1-s^2}{1+s^2}\right)^2 - \mu\right)(x - 2\sqrt{\mu}), \\ \dot{s} &= \frac{r}{2}(1-s^2). \end{aligned} \tag{4.14}$$

The choice of the compactification parameter α satisfies the compactification condition $0 < \alpha \leq 1$, but gives transverse eigenvectors that are not orthogonal to invariant subspaces $\{s = \pm 1\}$.

The different dynamics of system (4.14) are summarised in Fig. 4.5, which shows the (Δ, r) tipping diagram together with selected (x, s) phase portraits for $\mu = 0.04$, $\Delta = 1$ and different rates r. The main difference from the monotone input is the presence of two critical rates for the same shift magnitude. To start with, phase portraits (b)–(e) in Fig. 4.5 show a very similar scenario to the monotone input from Fig. 4.4. If r is sufficiently small, the unstable manifold $W^{u,[r,\Delta]}(\tilde{e}_1^-)$ closely approximates the moving stable equilibrium $e_1(rt)$, while the R-tipping threshold $W^{s,[r,\Delta]}(\tilde{\eta}^+)$ closely approximates the moving threshold/edge state $\eta(rt)$ [Fig. 4.5(b)]. When r reaches a critical rate r_{c1}, there is a heteroclinic $\tilde{e}_1^-$-to-$\tilde{\eta}^+$ connection that indicates a critical transition from tracking $e_1(rt)$ to irreversible e_1-to-e_2 R-tipping [Fig. 4.5(d)]. There the similarity ends. In contrast

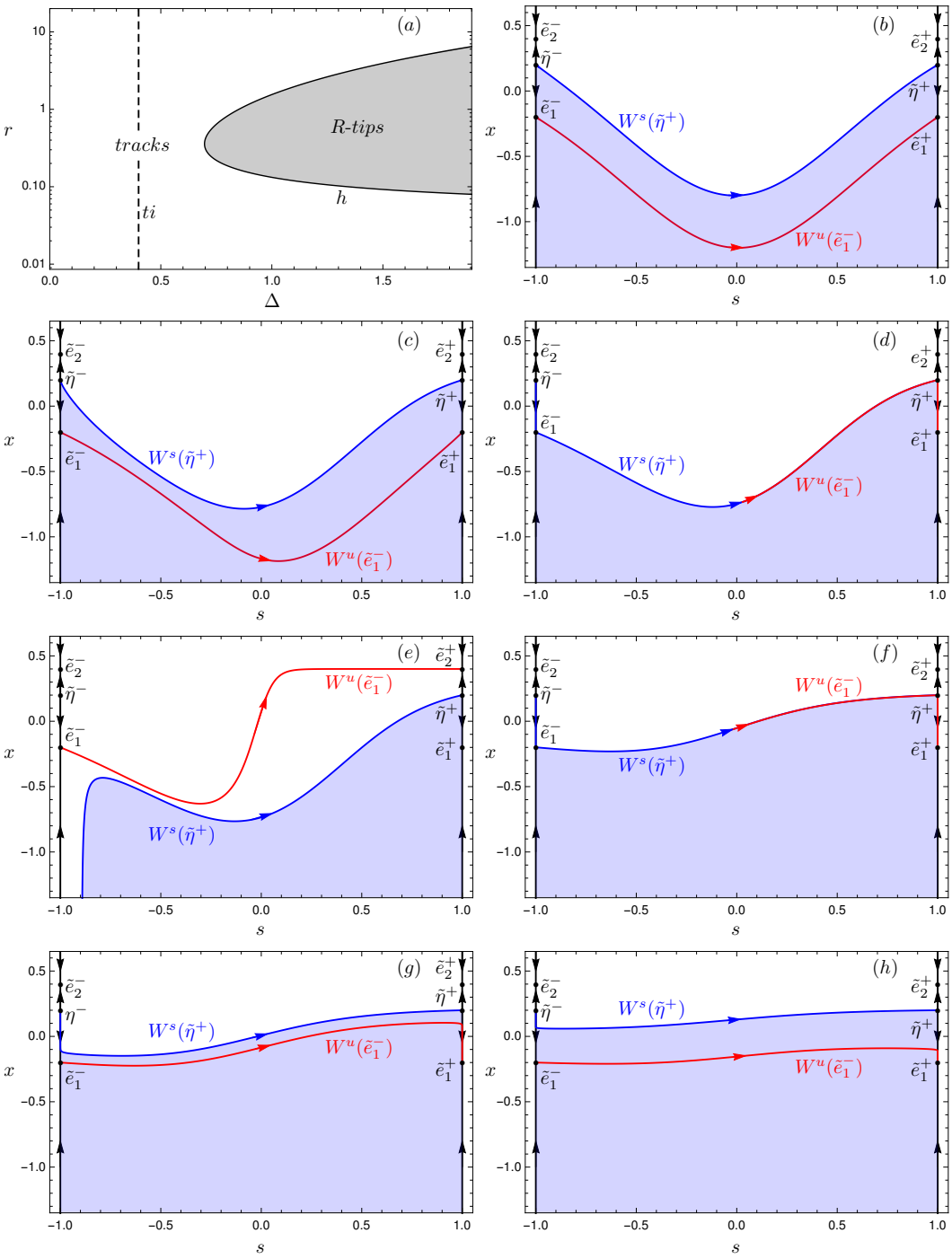

Figure 4.5: (a) The (Δ, r) tipping diagram for the canonical example (4.12) with non-monotone external input (4.3) contains regions of (white) tracking and (grey) irreversible R-tipping. The (dashed) ti line denotes the forward threshold instability boundary for e_1. (b)-(h) Phase portraits of the compactified system (4.14) for $\mu = 0.04$, $\Delta = 1$ and different 'rates' $r =$ (b) 0.01, (c) 0.09, (d) 0.13218379, (e) 0.15, (f) 1.56, (g) 2.0, and (h) 5.0. (d) and (f) Two heteroclinic $\tilde{e}_1^-$-to-$\tilde{\eta}^+$ connections define two tracking-tipping transitions.

to the monotone external input, the corresponding curve h of tracking-tipping transition in the (Δ, r) tipping diagram is folded so that there can be up to two

different critical rates for the same shift magnitude Δ. The (grey) region of irreversible e_1-to-e_2 R-tipping is now tongue-shaped and bounded away from the forward threshold instability boundary ti at $\Delta = 2\sqrt{\mu}$. As r is increased just above the first critical rate r_{c1}, $W^{u,[r,\Delta]}(\tilde{e}_1^-)$ accumulates on $\tilde{e}_2^+$, meaning that there is an open half-disk of initial states centred at $\tilde{e}_1^-$, all of which evolve on the other side of the threshold and converge to the other stable equilibrium $\tilde{e}_2^+$ [Fig. 4.5(e)]. However, as indicated by the tipping diagram in Fig. 4.5(a), for $\Delta = 1$ and even higher r, there is another critical rate $r_{c2} > r_{c1}$. This is evidenced by another heteroclinic connection from $\tilde{e}_1^-$ to $\tilde{\eta}^+$ [Fig. 4.5(f)]. The second critical transition brings the system from irreversible e_1-to-e_2 R-tipping back to tracking $e_1(rt)$. Indeed, for $r > r_{c2}$, $W^{u,[r,\Delta]}(\tilde{e}_1^-)$ accumulates on $\tilde{e}_1^+$ again, meaning that there is an open half-disk of initial states centred at $\tilde{e}_1^-$, all of which evolve on the e_1 side of the threshold and track the moving equilibrium $e_1(rt)$ [Fig. 4.5(g)-(h)].

4.2.3 Highlights of canonical example I

Numerical analysis of canonical example I demonstrates that main concept:

- Compactification transforms R-tipping problems into heteroclinic connection problems.

The numerical results are in agreement with rigorous R-tipping results derived in Ref. [44]:

- In one dimension, forward threshold stability guarantees that R-tipping is avoided for any rate r.
- In one dimension, forward threshold instability is necessary for R-tipping.

4.3 Canonical example II

This canonical example

- Is a simple system that exhibits reversible R-tipping.

Consider the following path in the directed graph from Fig. 4.1: one dimension $\rightarrow$ single timescale $\rightarrow$ regular thresholds $\rightarrow$ reversible R-tipping, together with the monostable but excitable frozen system defined on a unit circle:

$$\dot{x} = f(x, \lambda) = -\mu + \sin(x - \lambda), \tag{4.15}$$

where $x = S^1$, $\lambda \in \mathbb{R}$ is the fixed-in-time input parameter, and $|\mu| < 1$. The

system has one stable equilibrium

$$e(\lambda) = \pi - \sin^{-1}(\mu) + \lambda,$$

and one unstable equilibrium

$$\theta(\lambda) = \eta(\lambda) = \sin^{-1}(\mu) + \lambda,$$

which is the regular threshold and the edge state. The threshold $\theta(\lambda)$ is a basin boundary of one attractor (an excitability threshold), which is indicative of reversible R-tipping. The stable equilibrium is *threshold unstable* (but not basin unstable) on the parameter path

$$P_\lambda = \{\lambda : 0 \leq \lambda \leq \Delta\},$$

if $\Delta > \pi - 2\sin^{-1}(\mu)$.

One can analyse reversible R-tipping in the nonautonomous **canonical example II**:

$$\dot{x} = f(x, \Lambda(rt)) = -\mu + \sin(x - \Lambda(rt)), \quad x \in [0, 2\pi), \tag{4.16}$$

along the lines of the previous section. Here, we leave out the detailed R-tipping analysis of this example because of its similarity to canonical example I. The main difference is that, except for critical rate(s), this system always returns to the only stable equilibrium e.

4.4 Canonical example III

This canonical example:

- Highlights effects of limit-cycle thresholds and different parameter paths.
- Demonstrates R-tipping along parameter paths without threshold instability [85].

Consider the following two paths in the directed graph from Fig. 4.1: higher dimensions $\rightarrow$ single timescale/multiple timescales $\rightarrow$ regular thresholds $\rightarrow$ irreversible R-tipping, together with a frozen system in two dimensions akin to a forced van der Pol oscillator [111, Sec.2.1]:

$$\begin{aligned} \epsilon\dot{x_1} &= -\big(x_2 - \lambda_2\big) - \big(x_1 - \lambda_1\big) + \frac{1}{3}\big(x_1 - \lambda_1\big)^3, \\ \dot{x_2} &= -\mu + x_1 - \lambda_1, \end{aligned} \tag{4.17}$$

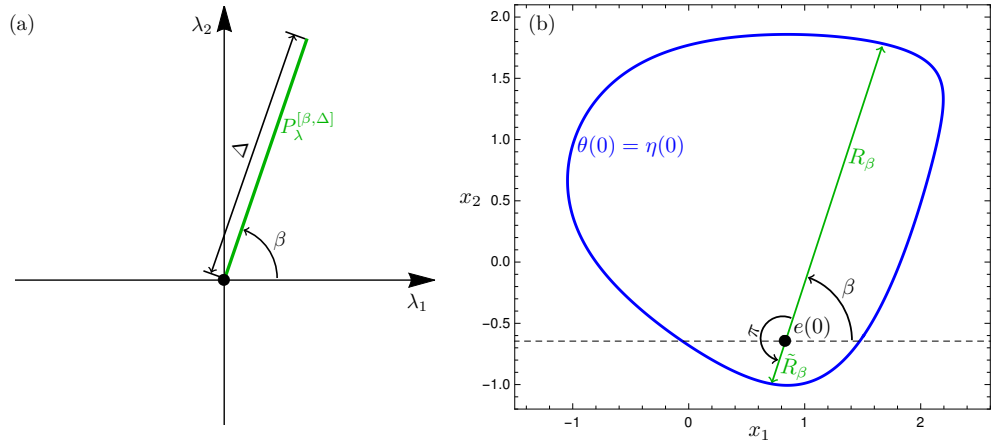

Figure 4.6: (a) A parameter path P_λ in the (λ_1, λ_2) parameter plane. (b) The (x_1, x_2) phase plane of the autonomous canonical example III (4.17) showing the stable equilibrium $e(\lambda)$ and the edge state $\eta(\lambda)$, which is the periodic orbit and also the regular threshold $\theta(\lambda)$, for $\lambda_1 = \lambda_2 = 0$, $\epsilon = 0.5$ and $\mu = 0.85$. As the input $\lambda(rt)$ traces the path P_λ from the origin in the parameter plane, the stable equilibrium $e(rt)$ and the threshold $\theta(rt)$ move in the direction of R_β in the phase plane.

where ϵ quantifies the time scale separation, μ is the constant forcing term, and λ_1 and λ_2 are the two components of the external input $\lambda \in \mathbb{R}^2$. System (4.17) has one equilibrium that is stable

$$e(\lambda) = \left(\mu + \lambda_1, -\mu\left(1 - \frac{\mu^2}{3}\right) + \lambda_2\right),$$

and one repelling limit cycle which forms the regular threshold $\theta(\lambda)$ and the edge state $\eta(\lambda)$ at the same time. Figure 4.6(b) shows $e(\lambda)$ and $\theta(\lambda) = \eta(\lambda)$ for $\lambda = (0, 0)$.

For simplicity, we represent the external input in the polar coordinates

$$\lambda = \begin{pmatrix}\lambda_1 \\ \lambda_2\end{pmatrix} = \begin{pmatrix}|\lambda|\cos\beta \\ |\lambda|\sin\beta\end{pmatrix}, \quad \beta \in [-\pi, \pi], \tag{4.18}$$

and consider *parameter paths* that are straight half-lines from the origin

$$P_\lambda^{[\beta,\Delta]} = \left\{(\lambda_1, \lambda_2) \in \mathbb{R}^2 : \lambda_1 = |\lambda|\cos\beta,\ \lambda_2 = |\lambda|\sin\beta,\ |\lambda| \in [0, \Delta],\ \beta = \text{const.}\right\}, \tag{4.19}$$

parametrised by the magnitude $\Delta > 0$ and the angle β; see Fig. 4.6(a). Positive angle β is measured counterclockwise from the positve λ_1-axis, whereas negative angle β is measured clockwise from the positve λ_1-axis. Associated with a path $P_\lambda^{[\beta,\Delta]}$ in the parameter plane, there are two *threshold radii* R_β and $\tilde{R}_\beta \geq 0$ in the

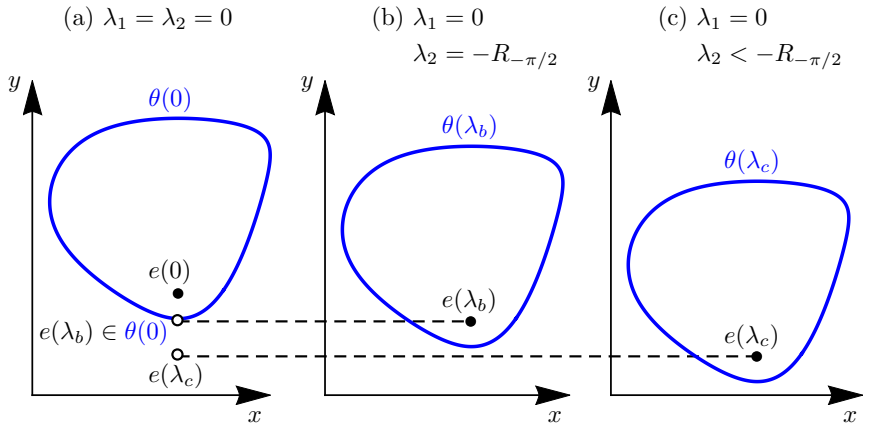

Figure 4.7: Phase portraits of the autonomous canonical example III (4.17) for $\lambda_1 = 0$ and different values of (a) $\lambda_2 = 0$, (b) $\lambda_2 = -R_\beta$ and (c) $\lambda_2 < -R_\beta$ depict threshold instability of the stable equilibrium e on $P_\lambda^{[-\pi/2,\Delta]}$ when $\Delta > R_\beta$.

phase plane defined in Fig. 4.6(b). Let

$$\lambda_\beta = (R_\beta \cos\beta, R_\beta \sin\beta) \text{ and } \tilde{\lambda}_\beta = (\tilde{R}_\beta \cos\beta, \tilde{R}_\beta \sin\beta),$$

and consider positions of $e(\lambda)$ and $\theta(\lambda)$ for different values of λ along a path $P_\lambda^{[\beta,\Delta]}$. If $\Delta > \tilde{R}_\beta$, then $e(0) \in \theta(\tilde{\lambda}_\beta)$ and $e(0)$ lies on different sides of $\theta(\lambda)$ for λ arbitrarily close to $\tilde{\lambda}_\beta$. Similarly, if $\Delta > R_\beta$, then $e(\lambda_\beta) \in \theta(0)$ and $e(\lambda)$ lies on different sides of $\theta(0)$ for λ arbitrarily close to λ_β. Thus, $e(\lambda)$ is *threshold unstable* (*basin unstable*) on $P_\lambda^{[\beta,\Delta]}$ if

$$\Delta > \min\{R_\beta, \tilde{R}_\beta\}.$$

Owing to the lack of rotational symmetry of $\theta(\lambda)$, the threshold instability condition depends on the angle β. Threshold instability of $e(\lambda)$ on the path $P_\lambda^{[-\pi/2,\Delta]}$ which aligns with the negative λ_2 axis is illustrated in Fig. 4.7.

We now analyse irreversible R-tipping from $e(rt)$ to infinity in the nonautonomous **canonical example III**:

$$\begin{aligned} \epsilon \dot{x_1} &= -\Big(x_2 - \Lambda(rt)\sin\beta\Big) - \Big(x_1 - \Lambda(rt)\cos\beta\Big) + \frac{1}{3}\left(x_1 - \Lambda(rt)\cos\beta\right)^3, \\ \dot{x_2} &= -\mu + x_1 - \Lambda(rt)\cos\beta, \end{aligned} \tag{4.20}$$

parametrised by ϵ, μ, the magnitude Δ and rate r of the parameter shift, and the angle β that fixes the orientation of the parameter path in the λ plane. When the external input traces a path $P_\lambda^{[\beta,\Delta]}$ away from the origin of the λ plane, $e(rt)$ and $\theta(rt)$ move in the direction of R_β. When the external input traces $P_\lambda^{[\beta,\Delta]}$ towards the origin, $e(rt)$ and $\theta(rt)$ move in the direction of $\tilde{R}_\beta$. Thus, the moving stable

equilibrium $e(rt)$ is *forward threshold unstable* on $P_\lambda^{[\beta,\Delta]}$ if $\Lambda(rt)$ increases from 0 to $\Delta > \tilde{R}_\beta$, or if $\Lambda(rt)$ decreases from $\Delta > R_\beta$ to 0; see Def. 3.3.2.

4.4.1 Monotone bi-asymptotically constant input

Combining (4.4), (4.7) with $\alpha = 1$, and (4.20) gives the compactified canonical example III with monotone external input:

$$\begin{aligned} \epsilon\dot{x_1} &= -\Big(x_2 - \Lambda(s)\sin\beta\Big) - \Big(x_1 - \Lambda(s)\cos\beta\Big) + \frac{1}{3}\Big(x_1 - \Lambda(s)\cos\beta\Big)^3, \\ \dot{x_2} &= -\mu + x_1 - \Lambda(s)\cos\beta, \\ \dot{s} &= \frac{r}{2}(1 - s^2), \end{aligned} \tag{4.21}$$

where

$$\Lambda(s) = \frac{\Delta}{2}\frac{(1+s)^2}{1+s^2}. \tag{4.22}$$

The choice of the compactification parameter α satisfies the compactification condition $0 < \alpha \leq 2$, and ensures that invariant subspaces $\{s = \pm 1\}$ have an orthogonal transverse eigenvector.

The different dynamics of system (4.21) are summarised in Fig. 4.8, which shows the (Δ, r) tipping diagram together with selected (x_1, x_2, s) phase portraits for $\epsilon = 0.5$, $\mu = 0.85$, $\Delta = 1.5$, different rates r, and $\beta = 0$ so that $e(rt)$ moves along the positive x_1 axis. The invariant subspace $\{s = -1\}$ contains the saddle $\tilde{e}^-$, which is stable within the subspace and unstable in the transverse s-direction, and the repelling limit cycle $\tilde{\eta}^-$. The invariant subspace $\{s = 1\}$ contains the stable equilibrium $\tilde{e}^+$, and the saddle limit cycle $\tilde{\eta}^+$ which is the *R-tipping edge state*. The *R-tipping threshold* is the basin boundary of $\tilde{e}^+$ given by the (blue) two-dimensional stable invariant manifold $W^{s,[r,\Delta]}(\tilde{\eta}^+)$ whose tubular shape depends on Δ and r.

If r is sufficiently small, the unstable manifold $W^{u,[r,\Delta]}(\tilde{e}^-)$ tracks the moving stable equilibrium $e(rt)$ and accumulates on $\tilde{e}^+$, meaning that there is an open half-ball of initial states centred at $\tilde{e}^-$, all of which evolve on the 'inner' side the R-tipping threshold and track the moving stable equilibrium $e(rt)$ [Fig. 4.8(b)]. As r is increased, there is a critical value r_c such that $W^{u,[r_c,\Delta]}(\tilde{e}^-)$ no longer accumulates on $\tilde{e}^+$ [Fig. 4.8(c)]. Rather, there is an $\tilde{e}^-$-to-$\tilde{\eta}^+$ (point to periodic orbit) heteroclinic connection, given by the intersecting invariant manifolds

$$W^{u,[r_c,\Delta]}(\tilde{e}^-) \cap W^{s,[r_c,\Delta]}(\tilde{\eta}^+).$$

Now, any open half-ball centred at $\tilde{e}^-$, however small, contains initial states

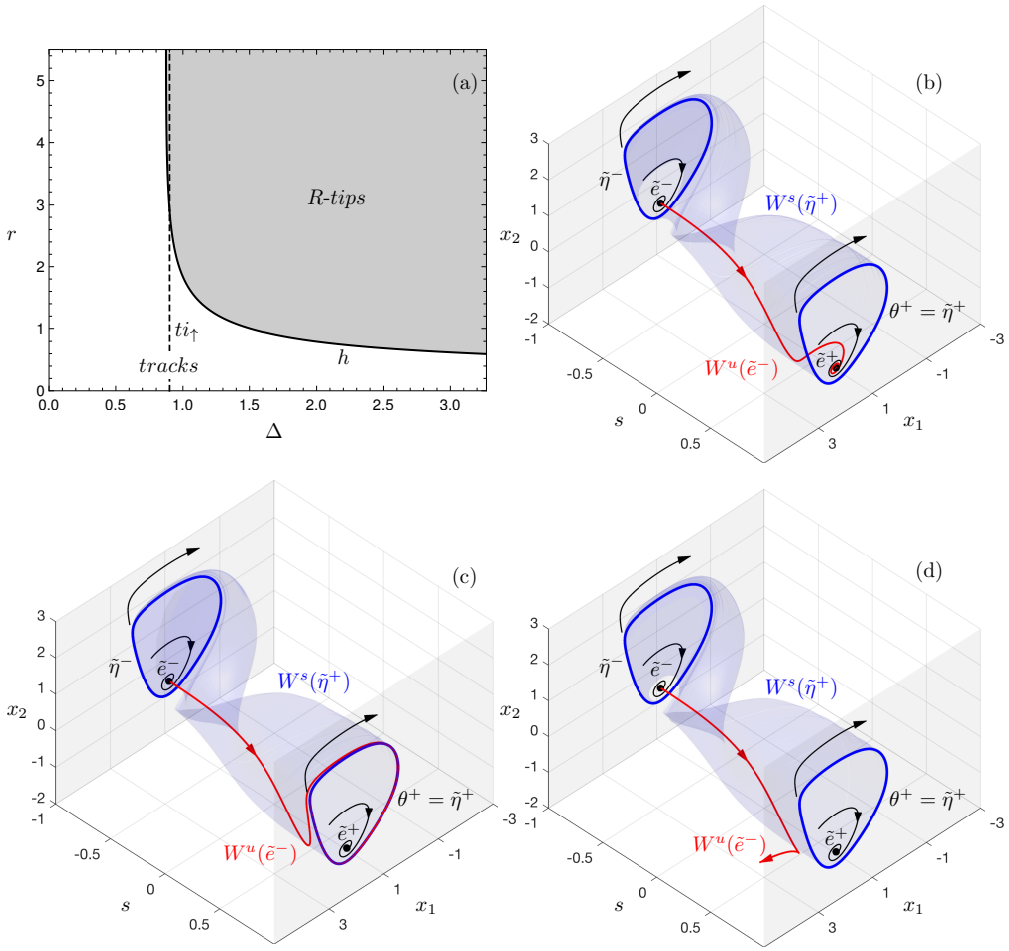

Figure 4.8: (a) The (Δ, r) tipping diagram for canonical example (4.20) with monotone external input (4.2) contains regions of (white) tracking the moving stable equilibrium $e(rt)$ and (grey) irreversible R-tipping from e to infinity. The (dashed) $ti_\uparrow$ line denotes the forward threshold instability boundary for e. (b)-(d) Phase portraits of the compactified system (4.21) for $\epsilon = 0.5$, $\mu = 0.85$, $\beta = 0$, $\Delta = 1.5$, and different 'rates' $r =$ (b) 0.90, (c) 0.99724339228, and (d) 1.10. (c) The heteroclinic $\tilde{e}^-$-to-$\tilde{\eta}^+$ connection for $r = r_c$ defines the tracking-tipping transition.

that converge to $\tilde{e}^+$ as well as initial states that diverge to infinity. The heteroclinic connection gives a computable condition for irreversible R-tipping that is continued in the space of the input parameters by implementing the Lin's method [109, 112] in the continuation software AUTO [110]. The result of numerical continuation in r and Δ is a tracking-tipping transition curve h in the (Δ, r) tipping diagram in Fig. 4.8(a). The curve separates the regions of (white) tracking $e(rt)$ and (grey) irreversible e-to-infinity R-tipping. This is evidenced by analysis of phase portraits for $r > r_c$, where $W^{u,[r,\Delta]}(\tilde{e}^-)$ diverges to infinity, meaning that all initial states from a sufficiently small open half-ball centred at $\tilde{e}^-$ evolve on the 'outer' side of the threshold and go off to infinity [Fig. 4.8(d)]. Note that the tracking-tipping transition curve h intersects the forward threshold

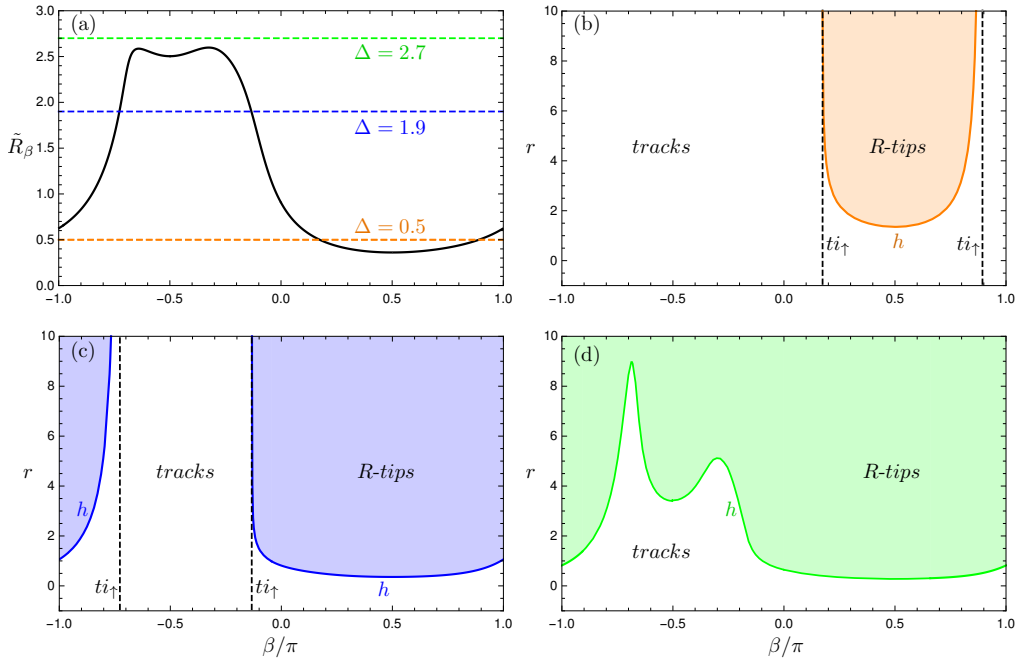

Figure 4.9: (a) The relation between $\tilde{R}_\beta$ and three fixed Δ respectively 0.5 in orange, 1.9 in blue, and 2.7 in green for all of $\beta \in [-\pi, \pi]$. (b)-(d) The (β, r) tipping diagrams for canonical example (4.20) with monotone external input (4.2), contain regions of (white) tracking the moving stable equilibrium $e(rt)$ and (shadowed) irreversible R-tipping for respectively $\Delta =$ (b) 0.5, (c) 1.9, and (d) 2.7. The (dashed) $ti_\uparrow$ lines denote the forward threshold instability boundaries for e.

instability boundary $ti_\uparrow$ and extends to the parameter region where the moving equilibrium $e(rt)$ is forward threshold stable.

Since λ is two-dimensional, the full tipping diagram 'lives' in the three-dimensional (Δ, r, β) space of the input parameters. One can view Fig. 4.8(a) as a two-dimensional (Δ, r) section defined by fixing the path angle $\beta = 0$. To give a more complete picture of the full tipping diagram, we obtain tracking-tipping transition curves h in two-dimensional (β, r) sections defined by fixing the shift amplitude $\Delta = 0.5, 1.9$ and 2.7 [Fig. 4.9 (b)-(d)]. The (forward) threshold instability boundaries $t_\uparrow$ for $e(rt)$ correspond to the intersection points between the (black) curve of $\tilde{R}_\beta$ and the (colour) horizontal lines of fixed Δ shown in Fig. 4.9 (a). Depending on Δ, the forward basin instability condition $\Delta > \tilde{R}_\beta$ is satisfied within different β-intervals. The ensuing region of R-tipping changes accordingly. For example, the narrow interval of forward threshold instability and the ensuing R-tipping region lie between the two $ti_\uparrow$ lines for $\Delta = 0.5$ [Fig. 4.9 (b)], expand noticeably for $\Delta = 1.9$ [Fig. 4.9 (c)], develop a disconnected component for $\Delta \approx 2.5$ [not shown], and cover the entire β-interval for $\Delta = 2.7$ [Fig. 4.9 (d)].

4.4.2 Non-monotone bi-asymptotically constant input

Combining (4.4), (4.9) with $\alpha = 0.5$, and (4.20) gives the compactified canonical example III with non-monotone external input:

$$\begin{aligned} \epsilon\dot{x_1} &= -\Big(x_2 - \Lambda(s)\sin\theta\Big) - \Big(x_1 - \Lambda(s)\cos\theta\Big) + \frac{1}{3}\Big(x_1 - \Lambda(s)\cos\theta\Big)^3, \\ \dot{x_2} &= -\mu + \Big(x_1 - \Lambda(s)\cos\theta\Big), \\ \dot{s} &= \frac{r}{4}(1-s^2), \end{aligned} \tag{4.23}$$

where

$$\Lambda(s) = \frac{\Delta(1-s^2)^2}{1+6s^2+s^4}. \tag{4.24}$$

The choice of the compactification parameter α satisfies the compactification condition $0 < \alpha \leq 1$ and ensures that invariant subspaces $\{s = \pm 1\}$ have an orthogonal transverse eigenvector.

The dynamics of system (4.23) are summarised in Fig. 4.10, which shows selected (x_1, x_2, s) phase portraits for $\epsilon = 0.5$, $\mu = 0.85$, $\beta = 0$, $\Delta = 1.5$, and different rates r, together with the (Δ, r) section of the full tipping diagram. To start with, phase portraits (b)–(d) in Fig. 4.10 show a very similar scenario to the monotone input from Fig. 4.8. When r is sufficiently small, the unstable manifold $W^{u,[r,\Delta]}(\tilde{e}^-)$ closely approximates the moving stable equilibrium $e(rt)$, while the tubular *R-tipping threshold* $W^{s,[r,\Delta]}(\tilde{\eta}^+)$ closely approximates the moving threshold/edge state $\theta(rt) = \eta(rt)$ [Fig. 4.10(b)]. When r reaches a critical rate r_{c1}, there is a heteroclinic $\tilde{e}^-$-to-$\tilde{\eta}^+$ connection that indicates a critical transition from tracking to irreversible R-tipping [Fig. 4.10(c)]. There the similarity ends. In contrast to the monotone external input, the curve h of tracking-tipping transition in the (Δ, r) section of the full tipping diagram is folded so that there can be up to two different critical rates for the same shift magnitude Δ. The (grey) region of irreversible R-tipping is now tongue-shaped. As r is increased just above the first critical rate r_{c1}, $W^{u,[r,\Delta]}(\tilde{e}_1^-)$ diverges to infinity, meaning that there is an open half-ball of initial states centred at $\tilde{e}^-$, all of which evolve on the 'outer' side of the threshold and diverge [Fig. 4.10(d)]. However, for even higher r, there is another heteroclinic connection from $\tilde{e}^-$ to $\tilde{\eta}^+$ [Fig. 4.10(e)]. This indicates another critical transition that brings the system from irreversible R-tipping back to tracking $e(rt)$. Indeed, for $r > r_{c2}$, $W^{u,[r,\Delta]}(\tilde{e}^-)$ accumulates on $\tilde{e}^+$ again, meaning that there is an open half-ball of initial states centred at $\tilde{e}^-$, all of which evolve on the 'inner' side of the R-tipping threshold and track the moving stable equilibrium $e(rt)$ [Fig. 4.10(f)].

In the (Δ, r) section of the full tipping diagram in Fig. 4.10(a) there are two

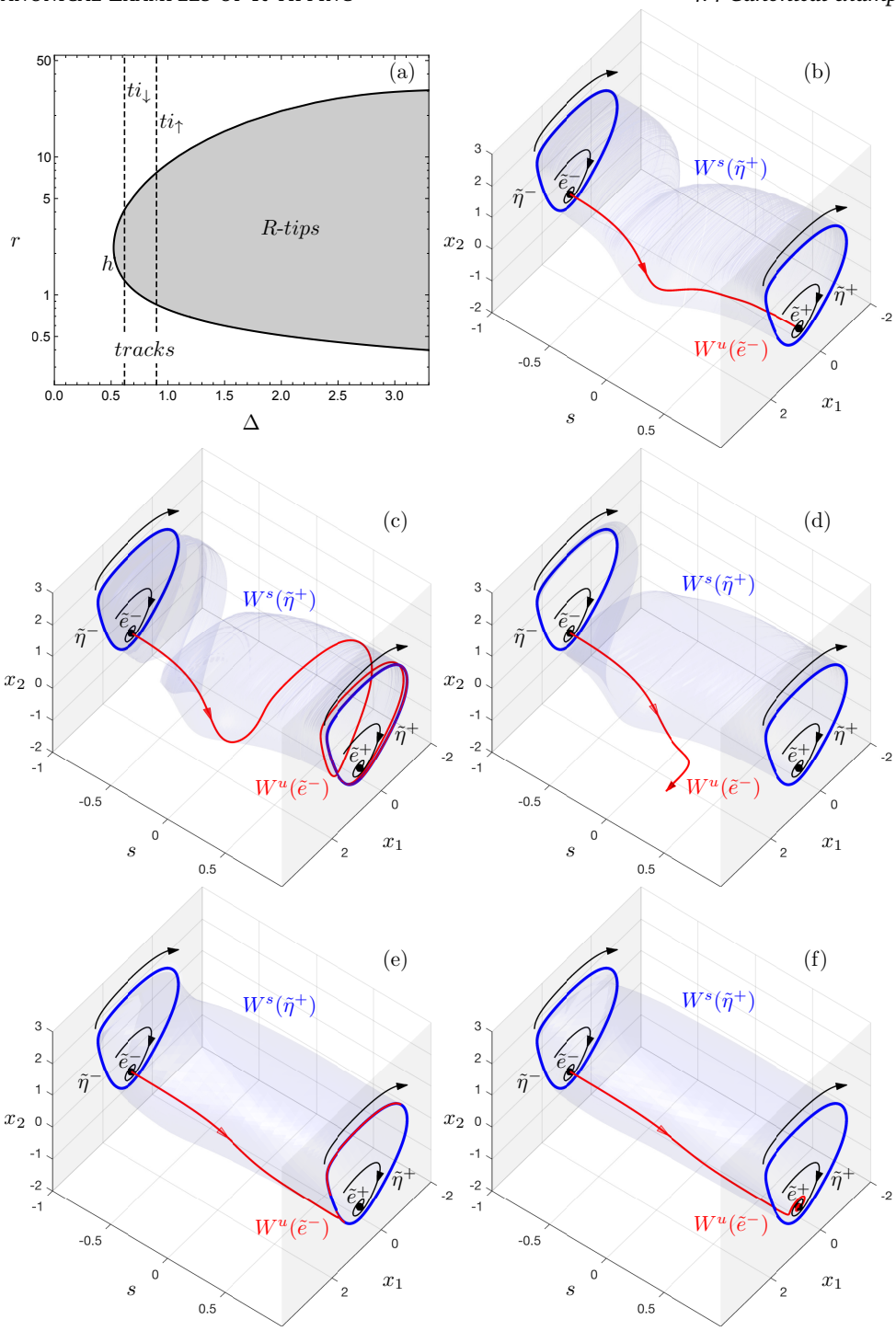

Figure 4.10: (a) The (Δ, r) tipping diagram for canonical example (4.20) with non-monotone external input (4.3). (b)-(f) Phase portraits of the compactified system (4.23) for $\epsilon = 0.5$, $a = 0.85$, $\beta = 0$, $\Delta = 1.5$, and different 'rates' $r =$ (b) 0.35, (c) 0.7829302654, (d) 2.00, (e) 8.957814844199484, and (f) 15.00. (c) and (e) Heteroclinic $\tilde{e}^-$-to-$\tilde{\eta}^+$ connections for respectively $r = r_{c1}$ and $r = r_{c2}$, indicate the transitions of R-tipping. The (dashed) $ti_\uparrow$ and $ti_\downarrow$ lines denote the forward threshold instability boundaries for e as $\Lambda(rt)$ respectively increases and decreases.

forward threshold instability boundaries for $e(rt)$: $ti_\downarrow$ and $ti_\uparrow$. The $ti_\downarrow$ line given

by $\Delta = R_0$ is the forward threshold instability boundary for decreasing $\Lambda(rt)$, whereas the $ti_\uparrow$ line given by $\Delta = \tilde{R}_0$ is the forward threshold instability boundary for increasing $\Lambda(rt)$. Note that the tracking-tipping transition curve h intersects both boundaries and extends to the parameter region where $\Delta < R_0 < \tilde{R}_0$ and $e(\lambda)$ is threshold stable (basin stable).

4.4.3 Highlights of canonical example III

There are two notable differences between canonical examples I and III. The first difference is that R-tipping in canonical example III is given by a heteroclinic equilibrium-to-periodic-orbit connection. The second difference is that the tracking-tipping transition curves h in example III intersect (forward) threshold instability boundaries, giving rise to an observable range of the input parameters where the system undergoes R-tipping in the absence of (forward) threshold instability. These numerical findings highlight more general differences between R-tipping in one dimension and R-tipping in higher dimensions [18, 85, 63]:

- In higher dimensions, R-tipping may be given by a heteroclinic connection from an equilibrium to a higher-dimensional compact invariant set.
- In higher dimensions, (forward) threshold stability does not guarantee that R-tipping is avoided for any rate r.
- In higher dimensions, (forward) threshold instability is sufficient but not necessary for R-tipping to occur.

4.5 Canonical example IV

This canonical example:

- Demonstrates reversible R-tipping near a homoclinic bifurcation.
- Demonstrates effects of 'winding' thresholds in higher dimensions.
- Uncovers tipping diagrams with nested regions of multipulse R-tipping.

Consider the following path in the directed graph from Fig. 4.1: higher dimensions $\rightarrow$ single timescale $\rightarrow$ regular thresholds $\rightarrow$ reversible R-tipping, together with the monostable but excitable frozen system in two dimensions [113, 114,

115]:

$$\begin{aligned} \dot{x_1} =& x_2 - \lambda_2, \\ \dot{x_2} =& \mu_1 + \mu_2(x_1 - \lambda_1) + \mu_3(x_1 - \lambda_1)^2 + \\ & (x_1 - \lambda_1)(x_2 - \lambda_2) - (x_2 - \lambda_2) - (x_1 - \lambda_1)^3, \end{aligned} \tag{4.25}$$

where μ_1, μ_2 and μ_3 are the system parameters, and λ_1 and λ_2 are the two components of the external input $\lambda \in \mathbb{R}^2$.

Table 4.1: Notations of different types of bifurcation

Notations	Bifurcation
SN	Saddle-node bifurcation
h	Homoclinic bifurcation
SNh	Saddle-node homoclinic bifurcation
H	Hopf bifurcation
BT	Bogdanov-Takens bifurcation
A	Non-central homoclinic bifurcation

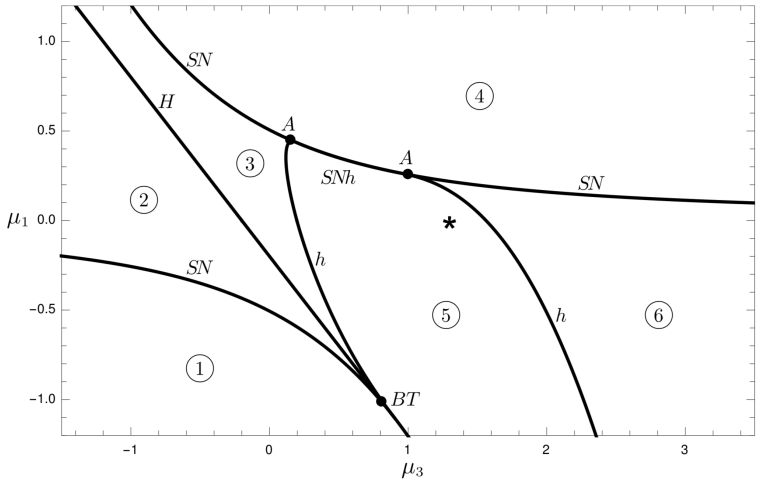

Figure 4.11: Bifurcation digram of system (4.25) in the (μ_1, μ_3) parameter space when $\mu_2 = 1.2$. The asterisk point indicates the selected (μ_1, μ_3) for the canonical example. Shown as Table 4.1, the curve SN indicates a saddle-node bifurcation, h a homoclinic bifurcation, SNh a saddle-node homoclinic bifurcation, with two points marked as A, where the bifurcation respectively starts and ends, H a hopf bifurcation, and the point BT where a Bogdanov-Takens bifurcation happens. These bifurcation curves separate the (μ_1, μ_3) parameter space into six numbered regions, with the corresponding selected phase portraits shown in Fig. 4.12.

The bifurcation diagram in Fig. 4.11 gives an overview of the dynamics of the frozen system (4.25) in the (μ_1, μ_3) parameter plane for fixed $\mu_2 = 1.2$ and $\lambda_1 = \lambda_2 = 0$. The bifurcation curves separate the (μ_1, μ_3) parameter plane into six regions with qualitatively different phase portraits shown in Fig. 4.12. For the notation of different bifurcation types, we refer to Table 4.1. We are interested in reversible R-tipping and focus our attention on the phase portrait in region 5

obtained for $\mu_1 = 0$ and $\mu_3 = 1.3$ [the asterisk in Fig. 4.11]. The phase portrait consists of one stable equilibrium $e_1(\lambda)$, an edge state $\eta(\lambda)$ which is the saddle equilibrium, a regular threshold $\theta(\lambda)$ which is the stable invariant manifold of the saddle, and a source $e_2(\lambda)$. The threshold $\theta(\lambda)$ is a basin boundary of one attractor, or an excitability threshold. The frozen system has two new properties that are of relevance to R-tipping. Firstly, for the parameter settings in region 5, the system exhibits excitability near a homoclinic bifurcation [116]. When disturbed from the stable equilibrium $e_1(\lambda)$ the system typically returns to $e_1(\lambda)$, but the response depends strongly on the disturbance: a disturbance from $e_1(\lambda)$ that does not cross the threshold $\theta(\lambda)$ results in a 'small' and linear response, whereas a disturbance from $e_1(\lambda)$ past $\theta(\lambda)$ results in a noticeably larger response. This is the key ingredient of reversible R-tipping. Secondly, the threshold $\theta(\lambda)$ winds around the stable equilibrium $e_1(\lambda)$ several times, meaning that a single disturbance may cross the threshold more than once. This opens up the possibility of different forms of reversible R-tipping depending on the number of crossings through $\theta(\lambda)$ [117].

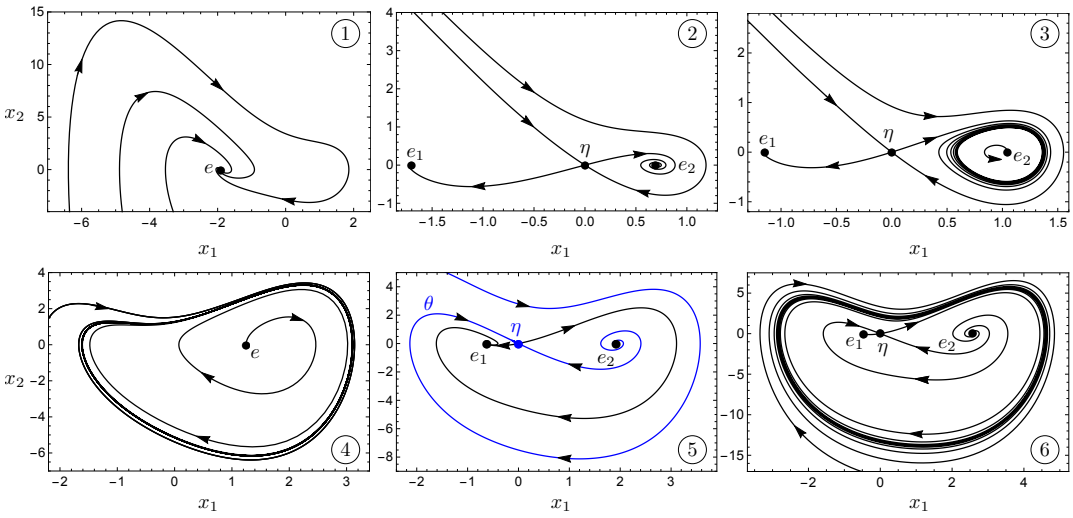

Figure 4.12: Selected phase portraits of system (4.25) in the corresponding six numbered regions shown in Fig. 4.11 when $\mu_2 = 1.2$, and the parameters $(\mu_1, \mu_3) =$ (1) $(-1.0, -1.0)$, (2) $(0, -1.0)$, (3) $(0, -0.1)$, (4) $(2.0, 0.5)$, (5) $(0, 1.3)$, (6) $(0, 2.1)$, where the black dots are equilibrium points, the thick black curves are limit cycles, and the curves with the arrows indicate the dynamics.

Similarly to canonical example III, we represent the external input λ in the polar coordinates (4.18) and consider *parameter paths* (4.19) that are straight half-lines from the origin of the λ plane, parametrised by the magnitude $\Delta > 0$ and the angle β. Associated with a path $P_\lambda^{[\beta,\Delta]}$ in the parameter plane, there are *threshold radii* in the phase plane. The simple limit-cycle threshold in Fig. 4.6 has only two threshold radii. In contrast, the winding threshold in phase portrait 5

in Fig. 4.12 has several threshold radii. We denote them as $0 < R^I_\beta < R^{II}_\beta < \ldots$, and $0 < \tilde{R}^I_\beta < \tilde{R}^{II}_\beta < \ldots$. Let

$$\lambda^I_\beta = (R^I_\beta \cos\beta, R^I_\beta \sin\beta) \text{ and } \tilde{\lambda}^I_\beta = (\tilde{R}^I_\beta \cos\beta, \tilde{R}^I_\beta \sin\beta),$$

and consider positions of $e_1(\lambda)$ and $\theta(\lambda)$ for different values of λ along a path $P^{[\beta,\Delta]}_\lambda$. If $\Delta > \tilde{R}^I_\beta$, then $e_1(0) \in \theta(\tilde{\lambda}^I_\beta)$ and $e_1(0)$ lies on different sides of $\theta(\lambda)$ for λ arbitrarily close to $\tilde{\lambda}^I_\beta$. If $\Delta > R^I_\beta$, then $e_1(\lambda^I_\beta) \in \theta(0)$ and $e_1(\lambda)$ lies on different sides of $\theta(0)$ for λ arbitrarily close to λ^I_β. Thus, $e_1(\lambda)$ is *threshold unstable* (but not basin unstable) on $P^{[\beta,\Delta]}_\lambda$ if

$$\Delta > \min\{R^I_\beta, \tilde{R}^I_\beta\}.$$

Figure 4.13 shows multiple threshold radii $\tilde{R}_\beta$ whose number and magnitude depend strongly on β. For example, for $\beta = -\pi/2$, there are two radii $\tilde{R}^I_{-\pi/2}$ and $\tilde{R}^{II}_{-\pi/2}$ within the range shown in the figure [red dots in Fig. 4.13]. Crossing of different threshold parts is illustrated in Fig. 4.14 for the param-

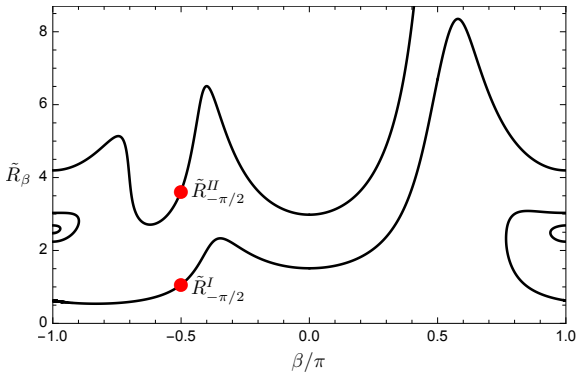

Figure 4.13: The opposite threshold radius $\tilde{R}$ for different fixed values of $\beta \in [-\pi, \pi]$ of system (4.25), with the consideration of input parameter λ (4.18) and parameter paths $P^{[\beta,\Delta]}_\lambda$ (4.19). The two red dots indicate the corresponding first two (the two smallest) $\tilde{R}_\beta$ when $\beta = -\pi/2$, denoted respectively $\tilde{R}^I_{-\pi/2}$ and $\tilde{R}^{II}_{-\pi/2}$. Note that there are larger values of $\tilde{R}_\beta$ for each β which we do not show in the figure.

eter path $P^{[-\pi/2,\Delta]}_\lambda$. If $\Delta > \tilde{R}^I_{-\pi/2}$, then $e_1(\lambda)$ is threshold unstable on $P^{[-\pi/2,\Delta]}_\lambda$ because $e_1(0) \in \theta(\tilde{\lambda}^I_{-\pi/2})$ and $e_1(0)$ lies on different sides of $\theta(\lambda)$ for λ arbitrarily close to $\tilde{\lambda}^I_{-\pi/2}$ [Fig. 4.14(a)–(c)]. For larger shift magnitudes Δ, there will be subsequent crossings. For example, let $\tilde{\lambda}^{II}_{-\pi/2} = (0, -\tilde{R}^{II}_{-\pi/2})$ and notice that $e_1(0) \in \theta(\tilde{\lambda}^{II}_{-\pi/2})$ and $e_1(0)$ lies on different sides of $\theta(\lambda)$ for λ arbitrarily close to $\tilde{\lambda}^{II}_{-\pi/2}$ [Fig. 4.14(c)–(e)].

We now analyse reversible R-tipping from $e_1(rt)$ in the nonautonomous **canon-**

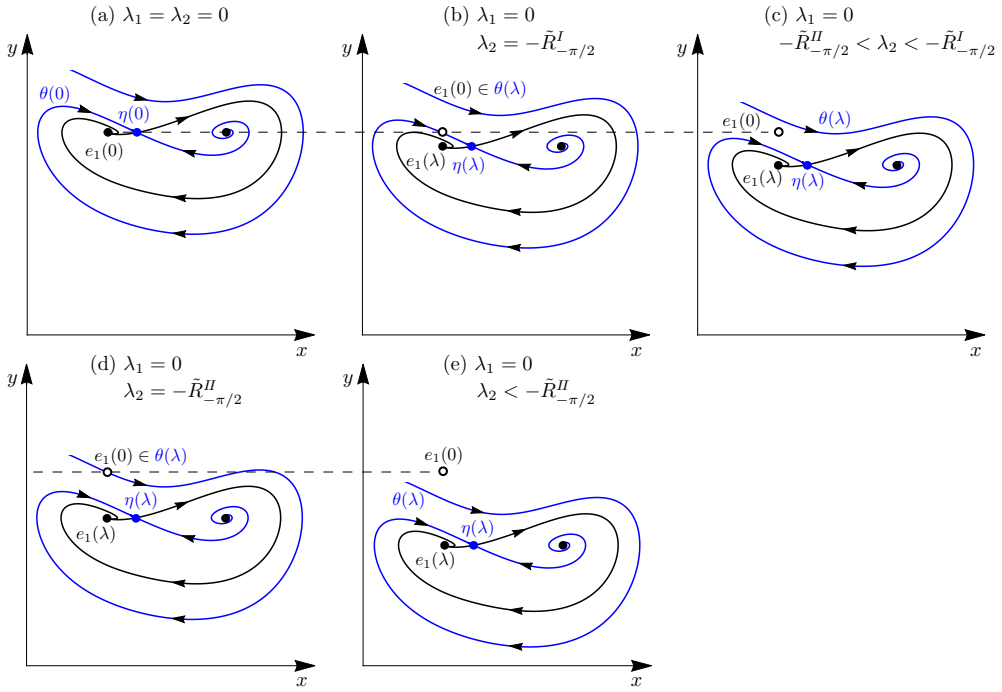

Figure 4.14: Phase portraits of the autonomous canonical example IV (4.25) for $\lambda_1 = 0$ and different values of (a) $\lambda_2 = 0$, (b) $\lambda_2 = -\tilde{R}^I_\beta$, (c) $-\tilde{R}^{II}_\beta < \lambda_2 < -\tilde{R}^I_\beta$, (d) $\lambda_2 = -\tilde{R}^{II}_\beta$ and (e) $\lambda_2 < -\tilde{R}^{II}_\beta$, depict threshold instability of the stable equilibrium e_1 on $P^{[-\pi/2,\Delta]}_\lambda$ when $\Delta > \tilde{R}^I_\beta$.

ical example IV:

$$\begin{aligned}\dot{x_1} =& x_2 - \Lambda(rt)\sin\beta,\\ \dot{x_2} =& \mu_1 + \mu_2\left(x_1 - \Lambda(rt)\cos\beta\right) + \mu_3(x_1 - \Lambda(rt)\cos\beta)^2 + \\ & (x_1 - \Lambda(rt)\cos\beta)\left(x_2 - \Lambda(rt)\sin\beta\right) - (x_2 - \Lambda(rt)\sin\beta) - (x_1 - \Lambda(rt)\cos\beta)^3.\end{aligned} \tag{4.26}$$

parametrised by μ_1, μ_2 and μ_3, the magnitude Δ and rate r of the parameter shift, and the angle β that fixes the orientation of the parameter path in the λ plane. When the external input traces $P^{[\beta,\Delta]}_\lambda$ away from the origin of the λ plane, $e_1(rt)$ and $\theta(rt)$ move in the direction of R_β. When the external input traces a path $P^{[\beta,\Delta]}_\lambda$ towards the origin, $e_1(rt)$ and $\theta(rt)$ move in the direction of $\tilde{R}_\beta$. Thus, the moving stable equilibrium $e_1(rt)$ is *forward threshold unstable* on $P^{[\beta,\Delta]}_\lambda$ if $\Lambda(rt)$ increases from 0 to $\Delta > \tilde{R}^I_\beta$, or if $\Lambda(rt)$ decreases from $\Delta > R^I_\beta$ to 0; see Def. 3.3.2.

4.5.1 Monotone bi-asymptotically constant input

Combining (4.4), (4.7) with $\alpha = 1/1.3$, $1/4$ or $1/6.5$, and (4.26) gives the compactified canonical example IV with monotone external input:

$$\begin{aligned}
\dot{x_1} =& x_2 - \Lambda(s)\sin\beta, \\
\dot{x_2} =& \mu_1 + \mu_2\left(x_1 - \Lambda(s)\cos\beta\right) + \mu_3(x_1 - \Lambda(s)\cos\beta)^2 + \\
& \left(x_1 - \Lambda(s)\cos\beta\right)\left(x_2 - \Lambda(s)\sin\beta\right) - \left(x_2 - \Lambda(s)\sin\beta\right) - \left(x_1 - \Lambda(s)\cos\beta\right)^3, \\
\dot{s} =& \frac{\alpha r}{2}(1 - s^2),
\end{aligned} \tag{4.27}$$

where

$$\Lambda(s) = \frac{\Delta(1+s)^{2/\alpha}}{(1-s)^{2/\alpha} + (1+s)^{2/\alpha}}. \tag{4.28}$$

All choices of the compactification parameter α satisfy the compactification condition $0 < \alpha \leq 2$, ensure that invariant subspaces $\{s = \pm 1\}$ have an orthogonal transverse eigenvector, and 'place' interesting dynamics sufficiently away from the invariant subspaces to facilitate visualisation of the R-tipping phenomena.

The different dynamics of system (4.27) are summarised in Fig. 4.15, which shows the (Δ, r) tipping diagram together with selected (x_1, x_2, s) phase portraits for $\mu_1 = 0$, $\mu_2 = 1.2$, $\mu_3 = 1.3$, $\alpha = 1/1.3$, $\Delta = 3.5$ so that $\tilde{R}^I_{-\pi/2} < \Delta < \tilde{R}^{II}_{-\pi/2}$, different rates r, and $\beta = -\frac{\pi}{2}$ so that $e_1(rt)$ moves along the negative x_2 axis. The invariant subspace $\{s = -1\}$ contains the saddle $\tilde{e}_1^-$ which is stable within the subspace and unstable in the transverse s-direction. Additionally, there are saddle $\tilde{\eta}^-$ and source $\tilde{e}_2^-$ which are not important for R-tipping. The invariant subspace $\{s = 1\}$ contains the only stable equilibrium $\tilde{e}_1^+$ and the saddle equilibrium $\tilde{\eta}^+$ which is the *R-tipping edge state*. The *R-tipping threshold* forms the basin boundary of the only attractor $\tilde{e}_1^+$, and is given by the (blue) two-dimensional stable invariant manifold $W^{s,[r,\Delta]}(\tilde{\eta}^+)$ whose shape depends on Δ and r.

If r is sufficiently small, the unstable manifold $W^{u,[r,\Delta]}(\tilde{e}_1^-)$ closely tracks the moving stable equilibrium $e_1(rt)$ and accumulates on $\tilde{e}_1^+$. In other words, there is an open half-ball of initial states centred at $\tilde{e}_1^-$, all of which track the moving stable equilibrium $e_1(rt)$ and evolve 'below' the R-tipping threshold as they converge to $\tilde{e}_1^+$ [Fig. 4.15(b)]. As r is increased, there is a critical value r_c^I such that $W^{u,[r_c^I,\Delta]}(\tilde{e}_1^-)$ does not accumulate on $\tilde{e}_1^+$ [Fig. 4.15(c)]. Rather, there is a heteroclinic connection from $\tilde{e}_1^-$ to $\tilde{\eta}^+$ given by the intersecting invariant manifolds

$$W^{u,[r_c^I,\Delta]}(\tilde{e}_1^-) \cap W^{s,[r_c^I,\Delta]}(\tilde{\eta}^+).$$

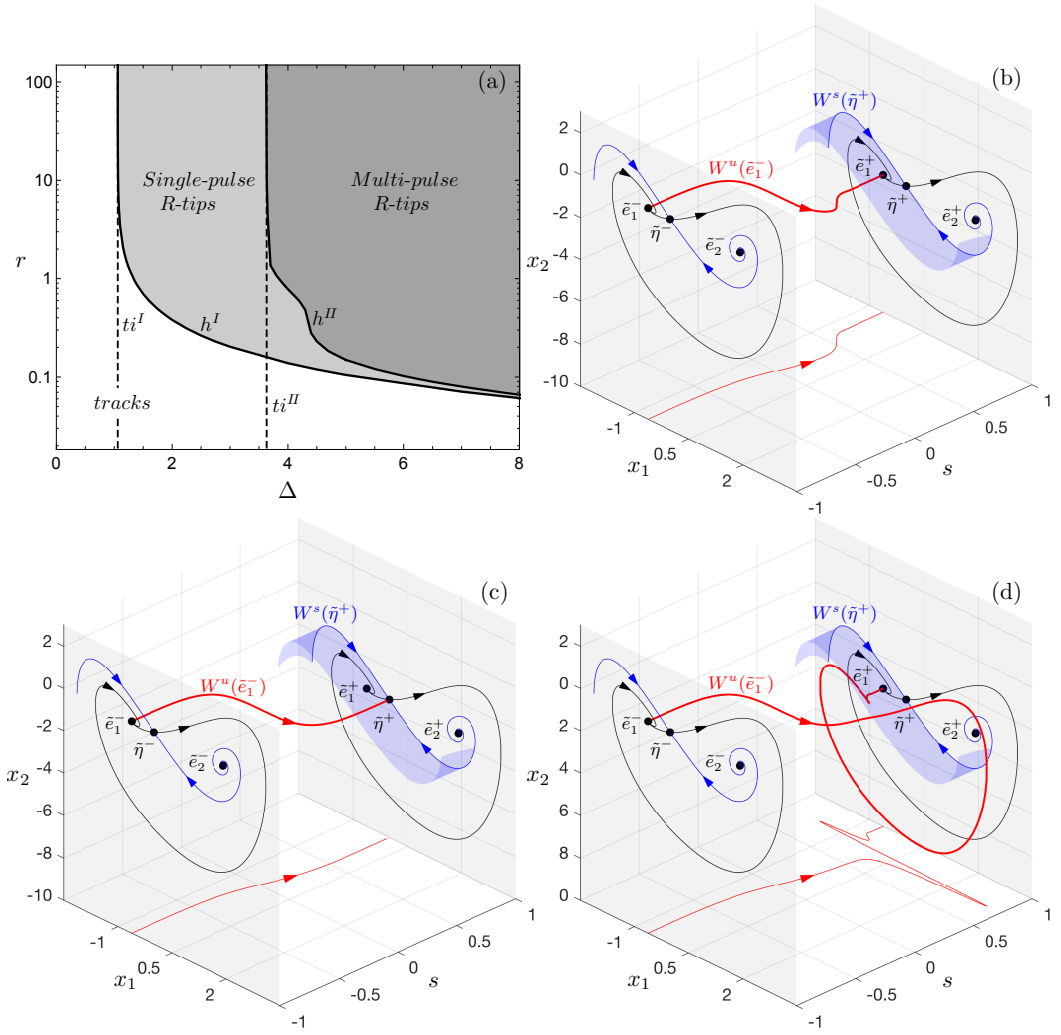

Figure 4.15: (a) The (Δ, r) tipping diagram for canonical example (4.26) with monotone external input (4.2), contains regions of (white) tracking the moving stable equilibrium $e_1(rt)$ 'closely' enough, (light grey) single-pulse reversible R-tipping from e_1, and (dark grey) multipulse reversible R-tipping from e_1. The (dashed) ti^I and ti^{II} lines denote the forward threshold instability boundaries respectively at $\Delta = \tilde{R}^I_{-\pi/2}$ and $\tilde{R}^{II}_{-\pi/2}$ for e_1. (b)-(d) Phase portraits of the compactified system (4.27) for $\mu_1 = 0$, $\mu_2 = 1.2$, $\mu_3 = 1.3$, $\Delta = 3.5$, $\beta = -\frac{\pi}{2}$, $\alpha = 1/1.3$ and different 'rates' $r =$ (b) 0.163, (c) $0.16397393602402347834 16$, and (d) 0.164. (c) The heteroclinic $\tilde{e}_1^-$-to-$\tilde{\eta}^+$ connection for $r = r_c^I$ defines the transition between tracking and single-pulse reversible R-tipping. For clarity, the Δ- and r-dependent invariant manifolds $W^{u,[r,\Delta]}(\tilde{e}_1^-)$ and $W^{s,[r,\Delta]}(\tilde{\eta}^+)$ are respectively labeled as $W^u(\tilde{e}_1^-)$ and $W^s(\tilde{\eta}^+)$.

Now, any open half-ball of initial states centred at $\tilde{e}_1^-$ contains initial states that track $e_1(rt)$ and evolve 'below' the R-tipping threshold as they converge to $\tilde{e}_1^+$, as well as initial states that evolve 'above' the R-tipping threshold and make a large single-pulse excursion in the phase space before they converge to $\tilde{e}_1^+$. In contrast to irreversible R-tipping, asymptotic behaviour for r just below and just above r_c^I is identical. Nonetheless, the heteroclinic connection at $r = r_c^I$ gives a

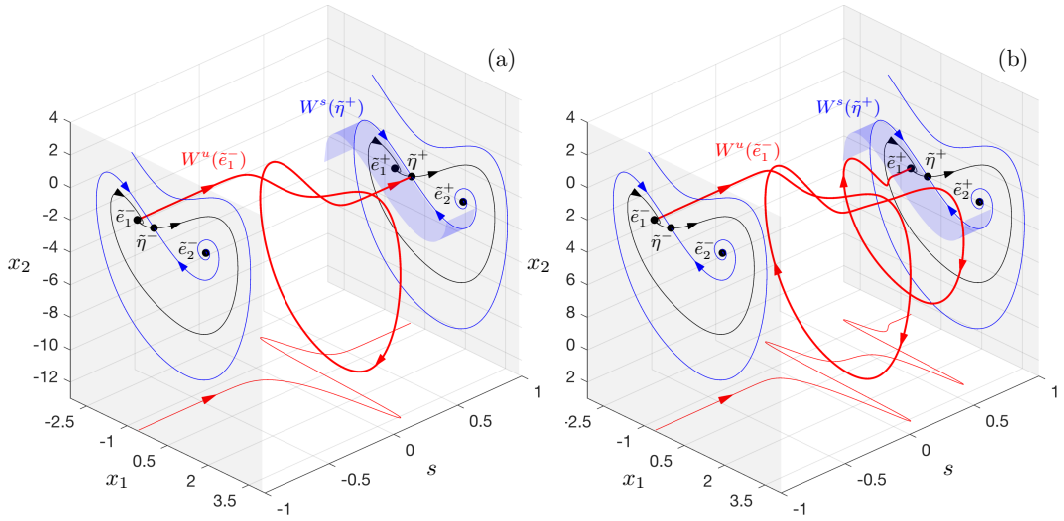

Figure 4.16: (a)-(b) Phase portraits of the compactified system (4.27) for $\mu_1 = 0$, $\mu_2 = 1.2$, $\mu_3 = 1.3$, $\Delta = 4$, $\beta = -\frac{\pi}{2}$ and different 'rates' r (a) $r = 0.7860447608792288654022 6$ with $\alpha = 1/4$, and (b) $r = 0.9$ with $\alpha = 1/6.5$. (a) The heteroclinic $\tilde{e}_1^-$-to-$\tilde{\eta}^+$ connection for $r = r_c^{II}$ defines the transition between single-pulse and multipulse reversible R-tipping.

computable condition for reversible R-tipping that is continued in the plane of the input parameters by a suitably designed shooting method [118] through checking if $W^{u,[r,\Delta]}(\tilde{e}_1^-)$ is on the orthogonal stable s-direction of $\tilde{\eta}^+$ at some fixed distance from $\tilde{\eta}^+$. The result of numerical continuation in Δ and r is a tracking-tipping transition curve h^I in the (Δ, r) tipping diagram that approaches the forward threshold instability boundary ti^I at $\Delta = \tilde{R}^I_{-\pi/2}$ from the right [Fig. 4.15(a)]. The curve separates regions of (white) tracking and (grey) reversible R-tipping from $e_1(rt)$. This is evidenced by analysis of phase portraits for r just above r_c^I, where $W^{u,[r,\Delta]}(\tilde{e}_1^-)$ evolves 'above' the R-tipping threshold and makes a large single-pulse excursion in the phase space before it accumulates on $\tilde{e}_1^+$. Now, there is an open half-ball of initial states centred at $\tilde{e}_1^-$, all of which make a large single-pulse excursion before accumulating on $\tilde{e}_1^+$ [Fig. 4.15(d)]. Another important difference from the previous examples is the whole sequence of heteroclinic curves $h^I, h^{II}, \ldots$ within the R-tipping region.

For example, if the shift amplitude Δ exceeds the second forward threshold instability boundary ti^{II} at $\Delta = \tilde{R}^{II}_{-\pi/2}$, there is another heteroclinic connection when r reaches the second critical rate $r_c^{II} > r_c^I$, given by the intersecting invariant manifolds

$$W^{u,[r_c^{II},\Delta]}(\tilde{e}_1^-) \cap W^{s,[r_c^{II},\Delta]}(\tilde{\eta}^+).$$

This time, the unstable manifold $W^{u,[r_c^{II},\Delta]}(\tilde{e}_1^-)$ makes a large single-pulse excursion in the phase space before it accumulates on $\tilde{\eta}^+$ [Fig. 4.16(a)]. The corresponding curve h^{II} approaches the line ti^{II} from the right, and separates the

regions of single-pulse and double-pulse reversible R-tipping [Fig. 4.15(a)]. This is evidenced by analysis of phase portraits for r just above r_c^{II}, where $W^{u,[r,\Delta]}(\tilde{e}_1^-)$ makes a large double-pulse excursion in the phase space before it accumulates on $\tilde{e}_1^+$ [Fig. 4.16(b)]. Such dynamical behaviour is reminiscent of multipulse excitability reported for instantaneous perturbations near n-homoclinics [119, 120], instantaneous perturbations near folded excitability thresholds [117] and ramped parameters near folded-saddle singularities [24].

4.5.2 Non-monotone bi-asymptotically constant input

Combining (4.4), (4.9) with $\alpha = 1/1.3$ or $1/35$, and (4.26) gives the compactified canonical example IV with non-monotone external input:

$$\begin{aligned}
\dot{x_1} =& x_2 - \Lambda(s)\sin\beta,\\
\dot{x_2} =& \mu_1 + \mu_2\left(x_1 - \Lambda(s)\cos\beta\right) + \mu_3(x_1 - \Lambda(s)\cos\beta)^2 +\\
& \left(x_1 - \Lambda(s)\cos\beta\right)\left(x_2 - \Lambda(s)\sin\beta\right) - \left(x_2 - \Lambda(s)\sin\beta\right) - \left(x_1 - \Lambda(s)\cos\beta\right)^3,\\
\dot{s} =& \frac{\alpha r}{2}(1 - s^2),
\end{aligned} \tag{4.29}$$

where

$$\Lambda(s) = \frac{2\Delta(1-s^2)^{1/\alpha}}{(1-s)^{2/\alpha} + (1+s)^{2/\alpha}}. \tag{4.30}$$

Both choices of the compactification parameter α satisfy the compactification condition $0 < \alpha \leq 1$, ensure that invariant subspaces $\{s = \pm 1\}$ have an orthogonal transverse eigenvector, and 'place' interesting dynamics sufficiently away from the invariant subspaces to facilitate visualisation of the R-tipping phenomena.

The dynamics of system (4.29) are summarised in Fig. 4.17, which shows the (Δ, r) tipping diagram together with examples of (x_1, x_2, s) phase portraits for $\mu_1 = 0$, $\mu_2 = 1.2$, $\mu_3 = 1.3$, $\Delta = 3.5$ so that $\tilde{R}^I_{-\pi/2} < \Delta < \tilde{R}^{II}_{-\pi/2}$, different rates r, and $\beta = -\frac{\pi}{2}$ so that $e_1(rt)$ moves along the negative x_2 axis. The main difference from the monotone input is existence of multiple critical rates associated with each threshold instability boundary ti^N.

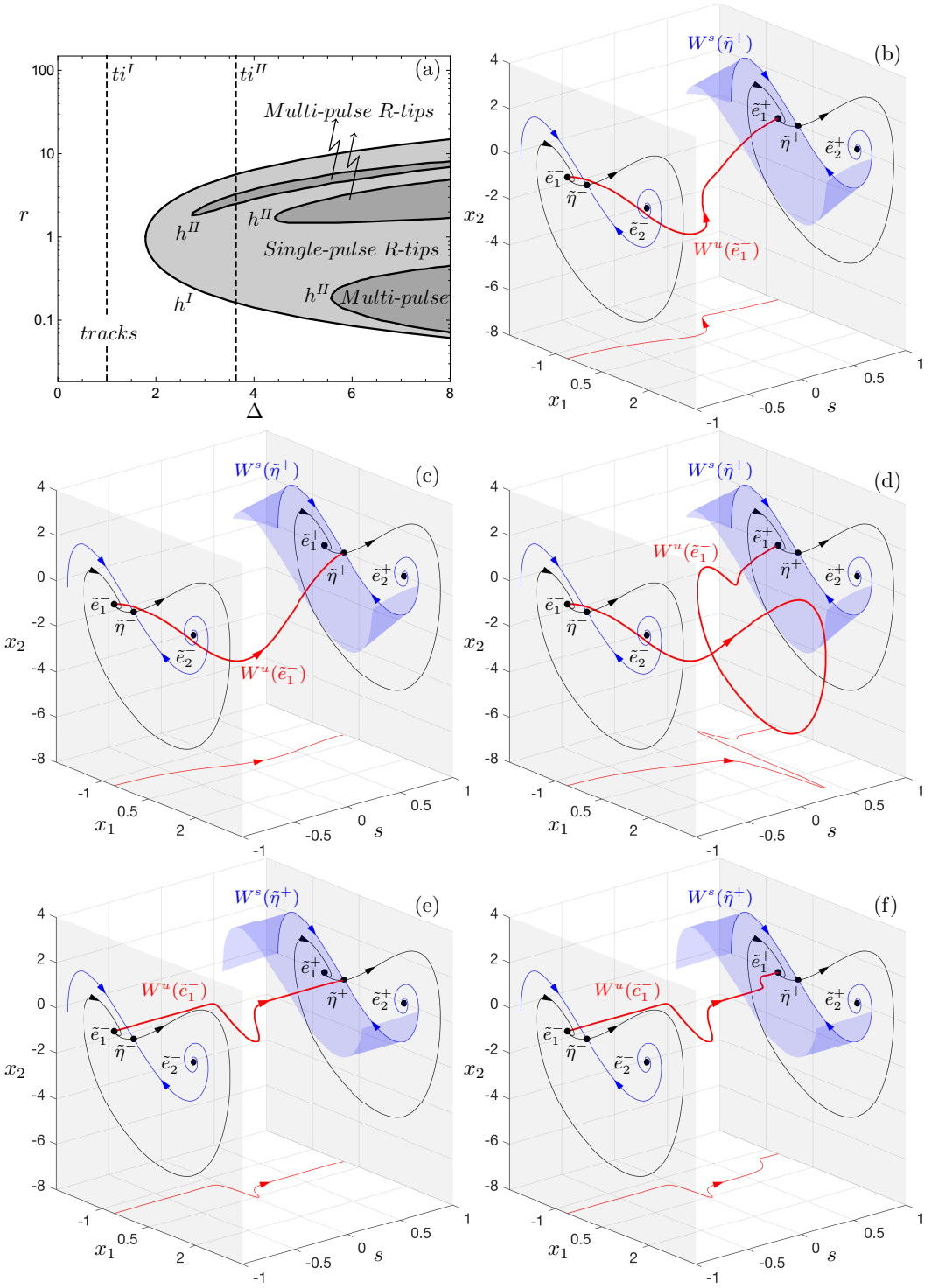

Figure 4.17: (a) The (Δ, r) tipping diagram for canonical example (4.26) with non-monotone external input (4.3). The (dashed) ti^I and ti^{II} lines are the forward threshold instability boundaries for e_1. (b)-(f) Phase portraits of the compactified system (4.29) for $\mu_1 = 0$, $\mu_2 = 1.2$, $\mu_3 = 1.3$, $\Delta = 3.5$, $\beta = -\frac{\pi}{2}$ and different 'rates' $r =$ (b) 0.169, (c) 0.1698655703481079943, (d) 0.170, (e) 5.3636719401204, and (f) 5.364. The heteroclinic $\tilde{e}_1^-$-to-$\tilde{\eta}^+$ connections in panel (c) and panel (e) define the tracking-tipping transitions relevant to transition curve h^I. $\alpha = 1/1.3$ for panel (b)-(d) and $\alpha = 1/35$ for panel (e)-(f).

To start with, the phase portraits (b)–(d) in Fig. 4.17 show a very similar scenario to the monotone input from Fig. 4.15. When r is sufficiently small, the unstable manifold $W^{u,[r,\Delta]}(\tilde{e}_1^-)$ closely approximates the moving stable equilibrium $e_1(rt)$, while the winding *R-tipping threshold* $W^{s,[r,\Delta]}(\tilde{\eta}^+)$ closely approximates the moving threshold $\theta(rt)$ [Fig. 4.17(b)]. When r reaches a critical rate r_{c1}^I, there is a heteroclinic $\tilde{e}_1^-$-to-$\tilde{\eta}^+$ connection that indicates a critical transition from tracking to reversible R-tipping [Fig. 4.17(c)]. There the similarity ends. In contrast to the monotone external input, the curve h^I of tracking-tipping transition in the (Δ, r) tipping diagram is folded. The (grey) region of reversible R-tipping is now tongue-shaped, meaning that there can be up to two different critical rates r_{c1}^I and r_{c2}^I for the same shift magnitude Δ, indicating critical transitions between tracking and reversible R-tipping [Fig. 4.17(d-f)]. Most interestingly, the R-tipping diagram contains new features that are not observed in the other canonical examples. Within the R-tipping tongue h^I, there are nested higher-order R-tipping tongues $h^{II}, h^{III}, \ldots$, which appear for larger shift magnitudes Δ. For example, Fig. 4.17(a) reveals three h^{II} tongues. This means that, as r is increased, the critical transition from tracking to single-pulse reversible R-tipping at $r = r_{c1}^I$ can be followed by up to six critical transitions at $r = r_{c1}^{II}, \ldots, r_{c6}^{II}$ where the system switches back and forth between single-pulse and double-pulse reversible R-tipping. Figure 4.18 illustrates critical transitions at $r = r_{c1}^{II}$ from single-pulse to double-pulse reversible R-tipping [Fig. 4.18(d1-d2)] and then at $r = r_{c2}^{II}$ back to single-pulse reversible R-tipping [Fig. 4.18(d2-d4)] as the rate r is increased across the top h^{II} tongue, which is the only h^{II} tongue for $\Delta = 3.5$. Critical transitions between different multipulse R-tipping are always followed by the critical transition at $r = r_{c2}^I$ from single-pulse reversible R-tipping back to tracking [Fig. 4.17(d-f)]. Interestingly, there is an observable region of double-pulse reversible R-tipping below the second threshold instability boundary ti^{II} at $\Delta = \tilde{R}_{-\pi/2}^{II}$ [the top h^{II} tongue in Fig. 4.17(a)].

What is more, there can be additional critical rates between r_{c1}^I and r_{c2}^I, which correspond to transitions between different multipulse reversible R-tipping due to $h^{III}, h^{IV}, \ldots$ tongues (not shown in the figure).

Finally, we note the presence of small-amplitude pulses at higher r, e.g. in Fig. 4.17(f), that arise gradually, without a heteroclinic bifurcation, as the h^N tongues are approached from above. Here, the rates r are high compared to the natural timescales of the frozen system and, and while a heteroclinic connection gives R-tipping by definition, there is only a small quantitative change in the amplitude of the pulse.

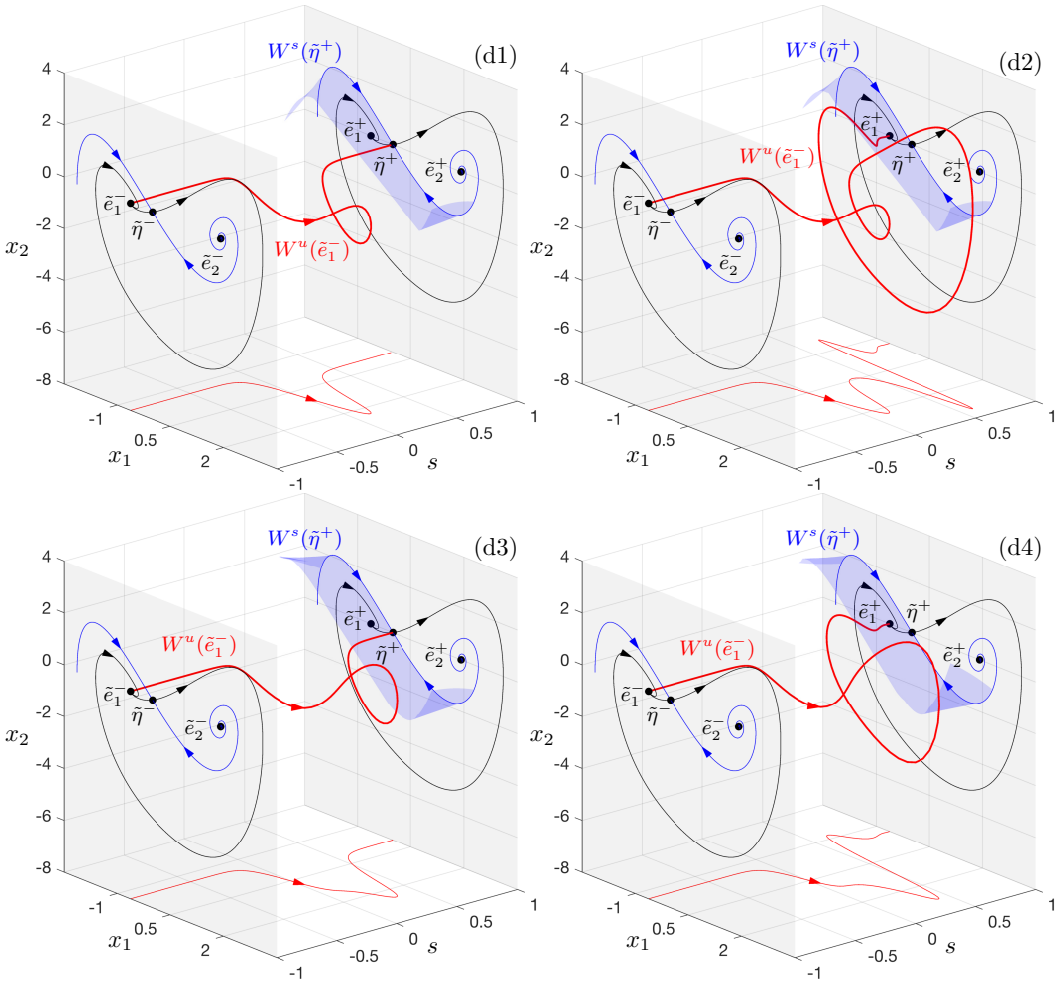

Figure 4.18: Phase portraits of the compactified system (4.29) for $\mu_1 = 0$, $\mu_2 = 1.2$, $\mu_3 = 1.3$, $\Delta = 3.5$, $\beta = -\frac{\pi}{2}$, $\alpha = 1/1.3$ and different 'rates' $r =$ (d1) 2.350195043, (d2) 2.39, (d3) 3.043230003 and (d4) 3.50, which fall between panels (d) and (e) from Fig. 4.17. The heteroclinic $\tilde{e}_1^-$-to-$\tilde{\eta}^+$ connections in panel (d1) and panel (d3) define the transitions between single-pulse and double-pulse reversible R-tipping relevant to transition curve h^{II}. (d1)–(d4) are phase portraits between panel (d) and panel (e) in Fig 4.17, where double-pulse reversible R-tipping happens due to crossing h^{II}.

4.5.3 Highlights of canonical example IV

The most notable difference from canonical examples I–III is the intricate tipping diagram in Fig. 4.17(a) consisting of a nested sequence of reversible multipulse R-tipping tongues. The tongues are bounded by N-heteroclinic connections h^N, where the unstable manifold of saddle $\tilde{e}_1$ makes a large $(N-1)$-pulse excursion in the phase space before converging to saddle $\tilde{\eta}^+$.

These numerical findings highlight some general properties of reversible R-tipping in higher dimensions. Namely, in addition to critical transitions between

tracking and reversible R-tipping, the R-tipping definition 3.2.14 captures critical transitions between different types of reversible R-tipping.

4.6 Canonical example V

According to Definition 3.2.6, a quasithreshold θ_ε requires that the frozen system (1.2) is slow-fast in the sense of the state variables evolving on different timescales, with the time-scale separation quantified by a small parameter $0 < \varepsilon \ll 1$. This means that x needs to be at least two-dimensional.

This canonical example:

- Demonstrates reversible R-tipping due to quasithresholds.
- Identifies singular R-tipping edge-states and singular R-tipping thresholds.
- Reveals different types of R-tipping quasithresholds.

Consider the following path in the directed graph from Fig. 4.1: higher dimensions $\rightarrow$ multiple timescales $\rightarrow$ quasithresholds $\rightarrow$ reversible R-tipping, together with a monostable slow-fast frozen system (3.4)–(3.5) in two dimensions:

$$\begin{aligned} \epsilon\frac{dY}{dt} &= -Y(Y^2-2)+Z+\lambda, \\ \frac{dZ}{dt} &= -Y-1, \end{aligned} \tag{4.31}$$

where $0 < \epsilon \ll 1$ is the small parameter, Y and $Z \in \mathbb{R}$ are the fast and slow components of the vector field, respectively, and $\lambda \in \mathbb{R}$ is the external input. System (4.31) has one equilibrium

$$e(\lambda) = (-1, 1-\lambda), \tag{4.32}$$

that is globally stable. The position of $e(\lambda)$ varies along the Z direction with λ.

The slow subsystem (3.10):

$$\frac{dz}{dt} = -y-1, \tag{4.33}$$

evolves on the one-dimensional critical manifold (3.11):

$$S_0(\lambda) = \{(y,z) \in \mathbb{R}^2 : -y(y^2-2)+z+\lambda = 0\}, \tag{4.34}$$

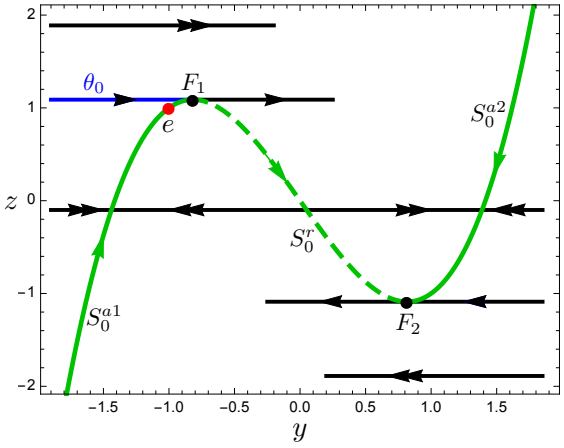

Figure 4.19: Critical manifold S_0 (4.34) colored in green with two (solid) attracting submanifolds S_0^{a1} and S_0^{a2}, and one (dashed) repelling submanifold S_0^r, which are separated by the two folds F_1 and F_2. The singular limit threshold θ_0 is shown in blue. The arrows indicate the dynamics of the fast subsystem (4.36), in particular the faster dynamics marked with double arrows.

with two quadratic fold points

$$\begin{aligned} F_1(\lambda) &= \left\{ (y,z) \in \mathbb{R}^2 : y = -\sqrt{\frac{2}{3}}, z = \frac{4\sqrt{6}}{9} - \lambda \right\}, \\ F_2(\lambda) &= \left\{ (y,z) \in \mathbb{R}^2 : y = \sqrt{\frac{2}{3}}, z = -\frac{4\sqrt{6}}{9} - \lambda \right\}, \end{aligned} \tag{4.35}$$

shown in Fig. 4.19. Alternatively, $S_0(\lambda)$ consists of a union of all equilibria of the fast subsystem (3.12):

$$\frac{dy}{d\tau} = -y(y^2 - 2) + z + \lambda, \tag{4.36}$$

where the slow variable z becomes an additional parameter. Stability analysis of equilibria for the fast subsystem (4.36) reveals that $S_0(\lambda)$ has two attractive submanifolds $S_0^{a1}(\lambda)$ and $S_0^{a2}(\lambda)$ that consist of stable hyperbolic equilibria, and one repelling submanifold $S_0^r(\lambda)$ that consists of unstable hyperbolic equilibria. The manifolds are separated by the two fold points $F_1(\lambda)$ and $F_2(\lambda)$ that correspond to non-hyperbolic equilibria or saddle-node bifurcations in the fast subsystem [Fig. 4.19]. The singular-limit threshold $\theta_0(\lambda)$ is given by the stable set of $F_1(\lambda)$. Now we have all the ingredients required to examine threshold instability of the stable equilibrium $e(\lambda)$ on parameter paths.

Fig. 4.20 shows $e(\lambda)$ and $\theta_0(\lambda)$ for three different values of the input parameter λ along the parameter path

$$P_\lambda^{[\Delta]} = \{\lambda : 0 \leq \lambda \leq \Delta\}.$$

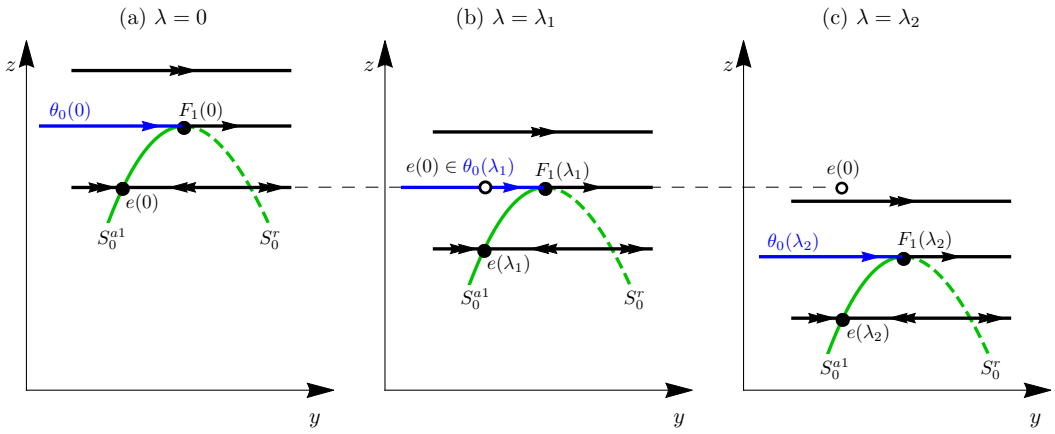

Figure 4.20: Singular-limit thresholds $\theta_0(\lambda)$ of the frozen system (4.31) for different values of λ = (a) 0, (b) $\lambda_1 > 0$, and (c) $\lambda_2 > \lambda_1$, illustrate threshold instability of the stable equilibrium e.

If $\Delta > \lambda_1$, then $e(0) \in \theta_0(\lambda_1)$ and $e(0)$ lies on different sides of $\theta_0(\lambda)$ for λ arbitrarily close to λ_1. This means the stable equilibrium $e(\lambda)$ is *threshold unstable* (but not basin unstable) on $P_\lambda^{[\Delta]}$; see Definition 3.3.2.

We now analyse reversible R-tipping from $e(rt)$ in the nonautonomous **canonical example V**:

$$\begin{aligned} \epsilon\frac{dY}{dt} &= -Y(Y^2-2) + Z + \Lambda(rt), \\ \frac{dZ}{dt} &= -Y - 1, \end{aligned} \tag{4.37}$$

parametrised by ϵ, and the magnitude Δ and rate r of the parameter shift.

Before we consider specific types of the external input $\Lambda(rt)$, it is convenient to compactify the problem and then derive the compactified desingularised slow subsystem for (4.37) that governs the slow dynamics in the limit $\epsilon = 0$. The compactification transformation (2.66) gives the following compactified slow-fast system (3.30)–(3.32):

$$\begin{aligned} \epsilon\frac{dY}{dt} &= -Y(Y^2-2) + Z + \Lambda(s), \\ \frac{dZ}{dt} &= -Y - 1, \\ \frac{ds}{dt} &= \frac{\alpha r}{2}(1-s^2), \end{aligned} \tag{4.38}$$

where $s \in [s_-, 1]$ becomes an additional slow variable and $s_- = 0$ or -1. The critical manifold in the compactified system is two-dimensional

$$S_0 = \{(y,z,s) \in \mathbb{R}^2 \times [s_-,1] : -y(y^2-2) + z + \Lambda(s) = 0\}, \tag{4.39}$$

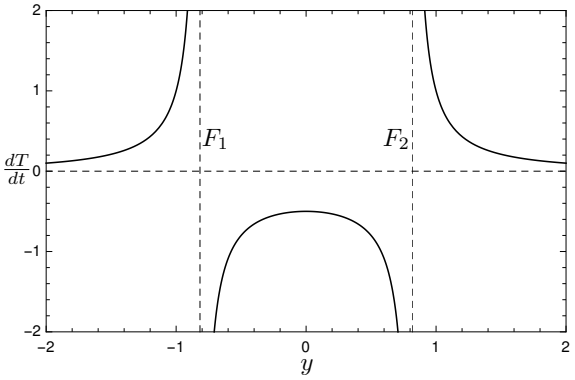

Figure 4.21: A graph of dT/dt with respect to y-component from (4.41), with two vertical dashed lines indicating the folds F_1 and F_2.

with two fold lines

$$\begin{aligned} F_1 &= \left\{ (y,z,s) \in \mathbb{R}^2 \times [s_-,1] : y = -\sqrt{\frac{2}{3}}, z = \frac{4\sqrt{6}}{9} - \Lambda(s) \right\}, \\ F_2 &= \left\{ (y,z,s) \in \mathbb{R}^2 \times [s_-,1] : y = \sqrt{\frac{2}{3}}, z = -\frac{4\sqrt{6}}{9} - \Lambda(s) \right\}. \end{aligned} \tag{4.40}$$

Using the state-dependent time rescaling (3.26):

$$dt = (3y^2 - 2)dT, \tag{4.41}$$

shown in Fig. 4.21, we obtain the compactified desingularised slow sub system (3.37)–(3.39):

$$\begin{aligned} \frac{dy}{dT} &= -y - 1 + \frac{d\Lambda(s)}{ds}\frac{\alpha r}{2}(1-s^2), \\ \frac{dz}{dT} &= (3y^2 - 2)(-y - 1), \\ \frac{ds}{dT} &= \frac{\alpha r}{2}(3y^2 - 2)(1 - s^2), \end{aligned} \tag{4.42}$$

that describes the slow dynamics of all three variables on the critical manifold (4.39) in the compactified (y, z, s) phase space in the new slow time T. Since the z-dynamics decouples from the y- and s-dynamics on S_0, the problem can be reduced to

$$\begin{aligned} \frac{dy}{dT} &= -y - 1 + \frac{d\Lambda(s)}{ds}\frac{\alpha r}{2}(1-s^2), \\ \frac{ds}{dT} &= \frac{\alpha r}{2}(3y^2 - 2)(1 - s^2). \end{aligned} \tag{4.43}$$

Figure 4.21 shows that, at the fold lines F_1 and F_2, the time T is infinitely faster than t and changes its direction of growth with respect to t. Thus, to obtain the

phase portrait on the critical manifold (4.39) in the slow time t, we first obtain the phase portrait for (4.43) in time T, and then reverse the direction of the flow between F_1 and F_2. The results are presented in two ways:

- Phase portraits for $\epsilon = 0$ showing trajectories on the critical manifold S_0 for the slow time t in projection onto the (y, s) plane.
- Phase portraits for $0 < \epsilon \ll 1$ showing trajectories of the compactified slow-fast system (4.38) in the (Y, Z, s) phase space.

4.6.1 Monotone asymptotically constant input: Folded saddle

Combining (4.38) with $\alpha = 1/2$ and (4.5) gives the compactified canonical example V with monotone asymptotically constant input

$$\begin{aligned} \epsilon\frac{dY}{dt} &= -Y(Y^2-2) + Z + \frac{4\Delta s}{(1+s)^2}, \\ \frac{dZ}{dt} &= -Y - 1, \\ \frac{ds}{dt} &= \frac{r}{4}(1-s^2), \end{aligned} \tag{4.44}$$

where $s \in [0, 1]$. The choice of α satisfies the compactification condition $0 < \alpha \leq 1$, and ensures that invariant subspace $\{s = 1\}$ has an orthogonal transverse eigenvector. We choose an initial condition on S_0^{a1} and denote it with I_0. The trajectories started from I_0 are plotted in red.

4.6.1.1 Slow dynamics in the singular limit $\varepsilon = 0$.

Before we analyse the slow-fast system (4.44), we describe the slow dynamics on S_0 for the slow time t in the limit $\varepsilon = 0$. To this end, we consider the compactified desingularised slow subsystem (4.43):

$$\begin{aligned} \frac{dy}{dT} &= -y - 1 + \frac{\Delta r(1-s)^2}{(1+s)^2}, \\ \frac{ds}{dT} &= \frac{r}{4}(3y^2-2)(1-s^2), \end{aligned} \tag{4.45}$$

and then translate from T to t by reversing the flow between F_1 and F_2. System (4.45) has one regular equilibrium - the globally stable node in the invariant subspace $\{s = 1\}$:

$$\tilde{e}^+ = (y, s) = (-1, 1). \tag{4.46}$$

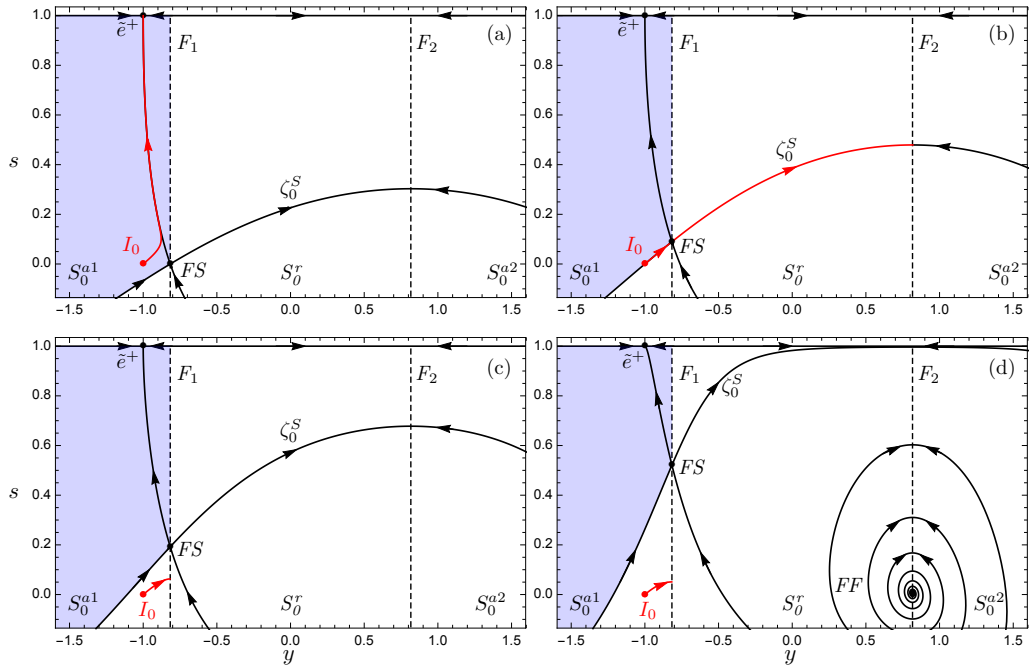

Figure 4.22: Phase portraits of system (4.44) on the critical manifold S_0 under the singular limit $\epsilon = 0$ with external input (4.1) in projection onto the (y, s) plane for $\Delta = 0.5$, initial state at $I_0 = (y, s) = (-1, 0)$ and different 'rates' $r =$(a) 0.3670, (b) 0.5261050891556, (c) 0.80, (d) 3.70. The critical manifold S_0 has two attractive submanifolds S_0^{a1} and S_0^{a2}, and one repelling submanifold S_0^r. The basin of attraction of $\tilde{e}^+$ is shaded in blue. In panel (b) the singular canard trajectory ζ_0^S intersects the chosen initial state I_0, namely the red dot, that indicates the critical rate $r_{c,0}$ for reversible R-tipping under the singular limit $\epsilon = 0$. FS and FF are respectively folded saddle and folded focus singularities.

Additionally, analysis of folded equilibria [see Eq. (3.25)] reveals a folded-saddle (denoted FS) on F_1:

$$(y, s) = \left(-\sqrt{\frac{2}{3}}, \frac{\sqrt{\Delta r} - \sqrt{1 - \sqrt{\frac{2}{3}}}}{\sqrt{\Delta r} + \sqrt{1 - \sqrt{\frac{2}{3}}}} \right),$$

and a folded sink (folded node FN or folded focus FF) on F_2:

$$(y, s) = \left(\sqrt{\frac{2}{3}}, \frac{\sqrt{\Delta r} - \sqrt{1 + \sqrt{\frac{2}{3}}}}{\sqrt{\Delta r} + \sqrt{1 + \sqrt{\frac{2}{3}}}} \right).$$

The dynamics within the critical manifold S_0 in the slow time t are summarised in Fig. 4.22, which shows selected phase portraits in projection onto the (y, s) plane for $\Delta = 0.5$ and different rates r. The folded saddle singularity FS is the *singular R-tipping edge state*. The *singular R-tipping threshold* within S_0 is given

by the singular folded-saddle canard trajectory, denoted ζ_0^S, that crosses from S_0^{a1} to S_0^r via FS. ζ_0^S forms the basin boundary of $\tilde{e}^+$ within S_0^{a1}, and is computed as the stable manifold of the folded-saddle equilibrium in system (4.45). The basin of attraction of $\tilde{e}^+$ is shaded in blue.

The folded singularities and the singular R-tipping threshold vary with r and Δ. If $0 < r < (1 - \sqrt{2/3})/\Delta$, the fold F_1 is repelling and I_0 is in the basin of attraction of $\tilde{e}^+$, meaning that trajectories started at I_0 cannot reach F_1 and have to converge to $\tilde{e}^+$ [Fig. 4.22(a)]. When $r = (1 - \sqrt{2/3})/\Delta$, the folded-saddle FS on F_1 enters the $s = [0, 1]$ interval. This opens up a subinterval of attracting jump points on F_1 and below FS [Fig. 4.22(a)]. When r reaches its critical value $r_{c,0}$, the trajectory started at I_0 no longer converges to $\tilde{e}^+$. Rather, $I_0 \in \zeta_0^S$, meaning the trajectory crosses the fold F_1 via the special point FS and continues on the repelling part S_0^r of the critical manifold until it ceases to exist at a jump point on F_2 [Fig. 4.22(b)]. For $r > r_{c,0}$, I_0 lies outside the basin of attraction of $\tilde{e}^+$ so that trajectories started at I_0 are attracted to a jump point on F_1 and cease to exist within S_0 [Fig. 4.22(c)]. Note that, when $r = (1 + \sqrt{2/3})/\Delta$, a folded focus FF on F_2 enters the $s = [0, 1]$ interval. However, this does not affect the dynamics on S_0^{a1} [Fig. 4.22(d)].

4.6.1.2 Slow-fast dynamics for $0 < \varepsilon \ll 1$.

The different dynamics of the slow-fast system (4.44) are summarised in Fig. 4.23, which shows the (Δ, r) tipping diagram together with selected (Y, Z, s) phase portraits for $\Delta = 0.5$, $\epsilon = 0.001$ and different rates r. The invariant subspace $\{s = 1\}$ contains the globally stable equilibrium

$$\tilde{e}^+ = (Y, Z, s) = (-1, 1 - \Delta, 1).$$

The normally hyperbolic components of the critical manifold persist as locally invariant *attracting slow manifolds* S_ε^{a1} and S_ε^{a2}, and a *repelling slow manifold* S_ε^r [47, 56, 75]. Typically, S_ε^a and S_ε^r detach along F, except near folded singularities where S_ε^a and S_ε^r intersect, possibly in a very complicated way [121, 108]. The singular folded-saddle canard ζ_0^S persists as a nearby folded-saddle canard ζ_ε^S, and can be computed in two ways: (i) as an intersection of the slow manifolds S_ε^{a1} and S_ε^r, or (ii) as the *maximal canard* trajectory that stays on the repelling slow manifold S_ε^r for the longest time. We refer to [122, 108] for computation of slow manifolds and canards. In Fig. 4.23, we plot S_0^{a1}, S_0^{a2}, S_0^r (in green) as approximations of S_ε^{a1}, S_ε^{a2} and S_ε^r, respectively. We plot ζ_0^S as an approximation of ζ_ε^S. For reference, we also include the remaining components of the singular limit system: the two fold lines F_1 and F_2, and the folded singularities FS and

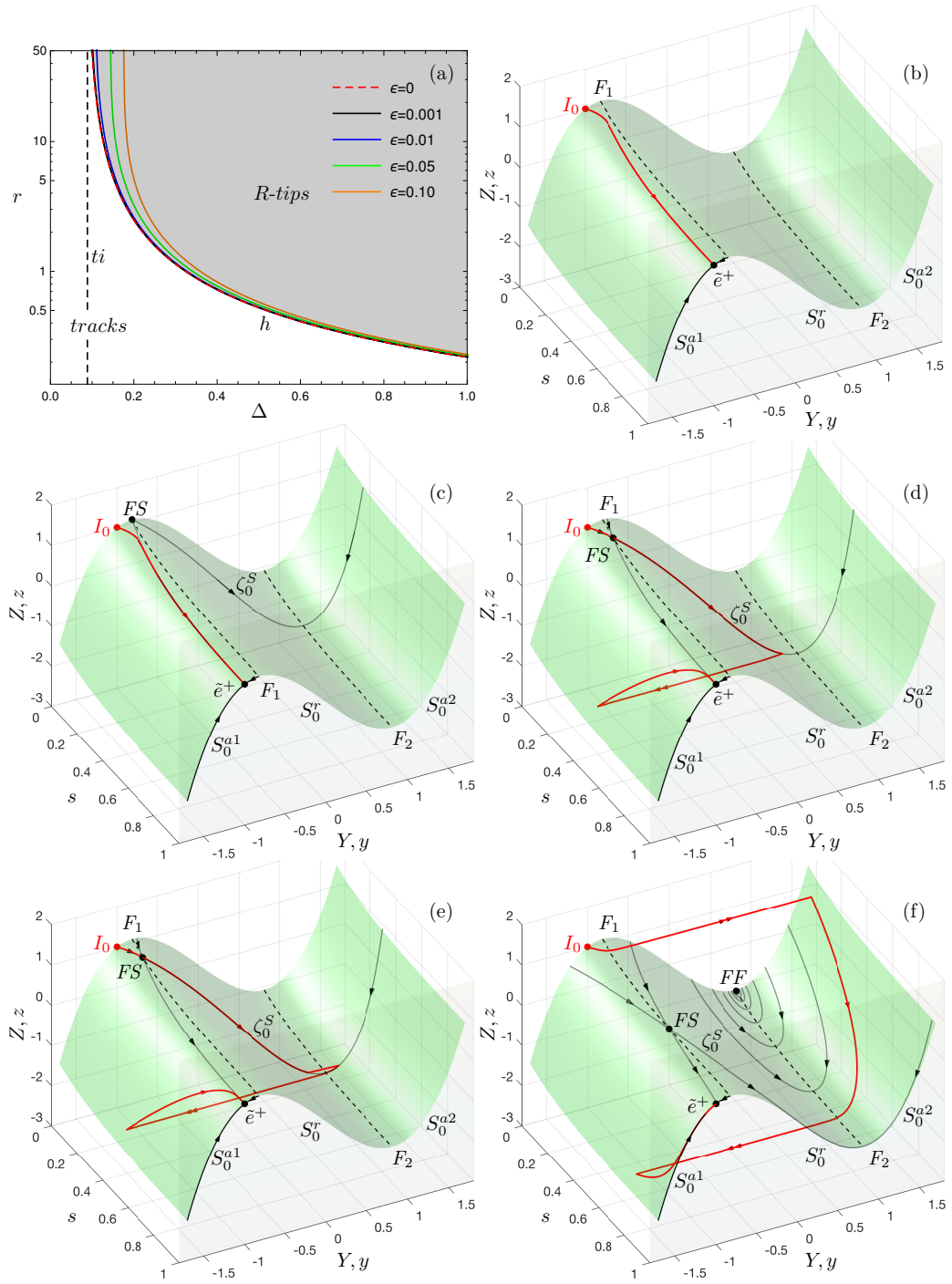

Figure 4.23: (a) The (Δ, r)-tipping diagrams of system (4.38) under $\epsilon = 0$, 0.001, 0.01, 0.05 and 0.10 with monotone external input (4.1), with the right regions of the relevant tipping curves h for the occurrence of reversible R-tipping. The (dashed) ti line is the (forward) threshold instability boundary for $\epsilon = 0$. (b)-(f) Phase portraits of system (4.44) for $\Delta = 0.5$, $\epsilon = 0.001$ and different 'rates' $r =$ (b) 0.36, (c) 0.3670, (d) 0.5261050891556,(e) 0.52611, and (f) 3.70. The critical manifold S_0, which is the green surface, has two attractive submanifolds S_0^{a1} and S_0^{a2}, and one repelling submanifold S_0^r. FS and FF are respectively folded saddle and folded focus singularities. ζ_0^S is the singular folded-saddle canard.

FF.

If r is sufficiently small, the system closely tracks the moving equilibrium $e(rt)$, stays within S_ε^{a1} and converges to $\tilde{e}^+$ [Fig. 4.23 (b)]. As r increases, the red trajectory continues to stay within S_ε^{a1}, but gets closer to F_1, which can be explained by the appearance of the folded saddle FS at $s = 0$ [Fig. 4.23 (c)]. Then, there is a small range of $r \approx r_{c,0}$, where the system leaves S_ε^{a1} along the folded-saddle canard trajectory ζ_ε^S, crosses F_1, and continues along the unstable manifold S_ε^r for some time. Within this range, there is a change in how the system leaves the neighbourhood of S_ε^r along the fast y-direction. Initially, the system goes directly to S_ε^{a1} before it converges to $\tilde{e}^+$ [Fig. 4.23 (d)]. For higher r, the system goes to S_ε^{a2} and then returns via F_2 to S_ε^{a1} before it converges to $\tilde{e}^+$ [Fig. 4.23 (e)].

The main characteristic of a quasithreshold is that the ensuing reversible R-tipping is a continuous transition that occurs within a *critical range of* r. The transition involves a family of canard trajectories, such as the red trajectories shown in Fig. 4.23 (d)-(e), that follow the folded-saddle canard ζ_ε^S on S_ε^r. The *R-tipping quasithreshold* can be defined as the folded-saddle-canard ζ_ε^S together with its stable set - the set of trajectories that converge towards ζ_ε^S for as long as ζ_ε^S exists. Figure 4.23 (a) shows that the critical rate $r_{c,0}$ for $\varepsilon = 0$ gives a good approximation of the critical range of r in the slow-fast canonical example (4.44) with $0 < \varepsilon \ll 1$. The approximation becomes less accurate at larger values of ε near the threshold instability boundary ti.

When r is increased further, the red trajectory leaves S_ε^{a1} near F_1, moves directly towards S_ε^{a2} along the fast y-direction, spends time on S_ε^{a2}, then leaves S_ε^{a2} near F_2 to return directly to S_ε^{a1} and converge to $\tilde{e}^+$ [Fig. 4.23 (f)]. Note that the slow evolution on S_ε^{a2} may change noticeably with r, which can be explained by the appearance of the folded focus FF on F_2 [Fig. 4.23 (f)].

4.6.2 Monotone bi-asymptotically constant input: Folded saddle-node type-I

Combining (4.38) with $\alpha = 1$ and (4.7) gives the compactified canonical example V with monotone bi-asymptotically constant input

$$\begin{aligned} \epsilon\frac{dY}{dt} &= -Y(Y^2-2) + Z + \frac{\Delta}{2}\frac{(1+s)^2}{(1+s^2)}, \\ \frac{dZ}{dt} &= -Y - 1, \\ \frac{ds}{dt} &= \frac{r}{2}(1-s^2), \end{aligned} \tag{4.47}$$

where $s \in [-1, 1]$. The choice of α satisfies the compactification condition $0 < \alpha \leq 2$, and ensures that invariant subspaces $\{s = \pm 1\}$ have an orthogonal transverse eigenvector.

Before we analyse the slow-fast system (4.47), we describe the slow dynamics on S_0 for the slow time t in the limit $\varepsilon = 0$. To this end, we consider the compactified desingularised slow subsystem (4.43):

$$\begin{aligned} \frac{dy}{dT} &= -y - 1 + \frac{\Delta r(1-s^2)^2}{2(1+s^2)^2}, \\ \frac{ds}{dT} &= \frac{r(3y^2-2)(1-s^2)}{2}, \end{aligned} \tag{4.48}$$

and then translate from T to t by reversing the flow between F_1 and F_2. System (4.48) has one stable equilibrium in the invariant subspace $\{s = 1\}$:

$$\tilde{e}^+ = (y, s) = (-1, 1), \tag{4.49}$$

and one saddle equilibrium in the invariant subspace $\{s = -1\}$:

$$\tilde{e}^- = (y, s) = (-1, -1). \tag{4.50}$$

Additionally, analysis of folded equilibria [see Eq. (3.25)] reveals a saddle-node bifurcation of folded equilibria on F_1 (denoted FSN) when

$$r = r_1^{FSN} = \frac{2}{\Delta}(1 - \sqrt{2/3}).$$

The bifurcation is referred to as a folded saddle-node type-I [105, 107, 104], and gives rise to a folded saddle (denoted FS) and a stable folded node (denoted FN) on F_1:

$$(y, s) = \left(-\sqrt{\frac{2}{3}}, \pm \sqrt{\frac{\sqrt{\Delta r} - \sqrt{2 - 2\sqrt{\frac{2}{3}}}}{\sqrt{\Delta r} + \sqrt{2 - 2\sqrt{\frac{2}{3}}}}} \right).$$

Similarly, there is another saddle node bifurcation of folded equilibria on F_2 when

$$r = r_2^{FSN} = \frac{2}{\Delta}(1 + \sqrt{2/3}),$$

It also gives rise to a folded saddle and a stable folded node, but is not relevant for R-tipping.

The presence of a stable folded node on F_1 opens up the possibility of having different R-tipping quasithresholds. In fact, there are two cases [51] which we describe below using different values of Δ.

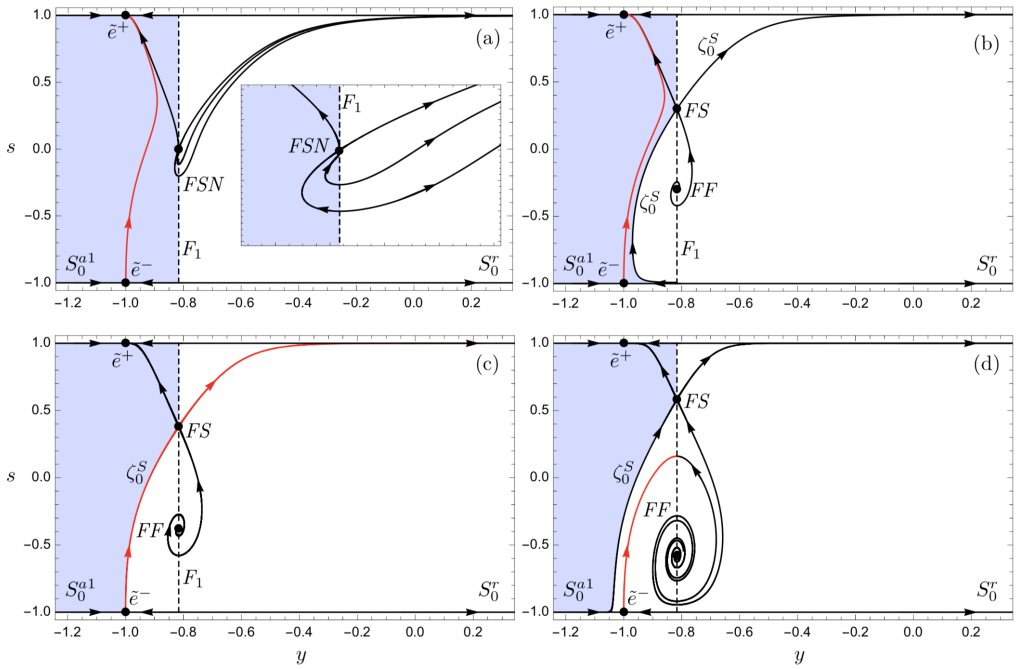

Figure 4.24: Phase portraits of system (4.47) on the critical manifold S_0 under the singular limit $\epsilon = 0$ with external input (4.2) in projection onto the (y, s) plane for $\Delta = 0.15$ and different 'rates' r =(a) 2.4467122543, (b) 3.50, (c) 4.38130658, (d) 10. The singular canard trajectory ζ_0^S intersects $\tilde{e}^-$, namely the heteroclinic $\tilde{e}^-$-to-FS connection in panel (c), that indicates the critical rate $r_{c,0}$ for reversible R-tipping under the singular limit $\epsilon = 0$. Panel (a) zooms in the areas around the folded saddle-node singularity FSN. FS and FF are respectively folded saddle and folded focus singularities.

4.6.2.1 Case 1: Simple R-tipping quasithreshold.

For sufficiently small Δ we find a *simple quasithreshold due to a folded saddle*, which is similar to the quasithreshold described for the asymptotically constant input above.

Slow dynamics in the singular limit $\varepsilon = 0$.

We set $\Delta = 0.15$ and summarise the dynamics of system (4.47) on the critical manifold S_0 in the slow time t in Fig. 4.24, which shows selected phase portraits in projection onto the (y, s) plane for different rates r. The invariant subspace $\{s = -1\}$ contains the saddle equilibrium $\tilde{e}^-$, which is stable within the subspace, and unstable in the transverse s-direction. The invariant subspace $\{s = 1\}$ contains the stable equilibrium $\tilde{e}^+$. The folded saddle singularity FS is the *singular R-tipping edge state*. The *singular R-tipping threshold* within S_0 is given by the singular folded-saddle canard trajectory, denoted ζ_0^S, that goes from S_0^{a1} to S_0^r via FS. ζ_0^S forms the basin boundary of $\tilde{e}^+$ within S_0^{a1}, and is computed as the stable manifold of the folded-saddle equilibrium in system (4.48). The basin of attraction of $\tilde{e}^+$ is shaded in blue.

If $0 < r < r_1^{FSN}$, the fold F_1 is repelling, meaning that the unstable manifold $W^{u,[r,\Delta]}(\tilde{e}^-)$ cannot reach F_1 and has to accumulate on $\tilde{e}^+$. As r is increased, there is a saddle-node bifurcation of folded singularities on F_1, but it does not interfere with $W^{u,[r,\Delta]}(\tilde{e}^-)$ [Fig. 4.24(a)]. Shortly past the bifurcation, the stable folded node FN turns into a stable folded focus FF. Note that there are no canards associated with folded foci. The points on F_1 that are below FS become attracting jump points. Since $W^{u,[r,\Delta]}(\tilde{e}^-)$ is separated from the attracting jump points on F_1 by the singular folded-saddle canard ζ_0^S, it continues to accumulate on $\tilde{e}^+$. In other words, there is an open half-circle of initial states centred at $\tilde{e}^-$, all of which evolve on one side of ζ_0^S, within the basin of attraction of $\tilde{e}^+$, and converge to $\tilde{e}^+$ [Fig. 4.24(b)]. As r is increased, $W^{u,[r,\Delta]}(\tilde{e}^-)$ gets closer to ζ_0^S. When r reaches the critical value $r_{c,0}$, $W^{u,[r_{c,0},\Delta]}(\tilde{e}^-)$ no longer accumulates on $\tilde{e}^+$. Rather, $W^{u,[r_{c,0},\Delta]}(\tilde{e}^-)$ becomes the folded-saddle canard ζ_0^S, crosses F_1 via FS, and continues on S_0^r [Fig. 4.24(c)]. In the compactified desingularised slow subsystem (4.48), this corresponds a (codimension-one) heteroclinic connection from the regular saddle equilibrium $\tilde{e}^-$ to the folded saddle equilibrium FS given by the coalescing invariant manifolds

$$W^{u,[r_{c,0},\Delta]}(\tilde{e}^-) \cap W^{s,[r_{c,0},\Delta]}(FS).$$

Now, any open half-circle of initial states centred at $\tilde{e}^-$ contains states that lie within the basin of attraction of $\tilde{e}^+$, as well as states that are attracted to a jump point on F_1 and cease to exist within S_0. This heteroclinic connection gives a computable condition for the approximation of the critical range of r. When $r > r_{c,0}$, the heteroclinic connection breaks so that ζ_0^S is on the other side of $W^{u,[r,\Delta]}(\tilde{e}^-)$, and $W^{u,[r,\Delta]}(\tilde{e}^-)$ itself reaches a jump point on F_1 and ceases to exist within S_0 [Fig. 4.24(d)]. Now, there is an open half-circle of initial states centred at $\tilde{e}^-$, all of which are outside the basin of attraction of $\tilde{e}^+$, arrive at jump points on F_1 and cease to exist within S_0.

Slow-fast dynamics for $0 < \varepsilon \ll 1$.

The dynamics of the slow-fast system (4.47) are summarised in Fig. 4.25, which shows selected (Y, Z, s) phase portraits for $\Delta = 0.15$, $\epsilon = 0.01$ and different rates r. The invariant subspace $\{s = 1\}$ contains the stable equilibrium

$$\tilde{e}^+ = (Y, Z, s) = (-1, 1 - \Delta, 1),$$

and the invariant subspace $\{s = -1\}$ contains the saddle equilibrium

$$\tilde{e}^- = (Y, Z, s) = (-1, 1, -1).$$

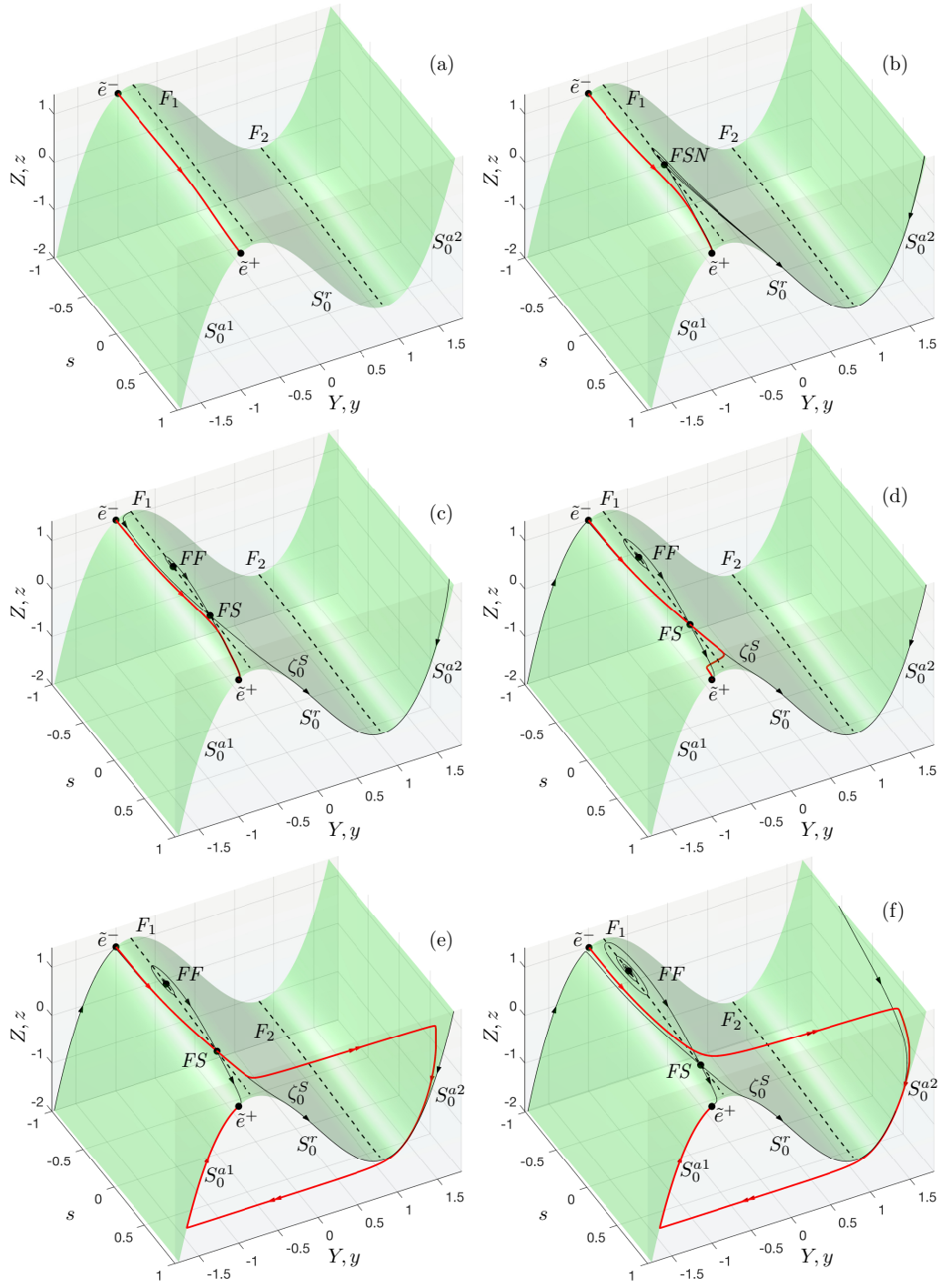

Figure 4.25: Phase portraits of system (4.47) with external input (4.2) for $\Delta = 0.15$, $\epsilon = 0.01$ and different 'rates' r =(a) 0.5, (b) 2.4467122543, (c) 3.50, (d) 4.8577, (e) 4.858, (f) 10.0. The critical manifold S_0, which is the green surface, has two attractive submanifolds S_0^{a1} and S_0^{a2}, and one repelling submanifold S_0^r. FSN, FS and FF are respectively folded saddle-node, folded saddle and folded focus singularities. ζ_0^S is the singular folded-saddle canard.

The normally hyperbolic components of the critical manifold persist as locally invariant *attracting slow manifolds* S_ε^{a1} and S_ε^{a2}, and a *repelling slow manifold* S_ε^r [47, 56, 75]. Typically, S_ε^a and S_ε^r detach along F, except near folded singular-

ities where S_ε^a and S_ε^r intersect, possibly in a very complicated way [121, 108]. The singular folded-saddle canard ζ_0^S persists as a nearby folded-saddle canard ζ_ε^S, and can be computed in two ways: (i) as an intersection of the slow manifolds S_ε^{a1} and S_ε^r, or (ii) as the *maximal canard* trajectory that stays on the repelling slow manifold S_ε^r for the longest time. We refer to [122, 108] for computation of slow manifolds and canards. In Fig. 4.25, we plot S_0^{a1}, S_0^{a2}, S_0^r (in green) as approximations of S_ε^{a1}, S_ε^{a2} and S_ε^r, respectively. We plot ζ_0^S as an approximation of ζ_ε^S. For reference, we also include the remaining components of the singular limit system: the two fold lines F_1 and F_2, and the folded singularities FS and FF.

If r is sufficiently small, the unstable manifold $W^{u,[r,\Delta]}(\tilde{e}^-)$ stays within S_ε^{a1}, closely tracks the moving stable equilibrium $e(rt)$, and then accumulates on $\tilde{e}^+$ [Fig. 4.25 (a)-(c)]. This happens despite the saddle-node type-I bifurcation giving rise to two folded singularities on F_1. In general, there is a complicated structure of folded-node canards associated with a folded node [105, 121, 107, 104]. This structure plays an important role in Case 2 ahead. In the case at hand, the stable folded node turns into a stable folded focus soon after the bifurcation, and the complicated canard structure disappears before it interferes with the R-tipping instability. As r is increased, $W^{u,[r,\Delta]}(\tilde{e}^-)$ gets closer to F_1 near the folded saddle FS [Fig. 4.25 (c)]. Then, there is a small range of $r \approx r_{c,0}$, where $W^{u,[r,\Delta]}(\tilde{e}^-)$ leaves S_ε^{a1}, crosses F_1, and follows the folded-saddle canard ζ_ε^S along the unstable manifold S_ε^r for some time. Within this range, there is a change in how the system leaves the neighbourhood of S_ε^r in the fast y-direction. Initially, the system goes directly to S_ε^{a1} before it converges to $\tilde{e}^+$ [Fig. 4.25 (d)]. For higher r, the system goes to S_ε^{a2} first, and then returns via F_2 to S_ε^{a1} before it converges to $\tilde{e}^+$ [Fig. 4.25 (e)].

The main characteristic of the *simple quasithreshold* is that the ensuing reversible R-tipping is a continuous transition that occurs within a *single critical range of* r. Throughout the transition, $W^{u,[r,\Delta]}(\tilde{e}^-)$ traces out a family of canard trajectories that follow the folded-saddle canard ζ_ε^S on S_ε^r for some time, such as the red trajectories shown in Fig. 4.25 (d)-(e). While it is clear the critical range of r is associated with the folded-saddle canard, the exact dynamical mechanism has not been identified so far. Figure 4.26 reveals that the critical range of r corresponds to an *infinite-time canard-bifurcation*. As r is increased, the folded-saddle canard ζ_ε^S approaches the regular saddle equilibrium $\tilde{e}^-$ [Fig. 4.26(c)], connects to $\tilde{e}^-$ from 'above' [Fig. 4.26(d-e)], and then reappears from 'below' [Fig. 4.26(f)]. In other words, the folded-saddle canard ζ_ε^S coalesces with the unstable manifold $W^{u,[r,\Delta]}(\tilde{e}^-)$ as they pass through each other in a transverse crossing. The *simple R-tipping quasithreshold* can be defined as the folded-saddle-

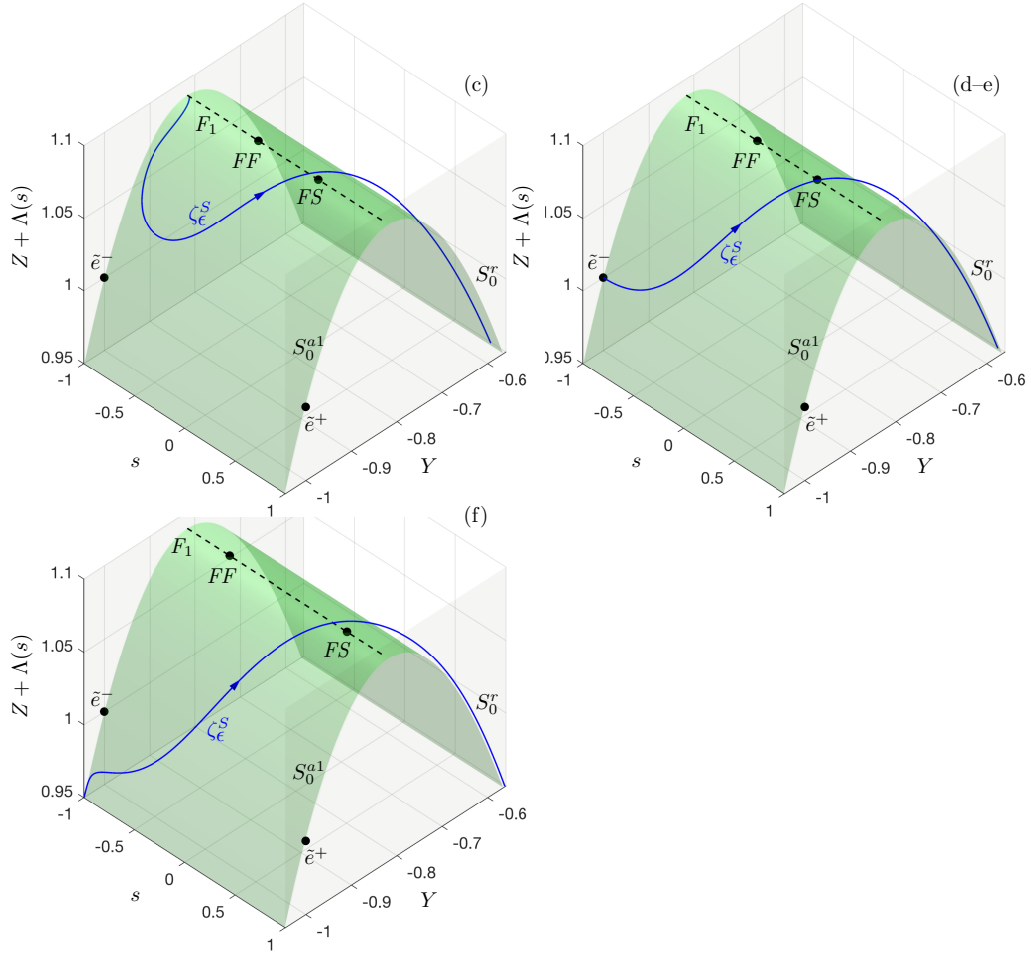

Figure 4.26: Canard evolution of system (4.47) with external input (4.2) for $\Delta = 0.15$, $\epsilon = 0.01$ and different 'rates' r =(c) 3.50, (d–e) 4.8577262570, (f) 10.0. Zoom in for observation of canard in Fig. 4.25, and ζ_ε^S is the folded-saddle canard.

canard ζ_ε^S together with its stable set - the set of trajectories that converge towards ζ_ε^S for as long as ζ_ε^S exists.

When r is increased further, the unstable manifold $W^{u,[r,\Delta]}(\tilde{e}^-)$ leaves S_ε^{a1} near F_1 along the fast y-direction, moves directly (i.e. without following S_ε^r) towards S_ε^{a2}, spends time on S_ε^{a2}, then leaves S_ε^{a2} near F_2 along the fast y-direction to return directly to S_ε^{a1} and converge to $\tilde{e}^+$ [Fig. 4.25 (f)].

4.6.2.2 Case 2: Complicated R-tipping quasithreshold.

For larger Δ we find a *complicated quasithreshold* due to a folded saddle-node type-I, which arises from an interplay of the complicated dynamics owing to a folded node, and the simple threshold behaviour owing to a folded saddle.

Slow dynamics in the singular limit $\varepsilon = 0$.

We set $\Delta = 0.8$ and summarise the dynamics of system (4.47) on the critical manifold S_0 in the slow time t in Fig. 4.27, which shows selected phase portraits in projection onto the (y, s) plane for different rates r. The invariant subspace $\{s = -1\}$ contains the saddle equilibrium $\tilde{e}^-$, which is stable within the subspace, and unstable in the transverse s-direction. The invariant subspace $\{s = 1\}$ contains the stable equilibrium $\tilde{e}^+$. When $\varepsilon = 0$, the main difference from the simple Case 1 is that there are two *singular R-tipping edge states*: the folded-node FN and the folded saddle FS singularities. Thus, the ensuing *singular R-tipping threshold* within S_0 consists of two components. The more relevant component, the singular strong folded-node canard, denoted ζ_0^N, is computed as the unique trajectory tangent to the strong eigenspace (corresponding to the largest magnitude eigenvalue) of the stable folded node in system (4.48). The other component, the singular folded-saddle canard, denoted ζ_0^S, is computed as the stable manifold of the folded saddle in system (4.48). ζ_0^N and ζ_0^S form the basin boundary of $\tilde{e}^+$ within S_0^{a1}. The basin of attraction of $\tilde{e}^+$ is shaded in blue.

If $0 < r < r_1^{FSN}$, the fold F_1 is repelling, meaning that the unstable manifold $W^{u,[r,\Delta]}(\tilde{e}^-)$ cannot reach F_1 and has to accumulate on $\tilde{e}^+$. When $r = r_1^{FSN}$, there is a saddle-node bifurcation of folded singularities on F_1. In contrast to Case 1, this bifurcation interferes with $W^{u,[r,\Delta]}(\tilde{e}^-)$ [Fig. 4.27]. Specifically, $W^{u,[r,\Delta]}(\tilde{e}^-)$ becomes the saddle-node centre manifold [Fig. 4.27(b)]. Shortly past the bifurcation, the part of F_1 between FS and FN consists of attracting jump points [Fig. 4.27(c)]. Trajectories started on S_0^{a1} between the singular strong folded-node ζ_0^N and the folded-saddle ζ_0^S canards are attracted to these jump points and cease to exist within S_0. What is more, $W^{u,[r,\Delta]}(\tilde{e}^-)$ becomes the singular weak folded-node canard ζ_0^w. In other words, there is a (codimension-zero) connection from $\tilde{e}^-$ to FN tangent to the weak eigenspace (corresponding to the smallest magnitude eigenvalue) of FN in system (4.48). Interestingly, there is an open half-circle of initial states centred at $\tilde{e}^-$, all of which pass through FN along ζ_0^w, continue to evolve along ζ_0^w on S_0^r, then re-enter S_0^{a1} via FS, and converge to $\tilde{e}^+$ [Fig. 4.27(c)]. When r reaches the critical value $r_{c,0}$, the folded node becomes a degenerate folded-node DFN, $W^{u,[r_{c,0},\Delta]}(\tilde{e}^-)$ and the singular strong folded-node canard ζ_0^N coalesce, and ζ_0^N is destroyed in the sense that it does not exist for $r > r_{c,0}$ [Fig. 4.27(d)]. Now, any open half-circle of initial states centred at $\tilde{e}^-$ contains states that lie within the basin of attraction of $\tilde{e}^+$, as well as states that are attracted to a jump point on F_1 and cease to exist within S_0; see the inset in Fig. 4.27(d) showing trajectories near DFN. The degenerate folded-node condition

$$\left[48\left(\sqrt{\frac{2}{3}} - \frac{2}{3}\right)\right]^2 \left[\Delta r_{c,0} - 2\left(1 - \sqrt{\frac{2}{3}}\right) r_{c,0} - \Delta = 0,\right.$$

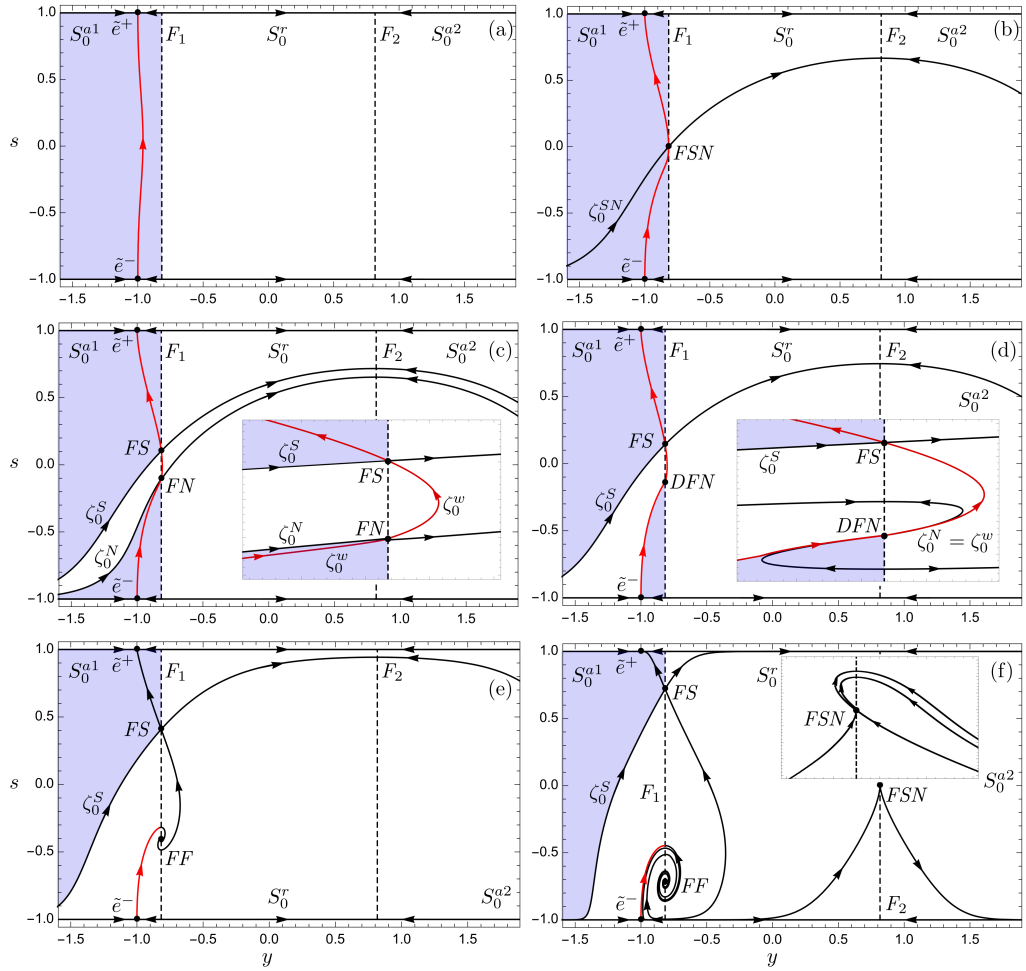

Figure 4.27: Phase portraits of system (4.47) on the critical manifold S_0 under the singular limit $\epsilon = 0$ with external input (4.2) in projection onto the (y, s) plane for $\Delta = 0.8$ and different 'rates' $r =$(a) 0.1, (b) 0.45875854768, (c) 0.47862301355, (d) 0.497612, (e) 0.9, (f) 4.541241452319314753. The folded node FN becomes a degenerate folded-node DFN, and the unstable manifold $W^{u,[r_{c,0},\Delta]}(\tilde{e}^-)$ of $\tilde{e}^-$ and the singular strong folded-node canard ζ_0^N coalesce in panel (d), that indicates the critical rate $r_{c,0}$ for reversible R-tipping under the singular limit $\epsilon = 0$.

gives a computable condition for the approximation of the whole series of critical ranges of r found for $0 < \varepsilon \ll 1$.

When $r > r_{c,0}$, the unstable manifold $W^{u,[r,\Delta]}(\tilde{e}^-)$ itself reaches a jump point on F_1 and ceases to exist within S_0 [Fig. 4.27(e)-(f)]. In other words, there is an open half-circle of initial states centred at $\tilde{e}^-$, all of which are outside the basin of attraction of $\tilde{e}^+$, arrive at jump points on F_1 and cease to exist within S_0.

Slow-fast dynamics for $0 < \varepsilon \ll 1$.

The dynamics of the slow-fast system (4.47) are summarised in Figs. 4.28, 4.30 and 4.29, which show selected (Y, Z, s) phase portraits for $\Delta = 0.8$, $\epsilon = 0.01$ and

different rates r. The invariant subspace $\{s = 1\}$ contains the stable equilibrium

$$\tilde{e}^+ = (Y, Z, s) = (-1, 1 - \Delta, 1),$$

and the invariant subspace $\{s = -1\}$ contains the saddle equilibrium

$$\tilde{e}^- = (Y, Z, s) = (-1, 1, -1).$$

The normally hyperbolic components of the critical manifold persist as locally invariant *attracting slow manifolds* S_ε^{a1} and S_ε^{a2}, and a *repelling slow manifold* S_ε^r [47, 56, 75]. Typically, S_ε^a and S_ε^r detach along F, except near folded singularities where S_ε^a and S_ε^r intersect, possibly in a very complicated way [121, 108]. In Figs. 4.28, 4.30 and 4.29, we plot S_0^{a1}, S_0^{a2}, S_0^r (in green) as approximations of S_ε^{a1}, S_ε^{a2} and S_ε^r, respectively. The singular folded-saddle ζ_0^S and the singular strong folded-node ζ_0^N canards persist as nearby folded-saddle ζ_ε^S and strong folded-node ζ_ε^N canards, respectively [76]. Additionally, there are secondary folded-node canards ξ_n arising from the complicated intersections of S_ε^{a1} and S_ε^r near FN [105, 121, 122], as well as composite canards ζ_ε^C arising from the interaction of folded-node and folded-saddle [51, 104]. In Figs. 4.28 and 4.29 we plot the unstable manifold $W^{u,[r,\Delta]}(\tilde{e}^-)$ (in red) together with singular canards (in black). For reference, we also include the remaining components of the singular limit system: the two fold lines F_1 and F_2, and the folded singularities FSN, FS, FN and FF. In Fig. 4.30, we plot the regular canards for $0 < \varepsilon \ll 1$ that were computed as solutions to a suitable boundary value problem using AUTO [122, 110].

If r is sufficiently small, the unstable manifold $W^{u,[r,\Delta]}(\tilde{e}^-)$ stays within S_ε^{a1}, closely tracks the moving stable equilibrium $e(rt)$, and then accumulates on $\tilde{e}^+$ [Fig. 4.28 (a)]. As r is increased, $W^{u,[r,\Delta]}(\tilde{e}^-)$ approaches F_1 [Fig. 4.28 (b)]. For higher r, $W^{u,[r,\Delta]}(\tilde{e}^-)$ leaves S_ε^{a1} momentarily as it rotates around F_1 [Fig. 4.28 (c)]. Despite the rotation, $W^{u,[r,\Delta]}(\tilde{e}^-)$ eventually re-enters S_ε^{a1} and continues to accumulate on $\tilde{e}^+$ [Fig. 4.28 (c)]. This behaviour can be explained by the folded saddle-node type-I bifurcation: the ensuing stable folded node FN gives rise to oscillations about F_1 while the folded-saddle FS provides the re-injection mechanism. Then, there is the *first critical range* of r, where the unstable manifold $W^{u,[r,\Delta]}(\tilde{e}^-)$ follows some maximal canard along the unstable manifold S_ε^r for some time. Within this range, there is a change in how the system leaves the neighbourhood of S_ε^r in the fast y-direction. Initially, the system goes straight to S_ε^{a1} before it converges to $\tilde{e}^+$ [Fig. 4.28 (d)]. For higher r, the system goes to S_ε^{a2} first, and then returns via F_2 to S_ε^{a1} before it converges to $\tilde{e}^+$ [Fig. 4.28 (e)]. Interestingly, the maximal canard in question appears to be neither ζ_ε^S nor ζ_ε^N. When r is increased further, there is a small interval of r where the system under-

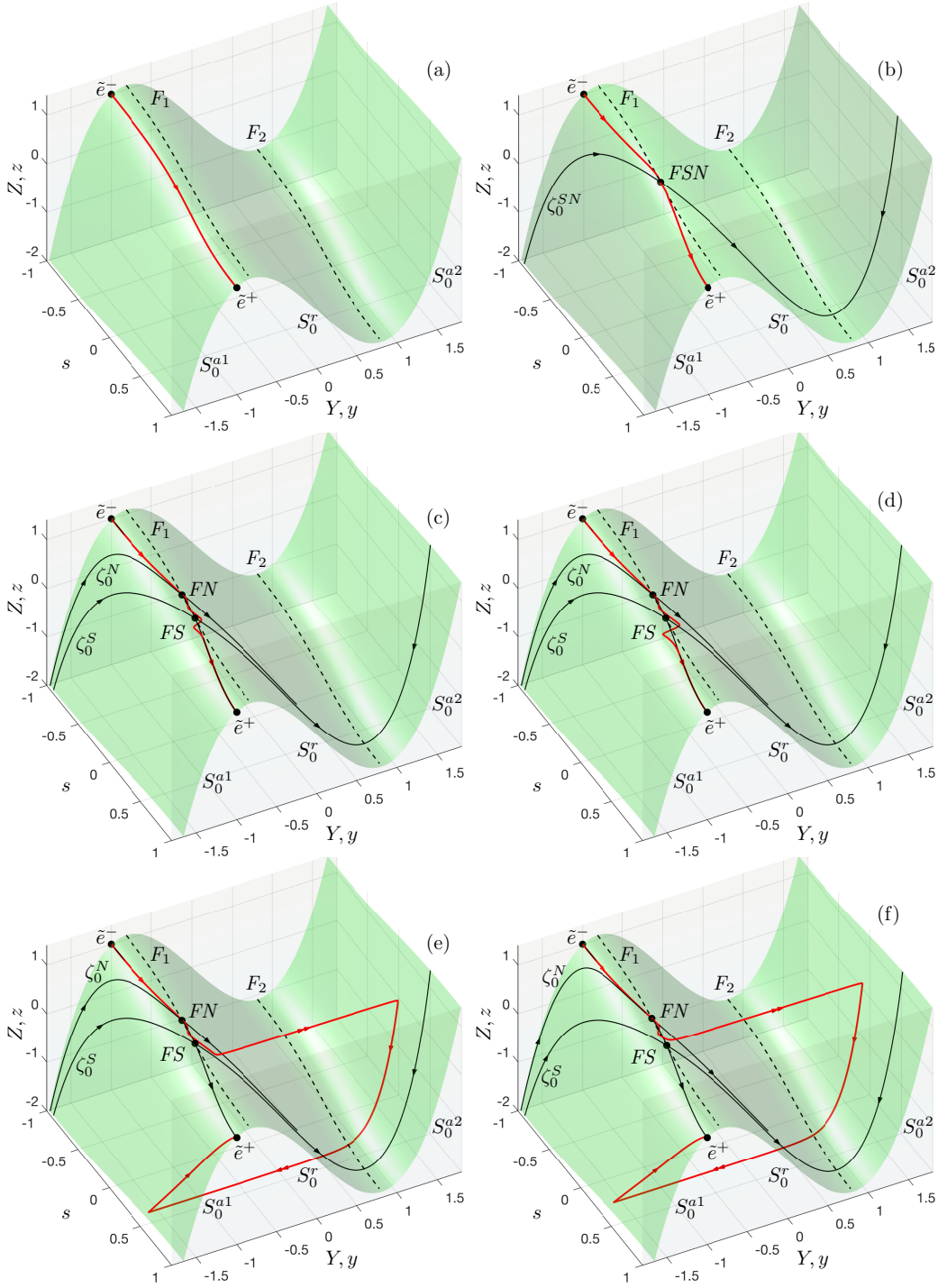

Figure 4.28: Phase portraits of system (4.47) with external input (4.2) for $\Delta = 0.8$, $\epsilon = 0.01$ and different 'rates' $r =$(a) 0.1, (b) 0.45875854768, (c) 0.47854780131, (d) 0.47862301355, (e) 0.47862302064504999577, (f) 0.48603. The critical manifold S_0, which is the green surface, has two attractive submanifolds S_0^{a1} and S_0^{a2}, and one repelling submanifold S_0^r. FSN, FS and FN are respectively folded saddle-node, folded saddle and folded node singularities. ζ_0^N and ζ_0^S are respectively the singular strong folded-node canard and singular folded-saddle canard.

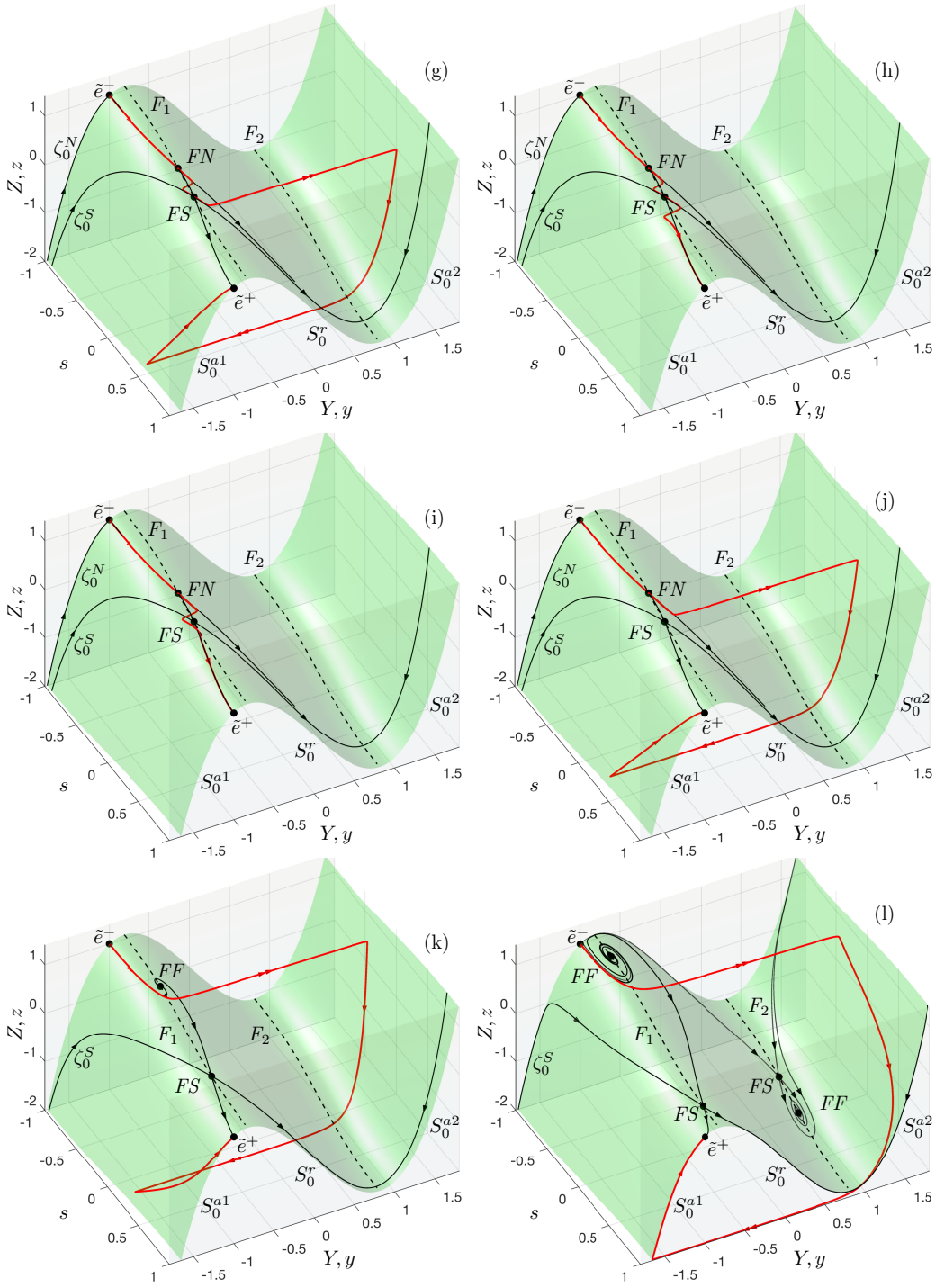

Figure 4.29: Phase portraits of system (4.47) with external input (4.2) for $\Delta = 0.8$, $\epsilon = 0.01$ and different 'rates' r =(g) 0.48975092687, (h) 0.4897509329, (i) 0.48975686478, (j) 0.489756871415, (k) 0.9, (l) 5.0. The critical manifold S_0, which is the green surface, has two attractive submanifolds S_0^{a1} and S_0^{a2}, and one repelling submanifold S_0^r. FS, FN and FF are respectively folded saddle, folded node and folded focus singularities. ζ_0^N and ζ_0^S are respectively the singular strong folded-node canard and singular folded-saddle canard.

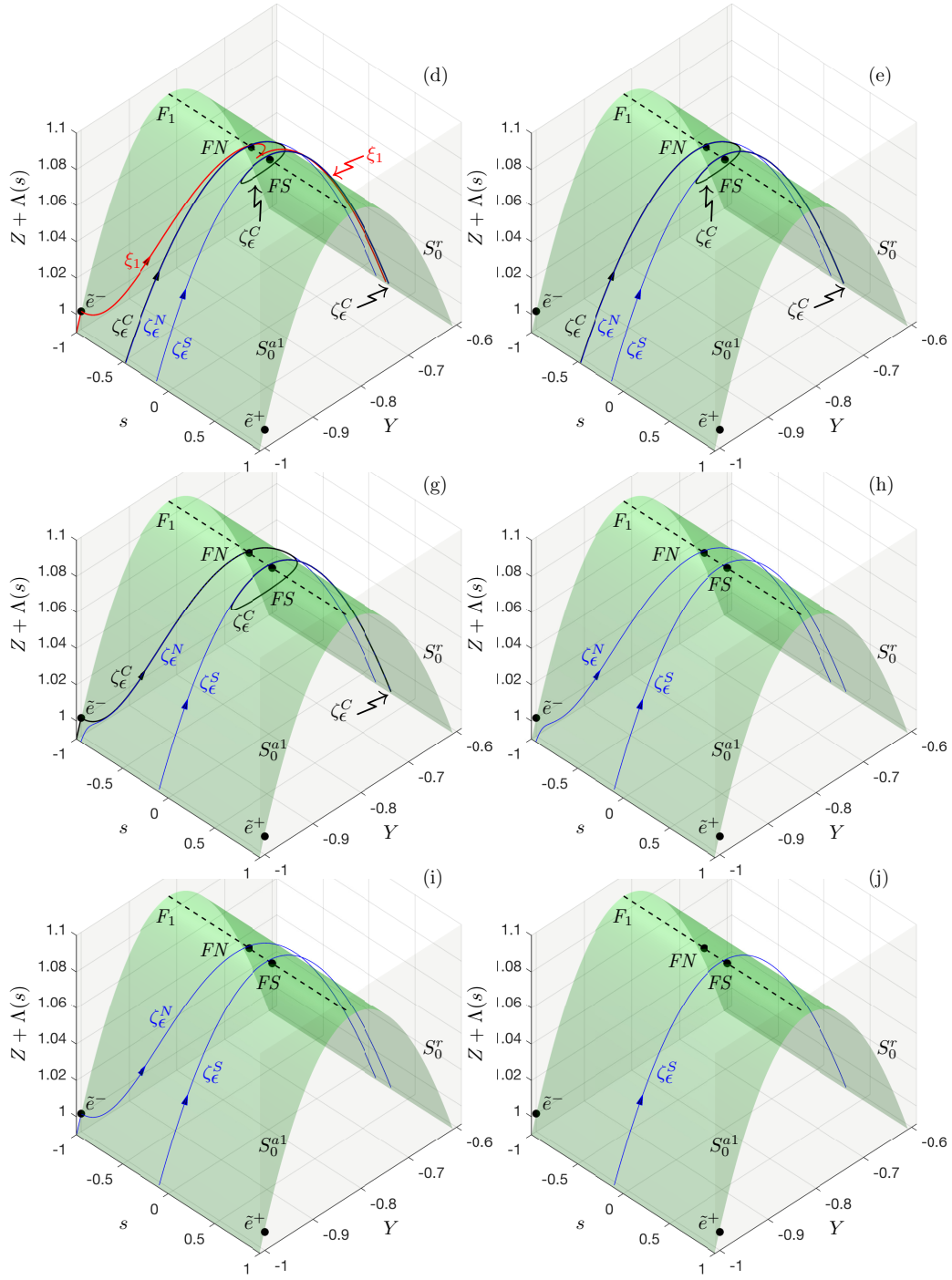

Figure 4.30: Canard evolution of system (4.47) with external input (4.2) for $\Delta = 0.8$, $\epsilon = 0.01$ and different 'rates' r =(d) 0.47862301355, (e) 0.47862302064504999577, (g) 0.48975092687, (h) 0.4897509329, (i) 0.48975686478, (j) 0.489756871415. Zoom in for observation of canards in Fig. 4.28 and Fig. 4.29, including the secondary folded-node canard ξ_1, the composite canard ζ_ε^C, the strong folded-node canard ζ_ε^N and the folded-saddle canard ζ_ε^S.

goes reversible R-tipping [Fig. 4.28 (f)]. This interval is followed by the *second critical range* of r. As the system switches from reversible R-tipping [Fig. 4.28 (f)]

back to tracking [Fig. 4.29 (i)], the unstable manifold $W^{u,[r,\Delta]}(\tilde{e}^-)$ follows a maximal canard that initially stays close to ζ_ε^N and then stays close to ζ_ε^S [Fig. 4.29 (g)-(h)]. When r is increased, the small interval of tracking is followed by the *third critical range* of r. As the system switches from tracking [Fig. 4.29 (i)] back to reversible R-tipping [Fig. 4.29 (k)], the unstable manifold $W^{u,[r,\Delta]}(\tilde{e}^-)$ follows the strong folded-node canard ζ_ε^N [Fig. 4.29 (i)-(j)]. For higher r, we observe reversible R-tipping. Specifically, the unstable manifold $W^{u,[r,\Delta]}(\tilde{e}^-)$ leaves S_ε^{a1} near F_1 along the fast y-direction, moves directly (i.e. without following S_ε^r) towards S_ε^{a2}, spends time on S_ε^{a2}, then leaves S_ε^{a2} near F_2 along the fast y-directionn to return directly to S_ε^{a1} and converge to $\tilde{e}^+$ [Fig. 4.29 (k)-(l)].

The main characteristic of the *complicated quasithreshold* is that the ensuing reversible R-tipping is a continuous transition that occurs via a *number of critical ranges of* r. In other words, the system switches repeatedly between tracking and reversible R-tipping during the transition. While it is clear that different critical ranges of r are associated with different maximal canards related to the stable folded node singularity [51], the exact dynamical mechanism has not been identified so far.

Figure 4.30 shows that critical ranges of r correspond to *infinite-time canard-bifurcations*, in which a maximal canard connects to the saddle $\tilde{e}^-$ from 'below' and disappears. In other words, the maximal canard coalesces with the unstable manifold $W^{u,[r,\Delta]}(\tilde{e}^-)$. In this canonical example, the first critical range of r corresponds to an infinite-time bifurcation of the secondary folded-node canard ξ_1 with one small rotation [Fig. 4.30 (d)]. The second critical range of r corresponds to an infinite-time bifurcation of the composite canard ζ_ε^C [51] that follows segments of the strong folded-node canard ζ_ε^N and the folded-saddle canard ζ_ε^S [Fig. 4.30 (e)-(g)]. The third critical range of r corresponds to an infinite-time bifurcation of the strong folded-node canard ζ_ε^N [Fig. 4.30 (h)-(i)]. The folded-saddle canard ζ_ε^S does not connect to $\tilde{e}^-$ [Fig. 4.30 (j)]. In general, the number of critical ranges depends on ε and the ratio μ of the weak and strong eigenvalues of the folded node equilibrium that controls the number of folded-node canards [76, 105, 58, 103]. The *complicated R-tipping quasithreshold* can be defined as the maximal canards identified in Fig. 4.30, together with their stable sets - the sets of trajectories that converge towards the maximal canard for as long as the canard exists.

Note the difference to the simple Case 1 that exhibits one critical range within which the folded-sadle canard ζ_ε^S connects to $\tilde{e}^-$ from one side and does not disappear, but reappears on the other side of $\tilde{e}^-$.

4.6.3 Highlights of canonical example V

Canonical example V:

- Identifies singular R-tipping edge-states as folded singularities.
- Identifies singular R-tipping thresholds as singular folded-saddle canards or singular strong folded-node canards.
- Shows that compactification transforms R-tipping with quasithresholds into heteroclinic connections from a regular equilibrium to a folded singularity.

The example reveals two types of R-tipping quasithreshold:

- A simple quasithreshold with a single critical range of r corresponds to a folded-saddle canard coalescing with the unstable manifold of a saddle from negative infinity.
- A complicated quasithreshold with multiple critical ranges of r corresponds to folded-node canards and composite canards coalescing with the unstable manifold of a saddle from negative infinity and disappearing in the process.

4.7 Canonical example VI

This canonical example

- Is an example of a slow-fast system with a regular threshold that exhibits reversible R-tipping.

Consider the following path in the directed graph from Fig. 4.1: higher dimensions $\rightarrow$ multiple timescales $\rightarrow$ regular thresholds $\rightarrow$ reversible R-tipping, together with the monostable but excitable slow-fast frozen system in polar coordinates:

$$\begin{aligned} \dot{\varphi} &= -\mu + \sin(\varphi - \lambda), \\ \varepsilon \dot{r} &= r(1-r), \end{aligned} \tag{4.51}$$

where $\varphi = S^1$ is the phase, $r \geq 0$ is the radius, $\lambda \in \mathbb{R}$ is the fixed-in-time input parameter, and $|\mu| < 1$. This system can be viewed as canonical example II augmented with a fast radial variable. In other words, the slow subsystem of (4.51) is the canonical example II.

One can analyse reversible R-tipping in the nonautonomous **canonical exam-**

ple VI:

$$\begin{aligned}\dot{\varphi} &= -\mu + \sin(\varphi - \Lambda(rt)),\\ \varepsilon\dot{r} &= r(1-r).\end{aligned} \tag{4.52}$$

Here, we leave out the detailed R-tipping analysis of this example.

4.8 Canonical example VII

In a system with a regular threshold and a regular edge state, such as the canonical examples I-IV, the R-tipping threshold is given by the stable invariant manifold of the R-tipping edge state $\tilde{\eta}^+$. In a slow-fast system with a quasithreshold that has no edge state, such as the canonical example V, the actual R-tipping quasithresholds are given by the maximal folded-saddle, folded-node or composite canards. This canonical example has both properties - it is slow-fast and has a regular threshold and a regular edge state η - and illustrates the two perspectives of R-tipping analysis that had to be used separately in the previous canonical examples:

- Stable invariant manifold of the R-tipping edge state $\tilde{\eta}^+$ and connecting heteroclinic orbits from $\tilde{e}^-$ to $\tilde{\eta}^+$.
- Canards that are contained in the stable invariant manifold of the R-tipping edge state $\tilde{\eta}^+$ and their bifurcations (connections to $\tilde{e}^-$).

Consider the following path in the directed graph from Fig. 4.1: higher dimensions $\rightarrow$ multiple timescales $\rightarrow$ regular thresholds $\rightarrow$ irreversible R-tipping, together with a bistable frozen system (3.4)–(3.5) in two-dimensions, which is a modified example (4.31):

$$\begin{aligned}\epsilon\frac{dY}{dt} &= -Y(Y^2-2) + Z + \lambda,\\ \frac{dZ}{dt} &= -Y - Z - \lambda,\end{aligned} \tag{4.53}$$

where $0 < \epsilon \ll 1$ is the small parameter, Y and $Z \in \mathbb{R}$ are the fast and slow components of the vector field, respectively, and $\lambda \in \mathbb{R}$ is the external input. System (4.53) has two stable equilibria

$$e_1(\lambda) = (-1, 1-\lambda),\ e_2(\lambda) = (1, -1-\lambda), \tag{4.54}$$

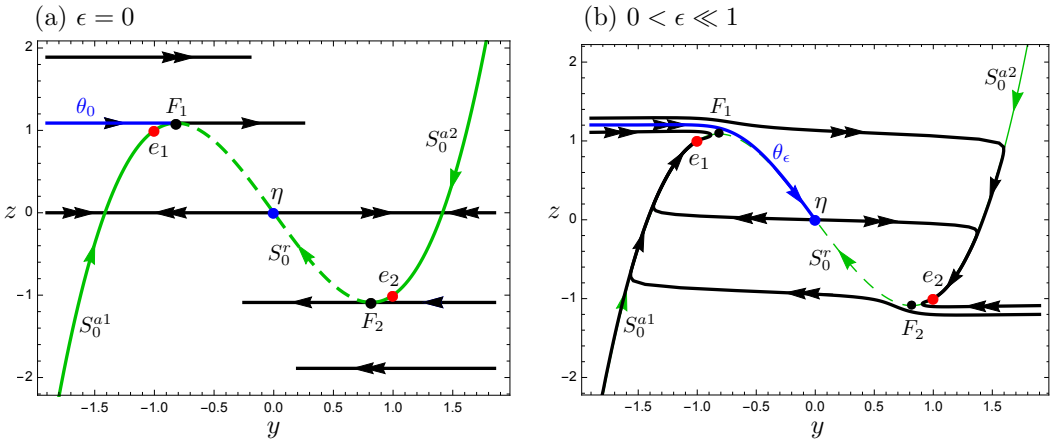

Figure 4.31: Critical manifold S_0 (4.57) colored in green with two (solid) attracting submanifolds S_0^{a1} and S_0^{a2}, and one (dashed) repelling submanifold S_0^r, which are separated by the two folds F_1 and F_2. (a) The singular limit threshold θ_0 (in blue) for $\epsilon = 0$ is given by the center-stable manifold of F_1, and (b) the corresponding threshold θ_ε (in blue) for $0 < \epsilon \ll 1$ is contained within the stable manifold of the unstable equilibrium η, which is also the edge state. Here we omit the center-stable manifold of F_2 since we are interested in the submanifold S_0^{a1} which has the stable equilibrium e_1. There is another stable equilibrium e_2 in the submanifold S_0^{a2}. Double arrows indicate fast solutions and single arrows indicate slow solutions.

and one unstable equilibrium, which is also the edge state

$$\eta(\lambda) = (0, -\lambda). \tag{4.55}$$

The position of $e_1(\lambda)$, $e_2(\lambda)$ and $\eta(\lambda)$ varies along the z-direction with λ.

The slow subsystem (3.10):

$$\frac{dz}{dt} = -y - z - \lambda, \tag{4.56}$$

evolves on the one-dimensional critical manifold (3.11):

$$S_0(\lambda) = \{(y, z) \in \mathbb{R}^2 : -y(y^2 - 2) + z + \lambda = 0\}, \tag{4.57}$$

with two quadratic fold points $F_1(\lambda)$ and $F_2(\lambda)$

$$\begin{aligned} F_1(\lambda) &= \left\{(y, z) \in \mathbb{R}^2 : y = -\sqrt{\frac{2}{3}}, z = \frac{4\sqrt{6}}{9} - \lambda\right\}, \\ F_2(\lambda) &= \left\{(y, z) \in \mathbb{R}^2 : y = \sqrt{\frac{2}{3}}, z = -\frac{4\sqrt{6}}{9} - \lambda\right\}, \end{aligned} \tag{4.58}$$

shown in Fig. 4.31. Alternatively, $S_0(\lambda)$ consists of a union of all equilibria of the

fast subsystem (3.12):

$$\frac{dy}{d\tau} = -y(y^2 - 2) + z + \lambda, \tag{4.59}$$

where the slow z-component becomes an additional parameter.

Note that system (4.53) shown in Fig. 4.31 and system (4.31) shown in Fig. 4.19 have the same singular limit threshold. Thus, the threshold instability arguments from Fig. 4.20 apply to this example after replacing $e(\lambda)$ with $e_1(\lambda)$.

We now analyse irreversible R-tipping from $e_1(rt)$ in the nonautonomous **canonical example VII**:

$$\begin{aligned} \epsilon\frac{dY}{dt} &= -Y(Y^2 - 2) + Z + \Lambda(rt), \\ \frac{dZ}{dt} &= -Y - Z - \Lambda(rt), \end{aligned} \tag{4.60}$$

parametrised by ϵ, and the magnitude Δ and rate r of the parameter shift.

4.8.1 Monotone bi-asymptotically constant input: Folded saddle-node type-I

Consider system (4.60) with monotone bi-asymptotically external input (4.2), and the common compactification transformation (2.66) with compactification parameter $\alpha = 1$ gives the compactified slow-fast system (3.30)–(3.32) as

$$\begin{aligned} \epsilon\frac{dY}{dt} &= -Y(Y^2 - 2) + Z + \frac{\Delta}{2}\frac{(1+s)^2}{(1+s^2)}, \\ \frac{dZ}{dt} &= -Y - Z - \frac{\Delta}{2}\frac{(1+s)^2}{(1+s^2)}, \\ \frac{ds}{dt} &= \frac{r}{2}(1 - s^2), \end{aligned} \tag{4.61}$$

where α satisfies the compactification condition $0 < \alpha \leq 2$, and ensures that invariant subspaces $\{s = \pm 1\}$ have an orthogonal transverse eigenvector. System (4.61) has two stable equilibria

$$\tilde{e}_1^+ = (-1, 1 - \Delta, 1),\ \tilde{e}_2^+ = (1, -1 - \Delta, 1), \tag{4.62}$$

one unstable equilibrium in the invariant subspace $\{s = 1\}$, which is also the R-tipping edge state

$$\tilde{\eta}^+ = (0, -\Delta, 1), \tag{4.63}$$

and three unstable equilibria in the invariant subspace $\{s = -1\}$

$$\tilde{e}_1^- = (-1, 1, -1),\ \tilde{\eta}^- = (0, 0, -1),\ \tilde{e}_2^- = (1, -1, -1). \tag{4.64}$$

Because system (4.61) has the same critical manifold S_0 and fast subsystem as system (4.47), we implement the same state-dependent time rescalling T defined as (4.41) to obtain the compactified desingularised slow subsystem (3.37)–(3.39) of system (4.61) as:

$$\begin{aligned}
\frac{dy}{dT} &= -y^3 + y + \frac{\Delta r(1-s^2)^2}{2(1+s^2)^2}, \\
\frac{dz}{dT} &= (3y^2 - 2)\left(-y - z - \frac{\Delta}{2}\frac{(1+s)^2}{(1+s^2)}\right), \\
\frac{ds}{dT} &= \frac{r(3y^2-2)(1-s^2)}{2},
\end{aligned} \tag{4.65}$$

that describes the slow dynamics of all three variables on the critical manifold S_0 in the compactified (y, z, s) phase space and evolves on the new slow timescale T, which can be reduced to

$$\begin{aligned}
\frac{dy}{dT} &= -y^3 + y + \frac{\Delta r(1-s^2)^2}{2(1+s^2)^2}, \\
\frac{ds}{dT} &= \frac{r(3y^2-2)(1-s^2)}{2},
\end{aligned} \tag{4.66}$$

in the projection onto the (y, s)-subspace, and then translate from T to t by reversing the flow between F_1 and F_2. In the invariant subspace $\{s = 1\}$, system (4.66) has two stable equilibria

$$\tilde{e}_1^+ = (-1, 1),\ \tilde{e}_2^+ = (1, 1), \tag{4.67}$$

and one unstable equilibrium, which is also the R-tipping edge state

$$\tilde{\eta}^+ = (0, 1). \tag{4.68}$$

In the invariant subspace $\{s = -1\}$, there are three unstable equilibria

$$\tilde{e}_1^- = (-1, -1),\ \tilde{\eta}^- = (0, -1),\ \tilde{e}_2^- = (1, -1), \tag{4.69}$$

and we will be interested in R-tipping from $\tilde{e}_1^-$.

Additionally, analysis of folded equilibria [see Eq. (3.25)] reveals a saddle-node

bifurcation of folded equilibria on F_1 (denoted FSN) when

$$r = r^{FSN} = \frac{2\sqrt{6}}{9\Delta}.$$

The bifurcation is referred to as a folded saddle-node type-I [105, 107, 104], and gives rise to a folded saddle (denoted FS) and a folded sink (folded node FN or folded focus FF) on F_1:

$$(y, s) = \left(-\sqrt{\frac{2}{3}}, \pm \sqrt{\frac{\sqrt{\Delta r} - \sqrt{\frac{2}{3}\sqrt{\frac{2}{3}}}}{\sqrt{\Delta r} + \sqrt{\frac{2}{3}\sqrt{\frac{2}{3}}}}} \right).$$

For simplicity, here we focus directly on the slow-fast dynamics for $0 < \epsilon \ll 1$ of system (4.61). The normally hyperbolic components of the critical manifold persist as locally invariant *attracting slow manifolds* S_ε^{a1} and S_ε^{a2}, and a *repelling slow manifold* S_ε^r [47, 56, 75]. Typically, S_ε^a and S_ε^r detach along F, except near folded singularities where S_ε^a and S_ε^r intersect, possibly in a very complicated way [121, 108]. In Fig. 4.32 and Fig. 4.33, we plot S_0^{a1}, S_0^{a2}, S_0^r (in green) as approximations of S_ε^{a1}, S_ε^{a2} and S_ε^r, respectively. We plot the unstable manifold $W^{u,[r,\Delta]}(\tilde{e}_1^-)$ (in red) together with folded-saddle ζ_ε^S and strong folded-node ζ_ε^N canards (in blue). For reference, we also include the remaining components of the singular limit system: the two fold lines F_1 and F_2, and the folded singularities FS and FN or FF.

Similar to canonical example V, there are two cases [51] which we describe below using different values of Δ.

Case 1: Folded-saddle canard

We set $\Delta = 0.5$, and the different dynamics of system (4.61) are summarised in Fig. 4.32, which shows selected (Y, Z, s) phase portraits for $\epsilon = 0.01$ and different rates r. The invariant subspace $\{s = -1\}$ contains the stable equilibrium $\tilde{e}_1^-$, which is stable within the subspace, and unstable in the transverse s-direction. The invariant subspace $\{s = 1\}$ contains two stable equilibria $\tilde{e}_1^+$ and $\tilde{e}_2^+$, and one unstable equilibrium $\tilde{\eta}^+$, which is also the R-tipping edge state.

On the one hand, R-tipping analysis can be carried out from the perspective of regular thresholds in terms of connecting orbits, meaning that we can ignore all the concepts related to the slow-fast nature of the problem (i.e. critical manifolds and folded singularities) and focus on the unstable manifold $W^{u,[r,\Delta]}(\tilde{e}_1^-)$ (in red) in relation to the R-tipping threshold $W^{s,[r,\Delta]}(\tilde{\eta}^+)$, see Fig 4.32.

If r is sufficiently small, the unstable manifold $W^{u,[r,\Delta]}(\tilde{e}_1^-)$ closely tracks the

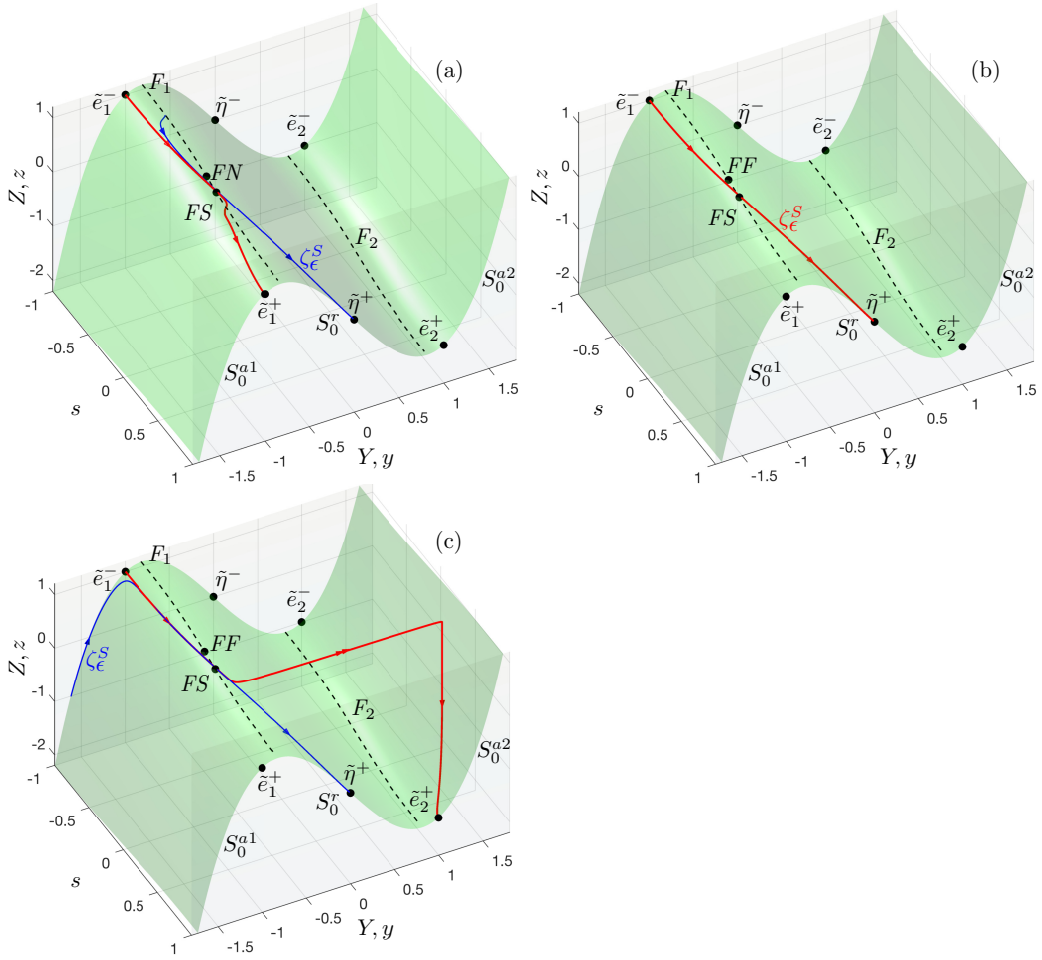

Figure 4.32: Phase portraits of system (4.61) with external input (4.2) for $\Delta = 0.5$, $\epsilon = 0.01$ and different 'rates' r=(a) 1.111, (b) 1.1156065895, (c) 1.1157796258. The heteroclinic $\tilde{e}_1^-$-to-$\tilde{\eta}^+$ connection or the infinite-time bifurcation of the folded-saddle canard ζ_ϵ^S (in blue) that connects to $\tilde{e}_1^-$ in panel (b) indicates the critical rate r_c for irreversible R-tipping. FS, FN and FF are respectively the folded saddle, folded node and folded focus singularities, and the system dynamics with trajectories colored in red.

moving stable equilibrium $e_1(rt)$, and accumulates on $\tilde{e}_1^+$ [Fig 4.32 (a)]. When r reaches the critical rate r_c, the unstable manifold $W^{u,[r,\Delta]}(\tilde{e}_1^-)$ accumulates on the R-tipping edge state $\tilde{\eta}^+$ [Fig 4.32 (b)]. This is a critical transition from tracking $e_1(rt)$ to irreversible R-tipping, characterized by the heteroclinic $\tilde{e}_1^-$-to-$\tilde{\eta}^+$ connection, which can be computed by the Lin's method [109] in AUTO [110]. When $r > r_c$, $W^{u,[r,\Delta]}(\tilde{e}_1^-)$ converges to the other stable equilibrium $\tilde{e}_2^+$ [Fig 4.32 (c)].

On the other hand, R-tipping analysis can be carried out from the perspective of folded singularities and canards. Figure 4.32 shows that the critical rate r_c corresponds to an *infinite-time canard-bifurcation*, in which the folded-saddle canard ζ_ε^S connects to the saddle $\tilde{e}_1^-$ from 'above' [Fig. 4.32 (a)] and reappears from 'below' [Fig. 4.32 (c)]. In other words, the maximal canard coalesces with the un-

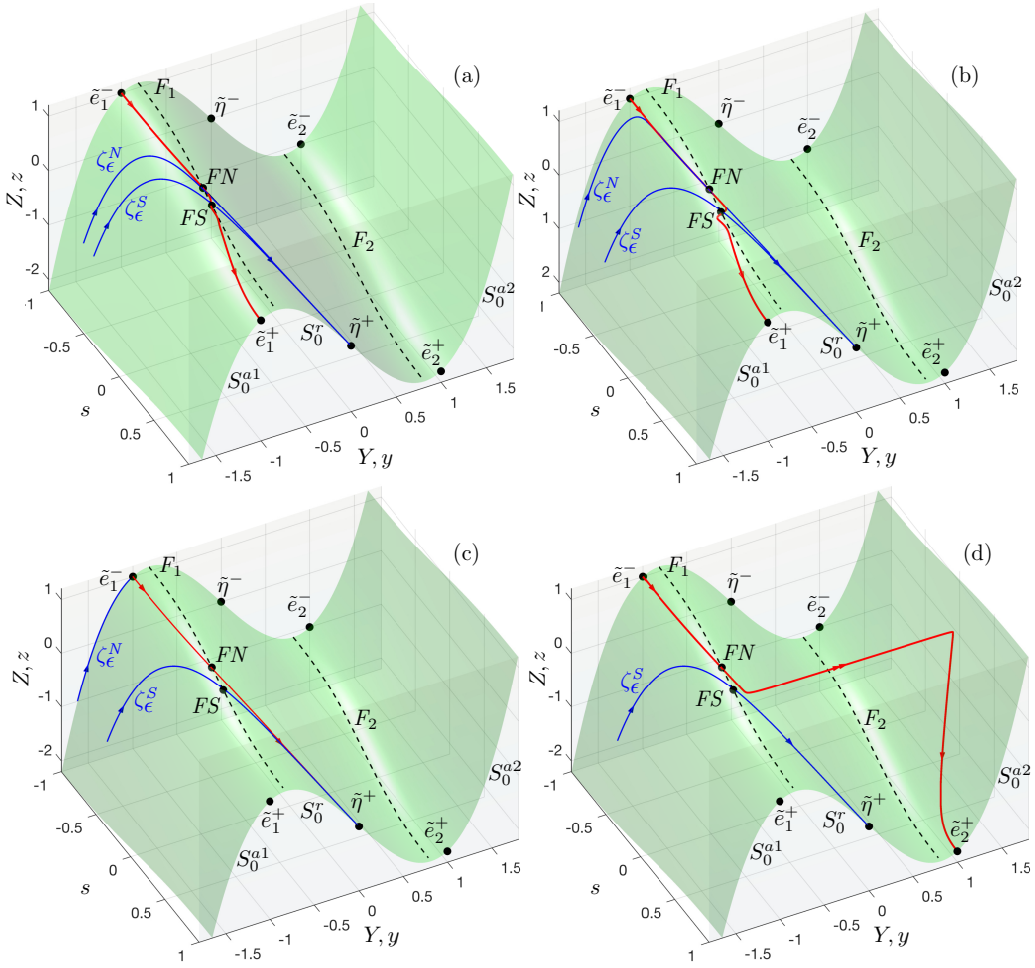

Figure 4.33: Phase portraits of system (4.61) with external input (4.2) for $\Delta = 1.0$, $\epsilon = 0.01$ and different 'rates' r =(a) 0.553, (b) 0.55958, (c) 0.5595884300528, (d) $r = 0.5595884360$. The heteroclinic $\tilde{e}_1^-$-to-$\tilde{\eta}^+$ connection or the infinite-time bifurcation of the strong folded-node canard ζ_ϵ^N (in blue) that connects to $\tilde{e}_1^-$ in panel (c) indicates the critical rate r_c for irreversible R-tipping. FS and FN are respectively the folded saddle and folded node singularities, the system dynamics with trajectories colored in red, and ζ_ϵ^S is the folded-saddle canard (in blue).

stable manifold $W^{u,[r,\Delta]}(\tilde{e}_1^-)$ [Fig. 4.32 (b)]. This is the same canard bifurcation as in canonical example V. Thus, we expect that the R-tipping transition takes place within a *single critical interval* of r. The main difference from canonical example V is that, in the current example, the folded-saddle canard ζ_ε^S is contained in the regular R-tipping threshold $W^{s,[r,\Delta]}(\tilde{\eta}^+)$. This means that, despite having a critical range of r, the ensuing irreversible R-tipping here is not a continuous critical transition and we are able to define a unique critical rate r_c in the following sense: $W^{u,[r,\Delta]}(\tilde{e}_1^-)$ accumulates on $\tilde{e}_1^+$ if $0 < r < r_c$, on $\tilde{\eta}^+$ if $r = r_c$, and on $\tilde{e}_2^+$ if $r > r_c$.

Case 2: Folded-node canard

We set $\Delta = 1.0$, and the different dynamics of system (4.61) are summarised in Fig. 4.33, which show selected (Y, Z, s) phase portraits for $\epsilon = 0.01$ and different rates r. The invariant subspace $\{s = -1\}$ contains the stable equilibrium $\tilde{e}_1^-$, which is stable within the subspace, and unstable in the transverse s-direction. The invariant subspace $\{s = 1\}$ contains two stable equilibria $\tilde{e}_1^+$ and $\tilde{e}_2^+$, and one unstable equilibrium $\tilde{\eta}^+$, which is also the R-tipping edge state.

On the one hand, R-tipping analysis can be carried out from the perspective of regular thresholds in terms of connecting orbits, meaning that we can ignore all the concepts related to the slow-fast nature of the problem (i.e. critical manifolds and folded singularities) and focus on the unstable manifold $W^{u,[r,\Delta]}(\tilde{e}_1^-)$ (in red) in relation to the R-tipping threshold $W^{s,[r,\Delta]}(\tilde{\eta}^+)$, see Fig 4.33.

If r is sufficiently small, the unstable manifold $W^{u,[r,\Delta]}(\tilde{e}_1^-)$ closely tracks the moving stable equilibrium $e_1(rt)$, and accumulates on $\tilde{e}_1^+$ [Fig 4.33 (a)-(b)]. When r reaches the critical rate r_c, the unstable manifold $W^{u,[r,\Delta]}(\tilde{e}_1^-)$ accumulates on the R-tipping edge state $\tilde{\eta}^+$ [Fig 4.33 (c)]. This is a critical transition from tracking $e_1(rt)$ to irreversible R-tipping, characterized by the heteroclinic $\tilde{e}_1^-$-to-$\tilde{\eta}^+$ connection, which can be computed by the Lin's method [109] in AUTO [110]. When $r > r_c$, $W^{u,[r,\Delta]}(\tilde{e}_1^-)$ converges to the other stable equilibrium $\tilde{e}_2^+$ [Fig 4.33 (d)].

On the other hand, R-tipping analysis can be carried out from the perspective of folded singularities and canards. Figure 4.33 shows that the critical rate r_c corresponds to an *infinite-time canard-bifurcation*, in which the strong folded-node canard ζ_ε^N connects to the saddle $\tilde{e}_1^-$ from 'below' [Fig. 4.33 (a)-(b)] and disappears [Fig. 4.33 (d)]. In other words, the maximal canard ζ_ε^N coalesces with the unstable manifold $W^{u,[r,\Delta]}(\tilde{e}_1^-)$ [Fig. 4.33 (c)]. In contrast to canonical example V, where the R-tipping transition occurs via a *number of critical ranges of* r that correspond to several infinite-time bifurcations of folded-node and composite canards, here we expect that the R-tipping transition takes place within a *single critical interval* of r that corresponds to the only infinite-time bifurcation of the strong folded-node canard ζ_ε^N. Moreover, in the current example, the strong folded-node canard ζ_ε^N is contained in the regular R-tipping threshold $W^{s,[r,\Delta]}(\tilde{\eta}^+)$. This means that, despite having a critical range of r, the ensuing irreversible R-tipping here is not a continuous critical transition and we are able to define a unique critical rate r_c in the following sense: $W^{u,[r,\Delta]}(\tilde{e}_1^-)$ accumulates on $\tilde{e}_1^+$ if $0 < r < r_c$, on $\tilde{\eta}^+$ if $r = r_c$, and on $\tilde{e}_2^+$ if $r > r_c$.

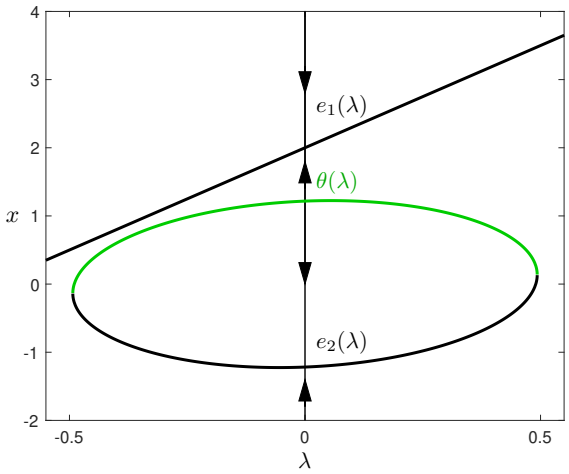

Figure 4.34: Bifurcation diagram of system (4.70) with respect to λ, with two stable equilibria $e_1(\lambda)$ and $e_2(\lambda)$ (in black), and one unstable equilibrium which is the threshold $\theta(\lambda)$ (in green).

4.8.2 Highlights of canonical example VII

Canonical example VII shows two perspectives of analyzing R-tipping due to regular thresholds in the slow-fast system: in terms of connecting heteroclinic orbits between regular equilibria, and in terms of folded singularities and canards.

4.9 Canonical example of R-B-tipping

Note that our theory requires the moving thresholds and edge states persistent until the future limit (the positive infinity) for R-tipping due to regular thresholds. However, R-tipping can still happen beyond our theory for example the thresholds disappear at some time or do not exist in the future limit. We show such an example of *R-B-tipping* to

- Highlight the R-B-tipping phenomenon, that is to say, R-tipping followed by B-tipping due to a bifurcation of the moving threshold.
- Present how to identify the critical rate of R-tipping in such a case.
- Illustrate the transitions between irreversible R-tipping and R-B-tipping.

Consider a frozen system in one-dimension

$$\dot{x} = \left(x^2 + (2.5\lambda - x/9)^2 - 1.5\right)(3\lambda - x + 2)\,, \tag{4.70}$$

where $\lambda \in \mathbb{R}$ is the fixed-in-time input parameter, and when $\lambda \in (-0.4929, 0.4929)$,

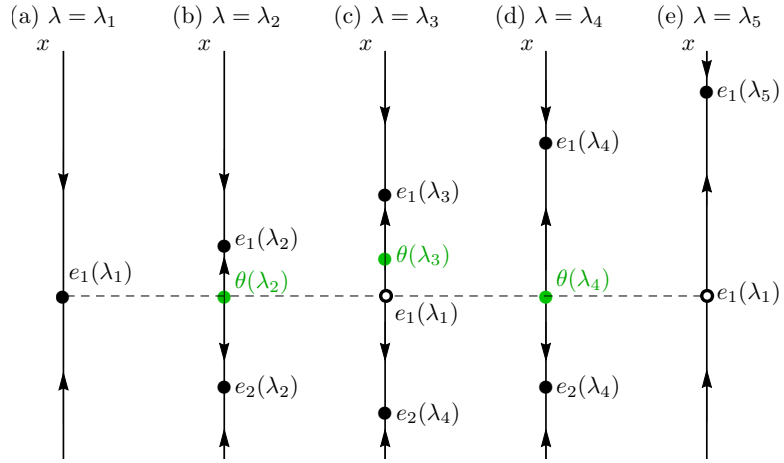

Figure 4.35: Phase portraits of system (4.70) for different values of the input parameter $\lambda =$ (a) $\lambda_1 = -0.5$, (b) $\lambda_2 > -0.4929$, (c) λ_3, (d) $\lambda_4 < 0.4929$, and (e) $\lambda_5 = 0.5$ illustrate threshold instability of the stable equilibrium e_1, where $\lambda_1 < \lambda_2 < \lambda_3 < \lambda_4 < \lambda_5$.

the system has two stable equilibria

$$e_1(\lambda) = 3\lambda + 2, \quad \text{and} \quad e_2(\lambda) = \frac{45\lambda - 9\sqrt{492 - 2025\lambda^2}}{164},$$

and one unstable equilibrium which is the regular threshold $\theta(\lambda)$ and edge state $\eta(\lambda)$ at the same time:

$$\theta(\lambda) = \frac{45\lambda + 9\sqrt{492 - 2025\lambda^2}}{164},$$

however, when $\lambda \in (-\infty, -0.4929)$ or $\lambda \in (0.4929, +\infty)$, the system has only one stable equilibrium $e_1(\lambda) = 3\lambda + 2$. The bifurcation diagram of system (4.70) with respect to λ is shown in Fig 4.34.

Fig 4.35 shows the phase portraits of system (4.70) for five different values of the input parameter λ along the parameter path

$$P_\lambda = \{\lambda : -0.5 \leq \lambda \leq 0.5\}.$$

If $\lambda > \lambda_2$, then $e_1(\lambda_1) = \theta(\lambda_2)$ and $e_1(\lambda_1)$ lies on different sides of $\theta(\lambda)$ for λ arbitrarily close to λ_2. This means the stable equilibrium $e_1(\lambda)$ is *threshold unstable* on P_λ; see Definition 3.3.2. Particularly here, the position of $e_1(\lambda_1)$ [Fig 4.35 (a)] overlaps the positions of $\theta(\lambda_2)$ [Fig 4.35 (b)] and $\theta(\lambda_4)$ [Fig 4.35 (d)]. Even though the threshold $\theta(\lambda)$ does not exist when $\lambda = \lambda_1$ and $\lambda = \lambda_5$, we can still qualitatively analyze R-tipping instability of the system by the concepts of the moving equilibria, moving thresholds, and threshold instability as before. Suppose the system with $\Lambda(rt)$ instead of λ, which increases from λ_1 to

λ_5 monotonously. If the increasing rate r is slow enough, the moving stable state $e_1(rt)$ always stays above the existed moving threshold $\theta(rt)$, where the system tracks $e_1(rt)$ continuously. If the increasing rate r is fast enough for λ changing to λ_3 [Fig 4.35 (c)] from λ_1, the moving stable state $e_1(rt)$ becomes below the existed $\theta(rt)$ and the system now tracks the existed moving stable state $e_2(rt)$, where R-tipping happens. As $e_2(rt)$ disappears with time, the system still finally converges to $e_1(rt)$, where B-tipping happens. The whole process includes R-tipping followed by B-tipping, hence the name R-B-tipping. When the increasing rate is even larger for λ changing to λ_5 [Fig 4.35 (e)] from λ_1, the existed moving threshold $\theta(rt)$ does not make any difference since it disappears too fast for the system to have any response. The system just ignores the existed moving threshold $\theta(rt)$ and converges to $e_1(rt)$.

Then we analyse R-tipping from e_1 in the nonautonomous **canonical example of R-B-tipping**:

$$\dot{x} = \left(x^2 + (2.5\Lambda(rt) - x/9)^2 - 1.5\right)(3\Lambda(rt) - x + 2), \tag{4.71}$$

with the consideration of respectively monotone bi-asymptotically external input

$$\Lambda(rt) = \frac{\Delta}{2}\tanh(rt), \tag{4.72}$$

where $\Lambda(rt) \in [-\frac{\Delta}{2}, \frac{\Delta}{2}]$, and non-monotone bi-asymptotically external input

$$\Lambda(rt) = \Delta\left(\mathrm{sech}(rt) - 0.5\right), \tag{4.73}$$

where $\Lambda(rt) \in [-\frac{\Delta}{2}, \frac{\Delta}{2}]$.

4.9.1 Monotone bi-asymptomatically constant input

Consider system (4.71) with monotone external input (4.72), and the common compactification transformation (2.66) with compactification parameter $\alpha = 1/1.2$. The choice of α satisfies the compactification condition $0 < \alpha \leq 2$, and ensures that invariant subspaces $\{s = \pm 1\}$ have an orthogonal transverse eigenvector. That gives the compactified system (4.4) as:

$$\begin{aligned} \dot{x} &= \left(x^2 + (2.5\Lambda(s) - x/9)^2 - 1.5\right)(3\Lambda(s) - x + 2), \\ \dot{s} &= \frac{5r}{12}(1 - s^2), \end{aligned} \tag{4.74}$$

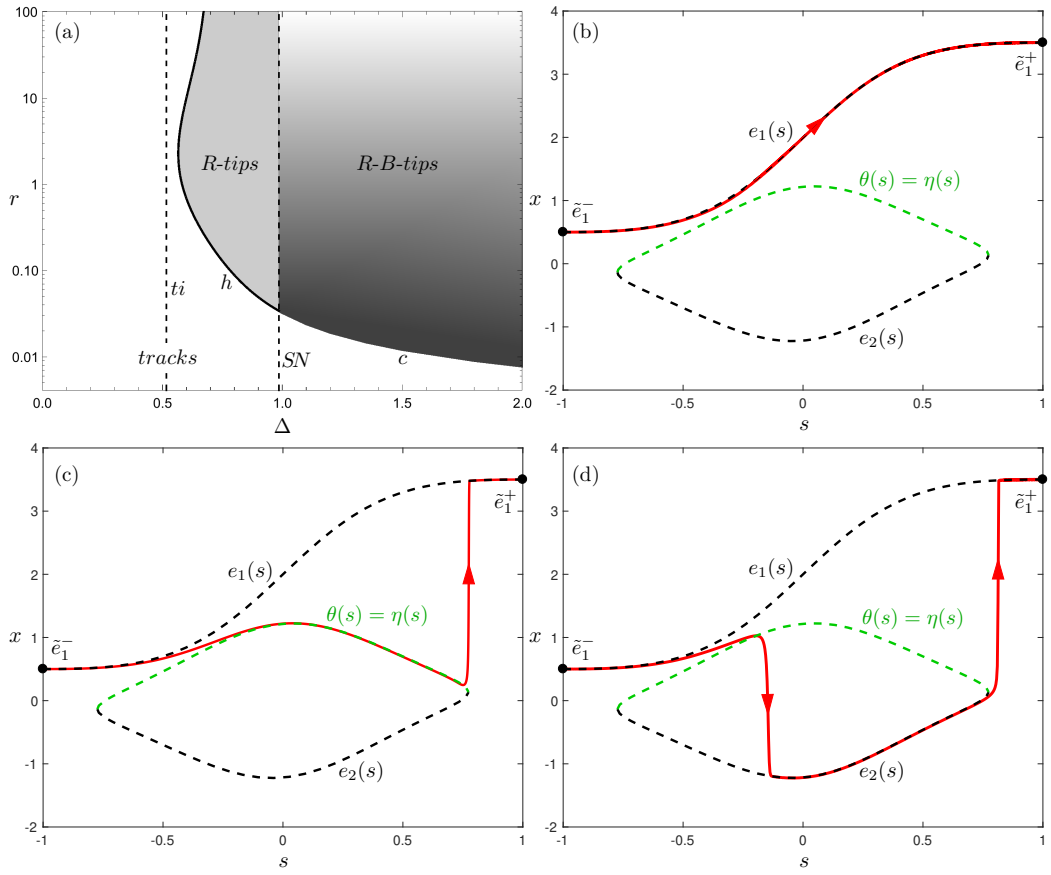

Figure 4.36: (a) The (Δ, r) tipping diagram for the canonical example (4.71) with monotone external input (4.72) contains regions of (white) tracking the moving stable equilibrium $e_1(rt)$ continuously and (grey) R-tipping. The (dashed) ti line denotes the forward threshold instability boundary for e_1, and SN line indicates where saddle-node bifurcation of θ and e_2 happens. We use respectively h and c to represent transition curves due to the conditions of heteroclinic connection and the maximum canard. (b)-(d) Phase states of system (4.74) in red when $\alpha = 1/1.2$ and $\Delta = 1$ for different rates $r =$ (b) 0.01, (c) 0.032434458316, and (d) 0.0326. The moving stable states $e_1(s)$ and $e_2(s)$ are indicated by the dashed black curves, and the moving unstable state $\theta(s)$, namely the moving threshold, indicated by the green dashed curve.

parametrised by Δ and r, and

$$\Lambda(s) = \frac{\Delta}{2}\frac{(1+s)^{2/\alpha} - (1-s)^{2/\alpha}}{(1+s)^{2/\alpha} + (1-s)^{2/\alpha}}. \tag{4.75}$$

The different dynamics of system (4.74) are summarised in Fig. 4.36, which shows the (Δ, r) tipping diagram together with selected (x, s) phase portraits of system (4.74) for $\Delta = 1$ and different 'rates' r. The invariant subspace $\{s = -1\}$ contains the saddle $\tilde{e}_1^-$, which is stable within the subspace and unstable in the transverse s-direction. The invariant subspace $\{s = 1\}$ contains the stable

equilibrium $\tilde{e}_1^+$. The moving stable states $e_1(s)$ and $e_2(s)$ are indicated by the dashed black curves, and the moving unstable state $\theta(s)$, namely the moving threshold, is indicated by the green dashed curve. The R-tipping threshold is given by the maximum canard, and we will introduce how to calculate it in the followings.

If r is sufficiently small, there is an open half-circle of initial states centred at $\tilde{e}_1^-$, all of which closely track the moving stable equilibrium $e_1(s)$ continuously [Fig. 4.36(b)]. As r is increased until a *critical range of* r, any open half-circle of initial states centred at $\tilde{e}_1^-$ contains initial states those track the moving stable equilibrium $e_1(s)$ continuously and converge to $\tilde{e}_1^+$, as well as initial states those track the moving stable equilibrium $e_1(s)$ for some time interval, afterwards track $e_2(s)$ intermediately but still converge to $\tilde{e}_1^+$, where R-B-tipping happens [Fig. 4.36(c)]. Such a *critical range of* r corresponds to the maximum canard, that follows the slow manifold with the longest time and gives a computable condition for the critical transition between this tracking and R-B-tipping, which can be solved by a boundary value problem [123] in AUTO [110]. Such a condition can be computed for different values of Δ so as to gain curve c part of (Δ, r) tipping diagram when Δ is larger than SN line shown in Fig. 4.36(a). Note that SN line indicates where saddle-node bifurcation of θ and e_2 happens. To be more precise, when Δ is larger than SN line only e_1 exists all the time, while when Δ is smaller than SN line, there are always three equilibria e_1, θ and e_2. In such a case, since the regular threshold θ and another stable equilibrium e_2 are persistent all the time, the ensuing R-B-tipping turns out to be irreversible e_1-to-e_2 R-tipping. As a result, we calculate the critical rate r_c given by the heteroclinic connection from $\tilde{e}_1^-$ to the edge state (namely the threshold itself) at $\{s = 1\}$ through the Lin's method [109], which can be continued on (Δ, r) parameter space to gain curve h part of (Δ, r) tipping diagram when Δ is smaller than SN line [Fig. 4.36(a)]. This is similar to our canonical example I in Section 4.2.

For higher r, there is an open half-circle of initial states centred at $\tilde{e}_1^-$, all of which track the moving stable equilibrium $e_1(s)$ for some time interval, afterwards track the moving stable equilibrium $e_2(s)$ intermediately with the final convergence to $\tilde{e}_1^+$ [Fig. 4.36(d)]. We do not show the case when r is even larger, where the system has no time to respond to the appearance and disappearance of the moving threshold $\theta(s)$ and the moving stable state $e_2(s)$. Instead, in Fig. 4.36(a) we mark the R-B-tipping area with gradient color to present the fact that as the rate r continues to increase after R-B-tipping, the system gradually ignores θ and e_2. Note that, as Δ increases, the transition condition of heteroclinic connection for irreversible R-tipping turns into the maximum canard for R-B-tipping.

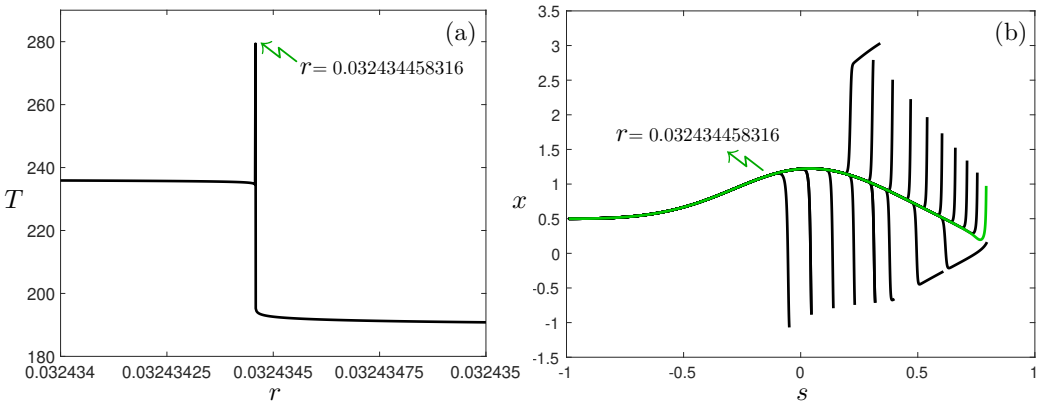

Figure 4.37: (a) Continuation parameter space (r, T) with the local maximum integration time T when $r = 0.032434458316$. Panel (b) shows a family of obits started from the fixed initial conditions $(x_T(0), s_T(0)) = (0.5, -1 + d)$ with the same arc length $L = 3.4$, where $d = 0.01$. The orbit in green is the computed maximum canard to follow the slow manifold with the longest time when $r = 0.032434458316$, which has the local maximum integration time T in panel (a).

Now we introduce how to calculate the maximum canard by a boundary value problem [123] in AUTO [110]. At first, rescale the vector field of system (4.74) as

$$\begin{aligned} \dot{x}_T &= T\dot{x}, \\ \dot{s}_T &= T\dot{s}, \end{aligned} \tag{4.76}$$

where any of the system orbits is parametrised over the unit time interval $[0, 1]$ and the corresponding integration time T turns out to be a separate parameter [124].

The boundary conditions are upon the initial conditions of the system orbits as

$$\begin{aligned} x_T(0) &= x \text{ of } \tilde{e}_1^-, \\ s_T(0) &= -1 + d, \end{aligned} \tag{4.77}$$

where it means that all the orbits start at a distance d from $\tilde{e}_1^-$ along the unstable eigenvector of the saddle $\tilde{e}_1^-$.

The integration condition gives constraints on the L_2-norm of the rescaled derivatives $\dot{x}_T$ and $\dot{s}_T$ as

$$\int_0^1 \sqrt{\dot{x}_T^2 + \dot{s}_T^2}\, dt = L, \tag{4.78}$$

where L is the fixed parameter of the arc length of the orbits.

So we fix the initial conditions of the orbit with a choice of the distance d

to $\tilde{e}_1^-$ along its unstable eigenvector, and let the orbit evolve with integration time T until it reaches a proper arc length L. Then we fix the arc length of the orbit L, and continue the solution with varying the two parameters including the rate r and the integration time T. We found a family of orbits started from the fixed initial conditions until the same selected arc length shown in Fig. 4.37(b). Fig. 4.37(a) shows the corresponding continuation (r, T)-parameter space, with the local maximum integration time T when varying the rate r until $r = 0.032434458316$. The orbit in green shown in Fig. 4.37(b) is the computed maximum canard to follow the slow manifold with the longest time, namely with the local maximum integration time in Fig. 4.37(a). The maximum canard is a separation between the scenario in Fig. 4.36(b) and the scenario in Fig. 4.36(d), where R-B-tipping happens.

To test the robustness of the choice of arc length L on the calculation of the maximum canard and identification of the rate r, we choose different arc lengths respectively $L = 2.6$, $L = 3$ and $L = 3.4$. Fig. 4.38(a) shows the continuation parameter space (r, T), with the local maximum integration time T for each selected arc length L. The corresponding computed maximum canards are shown in Fig. 4.38(b). The computed maximum canards are identical except the lengths shown in Fig. 4.38(b), all of which are identified at the same rate $r = 0.032434458316$ with the local maximum integration time T shown in Fig. 4.38(a). Note that an appropriate arc length L still needs to be chosen in the sense that the orbit with the arc length L should be long enough to approximate the position where the moving threshold $\theta(s)$ disappears in Fig. 4.36(c). A too large or small arc length L may cause the difficulty or impossibility in the identification of the local maximum integration time.

4.9.2 Non-monotone bi-asymptomatically constant input

Consider system (4.71) with non-monotone external input (4.73), and the common compactification transformation (2.66) with compactification parameter $\alpha = 1/1.2$. The choice of α satisfies the compactification condition $0 < \alpha \leq 1$, and ensures that invariant subspaces $\{s = \pm 1\}$ have an orthogonal transverse eigenvector. That gives the compactified system (4.4) as:

$$\begin{aligned} \dot{x} &= \left(x^2 + (2.5\Lambda(s) - x/9)^2 - 1.5\right)(3\Lambda(s) - x + 2), \\ \dot{s} &= \frac{5r}{12}(1 - s^2), \end{aligned} \tag{4.79}$$

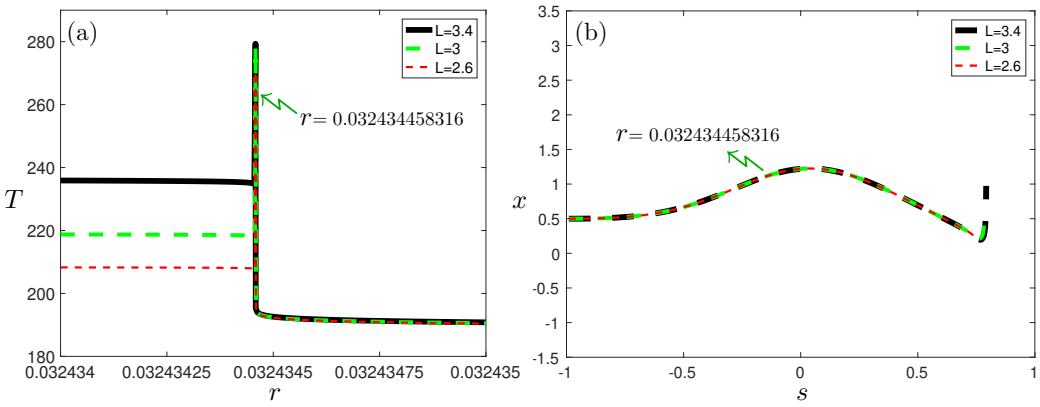

Figure 4.38: (a) Continuation parameter space (r, T) with the local maximum integration time T when $r = 0.032434458316$ for different arc lengths L respectively $L = 2.6$, $L = 3$, and $L = 3.4$. For the selected L, panel (b) shows the corresponding computed maximum canards started from the fixed initial conditions $(x_T(0), s_T(0)) = (0.5, -1 + d)$, where $d = 0.01$.

parametrised by Δ and r, and

$$\Lambda(s) = \frac{\Delta}{2}\frac{4(1-s^2)^{1/\alpha} - (1+s)^{2/\alpha} - (1-s)^{2/\alpha}}{(1+s)^{2/\alpha} + (1-s)^{2/\alpha}}. \tag{4.80}$$

The different dynamics of system (4.79) are summarised in Fig. 4.39, which shows the (Δ, r) tipping diagram together with selected (x, s) phase portraits of system (4.79) for $\Delta = 1$ and different 'rates' r. The invariant subspace $\{s = -1\}$ contains the saddle $\tilde{e}_1^-$, which is stable within the subspace and unstable in the transverse s-direction. The invariant subspace $\{s = 1\}$ contains the stable equilibrium $\tilde{e}_1^+$. The moving stable states $e_1(s)$ and $e_2(s)$ are indicated by the dashed black curves, and the moving unstable state $\theta(s)$, namely the moving threshold, is indicated by the green dashed curve. The main difference here from monotone external input is that there exist multiple maximum canards and the R-tipping thresholds are given by these maximum canards.

If r is sufficiently small, there is an open half-circle of initial states centred at $\tilde{e}_1^-$, all of which closely track the moving stable equilibrium $e_1(s)$ continuously [Fig. 4.39(b)]. As r is increased until the first *critical range of* r, any open half-circle of initial states centred at $\tilde{e}_1^-$ contains initial states those track the moving stable equilibrium $e_1(s)$ continuously and converge to $\tilde{e}_1^+$, as well as initial states those track the moving stable equilibrium $e_1(s)$ for some time interval, then track $e_2(s)$ intermediately but return to track $e_1(s)$ and still converge to $\tilde{e}_1^+$, where R-B-tipping happens [Fig. 4.39(c)]. The first *critical range of* r corresponds to the first maximum canard that gives a computable condition for the critical transition

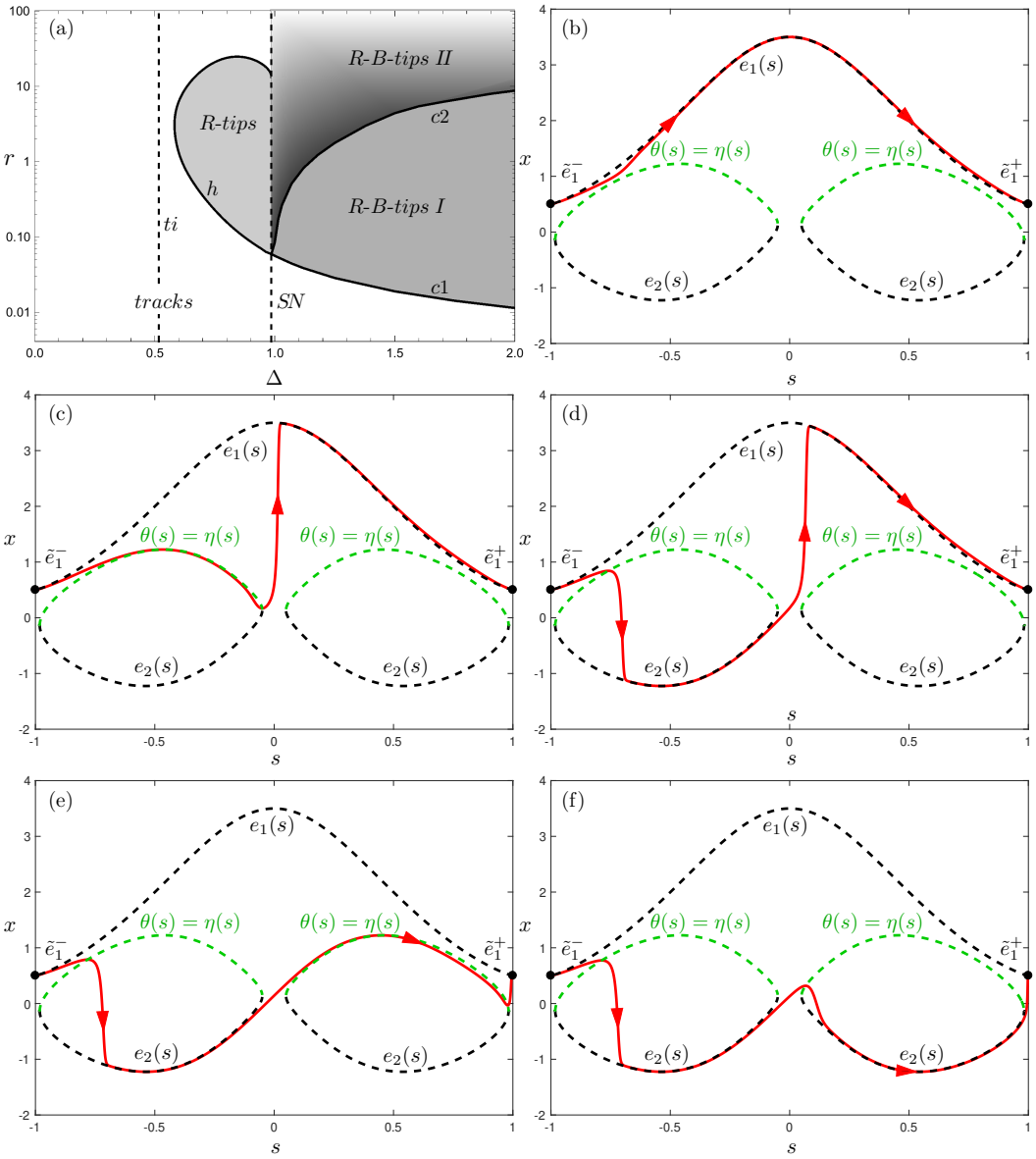

Figure 4.39: (a) The (Δ, r) tipping diagram for the canonical example (4.71) with monotone external input (4.73) contains regions of (white) tracking the moving stable equilibrium $e_1(rt)$ continuously and (grey) R-tipping. The (dashed) ti line denotes the forward threshold instability boundary for e_1, and SN line indicates where saddle-node bifurcation of θ and e_2 happens. We use h to represent transition curve due to the condition of the heteroclinic connection, and c_1 and c_2 to represent the transition curves due to two maximum canards. (b)-(f) Phase states of system (4.79) in red when $\alpha = 1/1.2$ and $\Delta = 1$ for different rates $r =$ (b) 0.05, (c) 0.0560157, (d) 0.07, (e) 0.084067, and (f) 0.09. The moving stable states $e_1(s)$ and $e_2(s)$ are indicated by the dashed black curves, and the moving unstable state $\theta(s)$, namely the moving threshold, indicated by the green dashed curve.

between this tracking and R-B-tipping, which can be solved by a boundary value problem [123] in AUTO [110] as we introduce before. Such a condition can be

computed for different values of Δ so as to gain curve $c1$ part of (Δ, r) tipping diagram when Δ is larger than SN line shown in Fig. 4.39(a). Recall that SN line indicates where saddle-node bifurcation of θ and e_2 happens, namely when Δ is larger than SN line only e_1 exists all the time, while when Δ is smaller than SN line, there are always three equilibria e_1, θ and e_2. In such a case, since the regular threshold θ and another stable equilibrium e_2 are persistent all the time, the ensuing R-B-tipping turns out to be irreversible e_1-to-e_2 R-tipping. As a result, we calculate the critical rate r_c given by the heteroclinic connection from $\tilde{e}_1^-$ to the edge state (namely the threshold itself) at $\{s = 1\}$ through the Lin's method [109], which can be continued on (Δ, r) parameter space to gain curve h part of (Δ, r) tipping diagram when Δ is smaller than SN line [Fig. 4.39(a)]. This is similar to our canonical example I in Section 4.2.

As r increases, there is an open half-circle of initial states centred at $\tilde{e}_1^-$, all of which track the moving stable equilibrium $e_1(s)$ for some time interval, then track $e_2(s)$ intermediately but return to track $e_1(s)$ with the final convergence to $\tilde{e}_1^+$ [Fig. 4.39(d)]. As r is increased until the second *critical range of* r, any open half-circle of initial states centred at $\tilde{e}_1^-$ contains initial states those track the moving stable equilibrium $e_1(s)$ for some time interval, then track $e_2(s)$ intermediately but return to track $e_1(s)$ and converge to $\tilde{e}_1^+$, as well as initial states those track the moving stable equilibrium $e_1(s)$ for some time interval, then track $e_2(s)$ intermediately without returning to track $e_1(s)$ but still converge to $\tilde{e}_1^+$ [Fig. 4.39(e)]. The second *critical range of* r corresponds to the second maximum canard that gives a computable condition for this critical transition, which can be solved by a boundary value problem [123] in AUTO [110] as we introduce before. Such a condition can be computed for different values of Δ so as to gain curve $c2$ part of (Δ, r) tipping diagram when Δ is larger than SN line shown in Fig. 4.39(a).

For higher r, there is an open half-circle of initial states centred at $\tilde{e}_1^-$, all of which track the moving stable equilibrium $e_1(s)$ for some time interval, then track $e_2(s)$ intermediately without returning to track $e_1(s)$ but still converge to $\tilde{e}_1^+$, namely with the shape of a "double well" shown in Fig. 4.39(f). We do not show the case when r is even larger, where the system has no time to respond to the appearance and disappearance of the moving threshold $\theta(s)$ and the moving stable state $e_2(s)$. Instead, in Fig. 4.39(a) we mark the R-B-tipping area with gradient color to present the fact that as the rate r continues to increase after the second R-B-tipping, the system gradually ignores θ and e_2. Note that, as Δ increases, the transition condition of heteroclinic connection for irreversible R-tipping turns into two maximum canards for R-B-tipping.

This example shows that when the moving thresholds (regular thresholds) do

not exist in the future limit beyond our theory, the concepts of our theory are still useful. Instead of studying the connecting orbits based on the R-tipping edge state in the future limit, here we can analyze R-tipping in terms of maximum canards. In fact, we can interpret the connecting orbits as the maximum canards when we analyze R-tipping due to regular thresholds. For example, the heteroclinic orbit that connects two saddle equilibria actually needs infinite integration time, and now has the global maximum integration time and can be seen as the maximum canard. For R-tipping due to quasithresholds, we do not require any R-tipping edge state in the future limit, and the nonautonomous R-tipping thresholds are the relevant canards and their stable sets.

In this chapter, we propose the bottom-up approach [Fig. 4.1] to study different R-tipping mechanisms by the exploration of the canonical examples. We demonstrate that the corresponding frozen system and the nonautonomous terms have useful information for R-tipping instability analysis of the original nonautonomous system, and distinguish two threshold types including regular thresholds and quasithresholds. Furthermore, based on the two types of thresholds, we study the nonautonomous R-tipping thresholds in terms of respectively the connecting orbits (R-tipping due to regular thresholds, requires external input asymptotically constant and compactification), and the folded singularities and maximum canards (R-tipping due to quasithresholds, does not require external input asymptotically constant or compactification). For both cases, we illustrate the nonautonomous R-tipping thresholds and the testable criteria for the occurrence of R-tipping in the nonauotonomous system. In addition, one example of R-B-tipping due to regular thresholds is also included to show the R-tipping phenomenon that our theory does not capture, but still can be studied in terms of the maximum canards.

Chapter 5

Conclusion

R-tipping is a genuine instability of nonautonomous system, which has been studied mainly in three aspects in the past: by relating nonautonomous system to autonomous system [18, 44]; by using the theory of nonautonomous dynamical systems [53, 54, 22]; by studying specific R-tipping thresholds for example non-obvious tipping thresholds in slow-fast systems [24, 51], or specific R-tipping indicators for example Steklov averages and Lyapunov vectors [62]. This thesis extends the previous work on R-tipping and provides an applicable mathematical framework that should be accessible to applied scientists with basic background in autonomous dynamical systems and numerical continuation.

We have presented a theoretical framework for analysing nonautonomous ODEs where nonautonomous terms need not be monotone but vary between two asymptotic values. We refer to such equations as asymptotically autonomous ODEs. The theoretical work is directly motivated by a wide range of problems from applications including pullback attractors, rate-induced critical transitions and nonlinear wave solutions, that fit naturally into the asymptotically autonomous setting and can be simplified by compactification. The analysis is based on a suitable compactification technique developed in Chapter 2 in conjunction with a dynamical system approach to studying the ensuing autonomous compactified system.

The main obstacle to the analysis of the original nonautonomous system is the absence of compact invariant sets, such as equilibria, limit cycles or tori, in its phase space. The basic idea to overcome this obstacle is twofold:

- *Introduce compact invariant sets to the problem:* the original nonautonomous system is reformulated into an autonomous compactified system by augmenting the phase space with an additional bounded variable and then extending the augmented vector field to flow-invariant subspaces that carry autonomous dynamics and compact invariant sets of the limit systems from

infinity.

- *Use autonomous dynamics and compact invariant sets of the limit systems from infinity to analyse the original nonautonomous system:* the solutions of interest are contained in invariant manifolds of saddles for the limit systems when embedded in the extended phase space of the compactified system.

In Chapter 2, we include the theoretical work of compactification for asymptotically autonomous systems. Asymptotically autonomous systems have been studied in the past in terms of asymptotic equivalence of two separate systems: the nonautonomous system (1.3) and the future limit system (3.1) [66, 82, 101]. Our approach is based on a compactified system (2.61)–(2.64) after the suitable compactification that contains the dynamics of (1.3), as well as the dynamics of (3.1) together with its compact invariant sets. We give rigorous statements on optimal sufficient conditions for the existence of compactification, derive two testable criteria for the compactified system to be continuously differentiable on the extended phase space, and construct examples of parametrised compactifications that can be implemented in actual practice. Most importantly, we show the compactification can greatly facilitate theoretical and numerical analysis of asymptotically autonomous differential equations. Extension of the compactification technique to other problems such as exponential dichotomies or infinite dimensions for PDEs remains an interesting research question for future study.

In Chapter 3, as we utilize the information and properties from the corresponding frozen system (1.2) and the nonautonomous terms, we define the necessary concepts of our framework including the parameter path, the moving stable equilibrium, regular threshold, singular limit threshold, quasithreshold, edge state, moving threshold and moving edge state, and threshold instability, and give testable criteria for R-tipping. Our notion of a regular threshold is in line with the concepts of "excitability thresholds" for excitable systems [96, 97], and "multi-basin boundaries" and "edge states" [98, 99, 100] for multistable systems, while a quasithreshold typically exists in slow-fast systems. The threshold instabilities for the corresponding frozen system are important indicators of R-tipping instabilities in the original nonautonomous system, which we illustrate in Chapter 4. These concepts and criteria extend the previous work of R-tipping [18, 44, 24, 51] in arbitrary dimension and are applicable to reversible R-tipping as well, and construct the basics of our framework to analyze R-tipping instabilities in the nonautonomous system.

In Chapter 4, based on the developed compactification techniques in Chapter 2 and the prescribed concepts in Chapter 3, we work on the analysis of R-tipping instabilities in a series of compactified systems of designed nonautonomous sys-

tems, which we refer to canonical examples. The design of these canonical examples is guided by several properties. In particular, besides the types of thresholds (regular thresholds vs. quasithresholds) and types of R-tipping (reversible vs. irreversible), we also include system dimension and timescales, and propose a bottom-up approach of R-tipping analysis in practice, which directs seven possible paths of R-tipping generations based on these properties [Fig. 4.1]. As a result, we design the canonical examples of R-tipping to cover theses possible generations of R-tipping, and highlight different characteristics. We always include the threshold instability analysis at first given the prescribed parameter paths P_λ and then analyze the nonautonomous R-tipping thresholds for these examples.

Canonical example I, II, III, IV are typically designed to show the cases of R-tipping due to regular thresholds with the consideration of monotone and non-monotone external input, during which we give the nonautonomous R-tipping threshold as the stable manifold of the R-tipping edge state. The regular thresholds with their edge states persist all the time in these examples. Canonical example I [Section 4.2] shows the case of irreversible R-tipping that is due to regular thresholds in one dimension. This example is in line with the theory that forward basin stability excludes R-tipping and forward basin instability is necessary for R-tipping in one-dimensional systems [44, Th.3.2]. Here we use the notion of threshold, which is defined in a more general context and embraces the definition of basin of attraction; see Definition 3.2.3, Definition 3.2.4, and Definition 3.2.5. Canonical example II [Section 4.3] gives a system of reversible R-tipping that is due to regular thresholds in one dimension. We leave out the R-tipping analysis in this example because of the simplicity and similarity to canonical example I.

Canonical example III [Section 4.4] shows the case of irreversible R-tipping that is due to regular thresholds in two dimensions with single-timescale, possibly multiple-timescale. This example gives a numerical demonstration that the theory for one-dimensional systems [44, Th.3.2] is not applicable for higher dimensional systems. That is to say, in higher dimensional systems neither forward basin stability can exclude R-tipping, nor forward basin instability can guarantee R-tipping. Instead, here we show the threshold instability is a good indicator for R-tipping instabilities. Because of the two-dimensional parameter paths P_λ, the threshold instability analysis here is more complex and nontrivial than that in canonical example I in one dimension.

Canonical example IV [Section 4.5] presents the case of reversible R-tipping that is due to regular thresholds in two dimensions with single-timescale. This example highlights the phenomenon of reversible R-tipping, illustrates that the

thresholds of excitability [114] are in line with our notion of regular thresholds, and shows the possibilities of multi-pulse R-tipping akin to excited pulses [120] and spike-adding mechanisms [125], and demonstrates the effects of the 'winding' thresholds on the nested multiple R-tipping transitions; see Fig. 4.15(a) and Fig. 4.17(a).

Canonical example V [Section 4.6] is typically designed to show the case of reversible R-tipping due to quasithresholds. We give the nonautonomous R-tipping thresholds as the relevant canards and their stable sets under the cases of isolated folded saddle and folded saddle-node type-I [105, 107, 104] respectively, which presents more views of exact dynamical mechanisms of R-tipping associated with those canards [51]. This example presents a slow-fast system, where quasithresholds typically exist. In fact, an asymptotically constant external input and a compactification are not required here. However, to study the interaction between the invariant sets and the folded singularities, we still consider those external inputs. We show that after the compactification and desingularisation, the singular R-tipping thresholds namely the singular canards for $\epsilon = 0$, give good approximations of those nonautonomous R-tipping thresholds for $0 < \epsilon \ll 1$, which are the canards. In particular, we illustrate that R-tipping corresponds to the infinite-time bifurcations of those canards, resulting in two cases of simple and complicated R-tipping quasithresholds respectively. As the regular thresholds have edge states, we interpret the relevant folded singularities as the edge states of the singular R-tipping thresholds. Canonical example VI [Section 4.7] also gives a system of reversible R-tipping in two dimensions but due to regular thresholds. We leave out the R-tipping analysis in this example because of the simplicity.

In contrast to canonical example V [Section 4.6], we design canonical exmaple VII [Section 4.8] to present the case of irreversible R-tipping due to regular thresholds in a slow-fast system. Now the regular thresholds have the edge states, and nonautonomous R-tipping threshold is again given by the stable manifold of the R-tipping edge state. Moreover, we show that the nonautonomous R-tipping threshold can still be studied in terms of the folded singularities and canards, while the relevant canards are contained in the stable invariant manifold of the R-tipping edge state.

Canonical example of R-B-tipping [Section 4.9] is the last example we give. All the examples of R-tipping due to regular thresholds above have the thresholds and edge states all the time, and the nonautonomous tipping threshold is given as the stable manifold of the R-tipping edge state in the future limit. This example presents a case of R-tipping where the regular threshold and its edge state do

not exist in the future limit, during which we give the nonautonomous R-tipping thresholds as the maximum canards, and the concepts of our framework such as moving equilibria, moving thresholds, and threshold instability are still useful here. We also include the R-tipping mechanism transition between the existence and disappearance of the regular threshold and its edge state in the future limit; see Fig 4.36(a) and Fig 4.39(a).

Then we summarize the two scenarios:

- when the moving thresholds (regular thresholds) always exist until the future limit, or R-tipping is associated with quasithresholds, our theory covers these, and the prescribed concepts and methods greatly simplify the analysis of R-tipping.
- when the moving thresholds (regular thresholds) do not exist in the future limit or R-tipping is not associated with any quasithreshold, the concepts of the moving equilibria and threshold instability are still useful while R-tipping may be studied in terms of the maximum canards. The computation can be much more complex than that in our example of R-B-tipping, which really depends on the systems and problems at hand.

In our framework, we give nonautonomous R-tipping thresholds and rigorous criteria to check whether R-tipping happens or not for a given initial condition, which can be done in terms of the nonautonomous R-tipping thresholds crossing the initial condition transversely. Moreover, Conjecture 3.1 gives quick testable criteria to check if there is any possibility of R-tipping given an arbitrary system. However, since our concepts only cover regular thresholds and quasithresholds, and exclude other specific cases such as "strange" attractors, and fractal basin boundaries and thresholds, it leaves an open question about the theory to deal with more general attractors and thresholds. As we distinguish R-tipping as irreversible and reversible, there can be some other types of R-tipping, e.g. partial tipping and weak tracking [55], which need more theoretical work to identify such types of R-tipping. Besides the theoretical aspects, we may pay more attention to the applications of R-tipping analysis in the future study, especially in climate, ecology, and biology. As bifurcation analysis appears in many courses of dynamical system theories in graduate programs, R-tipping analysis based on our framework can provide an easier access for these students and applied scientists to understand another mechanism of dynamical instability. The scientist community may utilize our framework in the education of R-tipping instabilities in dynamical systems, and promote more researchers to work on this topic.

References

[1] T.M. Lenton. Early warning of climate tipping points. *Nature Climate Change*, 1(4):201, 2011.

[2] H.A. Dijkstra. *Dynamical Oceanography*. Springer, Berlin, 2008.

[3] J.B. Smith, S.H. Schneider, M. Oppenheimer, G.W. Yohe, W. Hare, M.D. Mastrandrea, A. Patwardhan, I. Burton, J. Corfee-Morlot, C.H.D. Magadza, H.M. Füssel, A.B. Pittock, A. Rahman, A. Suarez, and J.P. van Ypersele. Assessing dangerous climate change through an update of the Intergovernmental Panel on Climate Change (IPCC) "reasons for concern". *Proc. Natl Acad. Sci. USA*, **106**:4133–4137, 2009.

[4] C.A. Boulton, L.C. Allison, and T.M. Lenton. Early warning signals of Atlantic Meridional Overturning Circulation collapse in a fully coupled climate model. *Nature Communications*, **5**(5752), 2014.

[5] A.V. Hill. Excitation and accomodation in nerve. *Proc. R. Soc. Lond. B*, **119**(814):305–355, 1936.

[6] AL Hodgkin. The local electric changes associated with repetitive action in a non-medullated axon. *The Journal of physiology*, **107**(2):165–81, 1948.

[7] C.J. Sherr and J.M. Roberts. Living with or without cyclins and cyclin-dependent kinases. *Genes & Dev.*, **18**:2699–2711, 2004.

[8] C. Bertoli, J.M. Skotheim, and R.A.M. de Bruin. Control of cell cycle transcription during G1 and S phases. *Nat Rev Mol Cell Biol*, **14**(8):518–528, 2013.

[9] J. Mitry, M. McCarthy, N. Kopell, and M. Wechselberger. Excitable neurons, firing threshold manifolds and canards. *Journal of Mathematical Neuroscience*, **3**:14, 2013.

[10] M. Scheffer. *Critical Transitions in Nature and Society*. Princeton University Press, Princeton, 2009.

[11] M. Scheffer, J. Bascompte, W.A. Brock, V. Brovkin, S.R. Carpenter, V. Dakos, H. Held, E.H. Van Nes, M. Rietkerk, and G. Sugihara. Early-warning signals for critical transitions. *Nature*, **461**(7260):53, 2009.

[12] M. Scheffer, E.H. Van Nes, M. Holmgren, and T. Hughes. Pulse-driven loss of top-down control: the critical-rate hypothesis. *Ecosystems*, **11**(2):226–237, 2008.

[13] P.E. O'Keeffe and S. Wieczorek. Tipping phenomena and points of no return in ecosystems: Beyond classical bifurcations. *arXiv:1902.01796*, 2019.

[14] I. Dobson and H.D. Chiang. Toward a theory of voltage collapse in electric-power systems. *Syst. Control Lett.*, **13**:253–262, 1989.

[15] C.J. Budd and J.P. Wilson. Bogdanov-takens bifurcation points and sil'nikov homoclinicity in a simple power-system model of voltage collapse. *IEEE Transactions on Circuits and Systems I: Fundamental Theory and Applications*, **49**(5):575–590, 2002.

[16] T. Kotoyori. *Critical Temperatures for the Thermal Explosion of Chemicals*. Industrial Safety Series, Volume 7, 2005.

[17] N.A. Alexander, O. Oddbjornsson, C.A. Taylor, H.M. Osinga, and D.E. Kelly. Exploring the dynamics of a class of post-tensioned, moment resisting frames. *Journal of Sound and Vibration*, **330**(15):3710–3728, 2011.

[18] P. Ashwin, S. Wieczorek, R. Vitolo, and P. Cox. Tipping points in open systems: bifurcation, noise-induced, and rate-dependent examples in the climate system. *Phil. Trans. Roy. Soc. A*, **370**:1166–1184, 2012.

[19] J.M.T. Thompson and J. Sieber. Predicting climate tipping as a noisy bifurcation: a review. *International Journal of Bifurcation and Chaos*, **21**(2):399–423, 2011.

[20] C. Kuehn. A mathematical framework for critical transitions: Bifurcations, fast-slow systems and stochastic dynamics. *Physica D*, **240**:1020–1035, 2011.

[21] E. Benoit (Ed.). *Lecture Notes in Math. 1493*. Springer, New York, 1991.

[22] M. Rasmussen. *Attractivity and Bifurcation for Nonautonomous Dynamical Systems*. Lecture Notes in Mathematics 1907, Springer, 2007.

[23] J.T. Morris, P.V. Sundareshwar, C.T. Nietch, B. Kjerfe, and D.R. Cahoon. Responses of coastal wetlands to rising sea level. *Ecology*, **83**(10):2869–2877, 2002.

[24] S. Wieczorek, P. Ashwin, C.M. Luke, and P.M. Cox. Excitability in ramped systems: the compost-bomb instability. *Proc. Roy. Soc. A*, **467**:1215–1242, 2011.

[25] K. Siteur, M.B. Eppinga, A. Doelman, E. Sierro, and M. Rietkerk. Ecosystems off track: rate-induced critical transitions in ecological models. *Oikos*, **125**(12):1689–1699, 2016.

[26] A. Vanselow, S. Wieczorek, and U. Feudel. When very slow is too fast - collapse of a predator-prey system. *Journal of Theoretical Biology*, **479**:64–72, 2019.

[27] E. Ott. *Chaos in Dynamical Systems*. Cambridge University Press, 1993.

[28] G. Buzsáki and A. Draguhn. Neuronal oscillations in cortical networks. *Science*, **304**:1926, 2004.

[29] M.T. Keating and M.C. Sanguinetti. Molecular and cellular mechanisms of cardiac arrhythmias. *Cell*, **104**(4):569–580, 2001.

[30] P.D. Ditlevsen and S. Johnsen. Tipping points: early warning and wishful thinking. *Geophys. Res. Letters*, **37**:L19703, 2010.

[31] W. Yan, R. Woodard, and D. Sornette. Diagnosis and prediction of tipping points in financial markets: Crashes and rebounds. *Physics Procedia*, **3**(5):1641–1657, 2010.

[32] HC Fogedby. Damped finite-time singularity driven by noise. *Phys Rev E Stat Nonlin Soft Matter Phys.*, **68**(5 Pt 1):051105, 2003.

[33] D. Smug, P. Ashwin, and D. Sornette. Predicting financial market crashes using ghost singularities. *PLoS ONE*, **13**(3):e0195265, 2018.

[34] R. Liu, P. Chen, K. Aihara, and L. Chen. Identifying early-warning signals of critical transitions with strong noise by dynamical network markers. *Scientific Reports*, **5**:17501, 2015.

[35] C.M. Luke and P.M. Cox. Soil carbon and climate change: from the jenkinson effect to the compost bomb instability. *European Journal of Soil Science*, **62**(1):5–12, 2011.

[36] R. Leemans and B. Eickhout. Another reason for concern: regional and global impacts on ecosystems for different levels of climate change. *Global Environmental Change*, **14**(3):219–228, 2004.

[37] T. Jezkova and J.J. Wiens. Rates of change in climatic niches in plant and animal populations are much slower than projected climate change. *Proc. R. Soc. B.*, **283**(1843), 2016.

[38] H. Wang, H. Zhang, R. Hu, E. Yao, and P. Guo. Estimation of the critical rate of temperature rise for thermal explosion of nitrocellulose using non-isothermal DSC. *J Therm Anal Calorim*, (115):1099–1110, 2013.

[39] A. Bahadori and A. Nouri. Prediction of critical oil rate for bottom water coning in anisotropic and homogeneous formations. *Journal of Petroleum Science and Engineering*, **82—83**:125–129, 2010.

[40] S.Y. Hsu and M.H. Shih. The tendency toward a moving equilibrium. *SIAM J. Appl. Dyn. Syst.*, **14**(4):1699—-1730, 2015.

[41] I. Idris and V.N. Biktashev. Critical fronts in initiation of excitation wave. *Phys Rev E*, **76**:021906, 2007.

[42] C. Hobbs, P. Ashwin, S. Wieczorek, R. Vitolo, and P. Cox. Tipping points in open systems: bifurcation, noise-induced, and rate-dependent examples in the climate system: Corrected version. *Phil. Trans. Roy. Soc. A*, 2013.

[43] C.G. Perryman. *How fast is too fast? Rate-induced bifurcations in multiple time-scale systems*. Ph.D. thesis, University of Exeter, 2015.

[44] P. Ashwin, C. Perryman, and S. Wieczorek. Parameter shifts for nonautonomous systems in low dimension: bifurcation- and rate-induced tipping. *Nonlinearity*, **30**(6):2185–2210, 2017.

[45] Z. Bishnani and R.S. MacKay. Safety criteria for aperiodically forced systems. *Dynamical Systems: An International Journal*, **18**(2):107–129, 2003.

[46] H. Osinga. Computing failure boundaries by continuation of a two-point boundary value problem. *Proc. of the 9th Int. Conf. on Structural Dynamics, EURODYN 2014, Porto, Portugal, 30 June–2 July*, pages 1891–1897, 2014.

[47] N. Fenichel. Geometric singular perturbation theory for ordinary differential equations. *J. Differential Equations*, **31**:53–98, 1979.

[48] L.P. Hansen and T.J. Sargent. Robust control and model uncertainty. *The American Economic Review*, **91**(2):60–66, 2001.

[49] A. Bemporad and M. Morari. Robust model predictive control: A survey. *Robustness in identification and control*, **245**:207–226, 1999.

[50] G. Galdos, A. Karimi, and R. Longchamp. Robust controller design by convex optimization based on finite frequency samples of spectral models.

49th IEEE Conference on Decision and Control (CDC), pages 4317–4322, 2010.

[51] C.G. Perryman and S. Wieczorek. Adapting to a changing environment: Non-obvious thresholds in multi-scale systems. *Proc. Roy. Soc. A*, **470**:20140226, 2014.

[52] L. Arnold. *Random Dynamical Systems*. Springer Monographs in Mathematics, Berlin, 1998.

[53] P. Kloeden and M. Rasmussen. Nonautonomous dynamical systems. *AMS Mathematical Surveys and Monographs*, **176**, 2011.

[54] C. Pötzsche. Nonautonomous bifurcation of bounded solutions i: a lyapunov-schmidt approach. *Discrete Contin. Dyn. Syst. Ser. B*, **14**(2):739–776, 2010.

[55] H. Alkhayuon and P. Ashwin. Rate-induced tipping from periodic attractors: Partial tipping and connecting orbits. *Chaos*, **28**, 033608, 2018.

[56] C.K.R.T. Jones. Geometric singular perturbation theory. *In: Johnson R. (eds) Dynamical Systems. Lecture Notes in Mathematics*, **1609**:44–118, 1995.

[57] P. Szmolyan and M. Wechselberger. Relaxation oscillations in $\mathbb{R}^3$. *Journal of Differential Equations*, **200**:69–104, 2004.

[58] M. Wechselberger. A propos de canards (apropos canards). *Transactions of the American Mathematical Society*, **364**(6):3289–3309, 2012.

[59] P. Ritchie and J. Sieber. Early-warning indicators for rate-induced tipping. *Choas*, **26**(9):093116, 2016.

[60] P. Ritchie and J. Sieber. Early-warning indicators in the dynamic regime. *arXiv:1609.07271*, 2016.

[61] P. Gienapp, M. Lof, T.E. Reed, J. McNamara, S. Verhulst, and M.E. Visser. Predicting demographically sustainable rates of adaptation: can great tit breeding time keep pace with climate change? *Phil. Trans. R. Soc. B*, **368**, 2013.

[62] A. Hoyer-Leitzel, A. Nadeau, A. Roberts, and A. Steyer. Detecting transient rate-tipping using steklov averages and lyapunov vectors. *arXiv:1702.02955*, 2018.

[63] S. Wieczorek, C. Xie, and P. Ashwin. Rate-Induced Tipping: Thresholds, Edge States and Testable Criteria. *preprint*, 2020.

[64] S. Wieczorek, C. Xie, and C.K.R.T. Jones. Compactification for Asymptotically Autonomous Dynamical Systems: Theory, Applications and Invariant Manifolds. *arXiv:2001.08733 [math.DS]*, 2020.

[65] C. Xie and S. Wieczorek. Rate-Induced Tipping: Canonical Examples, Connecting Orbits and Canards. *preprint*, 2020.

[66] L. Markus. Asymptotically autonomous differential systems. *Contributions to. Non-linear Oscillations*, **Vol. 3**, Princeton, NJ:Princeton University Press 17–29, 1956.

[67] J. Delgado, E.A. Lacomba, J. Llibre, and E. Pérez. *Poincaré Compactification of Hamiltonian Polynomial Vector Fields. In: Dumas H.S., Meyer K.S., Schmidt D.S. (eds) Hamiltonian Dynamical Systems*. The IMA Volumes in Mathematics and its Applications, vol 63. Springer, New York, 1995.

[68] B. Krauskopf. Bifurcations at ∞ in a model for 1:4 resonance. *Ergod. Th. & Dynam. Sys.*, **17**:899–931, 1997.

[69] F. Dumortier. Compactification and desingularization of spaces of polynomial Liénard equations. *J. Differential Equations*, **224**:296–313, 2006.

[70] M. Messaias. Dynamics at infinity and the existence of singularly degenerate heteroclinic cycles in the Lorenz system. *J. Phys. A: Math. Theor.*, **42**:115101, 2009.

[71] K. Matsue. On Blow-Up Solutions of Differential Equations with Poincaré-Type Compactifications. *SIAM Journal on Applied Dynamical Systems*, **17** (3):2249–2288, 2018.

[72] A. Giraldo, B. Krauskopf, and H.M. Osinga. Cascades of Global Bifurcations and Chaos near a Homoclinic Flip Bifurcation: A Case Study. *SIAM Journal on Applied Dynamical Systems*, **17** (4):2784–2829, 2018.

[73] R. McGehee. Triple collision in the collinear three-body problem. *Inventiones mathematicae*, **27**(3):191–227, 1974.

[74] F. Dumortier. Techniques in the theory of local bifurcations: Blow-up, normal forms, nilpotent bifurcations, singular perturbations. *Bifurcations and periodic orbits of vector fields*, Springer, Dordrecht, 19–73, 1993.

[75] M. Krupa and P. Szmolyan. Extending geometric singular perturbation theory to nonhyperbolic points—fold and canard points in two dimensions. *SIAM Journal on Mathematical Analysis*, **33**(2):286–314, 2001.

[76] P. Szmolyan and M. Wechselberger. Canards in $\mathbb{R}^3$. *Journal of Differential Equations*, **177**(2):419–453, 2001.

[77] I. Kosiuk and P. Szmolyan. Scaling in singular perturbation problems: blowing up a relaxation oscillator. *SIAM Journal on Applied Dynamical Systems*, **10**(4):1307–1343, 2011.

[78] C. Kuehn. Normal hyperbolicity and unbounded critical manifolds. *Nonlinearity*, **27**:1351–1366, 2014.

[79] K.U. Kristiansen. Blowup for flat slow manifolds. *Nonlinearity*, **30**:2138–2184, 2017.

[80] J.A. Langa, J.C. Robinson, and A. Suárez. Forwards and pullback behaviour of a non-autonomous lotka–volterra system. *Nonlinearity*, **16**(4):1277–1293, 2003.

[81] M. Rasmussen. Bifurcations of asymptotically autonomous differential equations. *Set-Valued Analysis*, **16**(7-8):821–849, 2008.

[82] H.R. Thieme. Asymptotically autonomous differential equations in the plane. *Rocky Mountain J. Math.*, **24**(1):351–380, 1993.

[83] J.C. Robinson. The asymptotic completeness of inertial manifolds. *Nonlinearity*, **9**:1325–1340, 1996.

[84] B. Aulbach, M. Rasmussen, and S. Siegmund. Invariant manifolds as pullback attractors of nonautonomous differential equations. *Discrete & Contin. Dyn. Syst. - A*, **15**(2):579–596, 2006.

[85] C. Kiers and C.K.R.T. Jones. On conditions for rate-induced tipping in multi-dimensional dynamical systems. *arXiv:1810.02808*, 2018.

[86] H. Alkhayuon, P. Ashwin, L.C. Jackson, C. Quinn, and R.A. Wood. Basin bifurcations, oscillatory instability and rate-induced thresholds for atlantic meridional overturning circulation in a global oceanic box model. *Proceedings of the Royal Society A*, **475** (2225):20190051, 2019.

[87] C. Jones and T. Küpper. On the infinitely many solutions of a semilinear elliptic equation. *SIAM Journal on Mathematical Analysis*, **17** (4):803–835, 1986.

[88] A. Scheel. Radially symmetric patterns of reaction-diffusion systems. *MEM. AMER. MATH. SOC*, **165**, 2003.

[89] T. Tao. A pseudoconformal compactification of the nonlinear Schrödinger equation and applications. *New York J. Math.*, **15**:265–282, 2009.

[90] R. Carles. Critical nonlinear Schrödinger equations with and without harmonic potential. *Mathematical Models and Methods in Applied Sciences*, **12** (10):1513–1523, 2002.

[91] B. Blackadar. A general implicit/inverse function theorem. *arXiv:1509.06025 [math.CA]*, 2015.

[92] S. Lang. *Differential Manifolds*. Springer New York, 2 edn, 1985.

[93] M. Spivak. *Calculus on Manifolds: A Modern Approach to Classical Theorems of Advanced Calculus*. Advanced book program. Avalon Publishing, 1965.

[94] P. Ashwin, J. Buescu, and I. Stewart. From attractor to chaotic saddle: a tale of transverse instability. *Nonlinearity*, **9** (3):703–737, 1996.

[95] C. Kuehn. *Multiple Time Scale Dynamics*. Springer Applied Math. Sci., 2015.

[96] R. FitzHugh. Mathematical models of threshold phenomena in the nerve membrane. *Bull. Math. Biophys.*, **17**:257–278, 1955.

[97] E.M. Izhikevich. *Dynamical systems in neuroscience*. MIT press, 2007.

[98] J.D. Skufka, J.A. Yorke, and B. Eckhardt. Edge of chaos in a parallel shear flow. *Phys. Rev. Lett.*, **96**:174101, 2006.

[99] T.M. Schneider, B. Eckhardt, and J.A. Yorke. Turbulence transition and the edge of chaos in pipe flow. *Physical review letters*, **99**:034502, 2007.

[100] T.M. Schneider, D. Marinc, and B. Eckhardt. Localized edge states nucleate turbulence in extended plane couette cells. *Journal of Fluid Mechanics*, **646**:441–451, 2010.

[101] C. Robinson. *Dynamical systems: stability, symbolic dynamics, and chaos*. CRC press, 1999.

[102] J. Aguirre, R.L. Viana, and M.A.F. Sanjuán. Fractal structures in nonlinear dynamics. *Rev. Mod. Phys.*, **81**(13-14):333–382, 2009.

[103] M. Wechselberger, J. Mitry, and J. Rinzel. *Canard theory and excitability*. In Nonautonomous Dynamical Systems in the Life Sciences (Vol. 2102, pp. 89-132). (Lecture Notes in Mathematics; Vol. 2102). Springer Verlag, 2013.

[104] T. Vo and M. Wechselberger. Canards of folded saddle-node type I. *SIAM J. Math. Anal.*, **47**(4):3235–3283, 2015.

[105] M. Wechselberger. Existence and bifurcation of canards in $\mathbb{R}^3$ in the case of a folded node. *SIAM J. Appl. Dyn. Syst.*, **4**(1):101–139, 2005.

[106] F. Dumortier and R. Roussarie. *Canard cycles and center manifolds*. Memoirs of the American Mathematical Society, Volume 121, Number 577, 1996.

[107] M. Krupa and M. Wechselberger. Local analysis near a folded saddle-node singularity. *J. Diff. Equ.*, **248**(12):2841–2888, 2010.

[108] M. Desroches, J. Guckenheimer, B. Krauskopf, C. Kuehn, H.M. Osinga, and M. Wechselberger. Mixed-mode oscillations with multiple time scales. *SIAM Rev.*, **54**(2):211–288, 2012.

[109] X.B. Lin. Using melnikov's method to solve silnikov's problems. *Proc. Roy. Soc. Edinburgh*, **116**(3-4):295–325, 1990.

[110] E.J. Doedel and B.E. Oldeman. *Auto-07p: Continuation and Bifurcation Software*. 2012.

[111] J. Guckenheimer, K. Hoffman, and W. Weckesser. The Forced van der Pol Equation I: The Slow Flow and Its Bifurcations. *SIAM J. Applied Dynamical Systems*, **2**(1):1–35, 2003.

[112] B. Krauskopf and T. Rieß. A lin's method approach to finding and continuing heteroclinic connections involving periodic orbits. *Nonlinearity*, **21**(8):1655–1690, 2008.

[113] M.C. Eguia, G.B. Mindlin, and M. Giudici. Low-frequency fluctuations in semiconductor lasers with optical feedback are induced with noise. *Physical Review E*, **58**(2):2636–2639, 1998.

[114] A.C. Ventura, G.B. Mindlin, and S.P. Dawson. Generic two-variable model of excitability. *Physical Review E*, **65**(4):046231, 2002.

[115] Y.A. Kuznetsov. *Elements of Applied Bifurcation Theory*. Springer New York, 2004.

[116] S. Wieczorek, T. B. Simpson, B. Krauskopf, and D. Lenstra. Bifurcation transitions in an optically injected diode laser: theory and experiment. *Optics Communications*, **215**(1-3):125–134, 2003.

[117] W. Coomans, L. Gelens, S. Beri, J. Danckaert, and G. Van der Sande. Solitary and coupled semiconductor ring lasers as optical spiking neurons. *Phys. Rev. E*, **84**:036209, 2011.

[118] H.B. Keller. *Numerical Solution of Two Point Boundary Value Problems*. Society for Industrial and Applied Mathematics, 1976.

[119] S. Wieczorek, B. Krauskopf, and D. Lenstra. Multipulse excitability in a semiconductor laser with optical injection. *Phys Rev Lett.*, **88**(6):063901, 2002.

[120] S. Wieczorek and D. Lenstra. Spontaneously excited pulses in an optically driven semiconductor laser. *Phys Rev E Stat Nonlin Soft Matter Phys*, 69:016218, 2004.

[121] M. Desroches, B. Krauskopf, and H. M. Osinga. The geometry of slow manifolds near a folded node. *SIAM J. Appl. Dyn. Syst.*, **7**(4):1131–1162, 2008.

[122] M. Desroches, B. Krauskopf, and H.M. Osinga. Numerical continuation of canard orbits in slow–fast dynamical systems. *Nonlinearity*, **23**(3):73–765, 2010.

[123] P. Langfield, B. Krauskopf, and H.M. Osinga. Solving winfree's puzzle: The isochrons in the fitzhugh-nagumo model. *chaos*, **24**(1):013131, 2014.

[124] E.J. Doedel. Lecture notes on numerical analysis of nonlinear equations. *Numerical Continuation Methods for Dynamical Systems*, pages 1–49, 2007.

[125] S. Farjami, V. Kirk, and H.M. Osinga. Transient spike adding in the presence of equilibria. *Eur. Phys. J. Spec. Top*, **225**(13-14):2601–2612, 2016.